Engineering Analysis with Boundary Elements 176 (2025) 106232

Contents lists available at ScienceDirect

Engineering Analysis with Boundary Elements

journal homepage: www.elsevier.com/locate/enganabound

Thermo-magneto-mechanical analysis of curved laminated structures with arbitrary variation of the material properties and novel recovery procedure

Francesco Tornabene [a,*], Matteo Viscoti [a], Rossana Dimitri [a], Timon Rabczuk [b]

[a] Department of Innovation Engineering, School of Engineering, University of Salento, 73100, Lecce, Italy
[b] Institute of Structural Mechanics, Bauhaus-Universität Weimar, 99423, Weimar, Germany

ARTICLE INFO

Keywords:
Higher-order theories
Generalized Differential Quadrature
Multifield analysis
Recovery procedure
Smart structures
Thermo-magneto-elastic materials
Unified Formulation

ABSTRACT

The paper introduces a novel methodology based on a generalized formulation and higher-order-theories for the fully-coupled multifield analysis of laminated curved structures subjected to thermal, magnetic, and mechanical loads. The formulation follows the Equivalent Single Layer approach, taking into account a generalized through-the-thickness expansion of displacement field components, scalar magnetic potential, and temperature variation with respect to the reference configuration. In addition, specific thickness functions are selected according to the Equivalent Layer Wise methodology, allowing the imposition of particular values of configuration variables in specific regions of the structure. The lamination scheme includes smart materials derived from an analytical homogenization technique, with material properties varying arbitrarily along the thickness direction within each layer. The fundamental relations are derived under thermodynamic equilibrium using curvilinear principal coordinates, and a semi-analytical Navier solution is derived for specific geometric, material, and loading conditions. A recovery procedure using Generalized Differential Quadrature is presented for reconstructing three-dimensional primary and secondary variables. In addition, a novel recovery procedure is presented for the first time, based on a Generalized Integral Quadrature. The model is validated through numerical examples involving straight and curved panels with various multifield load distributions, showing consistency and the computational efficiency when compared to three-dimensional reference solutions. New coupling effects between physical problems are explored, and parametric investigations highlight the influence of key governing parameters. Unlike the existing literature, this paper presents an efficient and accurate methodology for analyzing laminated smart structures of various curvatures with multifield couplings, not usually addressed by commercial software. This theory allows for arbitrary variations in multifield properties without using three-dimensional models that can be computationally expensive. In this way, novel possible design applications of smart materials and structures are offered in many engineering fields.

1. Introduction

Recent advances in various engineering fields [1,2], such as aerospace, biomedical engineering, monitoring systems, energy harvesting, and mechanical applications, have received an increased interest in materials and structures under mechanical loads and multifield actions [3], for which advanced modelling strategies are required for an accurate prediction of their mechanical response [4–6]. In this context, classical homogenization approaches, originally developed for mechanical elasticity problems, have been refined to reduce the computational cost associated with multiscale materials and structures in multifield applications [7]. Smart structures, usually made of laminated materials, are typically studied by using three-dimensional models to obtain an accurate prediction of the multifield response [8–10]. However, this modelling strategy leads to a high number of Degrees of Freedom (DOFs), significantly increasing the computational cost. In addition, many studies in literature address physical phenomena using uncoupled simulations when they are not directly coupled with mechanical elasticity through strain components, as happens, for instance, with thermo-mechanical interactions [11,12]. As a consequence, coupling effects associated with the value assumed by configuration variables are not considered within the simulation. This aspect may potentially result in inaccurate predictions of the structural response to multifield loads. For thin and moderately thick laminates, multifield

* Corresponding author.
E-mail address: francesco.tornabene@unisalento.it (F. Tornabene).

https://doi.org/10.1016/j.enganabound.2025.106232
Received 19 February 2025; Received in revised form 18 March 2025; Accepted 19 March 2025
Available online 28 March 2025

scalar quantities are often modelled with linear or parabolic profiles along the thickness direction [13]. This approach has been shown to align well with experimental results in common engineering applications. However, for more complex cases such as unusual lamination schemes and thick laminated structures, different distributions emerge along the thickness direction, usually with very complex profiles especially at the interface among layers [14,15]. To this end, three-dimensional simulations are usually employed, even though computationally expensive. To mitigate this issue, refined two-dimensional formulations have been introduced in literature which account for higher-order expansion of field variables along the thickness of the shell [16–18]. However, this expansion is highly dependent on the lamination scheme of the structure. As suggested for the first time by Washizu [19] and Reddy [20], variable kinematic models [21,22] can be developed to derive a generalized theory that encompasses a broad range of structural theories within a single formulation, based on the selection of the specific thickness functions. This approach can integrate even classical structural theories, such as classical plate theory, first-order shear deformation theory, and third-order shear deformation theory [23]. Traditional models assume a zero-stretching condition through the thickness direction during bending [24]. In contrast, Higher-order Shear Deformation Theories (HSDTs) introduce power polynomials to describe the variation of field variables along the thickness of the panel. In addition, the zigzag function, first proposed by Murakami [25,26], provides very accurate predictions of the interaction between adjacent laminae, even when the material properties of the neighboring layers vary significantly. By selecting appropriate expressions for the thickness functions, an Equivalent Single Layer (ESL) formulation can be derived, which reduces the three-dimensional solid at its reference surface, located at the middle thickness [27–29]. When Dirichlet boundary conditions are applied to the model, the Layer-Wise (LW) approach is commonly used among two-dimensional theories [30–32]. In the LW methodology, the governing equations are developed for each layer in the stacking sequence, and multifield kinematic compatibility conditions allow for the derivation of equations for the entire laminate. In this way, arbitrary values can be assigned at the external surfaces of the laminate. While effective, this approach can be computational demanding. For this reason, a hybrid method known as the Equivalent Layer-Wise (ELW) has been developed [33–35]. This approach combines the efficiency of ESL theories with the flexibility of LW models by using the thickness functions from LW theories along the overall laminate. As a result, it allows for the application of arbitrary values of multifield configuration variables with a significantly reduced computational effort, especially for an increased number of laminae.

The differential equations governing multifield problems can be solved analytically only in some specific cases with particular geometries, materials, and loading conditions. As a result, numerical methods have been widely adopted to obtain approximate results of engineering relevance. Among these, the Finite Element Method (FEM) is commonly used in various applications [36,37]. Starting from the first works on this topic, in FEM the unknown variables of a differential equation are expressed as local interpolations, within mesh cells, known as finite elements, where the DOFs are associated with the nodes of each element. The interpolating function, or shape function, transforms the differential problem into its weak form [38,39]. However, FEM can be computationally expensive, as it does not ensure a-priori a higher-order compatibility between adjacent elements. The high accuracy of results requires an increased number of elements, which further raises the computational cost. To this end, spectral collocation methods [40,41] have been developed in literature, using a global interpolation of the unknown variables across the entire domain. This approach ensures a higher-order interpolation throughout the physical domain, providing accurate results with fewer sampling points. One of these methods, the Generalized Differential Quadrature (GDQ), approximates derivatives of a function using its values at discrete grid points [42–44]. The weighting coefficients for this method are computed recursively, starting from the properties of Lagrange interpolating polynomials, making the algorithm independent from specific grid distributions [45–47]. Variations of the original GDQ method, such as Harmonic Differential Quadrature and Radial-Bases Differential Quadrature, can also be found in literature [48,49]. The GDQ method directly solves differential equations in their strong form by approximating numerically the derivatives. In the same way, Neumann boundary conditions can be similarly applied in their discrete form. The GDQ method has been widely used in structural applications, including static and vibration analysis of curved laminated panels, structures with non-homogeneous graded materials, fracture mechanics, and time history analysis, among others [50–53].

Moving from the GDQ numerical technique, the Generalized Integral Quadrature (GIQ) method offers an efficient approach for numerically evaluating the integral of a given function [54]. In fact, using the fundamental theorem of calculus, the GIQ weighting coefficients are derived from the inversion of the GDQ matrix for first-order derivatives. Alternatively, the Taylor-based GIQ (T-GIQ) method employs a Taylor expansion of the integrand function, and it does not necessitate of any matrix inversion as the quadrature coefficients are recursively derived. The validation of the numerical model is typically performed, under specific assumptions, using closed-form analytical solutions of the governing equations. The Navier approach is extensively used in the literature for simply-supported structures [55], while Levy's theory [56] is applied to structures with various boundary conditions. In addition, in Ref. [57–59] an interesting enhancement of classical Navier approach is introduced, known as boundary discontinuous method, which allows for the derivation of closed-form analytical solutions in the case of fully-clamped plates and shells.

Solutions derived from two-dimensional theories, even when employing higher-order kinematic models, may not accurately predict the actual response of the corresponding three-dimensional solid, especially for quantities related to the out-of-plane thickness direction [60]. To this end, a post-processing correction of results is often required which adopts a methodology based on the three-dimensional equilibrium equations [61]. More specifically, this procedure involves the derivation of numerical solutions along the thickness direction using the GDQ method, considering the in-plane strains and stresses obtained from the two-dimensional model. In some recent papers, such procedure has been extended to multifield analysis, enabling the reconstruction of the out-of-plane components of primary and secondary variables vectors [62,63].

Among the literature on multifield problems, two main categories of sensor and actuators are identified, known as concentrated and distributed systems [64,65]. Concentrated systems involve structures with multifield properties localized in some specific layers or patches that interacting with multifield actions. In contrast, in smart distributed structures, each layer within the stacking sequence react simultaneously to mechanical and multifield external actions. This category includes, for example, the piezoelectric sensors which generate an electric voltage in response to a mechanical deflection. On the other hand, in actuator configurations, an applied electric voltage induces mechanical deformations. In this way, the overall deflection of the panel is achieved through a mechanical compatibility between adjacent layers. When studying multifield distributed sensors and actuators, most applications account for homogeneous layers with different materials and orientation. In such cases, an abrupt variation of the material properties at the interfacial level may lead to stress concentrations, causing cracks and delaminations [66]. To mitigate these issues, Functionally Graded Materials (FGM) have been developed over the years [67–70]. These non-homogenous materials are characterized by a continuous variation of the material properties within the structure. From a manufacturing point of view, FGMs are created by combining two or more phases, typically an isotropic medium and inclusions with various shapes, sizes, and constitutive properties. As explored in the review papers [71,72], a continuous grading of the material properties is achieved by varying with continuity the concentration of constituents, inclusion shapes, and

their orientation, allowing the homogenized material to exhibit an intermediate behavior between its constituent phases. A recent research on FGM has been expanded to lattice materials [73,74], which consists of unit cells modelled as frame structures with periodic boundary conditions. The geometric variation of each beam within these unit cells, such as changes in width, length and orientation, results in a FGM medium with variable properties. In this way, common lattice materials like anisogrid and honeycomb structures [75,76] are enhanced for further applications. It should be noted that the modelling strategies used for FGM structures can be applied to analyze the material porosity, as demonstrated in Ref. [77–79]. A key aspect in such analysis is the accurate description of the material properties variation. A preliminary analysis often assumes an arbitrary distribution of the properties of the homogeneous material [80]. However, from a practical point of view, the determination of the material distribution is complex, because any direct relationship is established with the properties of the constituent phases. Therefore, some studies in literature employ homogenization algorithms by varying the concentration, shape, and orientation of inclusions at each point of the lamina. From an engineering perspective, the rule of mixture has been widely used to homogenize the multiphase materials for mechanical elasticity and multifield applications [81]. However, it is well-known that the homogenization of the material properties should be consistent with the physical aspects of the problem. Furthermore, the mutual interaction between the constituents should be taken into account during homogenization, as well as shape and distribution of inclusions within the unit cell, including the effect of curvature and agglomeration of dispersed phases [82]. Enhanced algorithms have been proposed to address these issues. Among others, the Mori-Tanaka's technique [83] has been demonstrated to predict the experimental results accurately. This method is based on the computation of the Eshelby tensor of the unit cell, whose components can be determined analytically for various composites, starting from the mathematical modelling of ellipsoidal inclusions [84,85].

The paper presents a two-dimensional generalized formulation employing higher-order theories for the multifield analysis of laminated curved panels under thermodynamic equilibrium. More specifically, the fundamental equations, derived from the Master Balance principle using the curvilinear principal coordinates, account for the coupling effects between mechanical, magnetic, and thermal fields, including thermal expansion, piezomagnetic, and pyromagnetic effects. A semi-analytical Navier solution is obtained by expanding the unknown field variables using trigonometric functions. The thermo-magneto-elastic kinematic model uses the higher-order polynomials and Murakami's zigzag function, following the ESL approach. In addition, the power functions are adopted to develop an ELW model that enables the prescription of arbitrary values for displacement field components, scalar magnetic potential, and temperature variation with respect to the reference configuration. Furthermore, arbitrary variations of the material properties along the thickness direction are modelled within each layer, taking into account various analytical distributions with appropriate positioning and scaling parameters. In the post-processing phase, a novel equilibrium-based recovery procedure is introduced for the first time. This method, based on GIQ, reconstructs efficiently the distribution of multifield primary and secondary variables along the thickness direction, starting from the solution of two-dimensional equations. Furthermore, the GDQ is used to compute the GIQ weighting coefficients for numerical integration. The accuracy of the model is demonstrated through several numerical examples, Some preliminary examples are presented where the accuracy of the model is checked against the results from existing literature. More specifically, the model is validated for mechanical simulations [86–88], magneto-elastic analysis [89,90], and thermo-mechanical simulations [91]. In addition to literature comparisons, laminated panels with zero, single, and double curvature subjected to generalized surface loads are analyzed. For each case, reference three-dimensional simulations based on 3D FEM are performed via commercial software. Furthermore, innovative simulations are conducted with fully coupled thermal, magnetic and mechanical fields. A general variation in the material properties is modelled within each layer, showing the sensitivity of the model to the governing parameters of the distribution.

The main novelty of the paper can thus be traced in the development of a higher-order two-dimensional formulation for the thermo-magneto-mechanical analysis of laminated curved structures, which consider the full coupling between magnetostatic equations, thermal conduction, and mechanical elasticity. Furthermore, the main contribution in this research topic is the development of an alternative approach to recover primary and secondary variables, based on GIQ, which is more computationally efficient compared to the classical GDQ-based recovery. Furthermore, we introduce an arbitrary functional variation of the multifield material along the thickness direction. This variation can be modelled within the formulation thanks to the adoption of higher-order theories and because the generalized constitutive coefficients are evaluated numerically with the GIQ method. The manuscript provides novel results for multifield simulations that can assist in the design of various engineering applications. In fact, classical commercial software cannot study the mutual interactions between temperature, thermal gradients, and magnetic flux components within the solid as they only consider the modification of magnetic fluxes induced by additional strains from thermal expansion. In contrast, this formulation allows to predict these physical phenomena in doubly-curved laminated structures, thus allowing to design novel temperature sensors and thermo-magnetic energy harvesters, among others [92]. Moreover, the higher-order generalized formulation can be applied to investigate the multifield response of a wide range of laminated shell structures under different loading conditions in thermal and magnetic environments.

2. Higher-order thermo-magneto-elastic theory for doubly-curved shells

Following the ELW approach, the position vector $\mathbf{R}$ of an arbitrary point of a doubly-curved shell solid is expressed in terms of the position vector $\mathbf{r}$ of the reference surface. The reference surface is located in the middle thickness of the shell, and it is described using the curvilinear principal coordinates $\alpha_i = \alpha_1,\alpha_2$, as reported below [28]:

$$\mathbf{R}(\alpha_1,\alpha_2,\zeta) = \mathbf{r}(\alpha_1,\alpha_2) + \frac{h}{2} z \mathbf{n}(\alpha_1,\alpha_2) \tag{1}$$

The previous relation identifies a limited region in the three-dimensional Euclidean space with $(\alpha_1, \alpha_2) \in \left[\alpha_1^0, \alpha_1^1\right] \times \left[\alpha_2^0, \alpha_2^1\right]$. The thickness coordinate ζ varies within the interval $[-h/2, h/2]$, where h represents the total thickness of the structure. The points located along the thickness direction are described using the dimensionless normalized coordinate $z = 2\zeta/h$ with $z \in [-1, 1]$. This normalization allows for a simplified representation of the position throughout the thickness. Furthermore, the outward unit vector $\mathbf{n}(\alpha_1,\alpha_2)$ of the reference surface $\mathbf{r}$ is defined at each (α_1,α_2) as follows, being $\mathbf{r}_{,i} = \partial \mathbf{r}/\partial \alpha_i$ the partial derivative of $\mathbf{r}$ with respect to α_i:

$$\mathbf{n}(\alpha_1,\alpha_2) = \frac{\mathbf{r}_{,1} \wedge \mathbf{r}_{,2}}{\left|\mathbf{r}_{,1} \wedge \mathbf{r}_{,2}\right|} \tag{2}$$

The doubly-curved shell solid is made of l superimposed laminae of various thicknesses. As a result, the total thickness h of the structure is equal to the sum of thickness h_k for each individual lamina k, with $k = 1, \ldots, l$, identified by the interval $[\zeta_k,\zeta_{k+1}]$ along the thickness direction. This aspect can be mathematically represented with the relation reported below:

$$h = \sum_{k=1}^{l} h_k = \sum_{k=1}^{l} (\zeta_{k+1} - \zeta_k) \tag{3}$$

The principal radius of curvature $R_i = R_1,R_2$ associated with the principal direction $\alpha_i = \alpha_1,\alpha_2$, is calculated using the following relation:

$$R_i(\alpha_1,\alpha_2) = -\frac{\mathbf{r}_{,i}\cdot\mathbf{r}_{,i}}{\mathbf{r}_{,ii}\cdot\mathbf{n}} \tag{4}$$

Here, $\mathbf{r}_{,ij} = \partial^2\mathbf{r}/(\partial\alpha_i\partial\alpha_j)$ represents the second-order partial derivative of $\mathbf{r}$ with respect to α_i,$\alpha_j = \alpha_1$,α_2 principal coordinates. Furthermore, the Lamé parameters $A_i = A_1$,A_2 can be calculated in each point of the physical domain as follows:

$$A_i(\alpha_1,\alpha_2) = \sqrt{\mathbf{r}_{,i}\cdot\mathbf{r}_{,i}} \tag{5}$$

Finally, the thickness scaling parameters $H_i = 1 + \zeta/R_i$ for $i = 1, 2$ are introduced at each height $\zeta \in [-h/2, h/2]$.

The introduction of A_i in Eq. (5) enables the definition of the curvilinear coordinate $s_i \in [0, L_i]$ with L_i representing the length along $\alpha_i = \alpha_1$,α_2 principal direction [28]:

$$ds_i = A_i d\alpha_i \tag{6}$$

It should be noted that in Eq. (6) it is required that the Lamé parameters are evaluated at each point of the reference surface. To this end, the partial derivative of the reference surface equation with respect to $\alpha_i = \alpha_1$,α_2 must be evaluated. If the analytical expression of $\mathbf{r}(\alpha_1,\alpha_2)$ is provided in curvilinear principal coordinates, these derivatives are evaluated analytically. On the other hand, if the reference surface is provided on a discrete grid, these derivatives must be evaluated numerically.

The multifield theory presented in this work considers the full coupling between mechanical elasticity equations, thermal conduction problems, and magnetostatic equations, using higher-order shear deformation theories. As a consequence, a generalized kinematic model is introduced that accounts for an arbitrary expansion of each unknown field variable. These variables include the elements $U_1^{(k)}$, $U_2^{(k)}$ and $U_3^{(k)}$, measured in meters [m], which represent the components of the displacement field vector with respect to the geometric reference system $\alpha_1, \alpha_2, \zeta$. In addition, the scalar quantities are included within the unknown variables, namely the temperature variation $\Delta T^{(k)} = T^{(k)} - T_0$, expressed in kelvin [K], with respect to the temperature T_0 associated with a stress-free reference configuration, and the variation $\Delta\psi^{(k)} = \psi^{(k)} - \psi_0$ of the scalar magnetic potential with respect to the reference value ψ_0, measured in ampere [A]. These unknown variables are conveniently arranged in vector $\mathbf{\Delta}^{(k)}$, represented as follows:

$$\mathbf{\Delta}^{(k)}(\alpha_1,\alpha_2,\zeta) = \begin{bmatrix} U_1^{(k)} & U_2^{(k)} & U_3^{(k)} & \Delta\psi^{(k)} & \Delta T^{(k)} \end{bmatrix}^T \tag{7}$$

The variation of the elements of vector $\mathbf{\Delta}^{(k)}$ along the thickness direction is described using an arbitrary expansion of N-th order, employing generalized thickness functions $F_\tau^{(k)\alpha_i} = F_\tau^{(k)\alpha_i}(\zeta)$ with $i = 1, ..., 5$ defined for each $\tau = 0, ..., N+1$. The following relation is, thus, obtained [28]:

$$\begin{bmatrix} U_1^{(k)} \\ U_2^{(k)} \\ U_3^{(k)} \\ \Delta\psi^{(k)} \\ \Delta T^{(k)} \end{bmatrix} = \sum_{\tau=0}^{N+1} \begin{bmatrix} F_\tau^{(k)\alpha_1} & 0 & 0 & 0 & 0 \\ 0 & F_\tau^{(k)\alpha_2} & 0 & 0 & 0 \\ 0 & 0 & F_\tau^{(k)\alpha_3} & 0 & 0 \\ 0 & 0 & 0 & F_\tau^{(k)\alpha_4} & 0 \\ 0 & 0 & 0 & 0 & F_\tau^{(k)\alpha_5} \end{bmatrix} \begin{bmatrix} u_1^{(\tau)} \\ u_2^{(\tau)} \\ u_3^{(\tau)} \\ \psi^{(\tau)} \\ \kappa^{(\tau)} \end{bmatrix} \tag{8}$$

where the quantities $u_1^{(\tau)}, u_2^{(\tau)}, u_3^{(\tau)}, \psi^{(\tau)}, \kappa^{(\tau)}$ are the configuration variables of the problem, associated with an arbitrary τ-th kinematic expansion order. In compact notation, Eq. (8) can be expressed as:

$$\mathbf{\Delta}^{(k)} = \sum_{\tau=0}^{N+1} \mathbf{F}_\tau^{(k)} \boldsymbol{\delta}^{(\tau)} \tag{9}$$

where $\boldsymbol{\delta}^{(\tau)}(\alpha_1,\alpha_2)$ represents the unknown vector that varies within the two-dimensional physical domain, and $\mathbf{F}_\tau^{(k)}$ is the thickness functions matrix with $\tau = 0, ..., N+1$, depending on the thickness coordinate ζ.

In this work, two sets of thickness functions are considered, associated with the ESL and the ELW approaches, respectively. When the model is developed using the ESL approach [22], the following relations apply to an arbitrary k-th layer of the stacking sequence, with $\tau = 0, ..., N+1$:

$$F_\tau^{(k)\alpha_i}(\zeta) = \begin{cases} \zeta^\tau & \text{for } \tau = 0, ..., N \\ (-1)^k z_k = (-1)^k \dfrac{2}{\zeta_{k+1} - \zeta_k}\zeta - \dfrac{\zeta_{k+1} + \zeta_k}{\zeta_{k+1} - \zeta_k} & \text{for } \tau = N+1 \end{cases} \tag{10}$$

Here, the thickness functions account for power polynomials of τ-th order for $\tau = 0, ..., N$, while the Murakami function is introduced at $\tau = N+1$ to consider the zigzag effects between subsequent layers. To identify the kinematic model adopted within the ESL framework, the following nomenclature is introduced:

$$\begin{matrix} \text{ED} - N \\ \text{EDZ} - N \end{matrix} \tag{11}$$

More specifically, "E" indicates that it refers to the ESL approach, while "D" refers to that the unknown variables of the model, i.e. the displacement field components. Finally, the letter "Z" denotes the presence of a zigzag function (10) in the implementation.

An alternative form of the kinematic model from Eq. (9) can be assessed through the ELW approach. To this end, the following expression is adopted for $F_\tau^{(k)\alpha_i}$ with $\tau = 0, ..., N$, as shown in Ref. [16]:

$$F_\tau^{(k)\alpha_i}(\zeta) = \begin{cases} \dfrac{1-\widetilde{z}}{2} & \text{for } \tau = 0 \\ \widetilde{z}^{\tau+1} - \widetilde{z}^{\tau-1} & \text{for } \tau = 1, .., N-1 \\ \dfrac{1+\widetilde{z}}{2} & \text{for } \tau = N \end{cases} \tag{12}$$

where $\widetilde{z} = 2\zeta/h \in [-1, 1]$. The last term of the kinematic expansion accounts for the modified zigzag function, which takes a value equal to zero at $\zeta = -h/2$ and $\zeta = h/2$:

$$F_{N+1}^{(k)\alpha_i}(\zeta) = \begin{cases} (-1)^k \widetilde{z}_k = -\dfrac{\zeta - \zeta_1}{\zeta_2 - \zeta_1} & \text{for } k = 1 \\ (-1)^k z_k = (-1)^k \left(2\dfrac{\zeta - \zeta_k}{\zeta_{k+1} - \zeta_k} - 1\right) & \text{for } k = 2, ..., l-1 \\ (-1)^k \widetilde{z}_k = (-1)^l \dfrac{\zeta - \zeta_{l+1}}{\zeta_{l+1} - \zeta_l} & \text{for } k = l \end{cases} \tag{13}$$

It should be noted that the ELW approach is completely different from the well-known LW methodology. In fact, in LW theories the kinematic expansion is performed within each k-th lamina, while in ELW the thickness functions are defined along the entire thickness of the structure. Furthermore, in LW theories the zigzag function cannot be defined, while in the present theory this function is introduced in Eq. (13). Furthermore, in the present theory the reference surface is located at the middle thickness of the shell, while in LW theories a reference surface is provided at the middle thickness of each lamina. This means that in ELW method a single geometric reference system is provided for the entire laminate, whereas l reference systems are defined in LW approaches, being l the total number of laminae of the structure.

To specify better the expansion of unknown kinematic variables, in the following the extended version of Eq. (8) is provided for $N = 4$, taking into account the zigzag function associated with $\tau = N+1$:

$$
\begin{aligned}
U_1^{(k)} &= F_0^{(k)\alpha_1} u_1^{(0)} + F_1^{(k)\alpha_1} u_1^{(1)} + F_2^{(k)\alpha_1} u_1^{(2)} + F_3^{(k)\alpha_1} u_1^{(3)} + F_4^{(k)\alpha_1} u_1^{(4)} + F_5^{(k)\alpha_1} u_1^{(5)} \\
U_2^{(k)} &= F_0^{(k)\alpha_2} u_2^{(0)} + F_1^{(k)\alpha_2} u_2^{(1)} + F_2^{(k)\alpha_2} u_2^{(2)} + F_3^{(k)\alpha_2} u_2^{(3)} + F_4^{(k)\alpha_2} u_2^{(4)} + F_5^{(k)\alpha_2} u_2^{(5)} \\
U_3^{(k)} &= F_0^{(k)\alpha_3} u_3^{(0)} + F_1^{(k)\alpha_3} u_3^{(1)} + F_2^{(k)\alpha_3} u_3^{(2)} + F_3^{(k)\alpha_3} u_3^{(3)} + F_4^{(k)\alpha_3} u_3^{(4)} + F_5^{(k)\alpha_3} u_3^{(5)} \\
\Delta\psi^{(k)} &= F_0^{(k)\alpha_4} \psi^{(0)} + F_1^{(k)\alpha_4} \psi^{(1)} + F_2^{(k)\alpha_4} \psi^{(2)} + F_3^{(k)\alpha_4} \psi^{(3)} + F_4^{(k)\alpha_4} \psi^{(4)} + F_5^{(k)\alpha_4} \psi^{(5)} \\
\Delta\mathrm{T}^{(k)} &= F_0^{(k)\alpha_5} \kappa^{(0)} + F_1^{(k)\alpha_5} \kappa^{(1)} + F_2^{(k)\alpha_5} \kappa^{(2)} + F_3^{(k)\alpha_5} \kappa^{(3)} + F_4^{(k)\alpha_5} \kappa^{(4)} + F_5^{(k)\alpha_5} \kappa^{(5)}
\end{aligned}
\tag{14}
$$

When the EDZ4 thickness functions of Eq. (10) are adopted, the 3D kinematic variables are expanded as in Eq. (14), and take the following aspect:

$$
\begin{aligned}
U_1^{(k)} &= u_1^{(0)} + \zeta u_1^{(1)} + \zeta^2 u_1^{(2)} + \zeta^3 u_1^{(3)} + \zeta^4 u_1^{(4)} + (-1)^k z_k u_1^{(5)} \\
U_2^{(k)} &= u_2^{(0)} + \zeta u_2^{(1)} + \zeta^2 u_2^{(2)} + \zeta^3 u_2^{(3)} + \zeta^4 u_2^{(4)} + (-1)^k z_k u_2^{(5)} \\
U_3^{(k)} &= u_3^{(0)} + \zeta u_3^{(1)} + \zeta^2 u_3^{(2)} + \zeta^3 u_3^{(3)} + \zeta^4 u_3^{(4)} + (-1)^k z_k u_3^{(5)} \\
\Delta\psi^{(k)} &= \psi^{(0)} + \zeta\psi^{(1)} + \zeta^2\psi^{(2)} + \zeta^3\psi^{(3)} + \zeta^4\psi^{(4)} + (-1)^k z_k \psi^{(5)} \\
\Delta\mathrm{T}^{(k)} &= \kappa^{(0)} + \zeta\kappa^{(1)} + \zeta^2\kappa^{(2)} + \zeta^3\kappa^{(3)} + \zeta^4\kappa^{(4)} + (-1)^k z_k \kappa^{(5)}
\end{aligned}
\tag{15}
$$

Similarly, the ELDZL4 theory accounts for the following expandion of 3D unknown variables, following Eqs. (12)-(13):

$$
\begin{aligned}
U_1^{(k)} &= \frac{1-\widetilde{z}}{2} u_1^{(0)} + \left(\widetilde{z}^2 - 1\right) u_1^{(1)} + \left(\widetilde{z}^3 - \widetilde{z}\right) u_1^{(2)} + \left(\widetilde{z}^4 - \widetilde{z}^2\right) u_1^{(3)} + \frac{1+\widetilde{z}}{2} u_1^{(4)} + (-1)^k \overline{\overline{z}}_k u_1^{(5)} \\
U_2^{(k)} &= \frac{1-\widetilde{z}}{2} u_2^{(0)} + \left(\widetilde{z}^2 - 1\right) u_2^{(1)} + \left(\widetilde{z}^3 - \widetilde{z}\right) u_2^{(2)} + \left(\widetilde{z}^4 - \widetilde{z}^2\right) u_2^{(3)} + \frac{1+\widetilde{z}}{2} u_2^{(4)} + (-1)^k \overline{\overline{z}}_k u_2^{(5)} \\
U_3^{(k)} &= \frac{1-\widetilde{z}}{2} u_3^{(0)} + \left(\widetilde{z}^2 - 1\right) u_3^{(1)} + \left(\widetilde{z}^3 - \widetilde{z}\right) u_3^{(2)} + \left(\widetilde{z}^4 - \widetilde{z}^2\right) u_3^{(3)} + \frac{1+\widetilde{z}}{2} u_3^{(4)} + (-1)^k \overline{\overline{z}}_k u_3^{(5)} \\
\Delta\psi^{(k)} &= \frac{1-\widetilde{z}}{2} \psi^{(0)} + \left(\widetilde{z}^2 - 1\right) \psi^{(1)} + \left(\widetilde{z}^3 - \widetilde{z}\right) \psi^{(2)} + \left(\widetilde{z}^4 - \widetilde{z}^2\right) \psi^{(3)} + \frac{1+\widetilde{z}}{2} \psi^{(4)} + (-1)^k \overline{\overline{z}}_k \psi^{(5)} \\
\Delta\mathrm{T}^{(k)} &= \frac{1-\widetilde{z}}{2} \kappa^{(0)} + \left(\widetilde{z}^2 - 1\right) \kappa^{(1)} + \left(\widetilde{z}^3 - \widetilde{z}\right) \kappa^{(2)} + \left(\widetilde{z}^4 - \widetilde{z}^2\right) \kappa^{(3)} + \frac{1+\widetilde{z}}{2} \kappa^{(4)} + (-1)^k \overline{\overline{z}}_k \kappa^{(5)}
\end{aligned}
\tag{16}
$$

setting $\overline{\overline{z}}_k = \widehat{z}_k, z_k, \breve{z}_k$ for $k = 1, \ldots, l$. It should be noted that the thickness functions introduced in Eqs. (12)-(13) assume a null value at the top and bottom surfaces of the laminate, except for those associated with $\tau = 0$ and $\tau = N$. Consequently, the arbitrary i-th element with $i = 1, \ldots, 5$ of the vectors $\Delta_i^{(1)}$ and $\Delta_i^{(l)}$ of three-dimensional configuration variables, evaluated at $\zeta = -h/2$ and $\zeta = h/2$, respectively, are equal to the i-th elements $\delta_i^{(0)}, \delta_i^{(N)}$ of the generalized unknown variables of the higher-order formulation:

$$
\begin{aligned}
\Delta_i^{(1)}\left(\alpha_1, \alpha_2, \zeta = -\frac{h}{2}\right) &= \delta_i^{(0)}(\alpha_1, \alpha_2) \\
\Delta_i^{(l)}\left(\alpha_1, \alpha_2, \zeta = \frac{h}{2}\right) &= \delta_i^{(N)}(\alpha_1, \alpha_2)
\end{aligned}
\tag{17}
$$

It should be noted that the mathematical expressions used to expand the thermo-magneto-mechanical unknown variables along the thickness direction have an important physical meaning. In fact, in higher-order ESL and ELW theories it is assumed that each layer undergoes a complicated deformation that can be described only with higher-order polynomials. This aspect, extensively studied for mechanical elasticity problems, is hereshown to be determining even for additional fields like magnetic potential and temperature variations along the thickness direction. Furthermore, the zigzag function, used in literature to predict the deformation of the laminate at the interfaces, is provided here for multifield analysis. In fact, in heterogeneous materials, a variation in the slope is observed at each interface when solving thermal conduction and magnetostatic equations, therefore zigzag function plays a crucial role for higher-order multifield theories. When the ELW approach is adopted, the nomenclature reported below is used instead of Eq. (11):

$$
\begin{matrix}
\mathrm{ELD} - N \\
\mathrm{ELDZL} - N
\end{matrix}
\tag{18}
$$

Here, the acronym "EL" stands for the ELW theory, while "D" refers to the generalized unknown multifield variables. Finally, "ZL" indicates the modified zigzag function already introduced in Eq. (13).

At this point, the definition equations are evaluated within the higher-order two-dimensional theory for mechanical, thermal, and magnetic fields. To this end, the generalized kinematic model of Eq. (9) is employed to express the configuration variables within the thermo-magneto-mechanical definition equations for a three-dimensional solid described using the curvilinear principal coordinates. These three-dimensional equations are reported in the following compact form [28]:

$$
\begin{aligned}
\boldsymbol{\pi}^{(k)} = \mathbf{D}\boldsymbol{\Delta}^{(k)} = \mathbf{D}_{\zeta}\mathbf{D}_{\Omega}\boldsymbol{\Delta}^{(k)} \quad \Leftrightarrow \quad & \begin{bmatrix} \boldsymbol{\varepsilon}^{(k)} \\ \mathscr{K}^{(k)} \\ \widehat{\Delta\mathrm{T}}^{(k)} \\ \boldsymbol{\theta}^{(k)} \end{bmatrix} \\
= & \begin{bmatrix} \mathbf{D}_{(1)} & \mathbf{0} & \mathbf{0} \\ \mathbf{0} & \mathbf{D}_{(2)} & \mathbf{0} \\ \mathbf{0} & \mathbf{0} & 1 \\ \mathbf{0} & \mathbf{0} & \mathbf{D}_{(2)} \end{bmatrix} \begin{bmatrix} \mathbf{U}^{(k)} \\ \Delta\psi^{(k)} \\ \Delta\mathrm{T}^{(k)} \end{bmatrix}
\end{aligned}
\tag{19}
$$

Vector $\boldsymbol{\pi}^{(k)} = \left[\boldsymbol{\varepsilon}^{(k)T} \quad \mathscr{K}^{(k)T} \quad \widehat{\Delta\mathrm{T}}^{(k)} \quad \boldsymbol{\theta}^{(k)T}\right]^T$ is obtained by assembling the sub-vectors $\boldsymbol{\varepsilon}^{(k)}$, $\mathscr{K}^{(k)}$ and $\widehat{\Delta\mathrm{T}}^{(k)}, \boldsymbol{\theta}^{(k)}$, which are associated with each individual physical problem considered in the present multifield formulation:

$$
\begin{aligned}
\boldsymbol{\varepsilon}^{(k)} &= \left[\varepsilon_1^{(k)} \quad \varepsilon_2^{(k)} \quad \gamma_{12}^{(k)} \quad \gamma_{13}^{(k)} \quad \gamma_{23}^{(k)} \quad \varepsilon_3^{(k)}\right]^T \\
\mathscr{K}^{(k)} &= \left[\mathscr{K}_1^{(k)} \quad \mathscr{K}_2^{(k)} \quad \mathscr{K}_3^{(k)}\right]^T, \quad \boldsymbol{\theta}^{(k)} = \left[\theta_1^{(k)} \quad \theta_2^{(k)} \quad \theta_3^{(k)}\right]^T, \quad \widehat{\Delta\mathrm{T}}^{(k)} = \Delta\mathrm{T}^{(k)}
\end{aligned}
\tag{20}
$$

As can be seen from Eq. (19), the kinematic differential operator $\mathbf{D}$ is expressed in terms of sub-operators $\mathbf{D}_{(1)}$,$\mathbf{D}_{(2)}$. More specifically, $\mathbf{D}_{(1)}$ represents the symmetric part of the three-dimensional strain gradient operator, while $\mathbf{D}_{(2)}$ denotes the gradient operator of a scalar field. In the

definition relation reported in Eq. (19), the three-dimensional differential operator $\mathbf{D}$ is conveniently divided into sub-operators $\mathbf{D}_\zeta$ and $\mathbf{D}_\Omega$. Thus, the partial derivatives with respect to the thickness coordinate ζ are separated from those associated with the in-plane principal directions α_1, α_2:

$$\mathbf{D}_\zeta = \begin{bmatrix} \mathbf{D}_{\zeta(1)} & \mathbf{0} & \mathbf{0} & \mathbf{0} \\ \mathbf{0} & \mathbf{D}_{\zeta(2)} & \mathbf{0} & \mathbf{0} \\ \mathbf{0} & \mathbf{0} & \mathbf{D}_{\zeta(3)} & \mathbf{0} \\ \mathbf{0} & \mathbf{0} & \mathbf{0} & \mathbf{D}_{\zeta(2)} \end{bmatrix}, \quad \mathbf{D}_\Omega = \begin{bmatrix} \mathbf{D}_{\Omega(1)} & \mathbf{0} & \mathbf{0} \\ \mathbf{0} & \mathbf{D}_{\Omega(2)} & \mathbf{0} \\ \mathbf{0} & \mathbf{0} & \mathbf{D}_{\Omega(3)} \\ \mathbf{0} & \mathbf{0} & \mathbf{D}_{\Omega(2)} \end{bmatrix} \tag{21}$$

The sub-operators $\mathbf{D}_{\zeta(1)}$,$\mathbf{D}_{\zeta(2)}$,$\mathbf{D}_{\zeta(3)}$ associated to $\mathbf{D}_\zeta$ are reported below in expanded form:

$$\mathbf{D}_{\zeta(1)} = \begin{bmatrix} \frac{1}{H_1} & 0 & 0 & 0 & 0 & 0 & 0 & 0 & 0 \\ 0 & \frac{1}{H_2} & 0 & 0 & 0 & 0 & 0 & 0 & 0 \\ 0 & 0 & \frac{1}{H_1} & \frac{1}{H_2} & 0 & 0 & 0 & 0 & 0 \\ 0 & 0 & 0 & 0 & \frac{1}{H_1} & 0 & \frac{\partial}{\partial\zeta} & 0 & 0 \\ 0 & 0 & 0 & 0 & 0 & \frac{1}{H_2} & 0 & \frac{\partial}{\partial\zeta} & 0 \\ 0 & 0 & 0 & 0 & 0 & 0 & 0 & 0 & \frac{\partial}{\partial\zeta} \end{bmatrix}, \quad \mathbf{D}_{\zeta(2)} = \begin{bmatrix} \frac{1}{H_1} & 0 & 0 \\ 0 & \frac{1}{H_2} & 0 \\ 0 & 0 & \frac{\partial}{\partial\zeta} \end{bmatrix}, \quad \mathbf{D}_{\zeta(3)} = 1 \tag{22}$$

On the other hand, the quantities $\mathbf{D}_{\Omega(1)}$,$\mathbf{D}_{\Omega(2)}$,$\mathbf{D}_{\Omega(3)}$ take the following form:

$$\begin{aligned} \mathbf{D}_{\Omega(1)} &= [\,\overline{\mathbf{D}}_\Omega^{\alpha_1} \quad \overline{\mathbf{D}}_\Omega^{\alpha_2} \quad \overline{\mathbf{D}}_\Omega^{\alpha_3}\,] \\ \mathbf{D}_{\Omega(2)} &= \begin{bmatrix} -\frac{1}{A_1}\frac{\partial}{\partial\alpha_1} & -\frac{1}{A_2}\frac{\partial}{\partial\alpha_2} & -1 \end{bmatrix}^T \\ \mathbf{D}_{\Omega(3)} &= 1 \end{aligned} \tag{23}$$

where

$$\begin{aligned} \overline{\mathbf{D}}_\Omega^{\alpha_1} &= \begin{bmatrix} \frac{1}{A_1}\frac{\partial}{\partial\alpha_1} & \frac{1}{A_1A_2}\frac{\partial A_2}{\partial\alpha_1} & -\frac{1}{A_1A_2}\frac{\partial A_1}{\partial\alpha_2} & \frac{1}{A_2}\frac{\partial}{\partial\alpha_2} & -\frac{1}{R_1} & 0 & 1 & 0 & 0 \end{bmatrix}^T \\ \overline{\mathbf{D}}_\Omega^{\alpha_2} &= \begin{bmatrix} \frac{1}{A_1A_2}\frac{\partial A_1}{\partial\alpha_2} & \frac{1}{A_2}\frac{\partial}{\partial\alpha_2} & \frac{1}{A_1}\frac{\partial}{\partial\alpha_1} & -\frac{1}{A_1A_2}\frac{\partial A_2}{\partial\alpha_1} & 0 & -\frac{1}{R_2} & 0 & 1 & 0 \end{bmatrix}^T \\ \overline{\mathbf{D}}_\Omega^{\alpha_3} &= \begin{bmatrix} \frac{1}{R_1} & \frac{1}{R_2} & 0 & 0 & \frac{1}{A_1}\frac{\partial}{\partial\alpha_1} & \frac{1}{A_2}\frac{\partial}{\partial\alpha_2} & 0 & 0 & 1 \end{bmatrix}^T \end{aligned} \tag{24}$$

The kinematic operator $\mathbf{D}_\Omega$ is conveniently expressed as [28]:

$$\mathbf{D}_\Omega = \sum_{i=1}^{5} \mathbf{D}_\Omega^{\alpha_i} \tag{25}$$

whose elements $\mathbf{D}_\Omega^{\alpha_i}$ with $i = 1, \ldots, 5$, are expressed in terms of the sub-operators $\overline{\mathbf{D}}_\Omega^{\alpha_1}, \overline{\mathbf{D}}_\Omega^{\alpha_2}, \overline{\mathbf{D}}_\Omega^{\alpha_3}$ already introduced in Eq. (24), while $\overline{\mathbf{D}}_\Omega^{\alpha_4} = \overline{\mathbf{D}}_\Omega^{\alpha_5} = \mathbf{D}_{\Omega(2)}$ and $\widetilde{\mathbf{D}}_\Omega^{\alpha_5} = \mathbf{D}_{\Omega(3)}$:

$$\mathbf{D}_\Omega^{\alpha_1} = \begin{bmatrix} \overline{\mathbf{D}}_\Omega^{\alpha_1} & \mathbf{0} & \mathbf{0} & \mathbf{0} & \mathbf{0} \\ \mathbf{0} & \mathbf{0} & \mathbf{0} & \mathbf{0} & \mathbf{0} \\ \mathbf{0} & \mathbf{0} & \mathbf{0} & \mathbf{0} & \mathbf{0} \\ \mathbf{0} & \mathbf{0} & \mathbf{0} & \mathbf{0} & \mathbf{0} \end{bmatrix}, \quad \mathbf{D}_\Omega^{\alpha_2} = \begin{bmatrix} \mathbf{0} & \overline{\mathbf{D}}_\Omega^{\alpha_2} & \mathbf{0} & \mathbf{0} & \mathbf{0} \\ \mathbf{0} & \mathbf{0} & \mathbf{0} & \mathbf{0} & \mathbf{0} \\ \mathbf{0} & \mathbf{0} & \mathbf{0} & \mathbf{0} & \mathbf{0} \\ \mathbf{0} & \mathbf{0} & \mathbf{0} & \mathbf{0} & \mathbf{0} \end{bmatrix}, \quad \mathbf{D}_\Omega^{\alpha_3} = \begin{bmatrix} \mathbf{0} & \mathbf{0} & \overline{\mathbf{D}}_\Omega^{\alpha_3} & \mathbf{0} & \mathbf{0} \\ \mathbf{0} & \mathbf{0} & \mathbf{0} & \mathbf{0} & \mathbf{0} \\ \mathbf{0} & \mathbf{0} & \mathbf{0} & \mathbf{0} & \mathbf{0} \\ \mathbf{0} & \mathbf{0} & \mathbf{0} & \mathbf{0} & \mathbf{0} \end{bmatrix},$$

$$\mathbf{D}_\Omega^{\alpha_4} = \begin{bmatrix} \mathbf{0} & \mathbf{0} & \mathbf{0} & \mathbf{0} & \mathbf{0} \\ \mathbf{0} & \mathbf{0} & \mathbf{0} & \overline{\mathbf{D}}_\Omega^{\alpha_4} & \mathbf{0} \\ \mathbf{0} & \mathbf{0} & \mathbf{0} & \mathbf{0} & \mathbf{0} \\ \mathbf{0} & \mathbf{0} & \mathbf{0} & \mathbf{0} & \mathbf{0} \end{bmatrix}, \quad \mathbf{D}_\Omega^{\alpha_5} = \begin{bmatrix} \mathbf{0} & \mathbf{0} & \mathbf{0} & \mathbf{0} & \mathbf{0} \\ \mathbf{0} & \mathbf{0} & \mathbf{0} & \mathbf{0} & \mathbf{0} \\ \mathbf{0} & \mathbf{0} & \mathbf{0} & \mathbf{0} & \widetilde{\mathbf{D}}_\Omega^{\alpha_5} \\ \mathbf{0} & \mathbf{0} & \mathbf{0} & \mathbf{0} & \overline{\mathbf{D}}_\Omega^{\alpha_5} \end{bmatrix} \tag{26}$$

Introducing the generalized kinematic model of Eq. (9) by substituting into the three-dimensional definition Eq. (19) the three-dimensional configuration variables vector $\mathbf{\Delta}^{(k)}$ with the higher-order through-the-thickness expansion, the following relation is obtained [28]:

$$\begin{aligned} \boldsymbol{\pi}^{(k)} &= \sum_{\tau=0}^{N+1}\sum_{i=1}^{5} \mathbf{Z}^{(k\tau)\alpha_i}\boldsymbol{\pi}^{(\tau)\alpha_i} \quad \Leftrightarrow \quad \begin{bmatrix} \boldsymbol{\varepsilon}^{(k)} \\ \mathscr{K}^{(k)} \\ \widehat{\Delta\mathrm{T}}^{(k)} \\ \boldsymbol{\theta}^{(k)} \end{bmatrix} \\ &= \sum_{\tau=0}^{N+1}\sum_{i=1}^{5} \begin{bmatrix} \mathbf{Z}_1^{(k\tau)\alpha_i} & \mathbf{0} & \mathbf{0} & \mathbf{0} \\ \mathbf{0} & \mathbf{Z}_2^{(k\tau)\alpha_i} & \mathbf{0} & \mathbf{0} \\ \mathbf{0} & \mathbf{0} & \mathbf{Z}_3^{(k\tau)\alpha_i} & \mathbf{0} \\ \mathbf{0} & \mathbf{0} & \mathbf{0} & \mathbf{Z}_2^{(k\tau)\alpha_i} \end{bmatrix} \begin{bmatrix} \boldsymbol{\varepsilon}^{(\tau)\alpha_i} \\ \mathscr{K}^{(\tau)\alpha_i} \\ \widehat{\Delta\mathrm{T}}^{(\tau)\alpha_i} \\ \boldsymbol{\theta}^{(\tau)\alpha_i} \end{bmatrix} \end{aligned} \tag{27}$$

In the previous equation, $\mathbf{Z}^{(k\tau)\alpha_i} = \mathbf{D}_\zeta F_\tau^{(k)\alpha_i}$ represents the generalized higher-order kinematic operator for the entire formulation, while $\mathbf{Z}_m^{(k\tau)\alpha_i} = \mathbf{D}_{\zeta(m)} F_\tau^{(k)\alpha_i}$ with $m = 1, 2, 3$, is associated with each individual physical problem. In addition, vectors $\boldsymbol{\varepsilon}^{(\tau)\alpha_i}, \mathscr{K}^{(\tau)\alpha_i}, \widehat{\Delta\mathrm{T}}^{(\tau)\alpha_i}, \boldsymbol{\theta}^{(\tau)\alpha_i}$ of the generalized thermo-magneto-elastic primary variables are introduced for each τ-th order of the kinematic expansion, which do not depend on the thickness coordinate ζ. These vectors, defined at each (α_1,α_2) point within the physical domain, are presented in extended form, for a given $\tau = 0, \ldots, N+1$ as follows:

$$\begin{aligned} \boldsymbol{\varepsilon}^{(\tau)\alpha_i}(\alpha_1,\alpha_2) &= [\,\varepsilon_1^{(\tau)\alpha_i} \;\; \varepsilon_2^{(\tau)\alpha_i} \;\; \gamma_1^{(\tau)\alpha_i} \;\; \gamma_2^{(\tau)\alpha_i} \;\; \gamma_{13}^{(\tau)\alpha_i} \;\; \gamma_{23}^{(\tau)\alpha_i} \;\; \omega_{13}^{(\tau)\alpha_i} \;\; \omega_{23}^{(\tau)\alpha_i} \;\; \varepsilon_3^{(\tau)\alpha_i}\,]^T \\ \mathscr{K}^{(\tau)\alpha_i}(\alpha_1,\alpha_2) &= [\,\mathscr{K}_1^{(\tau)\alpha_i} \;\; \mathscr{K}_2^{(\tau)\alpha_i} \;\; \mathscr{K}_3^{(\tau)\alpha_i}\,]^T \\ \widehat{\Delta\mathrm{T}}^{(\tau)\alpha_i}(\alpha_1,\alpha_2) &= \widehat{\Delta\mathrm{T}}^{(\tau)\alpha_i}, \quad \boldsymbol{\theta}^{(\tau)\alpha_i}(\alpha_1,\alpha_2) = [\,\theta_1^{(\tau)\alpha_i} \;\; \theta_2^{(\tau)\alpha_i} \;\; \theta_3^{(\tau)\alpha_i}\,]^T \end{aligned} \tag{28}$$

The introduction of generalized configuration and primary variables in the higher-order expansion along the thickness allows, from a physical point of view, means that each quantity is reduced on the reference surface. In lower-order theories, a physical significance of each generalized unknown variable can be traced, for example, in the translaiton and the rotation of their through-the-thickness profile, while for higher-order kinematic models the physical meaning is not directly evident. At this point, the constitutive relation for the multifield problem is introduced. Thus, the vector $\boldsymbol{\chi}^{(k)}$ of the three-dimensional secondary variable is defined for each point of the doubly-curved three-dimensional solid. This vector embeds vectors $\boldsymbol{\sigma}^{(k)}$, $\mathscr{B}^{(k)}$, $\mathbf{h}^{(k)}$, which are the secondary variables associated with the mechanical elasticity, magnetostatics, and thermal conduction, respectively. Using an expanded notation, these quantities take the following form:

$$\boldsymbol{\sigma}^{(k)} = \begin{bmatrix} \sigma_1^{(k)} & \sigma_2^{(k)} & \tau_{12}^{(k)} & \tau_{13}^{(k)} & \tau_{23}^{(k)} & \sigma_3^{(k)} \end{bmatrix}^T$$
$$\mathscr{B}^{(k)} = \begin{bmatrix} \mathscr{B}_1^{(k)} & \mathscr{B}_2^{(k)} & \mathscr{B}_3^{(k)} \end{bmatrix}^T, \quad \mathbf{h}^{(k)} = \begin{bmatrix} h_1^{(k)} & h_2^{(k)} & h_3^{(k)} \end{bmatrix}^T \tag{29}$$

In particular, the magneto-thermo-elastic three-dimensional constitutive relation [28] is, thus, expressed as follows:

$$\boldsymbol{\chi}^{(k)} = \overline{\Gamma}^{(k)} \boldsymbol{\pi}^{(k)} \quad \Leftrightarrow \quad \begin{bmatrix} \boldsymbol{\sigma}^{(k)} \\ \mathscr{B}^{(k)} \\ \eta^{(k)} \\ \mathbf{h}^{(k)} \end{bmatrix} = \begin{bmatrix} \overline{\Gamma}_{\mathrm{C}}^{(k)} & -\overline{\Gamma}_{\mathrm{Q}}^{(k)T} & -\overline{\Gamma}_{\mathrm{z}}^{(k)T} & \mathbf{0} \\ \overline{\Gamma}_{\mathrm{Q}}^{(k)} & \overline{\Gamma}_{\mathrm{M}}^{(k)} & \overline{\Gamma}_{\mathrm{w}}^{(k)T} & \mathbf{0} \\ \overline{\Gamma}_{\mathrm{z}}^{(k)} & \overline{\Gamma}_{\mathrm{w}}^{(k)} & \overline{\Gamma}_{\mathrm{TT}}^{(k)} & \mathbf{0} \\ \mathbf{0} & \mathbf{0} & \mathbf{0} & \overline{\Gamma}_{\mathrm{K}}^{(k)} \end{bmatrix} \begin{bmatrix} \boldsymbol{\varepsilon}^{(k)} \\ \mathscr{K}^{(k)} \\ \Delta\mathrm{T}^{(k)} \\ \boldsymbol{\theta}^{(k)} \end{bmatrix} \tag{30}$$

Here, $\overline{\Gamma}^{(k)}$ is the multifield constitutive matrix, which is expressed with respect to the geometric reference system α_1,α_2,ζ. As can be seen, it is obtained from the assembly of the mechanical stiffness matrix $\overline{\Gamma}_{\mathrm{C}}^{(k)}$, the magnetostatic constitutive matrix $\overline{\Gamma}_{\mathrm{M}}^{(k)}$, and the thermal conductivity matrix $\overline{\Gamma}_{\mathrm{K}}^{(k)}$, along with the coupling matrices of the physical phenomena. More specifically, $\overline{\Gamma}_{\mathrm{Q}}^{(k)}$ is the piezomagnetic matrix, $\overline{\Gamma}_{\mathrm{w}}^{(k)}$ accounts for the pyromagnetic effect, $\overline{\Gamma}_{\mathrm{z}}^{(k)}$ is the thermal expansion vector. These quantities assume the following extended form:

$$\overline{\Gamma}_{\mathrm{C}}^{(k)} = \begin{bmatrix} \overline{C}_{11}^{(k)} & \overline{C}_{12}^{(k)} & \overline{C}_{16}^{(k)} & \overline{C}_{14}^{(k)} & \overline{C}_{15}^{(k)} & \overline{C}_{13}^{(k)} \\ \overline{C}_{12}^{(k)} & \overline{C}_{22}^{(k)} & \overline{C}_{26}^{(k)} & \overline{C}_{24}^{(k)} & \overline{C}_{25}^{(k)} & \overline{C}_{23}^{(k)} \\ \overline{C}_{16}^{(k)} & \overline{C}_{26}^{(k)} & \overline{C}_{66}^{(k)} & \overline{C}_{46}^{(k)} & \overline{C}_{56}^{(k)} & \overline{C}_{36}^{(k)} \\ \overline{C}_{14}^{(k)} & \overline{C}_{24}^{(k)} & \overline{C}_{46}^{(k)} & \overline{C}_{44}^{(k)} & \overline{C}_{45}^{(k)} & \overline{C}_{34}^{(k)} \\ \overline{C}_{15}^{(k)} & \overline{C}_{25}^{(k)} & \overline{C}_{56}^{(k)} & \overline{C}_{45}^{(k)} & \overline{C}_{55}^{(k)} & \overline{C}_{35}^{(k)} \\ \overline{C}_{13}^{(k)} & \overline{C}_{23}^{(k)} & \overline{C}_{36}^{(k)} & \overline{C}_{34}^{(k)} & \overline{C}_{35}^{(k)} & \overline{C}_{33}^{(k)} \end{bmatrix}$$

$$\overline{\Gamma}_{\mathrm{M}}^{(k)} = \begin{bmatrix} \overline{m}_{11}^{(k)} & \overline{m}_{12}^{(k)} & \overline{m}_{13}^{(k)} \\ \overline{m}_{12}^{(k)} & \overline{m}_{22}^{(k)} & \overline{m}_{23}^{(k)} \\ \overline{m}_{13}^{(k)} & \overline{m}_{23}^{(k)} & \overline{m}_{33}^{(k)} \end{bmatrix}, \quad \overline{\Gamma}_{\mathrm{K}}^{(k)} = \begin{bmatrix} \overline{k}_{11}^{(k)} & \overline{k}_{12}^{(k)} & \overline{k}_{13}^{(k)} \\ \overline{k}_{12}^{(k)} & \overline{k}_{22}^{(k)} & \overline{k}_{23}^{(k)} \\ \overline{k}_{13}^{(k)} & \overline{k}_{23}^{(k)} & \overline{k}_{33}^{(k)} \end{bmatrix}$$

$$\overline{\Gamma}_{\mathrm{Q}}^{(k)} = \begin{bmatrix} \overline{q}_{11}^{(k)} & \overline{q}_{12}^{(k)} & \overline{q}_{16}^{(k)} & \overline{q}_{14}^{(k)} & \overline{q}_{15}^{(k)} & \overline{q}_{13}^{(k)} \\ \overline{q}_{21}^{(k)} & \overline{q}_{22}^{(k)} & \overline{q}_{26}^{(k)} & \overline{q}_{24}^{(k)} & \overline{q}_{25}^{(k)} & \overline{q}_{23}^{(k)} \\ \overline{q}_{31}^{(k)} & \overline{q}_{32}^{(k)} & \overline{q}_{36}^{(k)} & \overline{q}_{34}^{(k)} & \overline{q}_{35}^{(k)} & \overline{q}_{33}^{(k)} \end{bmatrix}$$

$$\overline{\Gamma}_{\mathrm{z}}^{(k)} = \begin{bmatrix} \overline{z}_{11}^{(k)} & \overline{z}_{22}^{(k)} & \overline{z}_{12}^{(k)} & \overline{z}_{13}^{(k)} & \overline{z}_{23}^{(k)} & \overline{z}_{33}^{(k)} \end{bmatrix}^T$$

$$\overline{\Gamma}_{\mathrm{w}}^{(k)} = \begin{bmatrix} \overline{w}_{11}^{(k)} & \overline{w}_{22}^{(k)} & \overline{w}_{33}^{(k)} \end{bmatrix}^T, \quad \overline{\Gamma}_{\mathrm{TT}}^{(k)} = \overline{\xi}_{11}^{(k)} = \frac{\rho^{(k)} c_p^{(k)}}{\mathrm{T}_0} \tag{31}$$

The term $\overline{\xi}_{11}^{(k)}$ introduced above is used to derive the specific entropy of the system at each point within the three-dimensional solid in the stress-free reference configuration, characterized by the absolute temperature $\mathrm{T}_0 = 297\mathrm{K}$. In addition, $\rho^{(k)}$ represents the material density, while $c_p^{(k)}$ denotes the specific heat of the constituent material. The thermal expansion matrix $\overline{\Gamma}_{\mathrm{z}}^{(k)}$ occurring in Eq. (30) is evaluated in relation to the stiffness matrix $\overline{\Gamma}_{\mathrm{C}}^{(k)}$ according to the relation reported below [28]:

$$\overline{\Gamma}_{\mathrm{z}}^{(k)T} = \overline{\Gamma}_{\mathrm{C}}^{(k)} \overline{\Gamma}_{\mathrm{a}}^{(k)} \tag{32}$$

Here, $\overline{\Gamma}_{\mathrm{a}}^{(k)} = \begin{bmatrix} \overline{a}_{11}^{(k)} & \overline{a}_{22}^{(k)} & \overline{a}_{12}^{(k)} & \overline{a}_{13}^{(k)} & \overline{a}_{23}^{(k)} & \overline{a}_{33}^{(k)} \end{bmatrix}^T$ represents a column vector of size 6×1 that gathers the elements of matrix $\overline{\mathbf{A}}^{(k)}$ of the transformed coefficients referred to the geometric axes $\alpha_1, \alpha_2, \zeta$. The definition of this matrix is provided below:

$$\overline{\mathbf{A}}^{(k)} = \mathbf{Y}_\varepsilon \odot \left(\mathbf{H}^{(k)T} \widehat{\mathbf{A}}^{(k)} \mathbf{H}^{(k)} \right) \tag{33}$$

where the symbol $\odot$ denotes the Hadamard's product. The matrix $\widehat{\mathbf{A}}^{(k)}$ contains the well-known thermal expansion coefficients $\widehat{a}_{ij}^{(k)}$ with $i, j = 1, 2, 3$ of the k-th lamina, which are typically associated with the elements of the three-dimensional strain matrix. On the other hand, matrix $\mathbf{Y}_\varepsilon$ in Eq. (33) enables the derivation of the thermal expansion coefficients $a_{ij}^{(k)}$ with $i, j = 1, 2, 3$, that are consistent with the engineering strain components. This matrix is defined by the following relation expressed in the material reference system $\widehat{\alpha}_1^{(k)}, \widehat{\alpha}_2^{(k)}, \widehat{\zeta}^{(k)}$:

$$\mathbf{A}^{(k)} = \begin{bmatrix} a_{11}^{(k)} & a_{12}^{(k)} & a_{13}^{(k)} \\ a_{12}^{(k)} & a_{22}^{(k)} & a_{23}^{(k)} \\ a_{13}^{(k)} & a_{23}^{(k)} & a_{33}^{(k)} \end{bmatrix} = \begin{bmatrix} 1 & 2 & 2 \\ 2 & 1 & 2 \\ 2 & 2 & 1 \end{bmatrix} \odot \begin{bmatrix} \widehat{a}_{11}^{(k)} & \widehat{a}_{12}^{(k)} & \widehat{a}_{13}^{(k)} \\ \widehat{a}_{12}^{(k)} & \widehat{a}_{22}^{(k)} & \widehat{a}_{23}^{(k)} \\ \widehat{a}_{13}^{(k)} & \widehat{a}_{23}^{(k)} & \widehat{a}_{33}^{(k)} \end{bmatrix}$$
$$= \mathbf{Y}_\varepsilon \odot \widehat{\mathbf{A}}^{(k)} \tag{34}$$

The constitutive relation in Eq. (30) can be referred to the axes $\widehat{\alpha}_1^{(k)}$, $\widehat{\alpha}_2^{(k)}$, $\widehat{\zeta}^{(k)}$, which are defined at each point of the solid based on the symmetries of the constituent material, following the Newmann's principle. If $\widehat{\boldsymbol{\pi}}^{(k)}$ and $\widehat{\boldsymbol{\chi}}^{(k)}$ represent the vectors of primary and secondary variables in the material reference system, respectively, the following relation can be obtained:

$$\widehat{\boldsymbol{\chi}}^{(k)} = \boldsymbol{\Gamma}^{(k)} \widehat{\boldsymbol{\pi}}^{(k)} \quad \Leftrightarrow \quad \begin{bmatrix} \widehat{\boldsymbol{\sigma}}^{(k)} \\ \widehat{\mathscr{B}}^{(k)} \\ \eta^{(k)} \\ \widehat{\mathbf{h}}^{(k)} \end{bmatrix} = \begin{bmatrix} \boldsymbol{\Gamma}_{\mathrm{C}}^{(k)} & -\boldsymbol{\Gamma}_{\mathrm{Q}}^{(k)T} & -\boldsymbol{\Gamma}_{\mathrm{z}}^{(k)T} & \mathbf{0} \\ \boldsymbol{\Gamma}_{\mathrm{Q}}^{(k)} & \boldsymbol{\Gamma}_{\mathrm{M}}^{(k)} & \boldsymbol{\Gamma}_{\mathrm{w}}^{(k)T} & \mathbf{0} \\ \boldsymbol{\Gamma}_{\mathrm{z}}^{(k)} & \boldsymbol{\Gamma}_{\mathrm{w}}^{(k)} & \boldsymbol{\Gamma}_{\mathrm{TT}}^{(k)} & \mathbf{0} \\ \mathbf{0} & \mathbf{0} & \mathbf{0} & \boldsymbol{\Gamma}_{\mathrm{K}}^{(k)} \end{bmatrix} \begin{bmatrix} \widehat{\boldsymbol{\varepsilon}}^{(k)} \\ \widehat{\mathscr{K}}^{(k)} \\ \Delta\mathrm{T}^{(k)} \\ \widehat{\boldsymbol{\theta}}^{(k)} \end{bmatrix} \tag{35}$$

The previous equation is related to Eq. (30), with the introduction of a rotation matrix $\mathbf{H}^{(k)}$ of size 3×3, which contains the components of the material axes $\widehat{\alpha}_1^{(k)}, \widehat{\alpha}_2^{(k)}, \widehat{\zeta}^{(k)}$ in the geometric reference system and depends on the Euler angles of the rotated reference system. Assuming that $\widehat{\zeta}^{(k)}$ is parallel to the thickness direction, namely $\widehat{\zeta}^{(k)} = \zeta^{(k)}$, the matrix $\mathbf{H}^{(k)}$ depends only on the inclination angle, denoted by $\vartheta^{(k)}$, between $\widehat{\alpha}_1^{(k)}$ and α_1 axes, and takes the following form:

$$\mathbf{H}^{(k)} = \begin{bmatrix} \cos\vartheta^{(k)} & \sin\vartheta^{(k)} & 0 \\ -\sin\vartheta^{(k)} & \cos\vartheta^{(k)} & 0 \\ 0 & 0 & 1 \end{bmatrix} \tag{36}$$

In this way, the rotated multifield constitutive matrix is evaluated as:

$$\overline{\Gamma}^{(k)} = \begin{bmatrix} \mathbf{T}^{(k)} \boldsymbol{\Gamma}_{\mathrm{C}}^{(k)} \mathbf{T}^{(k)T} & -\mathbf{T}^{(k)} \boldsymbol{\Gamma}_{\mathrm{Q}}^{(k)T} \mathbf{H}^{(k)} & -\mathbf{T}^{(k)} \boldsymbol{\Gamma}_{\mathrm{C}}^{(k)} \mathbf{T}^{(k)T} \overline{\Gamma}_{\mathrm{a}}^{(k)} & \mathbf{0} \\ \mathbf{H}^{(k)T} \boldsymbol{\Gamma}_{\mathrm{Q}}^{(k)} \mathbf{T}^{(k)T} & \mathbf{H}^{(k)T} \boldsymbol{\Gamma}_{\mathrm{M}}^{(k)} \mathbf{H}^{(k)} & \mathbf{H}^{(k)T} \boldsymbol{\Gamma}_{\mathrm{w}}^{(k)T} & \mathbf{0} \\ \overline{\Gamma}_{\mathrm{a}}^{(k)T} \mathbf{T}^{(k)T} \boldsymbol{\Gamma}_{\mathrm{C}}^{(k)} \mathbf{T}^{(k)} & \boldsymbol{\Gamma}_{\mathrm{w}}^{(k)} \mathbf{H}^{(k)} & \boldsymbol{\Gamma}_{\mathrm{TT}}^{(k)} & \mathbf{0} \\ \mathbf{0} & \mathbf{0} & \mathbf{0} & \mathbf{H}^{(k)T} \boldsymbol{\Gamma}_{\mathrm{K}}^{(k)} \mathbf{H}^{(k)} \end{bmatrix} \tag{37}$$

Here, the matrix $\mathbf{T}^{(k)}$ of size 6×6 is derived from matrix $\overline{\mathbf{T}}^{(k)}$, by means of matrix $\mathbf{H}^{(k)}$ in Eq. (36), as follows:

$$\mathbf{T}^{(k)} = \overline{\mathbf{T}}^{(k)}_{([1,5,4,7,8,9]\times[1,5,2+4,3+7,6+8,9])}$$
$$= \left(\mathbf{H}^{(k)T} \otimes \left(\mathbf{H}^{(k)} \right)^{-1} \right)_{([1,5,4,7,8,9]\times[1,5,2+4,3+7,6+8,9])} \tag{38}$$

being $\otimes$ the well-known Kronecker product. Note that the matrix $\mathbf{T}^{(k)}$ is obtained from $\overline{\mathbf{T}}^{(k)}$ by selecting the rows indicated in the first square

brackets. On the other hand, the third, fourth, and fifth columns of $\mathbf{T}^{(k)}$ are derived as sum of the second and the fourth columns, the third and the seventh columns, the sixth and the eighth columns of $\overline{\mathbf{T}}^{(k)}$, respectively.

The governing equations of the present formulation are derived using an energy procedure. In this context, the virtual variation δY of the total energy of the solid must be evaluated within the ESL framework, employing the generalized unknown variables. This evaluation considers the elastic strain energy, the magnetic energy, the thermal energy, and all coupling terms among the involved physical phenomena. To this end, the vectors $\boldsymbol{\chi}^{(k)}$ and $\overline{\chi}^{(k)}$ are introduced at each point of the doubly-curved solid which collect the multifield secondary variables. These vectors are defined as follows, with $\mathbf{I}$ and $\widehat{\mathbf{I}}$ representing the identity matrices of sizes 3×3 and 6×6, respectively:

$$\overline{\chi}^{(k)} = \mathbf{B}\boldsymbol{\chi}^{(k)} \quad \Leftrightarrow \quad \begin{bmatrix} \boldsymbol{\sigma}^{(k)} \\ \mathscr{B}^{(k)} \\ \eta^{(k)} \\ \overline{\mathbf{h}}^{(k)} \end{bmatrix} = \begin{bmatrix} \widehat{\mathbf{I}} & \mathbf{0} & \mathbf{0} & \mathbf{0} \\ \mathbf{0} & \mathbf{I} & \mathbf{0} & \mathbf{0} \\ \mathbf{0} & \mathbf{0} & 1 & \mathbf{0} \\ \mathbf{0} & \mathbf{0} & \mathbf{0} & \dfrac{1}{\mathrm{T}_0}\mathbf{I} \end{bmatrix} \begin{bmatrix} \boldsymbol{\sigma}^{(k)} \\ \mathscr{B}^{(k)} \\ \eta^{(k)} \\ \mathbf{h}^{(k)} \end{bmatrix} \tag{39}$$

In addition, vector $\overline{\boldsymbol{\pi}}^{(k)T} = \left[\boldsymbol{\varepsilon}^{(k)T} \quad -\mathscr{H}^{(k)T} \quad -\widehat{\Delta \mathrm{T}}^{(k)} \quad \boldsymbol{\theta}^{(k)T} \right]^T$ is introduced, containing the sub-vectors of primary variables related to mechanical elasticity $\boldsymbol{\varepsilon}^{(k)}$, magnetostatics $\mathscr{H}^{(k)}$, and thermal conduction $\widehat{\Delta \mathrm{T}}^{(k)}, \boldsymbol{\theta}^{(k)}$. In this way, the virtual variation of the total energy of the shell Y is expressed as follows:

$$\delta Y = \sum_{k=1}^{l} \int_{\alpha_1} \int_{\alpha_2} \int_{\zeta_k}^{\zeta_{k+1}} (\delta \overline{\boldsymbol{\pi}}^{(k)T} \overline{\chi}^{(k)}) A_1 A_2 H_1 H_2 d\alpha_1 d\alpha_2 d\zeta =$$
$$= \sum_{k=1}^{l} \int_{\alpha_1} \int_{\alpha_2} \int_{\zeta_k}^{\zeta_{k+1}} \left(\delta \boldsymbol{\varepsilon}^{(k)T} \boldsymbol{\sigma}^{(k)} - \delta \mathscr{H}^{(k)T} \mathscr{B}^{(k)} - \delta \widehat{\Delta \mathrm{T}}^{(k)} \eta^{(k)} - \delta \boldsymbol{\theta}^{(k)T} \frac{\mathbf{h}^{(k)}}{\mathrm{T}_0} \right) A_1 A_2 H_1 H_2 d\alpha_1 d\alpha_2 d\zeta \tag{40}$$

The introduction of the higher-order generalized model from Eq. (9) into Eq. (40) leads to the definition of the generalized primary variables of the problem, defined for each τ-th order of the kinematic expasion, with $\tau = 0, ..., N+1$. By using Eq. (27) to express the virtual variation of the quantities $\delta\boldsymbol{\varepsilon}^{(k)}, \delta\mathscr{B}^{(k)}, \delta\widehat{\Delta \mathrm{T}}^{(k)}, \delta\boldsymbol{\theta}^{(k)}$, one gets [28]:

$$\delta Y = \sum_{k=1}^{l} \int_{\alpha_1} \int_{\alpha_2} \int_{\zeta_k}^{\zeta_{k+1}} \left(\sum_{\tau=0}^{N+1} \sum_{i=1}^{5} \mathbf{Z}^{(k\tau)\alpha_i} \delta \overline{\boldsymbol{\pi}}^{(\tau)\alpha_i} \right)^T \boldsymbol{\chi}^{(k)} A_1 A_2 H_1 H_2 d\zeta d\alpha_1 d\alpha_2 =$$
$$= \sum_{\tau=0}^{N+1} \sum_{i=1}^{5} \int_{\alpha_1} \int_{\alpha_2} (\delta \overline{\boldsymbol{\pi}}^{(\tau)\alpha_i})^T \left(\sum_{k=1}^{l} \int_{\zeta_k}^{\zeta_{k+1}} (\mathbf{Z}^{(k\tau)\alpha_i})^T \boldsymbol{\chi}^{(k)} H_1 H_2 d\zeta \right) A_1 A_2 d\alpha_1 d\alpha_2 =$$
$$= \sum_{\tau=0}^{N+1} \sum_{i=1}^{5} \int_{\alpha_1} \int_{\alpha_2} (\delta \overline{\boldsymbol{\pi}}^{(\tau)\alpha_i})^T \boldsymbol{\Sigma}^{(\tau)\alpha_i} A_1 A_2 d\alpha_1 d\alpha_2 \tag{41}$$

In the previous relation, the quantity $\overline{\boldsymbol{\pi}}^{(\tau)\alpha_i T} = \left[\boldsymbol{\varepsilon}^{(\tau)\alpha_i T} \quad -\mathscr{H}^{(\tau)\alpha_i T} \quad -\widehat{\Delta \mathrm{T}}^{(\tau)\alpha_i} \quad -\boldsymbol{\theta}^{(\tau)\alpha_i T} \right]^T$, defined for each $\tau = 0, ..., N+1$, collects the primary variables of the higher-order definition equations for each physical problem considered in the multiphysics model. On the other hand, the generalized secondary variables vector $\boldsymbol{\Sigma}^{(\tau)\alpha_i} = \left[\mathbf{S}^{(\tau)\alpha_i T} \quad \mathbf{B}^{(\tau)\alpha_i T} \quad E^{(\tau)\alpha_i} \quad \mathbf{H}^{(\tau)\alpha_i T} \right]^T$ incorporates the following quantities:

$$\mathbf{S}^{(\tau)\alpha_i} = \left[N_1^{(\tau)\alpha_i} \quad N_2^{(\tau)\alpha_i} \quad N_{12}^{(\tau)\alpha_i} \quad N_{21}^{(\tau)\alpha_i} \quad T_1^{(\tau)\alpha_i} \quad T_2^{(\tau)\alpha_i} \quad P_1^{(\tau)\alpha_i} \quad P_2^{(\tau)\alpha_i} \quad S_3^{(\tau)\alpha_i} \right]^T$$
$$\mathbf{B}^{(\tau)\alpha_i} = \left[B_1^{(\tau)\alpha_i} \quad B_2^{(\tau)\alpha_i} \quad B_3^{(\tau)\alpha_i} \right]^T, \quad \mathbf{H}^{(\tau)\alpha_i} = \left[H_1^{(\tau)\alpha_i} \quad H_2^{(\tau)\alpha_i} \quad H_3^{(\tau)\alpha_i} \right]^T \tag{42}$$

Each term of the vector $\boldsymbol{\Sigma}^{(\tau)\alpha_i}$ is evaluated for any $\tau = 0, ..., N+1$ by integrating along the thickness coordinate ζ, following the relation provided below in condensed form:

$$\boldsymbol{\Sigma}^{(\tau)\alpha_i} = \sum_{k=1}^{l} \int_{\zeta_k}^{\zeta_{k+1}} (\mathbf{Z}^{(k\tau)\alpha_i})^T \boldsymbol{\chi}^{(k)} H_1 H_2 d\zeta \tag{43}$$

Substituting the three-dimensional constitutive Eq. (30) and the generalized higher-order definition Eq. (27) into the previous relation, after some mathematical manipulation, a generalized version of the constitutive relation is derived for the entire laminate corresponding to an arbitrary τ-th order of kinematic expansion:

Table 1
Multifield constitutive coefficients of the materials employed in the simulations.

Material	Cobalt ferrite	TME-I	TME-II	TME-III	Barium titanate
V_f	0	0.2	0.4 [× 1/3]	0.6	1
T_0[K]	297	297	297	297	297
ρ[kg/m^3]	5300	5400	1833	5600	5800
M_∞[%]	0.01	0.01	0.02	0.01	0.03
c [J/kgK]	377.36	414.58	450.45	357.14	550.62
$C_{11} = C_{22}$ [× 10^9 N/m^2]	286	252.38	74.98	202.08	166
C_{12} [× 10^9 N/m^2]	173	144.72	40.78	104.26	77
$C_{13} = C_{23}$ [× 10^9 N/m^2]	170.5	143.99	40.89	105.13	78
$C_{66} = (C_{11} - C_{12})/2$ [× 10^9 N/m^2]	56.5	53.83	17.10	48.91	44.5
$C_{44} = C_{55}$ [× 10^9 N/m^2]	45.3	47.15	16.33	50.81	43
C_{33} [× 10^9 N/m^2]	269.5	24.11	72.41	196.54	162
$p_{14} = p_{25}$ [C/m^2]	0	0.04	0.03	0.23	11.6
$p_{31} = p_{32}$ [C/m^2]	0	−1.26	−0.76	−3.11	−4.4
p_{33} [C/m^2]	0	3.39	2.33	10.76	18.6
$q_{14} = q_{25}$ [Wb/m^2]	550	367.81	79.00	138.50	0
$q_{31} = q_{32}$ [Wb/m^2]	580.3	414.00	93.39	170.17	0
q_{33} [Wb/m^2]	−699.7	−602.79	−159.35	−332.94	0
$a_{11} = a_{22}$ [× 10^{-6} 1/K]	10	11.02	12.09	13.22	15.7
a_{33} [× 10^{-6} 1/K]	5	5.17	5.39	5.65	6.4
$b_{11} = b_{22}$ [× 10^{-4} m^3/kg]	1.1	0.90	0.70	0.48	0
b_{33} [× 10^{-4} m^3/kg]	0	0.01	0.17	0.02	0
$l_{11} = l_{22}$ [× 10^{-9} F/m]	0.08	11.94	0.06	0.31	11.2
l_{33} [× 10^{-9} F/m]	0.093	26.10	1.71	7.62	12.6
$d_{11} = d_{22}$ [× 10^{-12} s/m]	0	−2.56	−1.49	−5.91	0
d_{33} [× 10^{-9} s/m]	0	2.05	0.92	2.52	0
$m_{11} = m_{22}$ [× 10^{-6} H/m]	590	396.10	85.6	152.2	5
m_{33} [× 10^{-6} H/m]	157	127.87	32.86	69.1	10
o_{33} [× 10^{-5} C/m^{2}K]	0	3.60	0.27	11.51	20
g_{33} [× 10^{-4} Cm/kg]	0	−1.78	0	−2.20	0
w_{33} [× 10^{-4} T/K]	3.2	−2.69	−1.73	−5.19	0
f_{33} [Tm^3/kg]	0	−0.02	−0.01	−0.03	0
$k_{11} = k_{22}$ [J/mK]	3.2	3.03	0.96	2.74	2.5
k_{33} [J/mK]	3.2	3.06	0.97	2.78	2.5
$s_{11} = s_{22}$ [× 10^{-8} m^2] ($u_d = 0.1$, $\lambda\nu = 0.25$)	16	13.24	3.76	9.84	7.83
s_{33} [× 10^{-8} m^2] ($u_d = 0.1$, $\lambda\nu = 0.25$)	16	14.37	4.24	11.1	7.83
$x_{11} = x_{22}$ [× 10^{-8} kg/mK] ($u_d = 0.1$, $\lambda\nu = 0.25$)	4.08	4.46	1.54	4.66	4.57
x_{33} [× 10^{-8} kg/mK] ($u_d = 0.1$, $\lambda\nu = 0.25$)	4.08	4.50	1.56	4.73	4.57
$y_{11} = y_{22}$ [J/m^{2}K] ($u_d = 0.1$, $\lambda\nu = 0.25$)	3.14	2.25	0.59	1.45	1.07
y_{33} [J/m^{2}K] ($u_d = 0.1$, $\lambda\nu = 0.25$)	3.14	2.44	0.66	1.63	1.07

$$\begin{aligned}\boldsymbol{\Sigma}^{(\tau)\alpha_i} &= \sum_{\eta=0}^{N+1}\sum_{j=1}^{5}\left(\sum_{k=1}^{l}\int_{\zeta_k}^{\zeta_{k+1}}\left(\mathbf{Z}^{(k\tau)\alpha_i}\right)^T\overline{\Gamma}^{(k)}\mathbf{Z}^{(k\eta)\alpha_j}H_1H_2d\zeta\right)\boldsymbol{\pi}^{(\eta)\alpha_j}\\ &= \sum_{\eta=0}^{N+1}\sum_{j=1}^{5}\mathbf{A}^{(\tau\eta)\alpha_i\alpha_j}\boldsymbol{\pi}^{(\eta)\alpha_j}\end{aligned} \tag{44}$$

where $\mathbf{A}^{(\tau\eta)\alpha_i\alpha_j}$ is the higher-order multifield constitutive matrix of the laminate. This matrix takes into account the multifield properties of each lamina within the stacking sequence, as well as the curvature effects of the doubly-curved shell geometry. Further details can be found in Ref. [28]. By performing all matrix multiplications in Eq. (44), the following expression is derived for the arbitrary element of $\mathbf{A}^{(\tau\eta)\alpha_i\alpha_j}$, denoted by $A^{(\tau\eta)[fg]\ \alpha_i\alpha_j}_{rsnm\ (pq)}$ with r, $s = \varepsilon, \psi, \mathrm{T}$, setting $\partial^0 F_\tau^{(k)\alpha_i}/\partial\zeta^0 = F_\tau^{(k)\alpha_i}$ and $\partial^0 F_\eta^{(k)\alpha_j}/\partial\zeta^0 = F_\eta^{(k)\alpha_j}$:

$$A^{(\tau\eta)[fg]\ \alpha_i\alpha_j}_{rs\ nm\ (pq)} = \sum_{k=1}^{l}\int_{\zeta_k}^{\zeta_{k+1}}\overline{\mathrm{Y}}^{(k)}_{nm}\frac{\partial^f F_\tau^{(k)\alpha_i}}{\partial\zeta^f}\frac{\partial^g F_\eta^{(k)\alpha_j}}{\partial\zeta^g}\frac{H_1H_2}{H_1^pH_2^q}d\zeta \tag{45}$$

with $n, m = 1, \ldots, 13$, $p, q = 0, 1, 2$ and $f, g = 0, 1$. In the previous relation, the term $\overline{\mathrm{Y}}^{(k)}_{nm}$ refers to the arbitrary element of the multifield constitutive matrix $\overline{\Gamma}^{(k)}$ introduced in Eq. (30). An alternative form of Eq. (44) is presented below, which represents the generalized matrix $\mathbf{A}^{(\tau\eta)\alpha_i\alpha_j}$ based on the approach adopted in Eq. (35):

$$\begin{bmatrix}\mathbf{S}^{(\tau)\alpha_i}\\ \mathbf{B}^{(\tau)\alpha_i}\\ \mathbf{E}^{(\tau)\alpha_i}\\ \mathbf{H}^{(\tau)\alpha_i}\end{bmatrix} = \sum_{\eta=0}^{N+1}\sum_{j=1}^{5}\begin{bmatrix}\mathbf{A}^{(\tau\eta)\alpha_i\alpha_j}_{\varepsilon\varepsilon} & \mathbf{A}^{(\tau\eta)\alpha_i\alpha_j}_{\varepsilon\psi} & \mathbf{A}^{(\tau\eta)\alpha_i\alpha_j}_{\varepsilon\mathrm{T}} & \mathbf{0}\\ \mathbf{A}^{(\tau\eta)\alpha_i\alpha_j}_{\psi\varepsilon} & \mathbf{A}^{(\tau\eta)\alpha_i\alpha_j}_{\psi\psi} & \mathbf{A}^{(\tau\eta)\alpha_i\alpha_j}_{\psi\mathrm{T}} & \mathbf{0}\\ \mathbf{A}^{(\tau\eta)\alpha_i\alpha_j}_{\mathrm{T}\varepsilon} & \mathbf{A}^{(\tau\eta)\alpha_i\alpha_j}_{\mathrm{T}\psi} & \mathbf{A}^{(\tau\eta)\alpha_i\alpha_j}_{\mathrm{TT}} & \mathbf{0}\\ \mathbf{0} & \mathbf{0} & \mathbf{0} & \mathbf{A}^{(\tau\eta)\alpha_i\alpha_j}_{\vartheta\vartheta}\end{bmatrix}\begin{bmatrix}\boldsymbol{\varepsilon}^{(\eta)\alpha_j}\\ \boldsymbol{\gamma}^{(\eta)\alpha_j}\\ \widehat{\Delta\mathrm{T}}^{(\eta)\alpha_j}\\ \boldsymbol{\theta}^{(\eta)\alpha_j}\end{bmatrix} \tag{46}$$

According to Eq. (46), a constitutive equation is derived for the entire laminate, taking into account the material proeprties, the layer thickness, and the curvature of the structure. In this way, the model is transformed, from a physical point of view, into a rectangular physical domain with equivalent material properties which accounts for the geometry and the lamination scheme. The sub-matrices introduced in Eq. (46) are, thus, evaluated from the relations reported below:

$$\mathbf{A}_{\varepsilon\varepsilon}^{(\tau\eta)\alpha_i\alpha_j}=\sum_{k=1}^{I}\int_{\zeta_k}^{\zeta_{k+1}}\left(\mathbf{Z}_1^{(k\tau)\alpha_i}\right)^T\overline{\mathbf{\Gamma}}_{\mathrm{C}}^{(k)}\mathbf{Z}_1^{(k\eta)\alpha_j}H_1H_2d\zeta=\left[\left(A_{\varepsilon\varepsilon nm(pq)}^{(\tau\eta)[fg]\alpha_i\alpha_j}\right)_{hs}\right]_{\substack{h=1,\dots,9\\s=1,\dots,9}}=$$

$$=\left[\begin{array}{cccccc|ccc}
A_{11(20)}^{(\tau\eta)[00]\alpha_i\alpha_j} & A_{12(11)}^{(\tau\eta)[00]\alpha_i\alpha_j} & A_{16(20)}^{(\tau\eta)[00]\alpha_i\alpha_j} & A_{16(11)}^{(\tau\eta)[00]\alpha_i\alpha_j} & A_{14(20)}^{(\tau\eta)[00]\alpha_i\alpha_j} & A_{15(11)}^{(\tau\eta)[00]\alpha_i\alpha_j} & A_{14(10)}^{(\tau\eta)[01]\alpha_i\alpha_j} & A_{15(10)}^{(\tau\eta)[01]\alpha_i\alpha_j} & A_{13(10)}^{(\tau\eta)[01]\alpha_i\alpha_j}\\
A_{12(11)}^{(\tau\eta)[00]\alpha_i\alpha_j} & A_{22(02)}^{(\tau\eta)[00]\alpha_i\alpha_j} & A_{26(11)}^{(\tau\eta)[00]\alpha_i\alpha_j} & A_{26(02)}^{(\tau\eta)[00]\alpha_i\alpha_j} & A_{24(11)}^{(\tau\eta)[00]\alpha_i\alpha_j} & A_{25(02)}^{(\tau\eta)[00]\alpha_i\alpha_j} & A_{24(01)}^{(\tau\eta)[01]\alpha_i\alpha_j} & A_{25(01)}^{(\tau\eta)[01]\alpha_i\alpha_j} & A_{23(01)}^{(\tau\eta)[01]\alpha_i\alpha_j}\\
A_{16(20)}^{(\tau\eta)[00]\alpha_i\alpha_j} & A_{26(11)}^{(\tau\eta)[00]\alpha_i\alpha_j} & A_{66(20)}^{(\tau\eta)[00]\alpha_i\alpha_j} & A_{66(11)}^{(\tau\eta)[00]\alpha_i\alpha_j} & A_{46(20)}^{(\tau\eta)[00]\alpha_i\alpha_j} & A_{56(11)}^{(\tau\eta)[00]\alpha_i\alpha_j} & A_{46(10)}^{(\tau\eta)[01]\alpha_i\alpha_j} & A_{56(10)}^{(\tau\eta)[01]\alpha_i\alpha_j} & A_{36(10)}^{(\tau\eta)[01]\alpha_i\alpha_j}\\
A_{16(11)}^{(\tau\eta)[00]\alpha_i\alpha_j} & A_{26(02)}^{(\tau\eta)[00]\alpha_i\alpha_j} & A_{66(11)}^{(\tau\eta)[00]\alpha_i\alpha_j} & A_{66(02)}^{(\tau\eta)[00]\alpha_i\alpha_j} & A_{46(11)}^{(\tau\eta)[00]\alpha_i\alpha_j} & A_{56(02)}^{(\tau\eta)[00]\alpha_i\alpha_j} & A_{46(01)}^{(\tau\eta)[01]\alpha_i\alpha_j} & A_{56(01)}^{(\tau\eta)[01]\alpha_i\alpha_j} & A_{36(01)}^{(\tau\eta)[01]\alpha_i\alpha_j}\\
A_{14(20)}^{(\tau\eta)[00]\alpha_i\alpha_j} & A_{24(11)}^{(\tau\eta)[00]\alpha_i\alpha_j} & A_{46(20)}^{(\tau\eta)[00]\alpha_i\alpha_j} & A_{46(11)}^{(\tau\eta)[00]\alpha_i\alpha_j} & A_{44(20)}^{(\tau\eta)[00]\alpha_i\alpha_j} & A_{45(11)}^{(\tau\eta)[00]\alpha_i\alpha_j} & A_{44(10)}^{(\tau\eta)[01]\alpha_i\alpha_j} & A_{45(10)}^{(\tau\eta)[01]\alpha_i\alpha_j} & A_{34(10)}^{(\tau\eta)[01]\alpha_i\alpha_j}\\
A_{15(11)}^{(\tau\eta)[00]\alpha_i\alpha_j} & A_{25(02)}^{(\tau\eta)[00]\alpha_i\alpha_j} & A_{56(11)}^{(\tau\eta)[00]\alpha_i\alpha_j} & A_{56(02)}^{(\tau\eta)[00]\alpha_i\alpha_j} & A_{45(11)}^{(\tau\eta)[00]\alpha_i\alpha_j} & A_{55(02)}^{(\tau\eta)[00]\alpha_i\alpha_j} & A_{45(01)}^{(\tau\eta)[01]\alpha_i\alpha_j} & A_{55(01)}^{(\tau\eta)[01]\alpha_i\alpha_j} & A_{35(01)}^{(\tau\eta)[01]\alpha_i\alpha_j}\\
\hline
A_{14(10)}^{(\tau\eta)[10]\alpha_i\alpha_j} & A_{24(01)}^{(\tau\eta)[10]\alpha_i\alpha_j} & A_{46(10)}^{(\tau\eta)[10]\alpha_i\alpha_j} & A_{46(01)}^{(\tau\eta)[10]\alpha_i\alpha_j} & A_{44(10)}^{(\tau\eta)[10]\alpha_i\alpha_j} & A_{45(01)}^{(\tau\eta)[10]\alpha_i\alpha_j} & A_{44(00)}^{(\tau\eta)[11]\alpha_i\alpha_j} & A_{45(00)}^{(\tau\eta)[11]\alpha_i\alpha_j} & A_{34(00)}^{(\tau\eta)[11]\alpha_i\alpha_j}\\
A_{15(10)}^{(\tau\eta)[10]\alpha_i\alpha_j} & A_{25(01)}^{(\tau\eta)[10]\alpha_i\alpha_j} & A_{56(10)}^{(\tau\eta)[10]\alpha_i\alpha_j} & A_{56(01)}^{(\tau\eta)[10]\alpha_i\alpha_j} & A_{45(10)}^{(\tau\eta)[10]\alpha_i\alpha_j} & A_{55(01)}^{(\tau\eta)[10]\alpha_i\alpha_j} & A_{45(00)}^{(\tau\eta)[11]\alpha_i\alpha_j} & A_{55(00)}^{(\tau\eta)[11]\alpha_i\alpha_j} & A_{35(00)}^{(\tau\eta)[11]\alpha_i\alpha_j}\\
A_{13(10)}^{(\tau\eta)[10]\alpha_i\alpha_j} & A_{23(01)}^{(\tau\eta)[10]\alpha_i\alpha_j} & A_{36(10)}^{(\tau\eta)[10]\alpha_i\alpha_j} & A_{36(01)}^{(\tau\eta)[10]\alpha_i\alpha_j} & A_{34(10)}^{(\tau\eta)[10]\alpha_i\alpha_j} & A_{35(01)}^{(\tau\eta)[10]\alpha_i\alpha_j} & A_{34(00)}^{(\tau\eta)[11]\alpha_i\alpha_j} & A_{35(00)}^{(\tau\eta)[11]\alpha_i\alpha_j} & A_{33(00)}^{(\tau\eta)[11]\alpha_i\alpha_j}
\end{array}\right]$$

$$\mathbf{A}_{\psi\psi}^{(\tau\eta)\alpha_i\alpha_j}=\sum_{k=1}^{I}\int_{\zeta_k}^{\zeta_{k+1}}\mathbf{Z}_2^{(k\tau)\alpha_i}\overline{\mathbf{\Gamma}}_{\mathrm{M}}^{(k)}\mathbf{Z}_2^{(k\eta)\alpha_j}H_1H_2d\zeta=\left[\left(A_{\psi\psi nm(pq)}^{(\tau\eta)[fg]\alpha_i\alpha_j}\right)_{hs}\right]_{\substack{h=1,2,3\\s=1,2,3}}=\left[\begin{array}{cc|c}
M_{11(20)}^{(\tau\eta)[00]\alpha_i\alpha_j} & M_{12(11)}^{(\tau\eta)[00]\alpha_i\alpha_j} & M_{13(10)}^{(\tau\eta)[01]\alpha_i\alpha_j}\\
M_{12(11)}^{(\tau\eta)[00]\alpha_i\alpha_j} & M_{22(02)}^{(\tau\eta)[00]\alpha_i\alpha_j} & M_{23(01)}^{(\tau\eta)[01]\alpha_i\alpha_j}\\
\hline
M_{13(10)}^{(\tau\eta)[10]\alpha_i\alpha_j} & M_{23(01)}^{(\tau\eta)[10]\alpha_i\alpha_j} & M_{33(00)}^{(\tau\eta)[11]\alpha_i\alpha_j}
\end{array}\right]$$

$$\mathbf{A}_{\varepsilon\psi}^{(\tau\eta)\alpha_i\alpha_j}=-\sum_{k=1}^{I}\int_{\zeta_k}^{\zeta_{k+1}}\left(\mathbf{Z}_1^{(k\tau)\alpha_i}\right)^T\overline{\mathbf{\Gamma}}_{\mathrm{Q}}^{(k)T}\mathbf{Z}_2^{(k\eta)\alpha_j}H_1H_2d\zeta=\left[\left(A_{\varepsilon\psi nm(pq)}^{(\tau\eta)[fg]\alpha_i\alpha_j}\right)_{hs}\right]_{\substack{h=1,\dots,9\\s=1,2,3}}=$$

$$=-\left[\begin{array}{cccccc|ccc}
Q_{11(20)}^{(\tau\eta)[00]\alpha_i\alpha_j} & Q_{12(11)}^{(\tau\eta)[00]\alpha_i\alpha_j} & Q_{16(20)}^{(\tau\eta)[00]\alpha_i\alpha_j} & Q_{16(11)}^{(\tau\eta)[00]\alpha_i\alpha_j} & Q_{14(20)}^{(\tau\eta)[00]\alpha_i\alpha_j} & Q_{15(11)}^{(\tau\eta)[00]\alpha_i\alpha_j} & Q_{14(10)}^{(\tau\eta)[10]\alpha_i\alpha_j} & Q_{15(10)}^{(\tau\eta)[10]\alpha_i\alpha_j} & Q_{13(10)}^{(\tau\eta)[10]\alpha_i\alpha_j}\\
Q_{21(11)}^{(\tau\eta)[00]\alpha_i\alpha_j} & Q_{22(02)}^{(\tau\eta)[00]\alpha_i\alpha_j} & Q_{26(11)}^{(\tau\eta)[00]\alpha_i\alpha_j} & Q_{26(02)}^{(\tau\eta)[00]\alpha_i\alpha_j} & Q_{24(11)}^{(\tau\eta)[00]\alpha_i\alpha_j} & Q_{25(02)}^{(\tau\eta)[00]\alpha_i\alpha_j} & Q_{24(01)}^{(\tau\eta)[10]\alpha_i\alpha_j} & Q_{25(01)}^{(\tau\eta)[10]\alpha_i\alpha_j} & Q_{23(01)}^{(\tau\eta)[10]\alpha_i\alpha_j}\\
\hline
Q_{31(10)}^{(\tau\eta)[01]\alpha_i\alpha_j} & Q_{32(01)}^{(\tau\eta)[01]\alpha_i\alpha_j} & Q_{36(10)}^{(\tau\eta)[01]\alpha_i\alpha_j} & Q_{36(01)}^{(\tau\eta)[01]\alpha_i\alpha_j} & Q_{34(10)}^{(\tau\eta)[01]\alpha_i\alpha_j} & Q_{35(01)}^{(\tau\eta)[01]\alpha_i\alpha_j} & Q_{34(00)}^{(\tau\eta)[11]\alpha_i\alpha_j} & Q_{35(00)}^{(\tau\eta)[11]\alpha_i\alpha_j} & Q_{33(00)}^{(\tau\eta)[11]\alpha_i\alpha_j}
\end{array}\right]^T \tag{47}$$

$$\mathbf{A}_{\psi\varepsilon}^{(\tau\eta)\alpha_i\alpha_j}=\sum_{k=1}^{I}\int_{\zeta_k}^{\zeta_{k+1}}\mathbf{Z}_2^{(k\tau)\alpha_i}\overline{\mathbf{\Gamma}}_{\mathrm{Q}}^{(k)}\mathbf{Z}_1^{(k\eta)\alpha_j}H_1H_2d\zeta=\left[\left(A_{\psi\varepsilon nm(pq)}^{(\tau\eta)[fg]\alpha_i\alpha_j}\right)_{hs}\right]_{\substack{h=1,2,3\\s=1,\dots,9}}=$$

$$=\left[\begin{array}{cccccc|ccc}
Q_{11(20)}^{(\tau\eta)[00]\alpha_i\alpha_j} & Q_{12(11)}^{(\tau\eta)[00]\alpha_i\alpha_j} & Q_{16(20)}^{(\tau\eta)[00]\alpha_i\alpha_j} & Q_{16(11)}^{(\tau\eta)[00]\alpha_i\alpha_j} & Q_{14(20)}^{(\tau\eta)[00]\alpha_i\alpha_j} & Q_{15(11)}^{(\tau\eta)[00]\alpha_i\alpha_j} & Q_{14(10)}^{(\tau\eta)[01]\alpha_i\alpha_j} & Q_{15(10)}^{(\tau\eta)[01]\alpha_i\alpha_j} & Q_{13(10)}^{(\tau\eta)[01]\alpha_i\alpha_j}\\
Q_{21(11)}^{(\tau\eta)[00]\alpha_i\alpha_j} & Q_{22(02)}^{(\tau\eta)[00]\alpha_i\alpha_j} & Q_{26(11)}^{(\tau\eta)[00]\alpha_i\alpha_j} & Q_{26(02)}^{(\tau\eta)[00]\alpha_i\alpha_j} & Q_{24(11)}^{(\tau\eta)[00]\alpha_i\alpha_j} & Q_{25(02)}^{(\tau\eta)[00]\alpha_i\alpha_j} & Q_{24(01)}^{(\tau\eta)[101]\alpha_i\alpha_j} & Q_{25(01)}^{(\tau\eta)[101]\alpha_i\alpha_j} & Q_{23(01)}^{(\tau\eta)[101]\alpha_i\alpha_j}\\
\hline
Q_{31(10)}^{(\tau\eta)[10]\alpha_i\alpha_j} & Q_{32(01)}^{(\tau\eta)[10]\alpha_i\alpha_j} & Q_{36(10)}^{(\tau\eta)[10]\alpha_i\alpha_j} & Q_{36(01)}^{(\tau\eta)[10]\alpha_i\alpha_j} & Q_{34(10)}^{(\tau\eta)[10]\alpha_i\alpha_j} & Q_{35(01)}^{(\tau\eta)[10]\alpha_i\alpha_j} & Q_{34(00)}^{(\tau\eta)[11]\alpha_i\alpha_j} & Q_{35(00)}^{(\tau\eta)[11]\alpha_i\alpha_j} & Q_{33(00)}^{(\tau\eta)[11]\alpha_i\alpha_j}
\end{array}\right]$$

$$\mathbf{A}_{\varepsilon\mathrm{T}}^{(\tau\eta)\alpha_i\alpha_j}=-\sum_{k=1}^{I}\int_{\zeta_k}^{\zeta_{k+1}}\left(\mathbf{Z}_1^{(k\tau)\alpha_i}\right)^T\overline{\mathbf{\Gamma}}_{\mathrm{z}}^{(k)T}F_{\eta}^{(k)\alpha_j}H_1H_2d\zeta=\left[\left(A_{\varepsilon\mathrm{T}nm(pq)}^{(\tau\eta)[fg]\alpha_i\alpha_j}\right)_{hs}\right]_{h=1,\dots,9}=$$

$$=-\left[Z_{11(10)}^{(\tau\eta)[00]\alpha_i\alpha_j}\quad Z_{22(01)}^{(\tau\eta)[00]\alpha_i\alpha_j}\quad Z_{12(10)}^{(\tau\eta)[00]\alpha_i\alpha_j}\quad Z_{12(01)}^{(\tau\eta)[00]\alpha_i\alpha_j}\quad Z_{13(10)}^{(\tau\eta)[00]\alpha_i\alpha_j}\quad Z_{23(01)}^{(\tau\eta)[00]\alpha_i\alpha_j}\quad Z_{13(00)}^{(\tau\eta)[10]\alpha_i\alpha_j}\quad Z_{23(00)}^{(\tau\eta)[10]\alpha_i\alpha_j}\quad Z_{33(00)}^{(\tau\eta)[10]\alpha_i\alpha_j}\right]^T$$

$$\mathbf{A}_{\mathrm{T}\varepsilon}^{(\tau\eta)\alpha_i\alpha_j}=\sum_{k=1}^{I}\int_{\zeta_k}^{\zeta_{k+1}}F_{\tau}^{(k)\alpha_i}\overline{\mathbf{\Gamma}}_{\mathrm{z}}^{(k)}\mathbf{Z}_1^{(k\eta)\alpha_j}H_1H_2d\zeta=\left[\left(A_{\mathrm{T}\varepsilon nm(pq)}^{(\tau\eta)[fg]\alpha_i\alpha_j}\right)_{hs}\right]_{h=1,\dots,9}=$$

$$=\left[Z_{11(10)}^{(\tau\eta)[00]\alpha_i\alpha_j}\quad Z_{22(01)}^{(\tau\eta)[00]\alpha_i\alpha_j}\quad Z_{12(10)}^{(\tau\eta)[00]\alpha_i\alpha_j}\quad Z_{12(01)}^{(\tau\eta)[00]\alpha_i\alpha_j}\quad Z_{13(10)}^{(\tau\eta)[00]\alpha_i\alpha_j}\quad Z_{23(01)}^{(\tau\eta)[00]\alpha_i\alpha_j}\quad Z_{13(00)}^{(\tau\eta)[01]\alpha_i\alpha_j}\quad Z_{23(00)}^{(\tau\eta)[01]\alpha_i\alpha_j}\quad Z_{33(00)}^{(\tau\eta)[01]\alpha_i\alpha_j}\right]$$

$$\mathbf{A}_{\psi\mathrm{T}}^{(\tau\eta)\alpha_i\alpha_j}=\sum_{k=1}^{I}\int_{\zeta_k}^{\zeta_{k+1}}\mathbf{Z}_2^{(k\tau)\alpha_i}\overline{\mathbf{\Gamma}}_{\mathrm{w}}^{(k)T}F_{\eta}^{(k)\alpha_j}H_1H_2d\zeta=\left[\left(A_{\psi\mathrm{T}nm(pq)}^{(\tau\eta)[fg]\alpha_i\alpha_j}\right)_{hs}\right]_{h=1,2,3}=\left[W_{11(10)}^{(\tau\eta)[00]\alpha_i\alpha_j}\quad W_{22(01)}^{(\tau\eta)[00]\alpha_i\alpha_j}\quad W_{33(00)}^{(\tau\eta)[01]\alpha_i\alpha_j}\right]^T$$

$$\mathbf{A}_{\mathrm{T}\psi}^{(\tau\eta)\alpha_i\alpha_j}=\sum_{k=1}^{I}\int_{\zeta_k}^{\zeta_{k+1}}F_{\tau}^{(k)\alpha_i}\overline{\mathbf{\Gamma}}_{\mathrm{w}}^{(k)}\mathbf{Z}_2^{(k\eta)\alpha_j}H_1H_2d\zeta=\left[\left(A_{\mathrm{T}\psi nm(pq)}^{(\tau\eta)[fg]\alpha_i\alpha_j}\right)_{hs}\right]_{h=1\atop s=1,2,3}=\left[W_{11(10)}^{(\tau\eta)[00]\alpha_i\alpha_j}\quad W_{22(01)}^{(\tau\eta)[00]\alpha_i\alpha_j}\quad W_{33(00)}^{(\tau\eta)[10]\alpha_i\alpha_j}\right]$$

$$\mathbf{A}_{\mathrm{TT}}^{(\tau\eta)\alpha_i\alpha_j}=C_{11(00)}^{(\tau\eta)[00]\alpha_i\alpha_j}$$

$$\mathbf{A}_{\theta\theta}^{(\tau\eta)\alpha_i\alpha_j}=\left[\begin{array}{cc|c}
K_{11(20)}^{(\tau\eta)[00]\alpha_i\alpha_j} & K_{12(11)}^{(\tau\eta)[00]\alpha_i\alpha_j} & K_{13(10)}^{(\tau\eta)[01]\alpha_i\alpha_j}\\
K_{12(11)}^{(\tau\eta)[00]\alpha_i\alpha_j} & K_{22(02)}^{(\tau\eta)[00]\alpha_i\alpha_j} & K_{23(01)}^{(\tau\eta)[01]\alpha_i\alpha_j}\\
\hline
K_{13(10)}^{(\tau\eta)[10]\alpha_i\alpha_j} & K_{23(01)}^{(\tau\eta)[10]\alpha_i\alpha_j} & K_{33(00)}^{(\tau\eta)[11]\alpha_i\alpha_j}
\end{array}\right]$$

The generalized constitutive relation (44) is finally expressed in terms of the vector of generalized higher-order configuration variables $\boldsymbol{\delta}^{(\eta)}$, with $\eta = 0, ..., N+1$ by substituting the higher-order kinematic relations from Eq. (27) within Eq. (44). The following relation is, thus, derived [28]:

$$\boldsymbol{\Sigma}^{(\tau)\alpha_i} = \sum_{\eta=0}^{N+1} \sum_{j=1}^{5} \mathbf{A}^{(\tau\eta)\alpha_i\alpha_j} \mathbf{D}_{\Omega}^{\alpha_j} \boldsymbol{\delta}^{(\eta)} = \sum_{\eta=0}^{N+1} \mathbf{O}^{(\tau\eta)\alpha_i} \boldsymbol{\delta}^{(\eta)} \tag{48}$$

Regarding the external loads, it is assumed that the doubly-curved shell solid is subjected to multifield surface loads applied to its top (+) and bottom (−) surfaces, located at $\zeta = h/2$ and $\zeta = -h/2$, respectively. More specifically, the strucutre is subjected to the external mechanical pressures $q_1^{(+)}$, $q_2^{(+)}$, $q_3^{(+)}$ and $q_1^{(-)}$, $q_2^{(-)}$, $q_3^{(-)}$, thermal fluxes $q_{\mathrm{T}}^{(-)}$, $q_{\mathrm{T}}^{(+)}$ and magnetic fluxes $q_{\mathrm{B}}^{(-)}$, $q_{\mathrm{B}}^{(+)}$. Each external load is expressed in terms of a surface distribution $\widetilde{q}_{\alpha}^{(\pm)}(s_1, s_2)$ with $\alpha = 1, 2, 3, \mathrm{B}, \mathrm{T}$, which depends on the curvilinear coordinates s_1,s_2 as defined in Eq. (6), and a reference magnitude $\overline{q}_{\alpha}^{(\pm)}$:

$$q_{\alpha}^{(\pm)}(s_1, s_2) = \overline{q}_{\alpha}^{(\pm)} \widetilde{q}_{\alpha}^{(\pm)}(s_1, s_2) \tag{49}$$

The virtual work of the external surface loads of Eq. (49), denoted by δL_s, is evaluated as the sum of the contributions $\delta L_{es}, \delta L_{\psi s}, \delta L_{\mathrm{T}s}$ from mechanical, magnetic, and thermal loads, respectively. The following relation is obtained, where $H_1^{(+)}H_2^{(+)}$ and $H_1^{(-)}H_2^{(-)}$ are the scaling parameters introduced previously and evaluated at $\zeta = h/2$ and $\zeta = -h/2$, respectively:

$$\begin{aligned}
\delta L_s &= \delta L_{es} + \delta L_{\psi s} + \delta L_{\mathrm{T}s} = \\
&= \int_{\alpha_1}\int_{\alpha_2} \Bigg(\Bigg(q_1^{(-)}\delta U_1^{(-)} + q_2^{(-)}\delta U_2^{(-)} + q_3^{(-)}\delta U_3^{(-)} + q_{\mathrm{B}}^{(-)}\delta\Delta\psi^{(-)} + \frac{q_{\mathrm{T}}^{(-)}}{\mathrm{T}_0}\delta\Delta\mathrm{T}^{(-)} \Bigg) H_1^{(-)}H_2^{(-)} + \\
&+ \Bigg(q_1^{(+)}\delta U_1^{(+)} + q_2^{(+)}\delta U_2^{(+)} + q_3^{(+)}\delta U_3^{(+)} + q_{\mathrm{B}}^{(+)}\delta\Delta\psi^{(+)} + \frac{q_{\mathrm{T}}^{(+)}}{\mathrm{T}_0}\delta\Delta\mathrm{T}^{(+)} \Bigg) H_1^{(+)}H_2^{(+)} \Bigg) A_1A_2 d\alpha_1 d\alpha_2
\end{aligned} \tag{50}$$

It should be noted that the magnitude of the external loads in Eq. (49) does not depend on the configuration variables of the problem. In contrast, the actions $q_{1efk}^{(\pm)}, q_{2efk}^{(\pm)}, q_{3efk}^{(\pm)}$ induced by an external elastic foundation are expressed in terms of the three-dimensional displacement field variables $U_1^{(\pm)}, U_2^{(\pm)}, U_3^{(\pm)}$ at the top and bottom surface, according to the following definition [61]:

$$\begin{aligned}
q_{1efk}^{(\pm)} &= -k_{1f}^{(\pm)} U_1^{(\pm)} \\
q_{2efk}^{(\pm)} &= -k_{2f}^{(\pm)} U_2^{(\pm)} \\
q_{3efk}^{(\pm)} &= -k_{3f}^{(\pm)} U_3^{(\pm)} + G_f^{(\pm)} \nabla_{(\pm)}^2 U_3^{(\pm)}
\end{aligned} \tag{51}$$

The previous relation is based on the Winkler-Pasternak elastic foundation model. More specifically, the actions $q_{1efk}^{(\pm)}, q_{2efk}^{(\pm)}, q_{3efk}^{(\pm)}$ depend on the elastic stiffnesses $k_{1f}^{(\pm)}, k_{2f}^{(\pm)}$ and $k_{3f}^{(\pm)}$, respectively, as well as on the shear modulus $G_f^{(\pm)}$ of the foundation. Accordingly to the International Standards, the elastic stiffnesses are expressed in units of force per unit displacement, namely $[\mathrm{N/m^3}]$, while the units of $G_f^{(\pm)}$ are $[\mathrm{N/m^2}]$. Furthermore, the symbol $\nabla_{(\pm)}^2$ refers to the Laplacian operator, evaluated at $\zeta = h/2$ and $\zeta = -h/2$, whose expression is provided below using curvilinear principal coordinates α_1,α_2:

$$\begin{aligned}
\nabla_{(\pm)}^2 = &\left(\frac{1}{A_1^2 \left(H_1^{(\pm)}\right)^2} \frac{\partial^2}{\partial\alpha_1^2} + \frac{1}{A_2^2 \left(H_2^{(\pm)}\right)^2} \frac{\partial^2}{\partial\alpha_2^2} + \left(\frac{1}{A_1^2 A_2 \left(H_1^{(\pm)}\right)^2} \frac{\partial A_2}{\partial\alpha_1} - \frac{h}{2A_1^2 R_2^2 \left(H_1^{(\pm)}\right)^2 H_2^{(\pm)}} \frac{\partial R_2}{\partial\alpha_1} + \right.\right. \\
&- \frac{1}{A_1^3 \left(H_1^{(\pm)}\right)^2} \frac{\partial A_1}{\partial\alpha_1} - \frac{h}{2A_1^2 R_1^2 \left(H_1^{(\pm)}\right)^3} \frac{\partial R_1}{\partial\alpha_1} \Bigg) \frac{\partial}{\partial\alpha_1} + \left(\frac{1}{A_1 A_2^2 \left(H_2^{(\pm)}\right)^2} \frac{\partial A_1}{\partial\alpha_2} + \frac{h}{2A_2^2 R_1^2 \left(H_2^{(\pm)}\right)^2 H_1^{(\pm)}} \frac{\partial R_1}{\partial\alpha_2} + \right. \\
&\left.\left. - \frac{1}{A_2^3 \left(H_2^{(\pm)}\right)^2} \frac{\partial A_2}{\partial\alpha_2} - \frac{h}{2A_2^2 R_2^2 \left(H_2^{(\pm)}\right)^3} \frac{\partial R_2}{\partial\alpha_2} \right) \frac{\partial}{\partial\alpha_2} \right)
\end{aligned} \tag{52}$$

In this way, the virtual work δL_{efk} of the actions (51) from the elastic foundation is computed as:

$$\begin{aligned}
\delta L_{efk} = \int_{\alpha_1}\int_{\alpha_2} \Big(&\Big(q_{1efk}^{(-)}\delta U_1^{(-)} + q_{2efk}^{(-)}\delta U_2^{(-)} + q_{3efk}^{(-)}\delta U_3^{(-)} \Big) H_1^{(-)}H_2^{(-)} + \\
&+ \Big(q_{1efk}^{(+)}\delta U_1^{(+)} + q_{2efk}^{(+)}\delta U_2^{(+)} + q_{3efk}^{(+)}\delta U_3^{(+)} \Big) H_1^{(+)}H_2^{(+)} \Big) A_1A_2 d\alpha_1 d\alpha_2
\end{aligned} \tag{53}$$

By employing the static equivalence principle, it is possible to introduce generalized surface loads $q_{\alpha s}^{(\tau)}$ with $\alpha = 1, 2, 3, \mathrm{B}, \mathrm{T}$ and $i = 1, ..., 5$ for each $\tau = 0, ..., N+1$, which are applied at the reference surface of the shell solid, located at the mid-thickness. These multifield loads are calculated at each point of the rectangular physical domain using the relation provided below:

Table 2
Through-the-thickness smooth distributions of the material properties along each layer of the structure with algebraic and trigonometric functions. Furthermore, both symmetric and unsymmetric profiles are provided.

Denomination	Symbol	Analytical expression
Linear I	L-I	$g(\widehat{z}_k) = 1 - 2\lvert\widehat{z}_k\rvert$
Linear II	L-II	$g(\widehat{z}_k) = 2\lvert\widehat{z}_k\rvert$
Linear III	L-III	$g(\widehat{z}_k) = \dfrac{1+2\widehat{z}_k}{2}$
Linear IV	L-IV	$g(\widehat{z}_k) = \dfrac{1-2\widehat{z}_k}{2}$
Symmetric cosine I	SC-I	$g(\widehat{z}_k) = 1 - \cos(\pi\widehat{z}_k)^{\frac{1}{p}}$
Symmetric cosine II	SC-II	$g(\widehat{z}_k) = (\cos(\pi\widehat{z}_k))^{\frac{1}{p}}$
Unsymmetric cosine I	UC-I	$g(\widehat{z}_k) = 1 - \cos\left(\dfrac{\pi}{2}\widehat{z}_k + \dfrac{\pi}{4}\right)$
Unsymmetric cosine II	UC-II	$g(\widehat{z}_k) = \cos\left(\dfrac{\pi}{2}\widehat{z}_k + \dfrac{\pi}{4}\right)$
Unsymmetric cosine III	UC-III	$g(\widehat{z}_k) = 1 - \cos\left(\dfrac{\pi}{2}\widehat{z}_k - \dfrac{\pi}{4}\right)$
Unsymmetric cosine IV	UC-IV	$g(\widehat{z}_k) = \cos\left(\dfrac{\pi}{2}\widehat{z}_k - \dfrac{\pi}{4}\right)$
Hyperbolic sine I	HS-I	$g(\widehat{z}_k) = \dfrac{1}{2}\left(1 - \left(\dfrac{\sinh\widehat{z}_k}{\sinh\frac{1}{2}}\right)^{2p+1}\right)$
Hyperbolic sine II	HS-II	$g(\widehat{z}_k) = \dfrac{1}{2}\left(1 + \left(\dfrac{\sinh\widehat{z}_k}{\sinh\frac{1}{2}}\right)^{2p+1}\right)$
Hyperbolic tangent I	HT-I	$g(\widehat{z}_k) = \dfrac{1}{2}\left(1 - \left(\dfrac{\tanh\widehat{z}_k}{\tanh\frac{1}{2}}\right)^{3}\right)$
Hyperbolic tangent II	HT-II	$g(\widehat{z}_k) = \dfrac{1}{2}\left(1 + \left(\dfrac{\tanh\widehat{z}_k}{\tanh\frac{1}{2}}\right)^{3}\right)$
Exponential I	EXP-I	$g(\widehat{z}_k) = \dfrac{e^{\widehat{z}_k+\frac{1}{2}}-1}{e-1}$
Exponential II	EXP-II	$g(\widehat{z}_k) = 1 - \dfrac{e^{\widehat{z}_k+\frac{1}{2}}-1}{e-1}$

$$
\begin{aligned}
q_{1s}^{(\tau)} &= \left(q_1^{(-)} + q_{1efk}^{(-)}\right)F_\tau^{(1)\alpha_1(-)}H_1^{(-)}H_2^{(-)} + \left(q_1^{(+)} + q_{1efk}^{(+)}\right)F_\tau^{(l)\alpha_1(+)}H_1^{(+)}H_2^{(+)}\\
q_{2s}^{(\tau)} &= \left(q_2^{(-)} + q_{2efk}^{(-)}\right)F_\tau^{(1)\alpha_2(-)}H_1^{(-)}H_2^{(-)} + \left(q_2^{(+)} + q_{2efk}^{(+)}\right)F_\tau^{(l)\alpha_2(+)}H_1^{(+)}H_2^{(+)}\\
q_{3s}^{(\tau)} &= \left(q_3^{(-)} + q_{3efk}^{(-)}\right)F_\tau^{(1)\alpha_3(-)}H_1^{(-)}H_2^{(-)} + \left(q_3^{(+)} + q_{3efk}^{(+)}\right)F_\tau^{(l)\alpha_3(+)}H_1^{(+)}H_2^{(+)}\\
q_{\mathrm{Bs}}^{(\tau)} &= q_{\mathrm{B}}^{(-)}F_\tau^{(1)\alpha_4(-)}H_1^{(-)}H_2^{(-)} + q_{\mathrm{B}}^{(+)}F_\tau^{(l)\alpha_4(+)}H_1^{(+)}H_2^{(+)}\\
q_{\mathrm{Ts}}^{(\tau)} &= q_{\mathrm{T}}^{(-)}F_\tau^{(1)\alpha_5(-)}H_1^{(-)}H_2^{(-)} + q_{\mathrm{T}}^{(+)}F_\tau^{(l)\alpha_5(+)}H_1^{(+)}H_2^{(+)}
\end{aligned}
\tag{54}
$$

for $\tau = 0, \ldots, N+1$. In this way, it is assumed that the virtual work associated with $q_{\alpha s}^{(\tau)}$ is equal to the sum $\delta L_s + \delta L_{efk}$ of the virtual works defined in Eqs. (49) and (51). Finally, the generalized virtual work δL_{T} of the reference entropy of the shell solid at a given absolute temperature T_0, denoted by $\overline{\eta}^{(k)}$, is calculated as follows:

$$
\delta L_{\mathrm{T}} = -\sum_{k=1}^{l}\int_{\zeta_k}^{\zeta_{k+1}}\int_{\alpha_1}\int_{\alpha_2}\overline{\eta}^{(k)}\delta\Delta\mathrm{T}^{(k)}H_1H_2A_1A_2d\alpha_1d\alpha_2d\zeta \tag{55}
$$

Thus, the balance equations for the magneto-thermo-elastic problem can be evaluated using the Master Balance principle, as detailed in Ref. [28]. This approach considers the total free energy of the system from Eq. (41), the virtual works of the external loads from Eqs. (50) and (53), as well as the generalized virtual work from Eq. (55) associated with the reference entropy $\overline{\eta}^{(k)}$:

$$
\int_{t_1}^{t_2}\delta E\,dt = \int_{t_1}^{t_2}\left(\delta L_s + \delta L_{efk} + \delta L_{\mathrm{T}} - \delta Y\right)dt = 0 \tag{56}
$$

for any interval $[t_1,t_2]$, with $t_1 < t_2$. In particular, it is assumed that the model is under thermodynamic equilibrium conditions, such that the energy contribution δL_{T} in Eq. (55) is assumed null. The balance governing equations are derived from Eq. (56) for a stationary configuration of the solid. The application of the integration-by-parts rule yields, after some mathematical manipulation, the following relations for an arbitrary $\tau = 0, \ldots, N+1$:

$$
\sum_{i=1}^{5}\mathbf{D}_\Omega^{*\alpha_i}\boldsymbol{\Sigma}^{(\tau)\alpha_i} + \mathbf{q}_s^{(\tau)} = \sum_{i=1}^{5}\mathbf{D}_\Omega^{*\alpha_i}\boldsymbol{\Sigma}^{(\tau)\alpha_i} + \mathbf{q}_{efk}^{(\tau)} + \mathbf{q}^{(\tau)} = \mathbf{0} \tag{57}
$$

Here, $\mathbf{q}^{(\tau)} = \left[q_1^{(\tau)}\ \ q_2^{(\tau)}\ \ q_3^{(\tau)}\ \ q_{\mathrm{B}}^{(\tau)}\ \ q_{\mathrm{T}}^{(\tau)}\right]^T$ and $\mathbf{q}_{efk}^{(\tau)} = \left[q_{1efk}^{(\tau)}\ \ q_{2efk}^{(\tau)}\ \ q_{3efk}^{(\tau)}\ \ 0\ \ 0\right]^T$ are the vectors of generalized multifield external loads and the generalized actions induced by the elastic foundation, respectively, while $\mathbf{q}_s^{(\tau)} = \left[q_{1s}^{(\tau)}\ \ q_{2s}^{(\tau)}\ \ q_{3s}^{(\tau)}\ \ q_{\mathrm{Bs}}^{(\tau)}\ \ q_{\mathrm{Ts}}^{(\tau)}\right]^T$ is the vector of higher-order loads. Meanwhile, $\mathbf{D}_\Omega^{*\alpha_i}$ with $i = 1, \ldots, 5$ refer to the balance operators of the model, which take the following form:

$$
\mathbf{D}_\Omega^{*\alpha_1} = \begin{bmatrix} \overline{\mathbf{D}}_\Omega^{*\alpha_1} & \mathbf{0} & 0 & \mathbf{0}\\ \mathbf{0} & \mathbf{0} & 0 & \mathbf{0}\\ \mathbf{0} & \mathbf{0} & 0 & \mathbf{0}\\ \mathbf{0} & \mathbf{0} & 0 & \mathbf{0}\\ \mathbf{0} & \mathbf{0} & 0 & \mathbf{0} \end{bmatrix},\quad \mathbf{D}_\Omega^{*\alpha_2} = \begin{bmatrix} \mathbf{0} & \mathbf{0} & 0 & \mathbf{0}\\ \overline{\mathbf{D}}_\Omega^{*\alpha_2} & \mathbf{0} & 0 & \mathbf{0}\\ \mathbf{0} & \mathbf{0} & 0 & \mathbf{0}\\ \mathbf{0} & \mathbf{0} & 0 & \mathbf{0}\\ \mathbf{0} & \mathbf{0} & 0 & \mathbf{0} \end{bmatrix},\quad \mathbf{D}_\Omega^{*\alpha_3} = \begin{bmatrix} \mathbf{0} & \mathbf{0} & 0 & \mathbf{0}\\ \mathbf{0} & \mathbf{0} & 0 & \mathbf{0}\\ \overline{\mathbf{D}}_\Omega^{*\alpha_3} & \mathbf{0} & 0 & \mathbf{0}\\ \mathbf{0} & \mathbf{0} & 0 & \mathbf{0}\\ \mathbf{0} & \mathbf{0} & 0 & \mathbf{0} \end{bmatrix},
$$

$$
\mathbf{D}_\Omega^{*\alpha_4} = \begin{bmatrix} \mathbf{0} & \mathbf{0} & 0 & \mathbf{0}\\ \mathbf{0} & \mathbf{0} & 0 & \mathbf{0}\\ \mathbf{0} & \mathbf{0} & 0 & \mathbf{0}\\ \mathbf{0} & \overline{\mathbf{D}}_\Omega^{*\alpha_4} & 0 & \mathbf{0}\\ \mathbf{0} & \mathbf{0} & 0 & \mathbf{0} \end{bmatrix},\quad \mathbf{D}_\Omega^{*\alpha_5} = \begin{bmatrix} \mathbf{0} & \mathbf{0} & 0 & \mathbf{0}\\ \mathbf{0} & \mathbf{0} & 0 & \mathbf{0}\\ \mathbf{0} & \mathbf{0} & 0 & \mathbf{0}\\ \mathbf{0} & \mathbf{0} & 0 & \mathbf{0}\\ \mathbf{0} & \mathbf{0} & 0 & \overline{\mathbf{D}}_\Omega^{*\alpha_5} \end{bmatrix}
\tag{58}
$$

The quantities $\overline{\mathbf{D}}_\Omega^{*\alpha_i}$ for $i = 1, \ldots, 5$ are reported below in extended form:

$$
\overline{\mathbf{D}}_\Omega^{*\alpha_1} = \left[\frac{1}{A_1}\frac{\partial}{\partial\alpha_1} + \frac{1}{A_1A_2}\frac{\partial A_2}{\partial\alpha_1}\quad -\frac{1}{A_1A_2}\frac{\partial A_2}{\partial\alpha_1}\quad \frac{1}{A_1A_2}\frac{\partial A_1}{\partial\alpha_2}\quad \frac{1}{A_2}\frac{\partial}{\partial\alpha_2} + \frac{1}{A_1A_2}\frac{\partial A_1}{\partial\alpha_2}\quad \frac{1}{R_1}\quad 0\quad -1\quad 0\quad 0\right]
$$

$$
\overline{\mathbf{D}}_\Omega^{*\alpha_2} = \left[-\frac{1}{A_1A_2}\frac{\partial A_1}{\partial\alpha_2}\quad \frac{1}{A_2}\frac{\partial}{\partial\alpha_2} + \frac{1}{A_1A_2}\frac{\partial A_1}{\partial\alpha_2}\quad \frac{1}{A_1}\frac{\partial}{\partial\alpha_1} + \frac{1}{A_1A_2}\frac{\partial A_2}{\partial\alpha_1}\quad \frac{1}{A_1A_2}\frac{\partial A_2}{\partial\alpha_1}\quad 0\quad \frac{1}{R_2}\quad 0\quad -1\quad 0\right]
$$

$$
\overline{\mathbf{D}}_\Omega^{*\alpha_3} = \left[-\frac{1}{R_1}\quad -\frac{1}{R_2}\quad 0\quad 0\quad \frac{1}{A_1}\frac{\partial}{\partial\alpha_1} + \frac{1}{A_1A_2}\frac{\partial A_2}{\partial\alpha_1}\quad \frac{1}{A_2}\frac{\partial}{\partial\alpha_2} + \frac{1}{A_1A_2}\frac{\partial A_1}{\partial\alpha_2}\quad 0\quad 0\quad -1\right]
$$

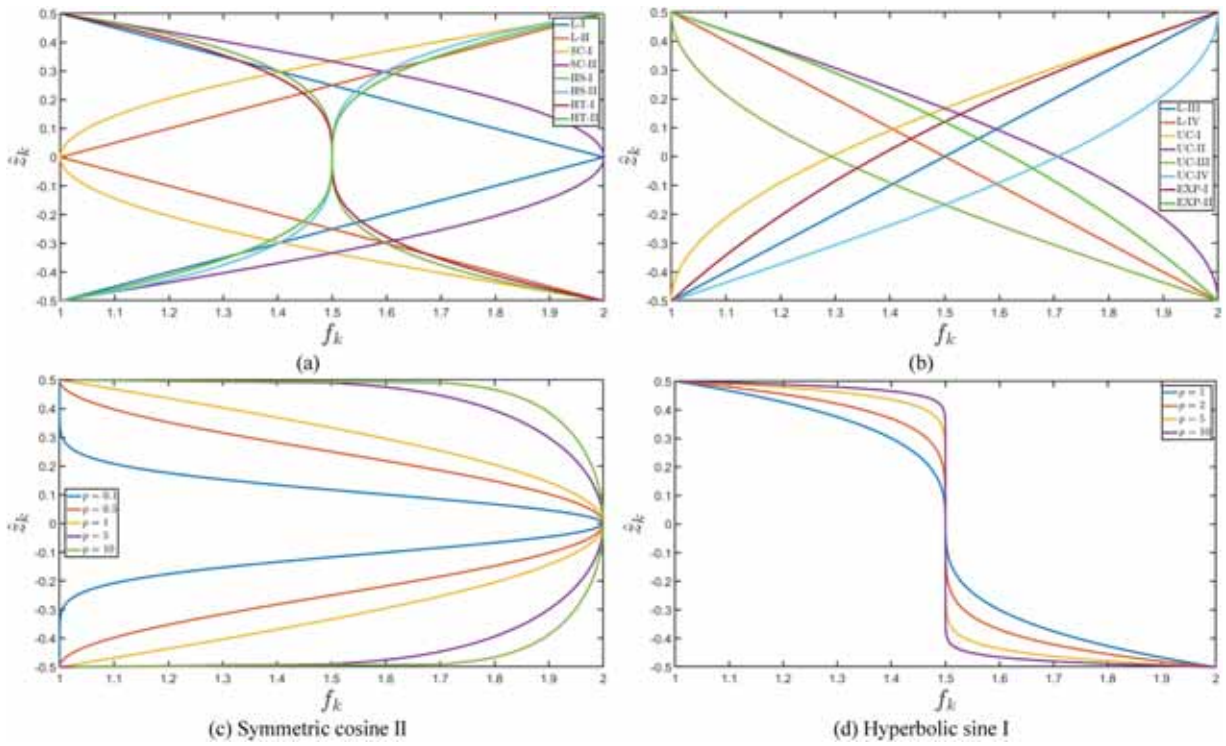

Fig. 1. One-dimensional analytical functions employed to describe the variation of the multifield material properties within an arbitrary layer in the stacking sequence of a doubly-curved shell laminate. (a) symmetric and anti-symmetric distributions; (b) unsymmetric distributions. Study on the profile in symmetric cosine II (c) and hyperbolic sine I (d) analytical functions for different values of the power coefficient p. The position and scaling parameters are set equal to $\delta_1 = 0$ and $\delta^{(k)} = 1$, respectively.

$$\overline{\mathbf{D}}_{\Omega}^{*\alpha_4} = \overline{\mathbf{D}}_{\Omega}^{*\alpha_5} = \left[\frac{1}{A_1}\frac{\partial}{\partial\alpha_1} + \frac{1}{A_1A_2}\frac{\partial A_2}{\partial\alpha_1} \quad \frac{1}{A_2}\frac{\partial}{\partial\alpha_2} + \frac{1}{A_1A_2}\frac{\partial A_1}{\partial\alpha_2} \quad -1\right] \tag{59}$$

The balance equations, presented in Eq. (57) in compact matrix form, are provided below in extended form [28]:

$$\begin{aligned}
&\frac{1}{A_1}\frac{\partial N_1^{(\tau)\alpha_1}}{\partial\alpha_1} + \frac{N_1^{(\tau)\alpha_1}}{A_1A_2}\frac{\partial A_2}{\partial\alpha_1} + \frac{1}{A_2}\frac{\partial N_{21}^{(\tau)\alpha_1}}{\partial\alpha_2} + \frac{N_{21}^{(\tau)\alpha_1}}{A_1A_2}\frac{\partial A_1}{\partial\alpha_2} + \frac{N_{12}^{(\tau)\alpha_1}}{A_1A_2}\frac{\partial A_1}{\partial\alpha_2} - \frac{N_2^{(\tau)\alpha_1}}{A_1A_2}\frac{\partial A_2}{\partial\alpha_1} \\
&\quad + \frac{T_1^{(\tau)\alpha_1}}{R_1} - P_1^{(\tau)\alpha_1} + q_{1s}^{(\tau)} \\
&\quad = 0 \\
&\frac{1}{A_2}\frac{\partial N_2^{(\tau)\alpha_2}}{\partial\alpha_2} + \frac{N_2^{(\tau)\alpha_2}}{A_1A_2}\frac{\partial A_1}{\partial\alpha_2} + \frac{1}{A_1}\frac{\partial N_{12}^{(\tau)\alpha_2}}{\partial\alpha_1} + \frac{N_{12}^{(\tau)\alpha_2}}{A_1A_2}\frac{\partial A_2}{\partial\alpha_1} + \frac{N_{21}^{(\tau)\alpha_2}}{A_1A_2}\frac{\partial A_2}{\partial\alpha_1} - \frac{N_1^{(\tau)\alpha_2}}{A_1A_2}\frac{\partial A_1}{\partial\alpha_2} \\
&\quad + \frac{T_2^{(\tau)\alpha_2}}{R_2} - P_2^{(\tau)\alpha_2} + q_{2s}^{(\tau)} \\
&\quad = 0 \\
&\frac{1}{A_1}\frac{\partial T_1^{(\tau)\alpha_3}}{\partial\alpha_1} + \frac{T_1^{(\tau)\alpha_3}}{A_1A_2}\frac{\partial A_2}{\partial\alpha_1} + \frac{1}{A_2}\frac{\partial T_2^{(\tau)\alpha_3}}{\partial\alpha_2} + \frac{T_2^{(\tau)\alpha_3}}{A_1A_2}\frac{\partial A_1}{\partial\alpha_2} - \frac{N_1^{(\tau)\alpha_3}}{R_1} - \frac{N_2^{(\tau)\alpha_3}}{R_2} - S_3^{(\tau)\alpha_3} \\
&\quad + q_{3s}^{(\tau)} \\
&\quad = 0 \\
&\frac{1}{A_1}\frac{\partial B_1^{(\tau)\alpha_4}}{\partial\alpha_1} + \frac{B_1^{(\tau)\alpha_4}}{A_1A_2}\frac{\partial A_2}{\partial\alpha_1} + \frac{1}{A_2}\frac{\partial B_2^{(\tau)\alpha_4}}{\partial\alpha_2} + \frac{B_2^{(\tau)\alpha_4}}{A_1A_2}\frac{\partial A_1}{\partial\alpha_2} - B_3^{(\tau)\alpha_4} + q_{\mathrm{Bs}}^{(\tau)} = 0 \\
&\frac{1}{A_1}\frac{\partial H_1^{(\tau)\alpha_5}}{\partial\alpha_1} + \frac{H_1^{(\tau)\alpha_5}}{A_1A_2}\frac{\partial A_2}{\partial\alpha_1} + \frac{1}{A_2}\frac{\partial H_2^{(\tau)\alpha_5}}{\partial\alpha_2} + \frac{H_2^{(\tau)\alpha_5}}{A_1A_2}\frac{\partial A_1}{\partial\alpha_2} - H_3^{(\tau)\alpha_5} + q_{\mathrm{Ts}}^{(\tau)} = 0
\end{aligned} \tag{60}$$

The natural boundary conditons, applied at the boundaries of the two-dimensional physical domain $\left[\alpha_1^0, \alpha_1^1\right] \times \left[\alpha_2^0, \alpha_2^1\right]$, are derived for an arbitrary $\tau = 0, ..., N+1$, by applying the integration-by-parts rule to the Master Balance principle in Eq. (56). The following relations are obtained for $\alpha_1 = \alpha_1^0$ or $\alpha_1 = \alpha_1^1$:

$$\begin{aligned}
&N_1^{(\tau)\alpha_1} = \overline{N}_1^{(\tau)\alpha_1} \quad \text{or} \quad u_1^{(\tau)} = \overline{u}_1^{(\tau)} \\
&N_{12}^{(\tau)\alpha_2} = \overline{N}_{12}^{(\tau)\alpha_2} \quad \text{or} \quad u_2^{(\tau)} = \overline{u}_2^{(\tau)} \\
&T_1^{(\tau)\alpha_3} = \overline{T}_1^{(\tau)\alpha_3} \quad \text{or} \quad u_3^{(\tau)} = \overline{u}_3^{(\tau)} \\
&B_1^{(\tau)\alpha_4} = \overline{B}_1^{(\tau)\alpha_4} \quad \text{or} \quad \psi^{(\tau)} = \overline{\psi}^{(\tau)} \\
&H_1^{(\tau)\alpha_5} = \overline{H}_1^{(\tau)\alpha_5} \quad \text{or} \quad \xi^{(\tau)} = \overline{\xi}^{(\tau)}
\end{aligned} \tag{61}$$

In the same way, the boundary conditions at $\alpha_2 = \alpha_2^0$ or $\alpha_2 = \alpha_2^1$ take the following form:

$$\begin{aligned}
&N_{21}^{(\tau)\alpha_1} = \overline{N}_{21}^{(\tau)\alpha_1} \quad \text{or} \quad u_1^{(\tau)} = \overline{u}_1^{(\tau)} \\
&N_2^{(\tau)\alpha_2} = \overline{N}_2^{(\tau)\alpha_2} \quad \text{or} \quad u_2^{(\tau)} = \overline{u}_2^{(\tau)} \\
&T_2^{(\tau)\alpha_3} = \overline{T}_2^{(\tau)\alpha_3} \quad \text{or} \quad u_3^{(\tau)} = \overline{u}_3^{(\tau)} \\
&B_2^{(\tau)\alpha_4} = \overline{B}_2^{(\tau)\alpha_4} \quad \text{or} \quad \psi^{(\tau)} = \overline{\psi}^{(\tau)} \\
&H_2^{(\tau)\alpha_5} = \overline{H}_2^{(\tau)\alpha_5} \quad \text{or} \quad \xi^{(\tau)} = \overline{\xi}^{(\tau)}
\end{aligned} \tag{62}$$

The boundary conditions specified in Eqs. (61)-(62) are characterized by prescribed values for multifield configuration and secondary variables, denoted by $\overline{u}_1^{(\tau)}, \overline{u}_2^{(\tau)}, \overline{u}_3^{(\tau)}, \overline{\psi}^{(\tau)}, \overline{\xi}^{(\tau)}, \overline{N}_1^{(\tau)\alpha_1}, \overline{N}_{12}^{(\tau)\alpha_2}, \overline{T}_1^{(\tau)\alpha_3}, \overline{B}_1^{(\tau)\alpha_4}, \overline{H}_1^{(\tau)\alpha_5}$ and $\overline{N}_{21}^{(\tau)\alpha_1}, \overline{N}_2^{(\tau)\alpha_2}, \overline{T}_2^{(\tau)\alpha_3}, \overline{B}_2^{(\tau)\alpha_4}, \overline{H}_2^{(\tau)\alpha_5}$, respectively, at each point along the edges of the physical domain. The combination of the conditions in Eqs. (61)-(62) yields various boundary conditions for multifield analysis. In all simulations performed in this work, the Simply-supported (S) boundary condition is considered, which is assessed as reported below:

$$\begin{aligned}
&N_1^{(\tau)\alpha_1} = 0, \quad u_2^{(\tau)} = u_3^{(\tau)} = \psi^{(\tau)} = \xi^{(\tau)} = 0 \quad \text{at} \quad \alpha_1 = \alpha_1^0 \text{ or } \alpha_1 = \alpha_1^1 \\
&N_2^{(\tau)\alpha_2} = 0, \quad u_1^{(\tau)} = u_3^{(\tau)} = \psi^{(\tau)} = \xi^{(\tau)} = 0 \quad \text{at} \quad \alpha_2 = \alpha_2^0 \text{ or } \alpha_2 = \alpha_2^1
\end{aligned} \tag{63}$$

At this point, the generalized kinematic model from Eq. (9) is introduced into Eq. (57) to express the magneto-thermo-elastic fundamental relations in terms of the unknown variables of the model, which are arranged in the vector $\boldsymbol{\delta}^{(\tau)}(\alpha_1,\alpha_2)$, for $\tau = 0, ..., N+1$. Thus, the generalized constitutive relation from Eq. (48) is substituted into Eq. (57), resulting in the provided reported below, which is explored in Ref. [28]:

$$\sum_{\eta=0}^{N+1} \mathbf{L}^{(\tau\eta)}\boldsymbol{\delta}^{(\eta)} + \mathbf{q}^{(\tau)} = \mathbf{0} \tag{64}$$

for $\tau = 0, ..., N+1$. In the previous equation, $\mathbf{L}^{(\tau\eta)}$ denotes the fundamental matrix of the system associated with any $\tau, \eta = 0, ..., N+1$. Based on an extended notation, this operator takes the following form:

$$\mathbf{L}^{(\tau\eta)} = \left[\begin{array}{ccc|c|c} L_{11}^{(\tau\eta)\alpha_1\alpha_1} - L_{11f}^{(\tau\eta)\alpha_1\alpha_1} & L_{12}^{(\tau\eta)\alpha_1\alpha_2} & L_{13}^{(\tau\eta)\alpha_1\alpha_3} & L_{14}^{(\tau\eta)\alpha_1\alpha_4} & L_{15}^{(\tau\eta)\alpha_1\alpha_5} \\ L_{21}^{(\tau\eta)\alpha_2\alpha_1} & L_{22}^{(\tau\eta)\alpha_2\alpha_2} - L_{22f}^{(\tau\eta)\alpha_2\alpha_2} & L_{23}^{(\tau\eta)\alpha_2\alpha_3} & L_{24}^{(\tau\eta)\alpha_2\alpha_4} & L_{25}^{(\tau\eta)\alpha_2\alpha_5} \\ L_{31}^{(\tau\eta)\alpha_3\alpha_1} & L_{32}^{(\tau\eta)\alpha_3\alpha_2} & L_{33}^{(\tau\eta)\alpha_3\alpha_3} - L_{33f}^{(\tau\eta)\alpha_3\alpha_3} & L_{34}^{(\tau\eta)\alpha_3\alpha_4} & L_{35}^{(\tau\eta)\alpha_3\alpha_5} \\ \hline L_{41}^{(\tau\eta)\alpha_4\alpha_1} & L_{42}^{(\tau\eta)\alpha_4\alpha_2} & L_{43}^{(\tau\eta)\alpha_4\alpha_3} & L_{44}^{(\tau\eta)\alpha_4\alpha_4} & L_{45}^{(\tau\eta)\alpha_4\alpha_5} \\ \hline L_{51}^{(\tau\eta)\alpha_5\alpha_1} & L_{52}^{(\tau\eta)\alpha_5\alpha_2} & L_{53}^{(\tau\eta)\alpha_5\alpha_3} & L_{54}^{(\tau\eta)\alpha_5\alpha_4} & L_{55}^{(\tau\eta)\alpha_5\alpha_5} \end{array}\right] \tag{65}$$

The elements $L_{ij}^{(\tau\eta)\alpha_i\alpha_j}$ with $i, j = 1, ..., 5$ of the fundamental matrix $\mathbf{L}^{(\tau\eta)}$ of Eq. (65) are evaluated from the sub-matrices of the generalized constitutive operator in Eq. (46), as reported below:

$$\begin{aligned}
L_{ij}^{(\tau\eta)\alpha_i\alpha_j} &= \overline{\mathbf{D}}_{\Omega}^{*\alpha_i}\mathbf{A}_{\varepsilon\varepsilon}^{(\tau\eta)\alpha_i\alpha_j}\overline{\mathbf{D}}_{\Omega}^{\alpha_j} \;\; i,j = 1,2,3 \\
L_{ij}^{(\tau\eta)\alpha_i\alpha_j} &= \overline{\mathbf{D}}_{\Omega}^{*\alpha_i}\mathbf{A}_{\varepsilon\psi}^{(\tau\eta)\alpha_i\alpha_j}\overline{\mathbf{D}}_{\Omega}^{\alpha_j} \;\; i,j = 1,2,3, \;\; j = 4 \\
L_{ij}^{(\tau\eta)\alpha_i\alpha_j} &= \overline{\mathbf{D}}_{\Omega}^{*\alpha_i}\mathbf{A}_{\varepsilon\mathrm{T}}^{(\tau\eta)\alpha_i\alpha_j}\overline{\mathbf{D}}_{\Omega}^{\alpha_j} \;\; i,j = 1,2,3, \;\; j = 5 \\
L_{ij}^{(\tau\eta)\alpha_i\alpha_j} &= \overline{\mathbf{D}}_{\Omega}^{*\alpha_i}\mathbf{A}_{\psi\varepsilon}^{(\tau\eta)\alpha_i\alpha_j}\overline{\mathbf{D}}_{\Omega}^{\alpha_j} \;\; i = 4 \;\; j = 1,2,3 \\
L_{ij}^{(\tau\eta)\alpha_i\alpha_j} &= \overline{\mathbf{D}}_{\Omega}^{*\alpha_i}\mathbf{A}_{\psi\psi}^{(\tau\eta)\alpha_i\alpha_j}\overline{\mathbf{D}}_{\Omega}^{\alpha_j} \;\; i,j = 4 \\
L_{ij}^{(\tau\eta)\alpha_i\alpha_j} &= \overline{\mathbf{D}}_{\Omega}^{*\alpha_i}\mathbf{A}_{\psi\mathrm{T}}^{(\tau\eta)\alpha_i\alpha_j}\overline{\mathbf{D}}_{\Omega}^{\alpha_j} \;\; i = 4 \;\; j = 5 \\
L_{ij}^{(\tau\eta)\alpha_i\alpha_j} &= \overline{\mathbf{D}}_{\Omega}^{*\alpha_i}\mathbf{A}_{\mathrm{TT}}^{(\tau\eta)\alpha_i\alpha_j}\overline{\mathbf{D}}_{\Omega}^{\alpha_j} \;\; i = 5 \;\; j = 5 \\
L_{ij}^{(\tau\eta)\alpha_i\alpha_j} &= 0 \;\; i = 5 \;\; j = 1, ..., 4 \\
L_{11f}^{(\tau\eta)\alpha_1\alpha_1} &= k_{1f}^{(-)}F_{\eta}^{(1)\alpha_1(-)}F_{\tau}^{(1)\alpha_1(-)}H_1^{(-)}H_2^{(-)} + k_{1f}^{(+)}F_{\eta}^{(l)\alpha_1(+)}F_{\tau}^{(l)\alpha_1(+)}H_1^{(+)}H_2^{(+)} \\
L_{22f}^{(\tau\eta)\alpha_2\alpha_2} &= k_{2f}^{(-)}F_{\eta}^{(1)\alpha_2(-)}F_{\tau}^{(1)\alpha_2(-)}H_1^{(-)}H_2^{(-)} + k_{2f}^{(+)}F_{\eta}^{(l)\alpha_2(+)}F_{\tau}^{(l)\alpha_2(+)}H_1^{(+)}H_2^{(+)} \\
L_{33f}^{(\tau\eta)\alpha_3\alpha_3} &= \left(k_{3f}^{(-)} - G_f^{(-)}\nabla_{(-)}^2\right)F_{\eta}^{(1)\alpha_3(-)}F_{\tau}^{(1)\alpha_3(-)}H_1^{(-)}H_2^{(-)} + \left(k_{3f}^{(+)} - G_f^{(+)}\nabla_{(+)}^2\right)F_{\eta}^{(l)\alpha_3(+)}F_{\tau}^{(l)\alpha_3(+)}H_1^{(+)}H_2^{(+)}
\end{aligned} \tag{66}$$

At this point, a semi-analytical solution to the higher-order fundamental Eq. (64) is derived using the well-known Navier approach [28]. To this end, the uniform radii of curvature (4) and Lamé parameters (5) are assumed throughout the physical domain. In other words, it is assumed that the derivatives of these quantities with respect to $s_i = s_1, s_2$ are null:

$$\begin{aligned}
\frac{\partial^{n+m}A_1}{\partial s_1^n \partial s_2^m} = 0, \quad \frac{\partial^{n+m}A_2}{\partial s_1^n \partial s_2^m} = 0 \\
\frac{\partial^{n+m}R_1}{\partial s_1^n \partial s_2^m} = 0, \quad \frac{\partial^{n+m}R_2}{\partial s_1^n \partial s_2^m} = 0
\end{aligned} \tag{67}$$

Under these assumptions, the quantities $L_i = L_1, L_2$ of the parametric lines along $\alpha_i = \alpha_1, \alpha_2$ can be expressed according to the following relation:

$$L_i = s_i^1 - s_i^0 = \left(\alpha_i^1 - \alpha_i^0\right)R_i \tag{68}$$

As a particular case of Eq. (68), lengths L_1, L_2 of a circular cylinder with a generatrix along α_1 and principal radii of curvature $R_1 = R$ and $R_2 = +\infty$ are derived as follows:

$$\begin{aligned}
L_1 &= s_1^1 - s_1^0 = \left(\alpha_1^1 - \alpha_1^0\right)R \\
L_2 &= s_2^1 - s_2^0 = \alpha_2^1 - \alpha_2^0
\end{aligned} \tag{69}$$

Similarly, if the generatrix of the cylinder is oriented along α_2, we consider the following relation:

$$\begin{aligned}
L_1 &= s_1^1 - s_1^0 = \alpha_1^1 - \alpha_1^0 \\
L_2 &= s_2^1 - s_2^0 = \left(\alpha_2^1 - \alpha_2^0\right)R
\end{aligned} \tag{70}$$

with $R_1 = +\infty$ and $R_2 = R$. The unknown configuration variables associated to an arbitrary $\tau = 0,...,N+1$ are expanded with two-dimensional trigonometric series with respect to the parametric coordinate $s_i = s_1, s_2$ as follows, setting $\widetilde{N} = \widetilde{M} = +\infty$:

$$
\begin{aligned}
u_1^{(\tau)}(s_1,s_2) &= \sum_{n=1}^{\tilde{N}}\sum_{m=1}^{\tilde{M}} \mathrm{U}_{1nm}^{(\tau)} \cos\left(\frac{n\pi}{L_1}s_1\right)\sin\left(\frac{m\pi}{L_2}s_2\right)\\
u_2^{(\tau)}(s_1,s_2) &= \sum_{n=1}^{\tilde{N}}\sum_{m=1}^{\tilde{M}} \mathrm{U}_{2nm}^{(\tau)} \sin\left(\frac{n\pi}{L_1}s_1\right)\cos\left(\frac{m\pi}{L_2}s_2\right)\\
u_3^{(\tau)}(s_1,s_2) &= \sum_{n=1}^{\tilde{N}}\sum_{m=1}^{\tilde{M}} \mathrm{U}_{3nm}^{(\tau)} \sin\left(\frac{n\pi}{L_1}s_1\right)\sin\left(\frac{m\pi}{L_2}s_2\right)\\
\psi^{(\tau)}(s_1,s_2) &= \sum_{n=1}^{\tilde{N}}\sum_{m=1}^{\tilde{M}} \Psi_{nm}^{(\tau)} \sin\left(\frac{n\pi}{L_1}s_1\right)\sin\left(\frac{m\pi}{L_2}s_2\right)\\
\xi^{(\tau)}(s_1,s_2) &= \sum_{n=1}^{\tilde{N}}\sum_{m=1}^{\tilde{M}} \Xi_{nm}^{(\tau)} \sin\left(\frac{n\pi}{L_1}s_1\right)\sin\left(\frac{m\pi}{L_2}s_2\right)
\end{aligned}
\tag{71}
$$

The unknown quantities introduced in Eq. (71) are collected, for any $n = 1, ..., \tilde{N}$ and $m = 1, ..., \tilde{M}$, in the vector $\mathbf{U}_{nm}^{(\tau)} = [\,\mathrm{U}_{1nm}^{(\tau)} \;\; \mathrm{U}_{2nm}^{(\tau)} \;\; \mathrm{U}_{3nm}^{(\tau)} \;\; \Psi_{nm}^{(\tau)} \;\; \Xi_{nm}^{(\tau)}\,]^T$. A similar approach is also adopted to express the actual distribution of external surface loads introduced in Eq. (49):

$$
\begin{aligned}
q_1^{(\tau)}(s_1,s_2) &= \sum_{n=1}^{\tilde{N}}\sum_{m=1}^{\tilde{M}} Q_{1snm}^{(\tau)} \cos\left(\frac{n\pi}{L_1}s_1\right)\sin\left(\frac{m\pi}{L_2}s_2\right)\\
q_2^{(\tau)}(s_1,s_2) &= \sum_{n=1}^{\tilde{N}}\sum_{m=1}^{\tilde{M}} Q_{2snm}^{(\tau)} \sin\left(\frac{n\pi}{L_1}s_1\right)\cos\left(\frac{m\pi}{L_2}s_2\right)\\
q_3^{(\tau)}(s_1,s_2) &= \sum_{n=1}^{\tilde{N}}\sum_{m=1}^{\tilde{M}} Q_{3snm}^{(\tau)} \sin\left(\frac{n\pi}{L_1}s_1\right)\sin\left(\frac{m\pi}{L_2}s_2\right)\\
q_{\mathrm{B}}^{(\tau)}(s_1,s_2) &= \sum_{n=1}^{\tilde{N}}\sum_{m=1}^{\tilde{M}} Q_{\mathrm{B}snm}^{(\tau)} \sin\left(\frac{n\pi}{L_1}s_1\right)\sin\left(\frac{m\pi}{L_2}s_2\right)\\
q_{\mathrm{T}}^{(\tau)}(s_1,s_2) &= \sum_{n=1}^{\tilde{N}}\sum_{m=1}^{\tilde{M}} Q_{\mathrm{T}snm}^{(\tau)} \sin\left(\frac{n\pi}{L_1}s_1\right)\sin\left(\frac{m\pi}{L_2}s_2\right)
\end{aligned}
\tag{72}
$$

The wave amplitudes in Eq. (72) are evaluated as follows and are collected in the vector $\mathbf{Q}_{snm}^{(\tau)} = [\,Q_{1snm}^{(\tau)} \;\; Q_{2snm}^{(\tau)} \;\; Q_{3snm}^{(\tau)} \;\; Q_{\mathrm{B}snm}^{(\tau)} \;\; Q_{\mathrm{T}snm}^{(\tau)}\,]^T$:

$$
\begin{aligned}
Q_{1snm}^{(\tau)} &= Q_{1snm}^{(-)} F_{\tau}^{(1)\alpha_1(-)} H_1^{(-)} H_2^{(-)} + Q_{1snm}^{(+)} F_{\tau}^{(l)\alpha_1(+)} H_1^{(+)} H_2^{(+)}\\
Q_{2snm}^{(\tau)} &= Q_{2snm}^{(-)} F_{\tau}^{(1)\alpha_2(-)} H_1^{(-)} H_2^{(-)} + Q_{2snm}^{(+)} F_{\tau}^{(l)\alpha_2(+)} H_1^{(+)} H_2^{(+)}\\
Q_{3snm}^{(\tau)} &= Q_{3snm}^{(-)} F_{\tau}^{(1)\alpha_3(-)} H_1^{(-)} H_2^{(-)} + Q_{3snm}^{(+)} F_{\tau}^{(l)\alpha_3(+)} H_1^{(+)} H_2^{(+)}\\
Q_{\mathrm{B}snm}^{(\tau)} &= Q_{\mathrm{B}snm}^{(-)} F_{\tau}^{(1)\alpha_4(-)} H_1^{(-)} H_2^{(-)} + Q_{\mathrm{B}snm}^{(+)} F_{\tau}^{(l)\alpha_4(+)} H_1^{(+)} H_2^{(+)}\\
Q_{\mathrm{T}snm}^{(\tau)} &= Q_{\mathrm{T}snm}^{(-)} F_{\tau}^{(1)\alpha_5(-)} H_1^{(-)} H_2^{(-)} + Q_{\mathrm{T}snm}^{(+)} F_{\tau}^{(l)\alpha_5(+)} H_1^{(+)} H_2^{(+)}
\end{aligned}
\tag{73}
$$

The coefficients $Q_{\alpha snm}^{(+)}$ and $Q_{\alpha snm}^{(-)}$ with $\alpha = 1, 2, 3, \mathrm{B}, \mathrm{T}$ depend, for any n, m, on the distribution of external loads applied at the top and bottom surfaces, respectively. Finally, it is assumed that the laminated structure is characterized by a cross-ply lamination scheme. In other words, an arbitrary k-th lamina of the structure is assumed to be orthotropic with a material orientation angle $\vartheta^{(k)}$ equal to 0 or $\pm\pi/2$. The following three-dimensional multifield constitutive matrices are thus considered:

$$
\begin{aligned}
\overline{\Gamma}_{\mathrm{C}}^{(k)} &= \begin{bmatrix}
\overline{C}_{11}^{(k)} & \overline{C}_{12}^{(k)} & 0 & 0 & 0 & \overline{C}_{13}^{(k)}\\
\overline{C}_{12}^{(k)} & \overline{C}_{22}^{(k)} & 0 & 0 & 0 & \overline{C}_{23}^{(k)}\\
0 & 0 & \overline{C}_{66}^{(k)} & 0 & 0 & 0\\
0 & 0 & 0 & \overline{C}_{44}^{(k)} & 0 & 0\\
0 & 0 & 0 & 0 & \overline{C}_{55}^{(k)} & 0\\
\overline{C}_{13}^{(k)} & \overline{C}_{23}^{(k)} & 0 & 0 & 0 & \overline{C}_{33}^{(k)}
\end{bmatrix}\\
\overline{\Gamma}_{\mathrm{M}}^{(k)} &= \begin{bmatrix}
\overline{m}_{11}^{(k)} & 0 & 0\\
0 & \overline{m}_{22}^{(k)} & 0\\
0 & 0 & \overline{m}_{33}^{(k)}
\end{bmatrix}, \quad
\overline{\Gamma}_{\mathrm{K}}^{(k)} = \begin{bmatrix}
\overline{k}_{11}^{(k)} & 0 & 0\\
0 & \overline{k}_{22}^{(k)} & 0\\
0 & 0 & \overline{k}_{33}^{(k)}
\end{bmatrix}\\
\overline{\Gamma}_{\mathrm{Q}}^{(k)} &= \begin{bmatrix}
0 & 0 & 0 & \overline{q}_{14}^{(k)} & 0 & 0\\
0 & 0 & 0 & 0 & \overline{q}_{25}^{(k)} & 0\\
\overline{q}_{31}^{(k)} & \overline{q}_{32}^{(k)} & 0 & 0 & 0 & \overline{q}_{33}^{(k)}
\end{bmatrix}, \quad
\overline{\Gamma}_{\mathrm{w}}^{(k)} = \begin{bmatrix} 0 & 0 & \overline{w}_{33}^{(k)} \end{bmatrix}\\
\overline{\Gamma}_{\mathrm{z}}^{(k)} &= \begin{bmatrix} \overline{z}_{11}^{(k)} & \overline{z}_{22}^{(k)} & 0 & 0 & 0 & \overline{z}_{33}^{(k)} \end{bmatrix}, \quad
\overline{\Gamma}_{\mathrm{TT}}^{(k)} = \begin{bmatrix} \overline{\xi}_{11}^{(k)} \end{bmatrix}
\end{aligned}
\tag{74}
$$

By substituting the harmonic expansion of unknown variables from Eq. (71) and of external loads from Eq. (72) into Eq. (64), and under the geometric and material assumptions of Eqs. (64) and (74), the higher-order fundamental relations (64) are transformed into the algebraic linear system presented below:

$$
\sum_{n=1}^{\tilde{N}}\sum_{m=1}^{\tilde{M}} \left(\sum_{\eta=0}^{N+1} \mathbf{L}_{nm}^{(\tau\eta)} \mathbf{U}_{nm}^{(\eta)} + \mathbf{Q}_{snm}^{(\tau)} \right) = \mathbf{0}
\tag{75}
$$

with $\tilde{N} = \tilde{M} = +\infty$. The analytical fundamental matrix $\mathbf{L}_{nm}^{(\tau\eta)}$ takes the following extended form for an arbitrary n, m, while vectors $\mathbf{U}_{nm}^{(\eta)}$ and $\mathbf{Q}_{snm}^{(\tau)}$ are introduced in Eqs. (71)-(72):

$$
\mathbf{L}_{nm}^{(\tau\eta)} = \left[\begin{array}{ccc|c|c}
L_{11nm}^{(\tau\eta)\alpha_1\alpha_1} - L_{11fnm}^{(\tau\eta)\alpha_1\alpha_1} & L_{12nm}^{(\tau\eta)\alpha_1\alpha_2} & L_{13nm}^{(\tau\eta)\alpha_1\alpha_3} & L_{14nm}^{(\tau\eta)\alpha_1\alpha_4} & L_{15nm}^{(\tau\eta)\alpha_1\alpha_5}\\
L_{21nm}^{(\tau\eta)\alpha_2\alpha_1} & L_{22nm}^{(\tau\eta)\alpha_2\alpha_2} - L_{22fnm}^{(\tau\eta)\alpha_2\alpha_2} & L_{23nm}^{(\tau\eta)\alpha_2\alpha_3} & L_{24nm}^{(\tau\eta)\alpha_2\alpha_4} & L_{25nm}^{(\tau\eta)\alpha_2\alpha_5}\\
L_{31nm}^{(\tau\eta)\alpha_3\alpha_1} & L_{32nm}^{(\tau\eta)\alpha_3\alpha_2} & L_{33nm}^{(\tau\eta)\alpha_3\alpha_3} - L_{33fnm}^{(\tau\eta)\alpha_3\alpha_3} & L_{34nm}^{(\tau\eta)\alpha_3\alpha_4} & L_{35nm}^{(\tau\eta)\alpha_3\alpha_5}\\
\hline
L_{41nm}^{(\tau\eta)\alpha_4\alpha_1} & L_{42nm}^{(\tau\eta)\alpha_4\alpha_2} & L_{43nm}^{(\tau\eta)\alpha_4\alpha_3} & L_{44nm}^{(\tau\eta)\alpha_4\alpha_4} & L_{45nm}^{(\tau\eta)\alpha_4\alpha_5}\\
\hline
L_{51nm}^{(\tau\eta)\alpha_5\alpha_1} & L_{52nm}^{(\tau\eta)\alpha_5\alpha_2} & L_{53nm}^{(\tau\eta)\alpha_5\alpha_3} & L_{54nm}^{(\tau\eta)\alpha_5\alpha_4} & L_{55nm}^{(\tau\eta)\alpha_5\alpha_5}
\end{array}\right]
\tag{76}
$$

A semi-analytical solution is derived for Eq. (75) by assuming $\tilde{N}$, $\tilde{M} \in \mathbb{N}$. The expressions for the coefficients $L_{ijnm}^{(\tau\eta)\alpha_i\alpha_j}$ with $i, j = 1, ..., 5$ and $L_{\beta\beta fnm}^{(\tau\eta)\alpha_\beta\alpha_\beta}$ for $\beta = 1, 2, 3$ are reported in Appendix I for given values of $n = 1, ..., \tilde{N}$, $m = 1, ..., \tilde{M}$ and $\tau, \eta = 0, ..., N+1$.

It should be noted that the solution provided in Eq. (75) is valid only under specific geometric, material, and loading constraints. For this reason, a numerical solution should be derived to overcome these limitations. For the sake of completeness, the reader can refer to [42] for the complete explanation of the GDQ-based numerical solution of the mechanical elasticity equations. The numerical implementation of the complete multifield equations presented in this paper can yield results

for more complicated structures even when the reference surface is not described with principal coordinates.

3. Generalized differential and integral quadrature method

The GDQ method is here used to compute derivatives of arbitrary order within the rectangular parametric domain. Referring to an arbitrary one-dimensional smooth function $f = f(x)$ with $x \in [a, b]$, the GDQ method enables the computation of the n-th order derivative of f at a discrete point $x_i \in [a, b]$ with $i = 1, ..., I_Q$, using a weighted sum of the values $f(x_j)$ with $j = 1, ..., I_Q$ at the sample points of the computational grid, as shown in Ref. [42]:

$$f^{(n)}(x_i) = \left.\frac{\partial^n f(x)}{\partial x^n}\right|_{x=x_i} \cong \sum_{j=1}^{I_Q} \varsigma_{ij}^{(n)} f(x_j) \tag{77}$$

where $\varsigma_{ij}^{(n)}$ with $i, j = 1, ..., I_Q$ are the GDQ weighting coefficients. These quantities are derived from the following recursive relation, which is based on the Weierstrass interpolation theorems. Here, the position $\varsigma_{ij}^{(0)} = \delta_{ij}$ is set with δ_{ij} for $i, j = 1, ..., I_Q$ as the Kronecker delta operator:

$$\begin{aligned} \varsigma_{ij}^{(1)} &= \frac{\mathscr{L}^{(1)}(x_i)}{(x_i - x_j)\mathscr{L}^{(1)}(x_j)}, \quad \varsigma_{ij}^{(n)} = n\left(\varsigma_{ij}^{(1)}\varsigma_{ii}^{(n-1)} - \frac{\varsigma_{ij}^{(n-1)}}{x_i - x_j}\right) && i \neq j \\ \varsigma_{ii}^{(n)} &= -\sum_{j=1 j\neq i}^{I_Q} \varsigma_{ij}^{(n)} && i = j \end{aligned} \tag{78}$$

The previous relation considers a generalized interpolation of function f using the Lagrange interpolating polynomials $\mathscr{L}$. Furthermore, $\mathscr{L}^{(1)}(x_i), \mathscr{L}^{(1)}(x_j)$ denote the first-order derivative of $\mathscr{L}$ evaluated at $x = x_i$ and $x = x_j$, respectively. The computation of the GDQ coefficients (78), which are collected in matrix $\boldsymbol{\varsigma}^{(n)}$ of size $I_Q \times I_Q$, depends on the selection of the sampling points within the computational domain. To this end, a non-uniform two-dimensional computational grid is defined, starting from the well-known Chebyshev-Gauss-Lobatto (CGL) distribution. The position of an arbitrary sampling point, denoted by $\overline{x}_i$ with $i = 1,...,I_Q$, in the CGL grid of size $I_Q \times 1$ within $[-1,1]$ reference interval, is evaluated as follows:

$$\overline{x}_i = -\cos\left(\frac{i-1}{I_Q - 1}\pi\right) \tag{79}$$

The GDQ coefficients derived through Eq. (78) for the reference interval $[-1,1]$ are denoted by $\widetilde{\varsigma}_{ij}^{(n)}$. On the other hand, the transformation provided below is used to extend Eq. (79) from $[-1,1]$ to an arbitrary definition domain $[a,b]$ with $a < b$:

$$x_i = \frac{x_{I_Q} - x_1}{\overline{x}_{I_Q} - \overline{x}_1}(\overline{x}_i - \overline{x}_1) + x_1 \tag{80}$$

The GDQ coefficients $\varsigma_{ij}^{(n)}$ for a given $n \in \mathbb{N}$ associated with the definition domain $[a, b]$ can be computed from those $\widetilde{\varsigma}_{ij}^{(n)}$ derived for the reference interval $[\ 1,1]$ employing the transformation reported below [42]:

$$\varsigma_{ij}^{(n)} = \left(\frac{\overline{x}_{I_Q} - \overline{x}_1}{x_{I_Q} - x_1}\right)^n \widetilde{\varsigma}_{ij}^{(n)} \tag{81}$$

Numerical integrations in this research are performed using the GIQ method [42]. Referring to the one-dimensional case, a similar form of the GDQ rule from Eq. (77) is adopted to compute the integral of an arbitrary smooth function $f = f(x)$, defined in a closed interval $[a,b]$, over the integration interval $[x_i,x_j] \subseteq [a,b]$:

$$\int_{x_i}^{x_j} f(x)dx = \sum_{k=1}^{I_Q} \widetilde{w}_k^{ij} f(x_k) = \sum_{k=1}^{I_Q} (w_{jk} - w_{ik}) f(x_k) \tag{82}$$

being $\widetilde{w}_k^{ij}$ the GIQ weighting coefficients with $i, j, k = 1, ..., I_Q$. The elements w_{ik}, w_{jk} in Eq. (82) are the GIQ coefficients for the integral of f evaluated over the intervals $[a, x_i] \subseteq [a,b]$ and $[a, x_j] \subseteq [a,b]$, respectively. These quantities are collected into the GIQ matrix $\mathbf{W}$ of size $I_Q \times I_Q$. This matrix is derived from the matrix $\overline{\boldsymbol{\varsigma}}^{(1)}$ of the GDQ shifted coefficients $\overline{\varsigma}_{ij}^{(1)}$ with $i,j=1,...,I_Q$ for the first-order derivative, which are evaluated as follows:

$$\overline{\varsigma}_{ij}^{(1)} = \begin{cases} \dfrac{\overline{x}_i - \varepsilon}{\overline{x}_j - \varepsilon}\widetilde{\varsigma}_{ij}^{(1)} & i \neq j \\ \dfrac{1}{\overline{x}_i - \varepsilon} + \widetilde{\varsigma}_{ij}^{(1)} & i = j \end{cases} \tag{83}$$

with $\varepsilon = 1 \times 10^{-10}$. Here, the quantities $\overline{x}_i, \overline{x}_j \in [-1, 1]$ with $i,j = 1,...,I_Q$ are evaluated from Eq. (80). Finally, it can be shown that the matrix $\mathbf{W}$ is equal to the inverse of the matrix of $\overline{\boldsymbol{\varsigma}}^{(1)}$ [42]:

$$\mathbf{W} = \left(\overline{\boldsymbol{\varsigma}}^{(1)}\right)^{-1} \tag{84}$$

When the numerical integration is performed over an arbitrary interval $[a, b]$ discretized with I_Q sampling points, the GIQ coefficients $\widetilde{w}_k^{1I_Q}$ associated with $[-1,1]$ are transformed into those, denoted by $w_k^{1I_Q}$, associated with the interval $[a,b]$ according to the following relation:

$$w_k^{1I_Q} = \frac{b-a}{2}\widetilde{w}_k^{1I_Q} \tag{85}$$

In this way, the integral of f over the interval $[a,b]$ is computed with the GIQ method as:

$$\int_a^b f(x)dx = \sum_{k=1}^{I_Q} w_k^{1I_Q} f(x_k) \tag{86}$$

4. Semi-analytical recovery with generalized integral quadrature

As stated in the previous section, an arbitrary layer of the laminate is identified along the thickness direction by the closed interval $[\zeta_k,\zeta_{k+1}]$, where ζ_{k+1} and ζ_k are the heights of the top and bottom boundaries of the k-th lamina, respectively. This interval is discretized with I_T sampling points, taking into account the CGL grid from Eq. (79). As a consequence, the vector $\boldsymbol{\zeta}^{(k)} = \left[\zeta_1^{(k)} \ \cdots \ \zeta_{\widetilde{m}}^{(k)} \ \cdots \ \zeta_{I_T}^{(k)}\right]^T$ is defined for $k=1,...,l$, being l the number of laminae in the structure. After that, the thickness points vector $\boldsymbol{\zeta}$ of size $lI_T \times 1$ is formed from the lamina vectors $\boldsymbol{\zeta}^{(k)}$. If $\zeta_{\widetilde{m}}^{(k)}$ is the arbitrary $\widetilde{m}$-th element of $\boldsymbol{\zeta}^{(k)}$, the vector $\boldsymbol{\zeta}$ is defined as follows:

$$\boldsymbol{\zeta} = \left[\boldsymbol{\zeta}^{(1)T} \ \cdots \ \boldsymbol{\zeta}^{(k)T} \ \cdots \ \boldsymbol{\zeta}^{(l)T}\right] \tag{87}$$

Here, ζ_m is the arbitrary element of $\boldsymbol{\zeta}$ with $m = (k-1)I_T + \widetilde{m}$. It should be noted that the I_T-th element $\zeta_{I_T}^{(k)} = \zeta_{kI_T}$ of the k-th lamina is located at the same height as the first element of the k+1-th layer, namely $\zeta_1^{(k+1)} = \zeta_{(k+1)\,1}$. This correspondence is crucial for modelling the interface between adjacent laminae within the lamination scheme.

The vector $\boldsymbol{\Delta}_{(ijm)}^{(k)}$ of the unknown configuration variables of the model is, thus, derived for each point $(s_{1i}, s_{2j}, \zeta_m)$ of the three-dimensional solid i=1,...,I_N, j=1,...,I_M and m=1,...,lI_T from the discrete form of the kinematic model in Eq. (9):

$$\boldsymbol{\Delta}_{(ijm)}^{(k)} = \sum_{\tau=0}^{N+1} \mathbf{F}_{\tau(m)}^{(k)} \boldsymbol{\delta}_{(ij)}^{(\tau)} \tag{88}$$

where the thickness functions matrix $\mathbf{F}_{\tau(m)}^{(k)}$ contains the values assumed

by each thickness function at $\zeta = \zeta_m$. Furthermore, the vector $\boldsymbol{\delta}_{(ij)}^{(\tau)}$ of generalized unknown variables is evaluated for an arbitrary point (s_{1i}, s_{2j}) in the physical domain. Similarly, the three-dimensional magneto-thermo-elastic primary variables are derived as follows:

$$\boldsymbol{\pi}_{(ijm)}^{(k)} = \sum_{\tau=0}^{N+1} \sum_{i=1}^{5} \mathbf{Z}_{(ijm)}^{(k\tau)\alpha_i} \boldsymbol{\pi}_{(ij)}^{(\tau)\alpha_i} \tag{89}$$

where $\boldsymbol{\pi}_{(ij)}^{(\tau)\alpha_i}$ is expressed in terms of $\boldsymbol{\delta}_{(ij)}^{(\tau)}$. The matrix $\mathbf{Z}_{(ijm)}^{(k\tau)\alpha_i}$ collects the values assumed by the kinematic operator $\mathbf{Z}^{(k\tau)\alpha_i}$ from Eq. (27) at $(s_{1i}, s_{2j}, \zeta_m)$. Finally, three-dimensional in-plane secondary variables are obtained from the constitutive relation in Eq. (30), leading to the following expression:

$$\begin{aligned}
\sigma_{1(ijm)}^{(k)} &= \overline{C}_{11(ijm)}^{(k)} \varepsilon_{1(ijm)}^{(k)} + \overline{C}_{12(ijm)}^{(k)} \varepsilon_{2(ijm)}^{(k)} + \overline{C}_{13(ijm)}^{(k)} \varepsilon_{3(ijm)}^{(k)} - \overline{q}_{31(ijm)}^{(k)} \mathscr{H}_{3(ijm)}^{(k)} - \overline{z}_{11(ijm)}^{(k)} \widehat{\Delta T}_{(ijm)}^{(k)} \\
\sigma_{2(ijm)}^{(k)} &= \overline{C}_{12(ijm)}^{(k)} \varepsilon_{1(ijm)}^{(k)} + \overline{C}_{22(ijm)}^{(k)} \varepsilon_{2(ijm)}^{(k)} + \overline{C}_{23(ijm)}^{(k)} \varepsilon_{3(ijm)}^{(k)} - \overline{q}_{32(ijm)}^{(k)} \mathscr{H}_{3(ijm)}^{(k)} - \overline{z}_{22(ijm)}^{(k)} \widehat{\Delta T}_{(ijm)}^{(k)} \\
\tau_{12(ijm)}^{(k)} &= \overline{C}_{66(ijm)}^{(k)} \gamma_{12(ijm)}^{(k)} \\
\mathscr{B}_{1(ijm)}^{(k)} &= \overline{q}_{14(ijm)}^{(k)} \gamma_{13(ijm)}^{(k)} + \overline{m}_{11(ijm)}^{(k)} \mathscr{H}_{1(ijm)}^{(k)} \\
\mathscr{B}_{2(ijm)}^{(k)} &= \overline{q}_{25(ijm)}^{(k)} \gamma_{23(ijm)}^{(k)} + \overline{m}_{22(ijm)}^{(k)} \mathscr{H}_{2(ijm)}^{(k)} \\
h_{1(ijm)}^{(k)} &= \overline{k}_{11(ijm)}^{(k)} \theta_{1(ijm)}^{(k)} \\
h_{2(ijm)}^{(k)} &= \overline{k}_{22(ijm)}^{(k)} \theta_{2(ijm)}^{(k)}
\end{aligned} \tag{90}$$

At this point, the out-of-plane shear stresses $\tau_{13}^{(k)}$ and $\tau_{23}^{(k)}$ are evaluated from the solution of the three-dimensional equilibrium equations along the thickness direction, which are detailed below [28]:

$$\begin{aligned}
&\frac{\partial \tau_{13}^{(k)}}{\partial \zeta} + \left(\frac{2}{R_1+\zeta} + \frac{1}{R_2+\zeta}\right)\tau_{13}^{(k)} = -\frac{1}{A_1(1+\zeta/R_1)}\frac{\partial \sigma_1^{(k)}}{\partial \alpha_1} + \\
&\quad + \frac{\sigma_2^{(k)} - \sigma_1^{(k)}}{A_1A_2(1+\zeta/R_2)}\frac{\partial A_2}{\partial \alpha_1} - \frac{1}{A_2(1+\zeta/R_2)}\frac{\partial \tau_{12}^{(k)}}{\partial \alpha_2} - \frac{2\tau_{12}^{(k)}}{A_1A_2(1+\zeta/R_1)}\frac{\partial A_1}{\partial \alpha_2} \\
&\frac{\partial \tau_{23}^{(k)}}{\partial \zeta} + \left(\frac{1}{R_1+\zeta} + \frac{2}{R_2+\zeta}\right)\tau_{23}^{(k)} = -\frac{1}{A_2(1+\zeta/R_2)}\frac{\partial \sigma_2^{(k)}}{\partial \alpha_2} + \\
&\quad + \frac{\sigma_1^{(k)} - \sigma_2^{(k)}}{A_1A_2(1+\zeta/R_1)}\frac{\partial A_1}{\partial \alpha_2} - \frac{1}{A_1(1+\zeta/R_1)}\frac{\partial \tau_{12}^{(k)}}{\partial \alpha_1} - \frac{2\tau_{12}^{(k)}}{A_1A_2(1+\zeta/R_2)}\frac{\partial A_2}{\partial \alpha_1}
\end{aligned} \tag{91}$$

Here, the partial derivatives of $\sigma_1^{(k)}, \sigma_2^{(k)}$ and $\tau_{12}^{(k)}$ shear stresses over α_1, α_2 are computed analytically from the derivatives in Eq. (71) and the constitutive relation in Eq. (90). The solution of Eqs. (91) is derived for any $k = 1,...,l$ through the following boundary conditions, which describe the loading conditions at the bottom surface and ensure the interlaminar stress compatibility:

$$\begin{aligned}
k = 1 \;\Rightarrow\; &\begin{cases} \overline{\tau}_{13(ij1)}^{(1)} = q_{1s(ij)}^{(-)} \\ \overline{\tau}_{23(ij1)}^{(1)} = q_{2s(ij)}^{(-)} \end{cases} \\
k \neq 1 \;\Rightarrow\; &\begin{cases} \overline{\tau}_{13(ij((k-1)I_T+1))}^{(k)} = \overline{\tau}_{13(ij((k-1)I_T))}^{(k-1)} \\ \overline{\tau}_{23(ij((k-1)I_T+1))}^{(k)} = \overline{\tau}_{23(ij((k-1)I_T))}^{(k-1)} \end{cases}
\end{aligned} \tag{92}$$

with $q_{1s}^{(\pm)} = q_1^{(\pm)} + q_{1efk}^{(\pm)}$ and $q_{2s}^{(\pm)} = q_2^{(\pm)} + q_{2efk}^{(\pm)}$. The shear stresses $\overline{\tau}_{13}^{(k)}$ and $\overline{\tau}_{23}^{(k)}$, derived from Eq. (91) through Eq. (92), are thus adjusted at any $m=1,...,lI_T$ point along the thickness direction for any $i=1,...,I_N$ and $j=1,...,I_M$ to account for the loading conditions at the top surface of the panel. This adjustment is achieved through the following linear transformation [28]:

$$\begin{aligned}
\tau_{13(ijm)}^{(k)} &= \overline{\tau}_{13(ijm)}^{(k)} + \frac{q_{1s(ij)}^{(+)} - \overline{\tau}_{13(ij(lI_T))}^{(l)}}{h}\left(\zeta_m + \frac{h}{2}\right) \\
\tau_{23(ijm)}^{(k)} &= \overline{\tau}_{23(ijm)}^{(k)} + \frac{q_{2s(ij)}^{(+)} - \overline{\tau}_{23(ij(lI_T))}^{(l)}}{h}\left(\zeta_m + \frac{h}{2}\right)
\end{aligned} \tag{93}$$

Once the recovered profiles of $\tau_{13}^{(k)}$ and $\tau_{23}^{(k)}$ are derived from Eq. (93), the actual distributions of the out-of-plane normal stress $\sigma_3^{(k)}$, the magnetic flux $\mathscr{B}_3^{(k)}$, and the thermal flux $h_3^{(k)}$ are obtained from the following three-dimensional balance equations [28]:

$$\begin{aligned}
&\frac{\partial \sigma_3^{(k)}}{\partial \zeta} + \sigma_3^{(k)}\left(\frac{1}{R_1+\zeta} + \frac{1}{R_2+\zeta}\right) = -\frac{1}{A_1(1+\zeta/R_1)}\frac{\partial \tau_{13}^{(k)}}{\partial \alpha_1} - \frac{\tau_{13}^{(k)}}{A_1A_2(1+\zeta/R_2)}\frac{\partial A_2}{\partial \alpha_1} + \\
&\quad - \frac{1}{A_2(1+\zeta/R_2)}\frac{\partial \tau_{23}^{(k)}}{\partial \alpha_2} - \frac{\tau_{23}^{(k)}}{A_1A_2(1+\zeta/R_1)}\frac{\partial A_1}{\partial \alpha_2} + \frac{\sigma_1^{(k)}}{R_1+\zeta} + \frac{\sigma_2^{(k)}}{R_2+\zeta} \\
&\frac{\partial \mathscr{B}_3^{(k)}}{\partial \zeta} + \mathscr{B}_3^{(k)}\left(\frac{1}{R_1+\zeta} + \frac{1}{R_2+\zeta}\right) = -\frac{1}{A_1(1+\zeta/R_1)}\frac{\partial \mathscr{B}_1^{(k)}}{\partial \alpha_1} - \frac{\mathscr{B}_1^{(k)}}{A_1A_2(1+\zeta/R_2)}\frac{\partial A_2}{\partial \alpha_1} + \\
&\quad - \frac{1}{A_2(1+\zeta/R_2)}\frac{\partial \mathscr{B}_2^{(k)}}{\partial \alpha_2} - \frac{\mathscr{B}_2^{(k)}}{A_1A_2(1+\zeta/R_1)}\frac{\partial A_1}{\partial \alpha_2} \\
&\frac{\partial h_3^{(k)}}{\partial \zeta} + h_3^{(k)}\left(\frac{1}{R_1+\zeta} + \frac{1}{R_2+\zeta}\right) = -\frac{1}{A_1(1+\zeta/R_1)}\frac{\partial h_1^{(k)}}{\partial \alpha_1} - \frac{h_1^{(k)}}{A_1A_2(1+\zeta/R_2)}\frac{\partial A_2}{\partial \alpha_1} + \\
&\quad - \frac{1}{A_2(1+\zeta/R_2)}\frac{\partial h_2^{(k)}}{\partial \alpha_2} - \frac{h_2^{(k)}}{A_1A_2(1+\zeta/R_1)}\frac{\partial A_1}{\partial \alpha_2}
\end{aligned} \tag{94}$$

The boundary conditions for Eq. (94) are reported in the following, setting $q_{3s}^{(\pm)} = q_3^{(\pm)} + q_{3efk}^{(\pm)}$:

$$\begin{aligned}
k = 1 \;\Rightarrow\; &\begin{cases} \overline{\sigma}_{3(ij1)}^{(1)} = q_{3s(ij)}^{(-)} \\ \overline{\mathscr{B}}_{3(ij1)}^{(1)} = q_{\mathrm{B}(ij)}^{(-)} \\ \overline{h}_{3(ij1)}^{(1)} = q_{\mathrm{T}(ij)}^{(-)} \end{cases} \quad k \\
\neq 1 \;\Rightarrow\; &\begin{cases} \overline{\sigma}_{3(ij((k-1)I_T+1))}^{(k)} = \overline{\sigma}_{3(ij((k-1)I_T))}^{(k-1)} \\ \overline{\mathscr{B}}_{3(ij((k-1)I_T+1))}^{(k)} = \overline{\mathscr{B}}_{3(ij((k-1)I_T))}^{(k-1)} \\ \overline{h}_{3(ij((k-1)I_T+1))}^{(k)} = \overline{h}_{3(ij((k-1)I_T))}^{(k-1)} \end{cases}
\end{aligned} \tag{95}$$

Finally, the out-of-plane secondary variables $\sigma_3^{(k)}, \mathscr{B}_3^{(k)}$ and $h_3^{(k)}$ are obtained from those denoted by $\overline{\sigma}_3^{(k)}, \overline{\mathscr{B}}_3^{(k)}$ and $\overline{h}_3^{(k)}$, derived from Eq. (94) through Eq. (95) at any ζ_m with $m = 1,...,lI_T$. This approach ensures that

the loading conditions at the top surface are respected [28]:

$$\sigma^{(k)}_{3(ijm)} = \overline{\sigma}^{(k)}_{3(ijm)} + \frac{q^{(+)}_{3s(ij)} - \overline{\sigma}^{(l)}_{3(ij(lI_T))}}{h}\left(\zeta_m + \frac{h}{2}\right)$$

$$\mathscr{B}^{(k)}_{3(ijm)} = \overline{\mathscr{B}}^{(k)}_{3(ijm)} + \frac{q^{(+)}_{\mathrm{B}(ij)} - \overline{\mathscr{B}}^{(l)}_{3(ij(lI_T))}}{h}\left(\zeta_m + \frac{h}{2}\right)$$

$$\overline{h}^{(k)}_{3(ijm)} = \overline{h}^{(k)}_{3(ijm)} + \frac{q^{(+)}_{h(ij)} - \overline{h}^{(l)}_{3(ij(lI_T))}}{h}\left(\zeta_m + \frac{h}{2}\right) \tag{96}$$

The solution of Eqs. (91) and (94), using the boundary conditions in Eqs. (92) and (95), is derived by adopting two different approaches. The first methodology, known as GDQ-based recovery procedure, accounts for the derivation of the numerical solution employing the GDQ method of Eq. (77) in its one-dimensional form. Further details can be found in Ref. [28]. In this paper, a novel alternative approach is presented to solve the first-order differential equations in Eqs. (91) and (94). The main advantage of this methodology is that its numerical implementation does not require the solution of any algebraic linear system, thus eliminating the requirement of matrix inversion algorithms. The proposed procedure, indeed, relies on the GIQ numerical method to compute the integral of a known function, depending on the parameters of the equation. The key point of the method is that Eqs. (91) and (94) are first-order equations depending on the thickness coordinate ζ. These equations can be expressed in a general form as follows:

$$\frac{\partial y}{\partial \zeta} + a(\zeta)y(\zeta) = b(\zeta) \tag{97}$$

where y is the unknown function, whereas the variable coefficients $a = a(\zeta)$ and $b = b(\zeta)$ take the following form:

$$\begin{aligned} a(\zeta) &= \frac{c}{R_1+\zeta} + \frac{d}{R_2+\zeta} \\ b(\zeta) &= \frac{B_1(\zeta)}{R_1+\zeta} + \frac{B_2(\zeta)}{R_2+\zeta} \end{aligned} \tag{98}$$

with $c, d = 1, 2$. The solution of Eq. (97) is expressed in its general form as:

$$y(\zeta) = e^{-A(\zeta)}\int e^{A(\zeta)}b(\zeta)d\zeta + y_1 = e^{-A(\zeta)}\int f(\zeta)d\zeta + y_1 \tag{99}$$

In other words, the solution in Eq. (99) is obtained by introducing into Eq. (97) a proper integration factor, defined from the exponential function of $A = A(\zeta)$. The computation of A can be performed in closed form as the variable coefficient a takes the general expression reported in Eq. (98). To this end, it is assumed, without loss of generality, that the unknown function $y = y(\zeta)$ takes the value y_1 at the bottom of the integration interval, namely $y_1 = y(\zeta = 0)$, while $A = A(\zeta)$ is a primitive function of the coefficient $a = a(\zeta)$, which takes the expression reported below:

$$A(\zeta) = \int a(\zeta)d\zeta = \begin{cases} \log\left((R_1+\zeta)^c(R_2+\zeta)^d\right) & R_1 \neq \infty, R_2 \neq \infty \\ \log\left((R_2+\zeta)^d\right) & R_1 = \infty, R_2 \neq \infty \\ \log\left((R_1+\zeta)^c\right) & R_1 \neq \infty, R_2 = \infty \\ 0 & R_1 = R_2 = \infty \end{cases} \tag{100}$$

As a consequence, one gets:

$$e^{A(\zeta)} = g = \begin{cases} (R_1+\zeta)^c(R_2+\zeta)^d & R_1 \neq \infty, R_2 \neq \infty \\ (R_2+\zeta)^d & R_1 = \infty, R_2 \neq \infty \\ (R_1+\zeta)^c & R_1 \neq \infty, R_2 = \infty \\ 1 & R_1 = R_2 = \infty \end{cases} \tag{101}$$

and

$$e^{-A(\zeta)} = \frac{1}{g} = \begin{cases} \dfrac{1}{(R_1+\zeta)^c(R_2+\zeta)^d} & R_1 \neq \infty, R_2 \neq \infty \\ \dfrac{1}{(R_2+\zeta)^d} & R_1 = \infty, R_2 \neq \infty \\ \dfrac{1}{(R_1+\zeta)^c} & R_1 \neq \infty, R_2 = \infty \\ 1 & R_1 = R_2 = \infty \end{cases} \tag{102}$$

The function $f = f(\zeta)$ in Eq. (99) can thus be provided as:

$$f(\zeta) = \begin{cases} (R_1+\zeta)^c(R_2+\zeta)^d b(\zeta) & R_1 \neq \infty, R_2 \neq \infty \\ (R_2+\zeta)^d b(\zeta) & R_1 = \infty, R_2 \neq \infty \\ (R_1+\zeta)^c b(\zeta) & R_1 \neq \infty, R_2 = \infty \\ b(\zeta) & R_1 = R_2 = \infty \end{cases} \tag{103}$$

This general approach is now specialized within each layer of the stacking sequence. By using the thickness coordinate $\zeta^{(k)} \in [\zeta_k, \zeta_{k+1}]$ for any $k = 1,\ldots,l$, Eq. (99) becomes:

$$\begin{aligned} y\left(\zeta^{(k)}\right) &= e^{-A\left(\zeta^{(k)}\right)}\int_{\zeta_1^{(k)}}^{\zeta^{(k)}} e^{A\left(\zeta^{(k)}\right)}b\left(\zeta^{(k)}\right)d\zeta^{(k)} + y_1^{(k)} \\ &= e^{-A\left(\zeta^{(k)}\right)}\int_{\zeta_1^{(k)}}^{\zeta^{(k)}} f\left(\zeta^{(k)}\right)d\zeta^{(k)} + y_1^{(k)} \end{aligned} \tag{104}$$

Employing the GIQ rule as outlined in Eq. (86), the integral in Eq. (104) can be evaluated numerically in an arbitrary kth lamina with $k = 1,\ldots,l$, as follows:

$$\int_{\zeta_1^{(k)}}^{\zeta_{\tilde{m}}^{(k)}} f\left(\zeta^{(k)}\right)d\zeta^{(k)} = \sum_{i=1}^{I_T}\left(w_{\tilde{m}i} - w_{1i}\right)f\left(\zeta_i^{(k)}\right) = \sum_{i=1}^{I_T} w_i^{1\tilde{m}} f\left(\zeta_i^{(k)}\right) \tag{105}$$

being $\zeta_{\tilde{m}}^{(k)} \in [\zeta_k, \zeta_{k+1}]$ a discrete point along the layer thickness. The quantity f in Eq. (103) is provided in its discrete form by introducing the column vectors $\mathbf{f}^{(k)}$ and $\mathbf{b}^{(k)}$, which contain the values of functions f and b, respectively, at each $\zeta_{\tilde{m}}^{(k)}$:

$$\mathbf{f}^{(k)} = \mathbf{g}^{(k)} \odot \mathbf{b}^{(k)} = \mathbf{G}^{(k)}\mathbf{b}^{(k)} \tag{106}$$

where $\mathbf{G}^{(k)} = \mathrm{diag}(\mathbf{g}^{(k)})$, while the symbol $\odot$ refers to the Hadamard product. The arbitrary element of the vector $\mathbf{g}$, denoted by $g_{\tilde{m}}^{(k)}$, is defined as follows:

$$g_{\tilde{m}}^{(k)} = \begin{cases} \left(R_1+\zeta_{\tilde{m}}^{(k)}\right)^c\left(R_2+\zeta_{\tilde{m}}^{(k)}\right)^d & R_1 \neq \infty, R_2 \neq \infty \\ \left(R_2+\zeta_{\tilde{m}}^{(k)}\right)^d & R_1 = \infty, R_2 \neq \infty \\ \left(R_1+\zeta_{\tilde{m}}^{(k)}\right)^c & R_1 \neq \infty, R_2 = \infty \\ 1 & R_1 = R_2 = \infty \end{cases} \tag{107}$$

In the same way, the reciprocal value of $g_{\tilde{m}}^{(k)}$ is expressed as:

$$\frac{1}{g_{\tilde{m}}^{(k)}} = \begin{cases} \dfrac{1}{\left(R_1+\zeta_{\tilde{m}}^{(k)}\right)^c\left(R_2+\zeta_{\tilde{m}}^{(k)}\right)^d} & R_1 \neq \infty, R_2 \neq \infty \\ \dfrac{1}{\left(R_2+\zeta_{\tilde{m}}^{(k)}\right)^d} & R_1 = \infty, R_2 \neq \infty \\ \dfrac{1}{\left(R_1+\zeta_{\tilde{m}}^{(k)}\right)^c} & R_1 \neq \infty, R_2 = \infty \\ 1 & R_1 = R_2 = \infty \end{cases} \tag{108}$$

Finally, the discrete solution of Eq. (104) is derived within each k-th

lamina as follows:

$$y\left(\zeta_{\bar{m}}^{(k)}\right)=\frac{1}{g_{\bar{m}}^{(k)}}\sum_{i=1}^{I_T} w_i^{1\bar{m}} g_i^{(k)} b\left(\zeta_i^{(k)}\right)+y_1^{(k)} \Rightarrow \mathbf{y}^{(k)}=\left(\mathbf{G}^{(k)}\right)^{-1}\mathbf{W}^{(k)}\mathbf{G}^{(k)}\mathbf{b}^{(k)}+y_1^{(k)} \tag{109}$$

In order to simplify the expression (109), we can assume that $\zeta_i^{(k)}$, $\zeta_{\bar{m}}^{(k)} \ll R_1, R_2$. Thus, the relation $\mathbf{G}^{(k)} \cong \mathbf{I}$ can be considered and Eq. (109) becomes:

$$y\left(\zeta_{\bar{m}}^{(k)}\right)=\sum_{i=1}^{I_T} w_i^{1\bar{m}} b\left(\zeta_i^{(k)}\right)+y_1^{(k)} \Rightarrow \mathbf{y}^{(k)}=\mathbf{W}^{(k)}\mathbf{b}^{(k)}+y_1^{(k)} \tag{110}$$

It should be noted that the approach presented above is more computationally efficient than the classical GDQ-based approach presented in previous works. In fact, in the GIQ-based recovery the solution is provided analytically within each layer according to Eq. (104), while the GDQ-based approach requires the inversion of the GDQ weighting coefficients matrix. In the novel procedure, instead, it is only required to numerically compute the integral of the quantity denoted by f with a matrix multiplication operation, as shown in Eq. (109). In this way, all the computational issues related to matrix inversion are avoided without any accuracy loss, and the computational time is reduced.

Once the out-of-plane multifield secondary variables are obtained from the recovery procedure, the out-of-plane primary variables in vector $\mathbf{x}_{(ijm)}^{(k)} = \left[\gamma_{13(ijm)}^{(k)} \quad \gamma_{23(ijm)}^{(k)} \quad \varepsilon_{3(ijm)}^{(k)} \quad \mathscr{D}_{3(ijm)}^{(k)} \quad h_{3(ijm)}^{(k)}\right]^T$, are determined for an arbitrary point $\left(s_{1i}, s_{2j}, \zeta_m\right)$ within the doubly-curved three-dimensional solid. To this end, Ref. [28] presents a procedure in which the three-dimensional multifield constitutive relation from Eq. (30) is used to assess the following algebraic linear system:

Table 3
Validation of the theory for mechanical elasticity against literature results. Static analysis of laminated shallow spherical shells with cross-ply configurations. Effect of geometric ratios L_2/h and $R_1/L_1 = R_2/L_1 = R/L_1$.

L_2 /h	R /L_1	Exact [87]	HTFE [88]	EDZ4 GDQ	EDZ4	EDZ7	ELDZL4	ELDZL7
(0/90/0)								
U_3^*								
10	5	0.7330	0.7726	0.7243	0.7323	0.7326	0.7323	0.7326
10	10	0.7513	0.7209	0.7491	0.7513	0.7515	0.7513	0.7515
100	5	0.1036	0.1037	0.1033	0.1036	0.1036	0.1036	0.1036
100	10	0.2417	0.2423	0.2417	0.2417	0.2417	0.2417	0.2417
σ_1^*								
10	5	0.5865	0.5390	0.5800	0.5827	0.5829	0.5827	0.5829
10	10	0.5958	0.5625	0.5931	0.5938	0.5940	0.5938	0.5940
100	5	0.1558	0.1503	0.1563	0.1557	0.1557	0.1557	0.1557
100	10	0.3318	0.3312	0.3318	0.3317	0.3317	0.3317	0.3317
σ_2^*								
10	5	0.3123	0.2777	0.3096	0.3123	0.3125	0.3123	0.3125
10	10	0.3022	0.2744	0.3015	0.3023	0.3024	0.3023	0.3024
100	5	0.0956	0.0958	0.0958	0.0956	0.0956	0.0956	0.0956
100	10	0.1618	0.1621	0.1620	0.1618	0.1618	0.1618	0.1618
τ_{13}^*								
10	5	0.3474	0.3451	0.3463	0.3472	0.3474	0.3472	0.3474
10	10	0.3564	0.3651	0.3559	0.3562	0.3564	0.3562	0.3564
100	5	0.1018	0.1021	0.1028	0.1018	0.1018	0.1018	0.1018
100	10	0.2275	0.2302	0.2275	0.2275	0.2275	0.2275	0.2275
τ_{23}^*								
10	5	0.1194	0.1240	0.1207	0.1201	0.1197	0.1201	0.1197
10	10	0.1224	0.1293	0.1231	0.1230	0.1226	0.1230	0.1226
100	5	0.0262	0.0262	0.0263	0.0263	0.0263	0.0263	0.0263
100	10	0.0498	0.0499	0.0494	0.0498	0.0498	0.0498	0.0498
(0/90/0/90)								
U_3^*								
10	5	0.7412	0.7321	0.7351	0.7347	0.7374	0.7351	0.7382
10	10	0.7604	0.7587	0.7542	0.7541	0.7569	0.7545	0.7578
100	5	0.1067	0.1068	0.1067	0.1067	0.1067	0.1067	0.1067
100	10	0.2620	0.2623	0.2620	0.2620	0.2620	0.2620	0.2620
σ_1^*								
10	5	0.5044	0.4924	0.5091	0.5090	0.5093	0.5080	0.5087
10	10	0.5057	0.4926	0.5104	0.5103	0.5107	0.5093	0.5100
100	5	0.1344	0.1347	0.1343	0.1344	0.1344	0.1344	0.1344
100	10	0.2843	0.2845	0.2843	0.2843	0.2843	0.2843	0.2843
σ_2^*								
10	5	0.5334	0.5162	0.5292	0.5291	0.5289	0.5293	0.5290
10	10	0.5389	0.5168	0.5367	0.5366	0.5363	0.5369	0.5365
100	5	0.1394	0.1391	0.1395	0.1393	0.1393	0.1393	0.1393
100	10	0.2968	0.2966	0.2967	0.2966	0.2966	0.2966	0.2966
τ_{13}^*								
10	5	0.2633	0.2648	0.2655	0.2672	0.2665	0.2671	0.2664
10	10	0.2706	0.2723	0.2722	0.2730	0.2724	0.2730	0.2723
100	5	0.0585	0.0594	0.0586	0.0586	0.0586	0.0586	0.0586
100	10	0.1441	0.1473	0.1442	0.1442	0.1442	0.1442	0.1442
τ_{23}^*								
10	5	0.2649	0.2681	0.2643	0.2632	0.2629	0.2631	0.2628
10	10	0.2715	0.2731	0.2716	0.2709	0.2705	0.2709	0.2704
100	5	0.071	0.0714	0.0698	0.0709	0.0709	0.0709	0.0709
100	10	0.1575	0.1584	0.1573	0.1574	0.1574	0.1574	0.1574

Table 4
Validation of the theory for mechanical elasticity against literature results. Static analysis of laminated shallow spherical shells with angle-ply configurations. Effect of geometric ratios L_2/h and $R_1/L_1 = R_2/L_1 = R/L_1$.

		(− 30/30/ − 30/30)			(− 45/45/ − 45/45)		
L_2 /h	R /L_1	Exact [87]	HTFE [88]	EDZ4 GDQ	Exact [87]	HTFE [88]	EDZ4 GDQ
U_3^*							
10	5	0.5087	0.5083	0.5120	0.4319	0.4285	0.4415
10	10	0.5496	0.5476	0.5504	0.5119	0.4879	0.5150
100	5	0.0381	0.0387	0.0391	0.0180	0.0186	0.0187
100	10	0.1123	0.1117	0.1126	0.0605	0.0616	0.0622
σ_1^*							
10	5	0.2901	0.2837	0.3119	0.1961	0.1828	0.2055
10	10	0.2972	0.2933	0.3229	0.1993	0.1874	0.2118
100	5	0.0506	0.0511	0.0551	0.0327	0.0341	0.0328
100	10	0.1195	0.1233	0.1290	0.0704	0.0707	0.0720
σ_2^*							
10	5	0.1323	0.1283	0.1391	0.1961	0.1828	0.2058
10	10	0.1269	0.1258	0.1356	0.1993	0.1874	0.2118
100	5	0.0331	0.0338	0.0346	0.0327	0.0341	0.0330
100	10	0.0659	0.0668	0.0686	0.0704	0.0707	0.0722
τ_{13}^*							
10	5	0.3055	0.3083	0.2690	0.2132	0.2231	0.1910
10	10	0.3306	0.3321	0.2898	0.2530	0.2603	0.2221
100	5	0.0425	0.0431	0.0460	0.0180	0.0189	0.0238
100	10	0.1256	0.1263	0.1186	0.0605	0.0621	0.0630
τ_{23}^*							
10	5	0.1805	0.1833	0.1576	0.2132	0.2231	0.1915
10	10	0.1951	0.1973	0.1696	0.2530	0.2603	0.2222
100	5	0.0250	0.0255	0.0235	0.0180	0.0189	0.0239
100	10	0.0738	0.0741	0.0675	0.0605	0.0621	0.0629

$$\mathbf{A}_{(ijm)}^{(k)}\mathbf{x}_{(ijm)}^{(k)} = \mathbf{B}_{(ijm)}^{(k)} \tag{111}$$

More specifically, matrix $\mathbf{A}_{(ijm)}^{(k)}$ contains the three-dimensional constitutive coefficients of matrices in Eq. (31), while the elements of vector $\mathbf{B}_{(ijm)}^{(k)}$ depend on values assumed by the recovered secondary variables of the multifield model. The solution of Eq. (111) provides the updated values for the out-of-plane primary variables. Finally, the values of the in-plane secondary variables can be updated using an iterative procedure based on the three-dimensional constitutive relation, where recovered in-plane and out-of-plane primary variables are used to compute the updated values of the in-plane secondary variables. This procedure terminates when the convergence of results is achieved between the next steps.

5. Applications and results

In the present section, the formulation introduced in the paper is applied to predict the multifield response of flat and curved laminated panels subjected to mechanical, magnetic, and thermal external loads. The analysis focuses on simply-supported rectangular plates, but also on circular cylinders, and a spherical laminated panel under various loading conditions. The lamination scheme consists of a combination of two materials, namely cobalt ferrite ($CoFe_2O_4$) and barium titanate ($BaTiO_3$), representing the metal (M) and the ceramic (C) phase, respectively. The thermo-magneto-elastic constitutive coefficients of the materials are detailed in Table 1. In addition, composite materials are considered, consisting of $BaTiO_3$ cylinders with a volume fraction V_f embedded in a metal phase of $CoFe_2O_4$ with volume fraction V_m. The total absence of voids is assumed within the composite, such that $V_f + V_m = 1$ is assumed. The homogenization algorithm follows the procedure, based on Mori-Tanaka's technique [83], as described in Ref. [85], and reported in Appendix II. In this way, two materials are obtained, namely TME-III and TME-I, characterized by fiber volume fractions equal to $V_f = 0.6$ and $V_f = 0.2$, respectively. For each example, an arbitrary variation in the material properties along their thickness is modelled using the following relation, where $\overline{\Gamma}_{0nm}^{(k)}$ and $\rho_0^{(k)}$ are the reference values of the multifield constitutive coefficient and the material density, respectively:

$$\begin{aligned}\overline{\Gamma}_{nm}^{(k)}(\zeta) &= \overline{\Gamma}_{0nm}^{(k)} f_k(\zeta) = \overline{\Gamma}_{0nm}^{(k)} f_k(\widehat{z}_k) = \overline{\Gamma}_{0nm}^{(k)}\left(1 + \delta^{(k)}\left(\delta_0^{(k)} + g(\widehat{z}_k)\right)\right)\\ \rho^{(k)}(\zeta) &= \rho_0^{(k)} f_k(\zeta) = \rho_0^{(k)} f_k(\widehat{z}_k) = \rho_0^{(k)}\left(1 + \delta^{(k)}\left(\delta_0^{(k)} + g(\widehat{z}_k)\right)\right)\end{aligned} \tag{112}$$

Here, a dimensionless coordinate $\widehat{z}_k \in [-1/2, 1/2]$ is introduced within each k-th lamina of the shell, as function of the thickness ζ, defined as follows:

$$\widehat{z}_k = \frac{\zeta - \zeta_k}{\zeta_{k+1} - \zeta_k} - \frac{1}{2} = \frac{\zeta - \zeta_k}{h_k} - \frac{1}{2} \tag{113}$$

The analytical expressions for the function $g = g(\widehat{z}_k)$ can be found in Table 2, and a graphical representation of these functions is shown in Fig. 1. Each distribution is characterized by a position parameter $\delta_0^{(k)}$ and a shape parameter $\delta^{(k)}$.

To validate the model, some preliminary examples are presented where the results from the present theory are compared with those from existing literature. A static analysis is performed of rectangular plates and shallow spherical shells, focusing on mechanical elasticity simulations, as well as thermo-elastic and magneto-elastic numerical investigations.

The first example focuses on a laminated shallow spherical shell with total thickness $h = 3 \times 10^{-3}$m. Each layer is made of a composite material whose mechanical properties are provided in terms of the orthotropic engineering constants:

$$\begin{aligned}&E_1 = 25E_2, \quad E_2 = E_3 = 6.9 \times 10^9\,\mathrm{N/m^2},\\ &G_{12} = G_{13} = 0.5E_2, \quad G_{23} = 0.2E_2,\\ &\nu_{12} = \nu_{13} = \nu_{23} = 0.25\end{aligned} \tag{114}$$

The corresponding elastic stiffness constitutive coefficients are derived using the expressions reported in Ref. [28]. The structure is subjected to a sinusoidal ($n = m = 1$) surface pressure at the top surface (+) with magnitude $\overline{q}_\alpha^{(+)} = \overline{q}_3^{(+)} = 1\ \mathrm{N/m^2}$.

$$\widetilde{q}_\alpha^{(+)}(s_1, s_2) = \sin\left(\frac{n\pi}{L_1}s_1\right)\sin\left(\frac{m\pi}{L_2}s_2\right) \tag{115}$$

The maximum values of the vertical deflection U_3, the in-plane normal stresses σ_1,σ_2, and the out-of-plane shear stresses τ_{13},τ_{23} are reported in Tables 3 and 4 for two different lamination schemes. The first case accounts for three layers of thickness $h_1 = h_2 = h_3 = h/3$ and cross-ply lamination scheme (0/90/0). Furthermore, an additional set of numerical simulations is conducted in the case of four layers of thickness $h_1 = h_2 = h_3 = h_4 = h/4$ with lamination scheme (0/90/0/90). Finally, two angle-ply stacking sequences are considered with $(-\widehat{\vartheta}/\widehat{\vartheta}/-\widehat{\vartheta}/\widehat{\vartheta})$ for $\widehat{\vartheta} = \pi/6$ and $\widehat{\vartheta} = \pi/4$ in Table 4. Reference solutions are those reported in Refs. [87,88], derived with an exact solution and the Hybrid Trefftz Finite Element (HTFE) method. The numerical predictions from the present theory are derived employing the EDZ4 and ELDZL4 kinematic models. For completeness, the results are also provided from the GDQ-based numerical solution of the mechanical elasticity equations. The results are presented in terms of the dimensionless quantities $U_3^*, \sigma_1^*, \sigma_2^*, \tau_{13}^*, \tau_{23}^*$, defined as follows:

$$\begin{aligned}U_3^* &= \frac{100E_2}{L_2 S^3 \overline{q}_3^{(+)}}U_3, \quad \sigma_1^* = \frac{1}{S^2\overline{q}_3^{(+)}}\sigma_1, \quad \sigma_2^* = \frac{1}{S^2\overline{q}_3^{(+)}}\sigma_2, \quad \tau_{13}^* = \frac{1}{S\overline{q}_3^{(+)}}\tau_{13}, \quad \tau_{23}^*\\ &= \frac{1}{S\overline{q}_3^{(+)}}\tau_{23}\end{aligned} \tag{116}$$

with $S = L_2/h$. As can be seen, a perfect alignment between the various approaches is seen for both EDZ4 and ELDZL4 kinematic assumptions and for every geometric and material configuration.

A literature comparison is now conducted for thermo-mechanical and magneto-mechanical numerical investigations. To this end, a

Table 5
Validation of the theory for thermo-mechanical elasticity against literature results. Static analysis of laminated rectangular plate with cross-ply configuration. Effect of geometric ratio L_1/h.

L_1/h	2	4	10	20	50	100
U_3^*						
A [91]	96.80	42.69	17.39	12.12	10.50	10.26
B [91]	96.80	42.69	17.39	12.12	10.50	10.26
C [91]	48.87	32.12	16.39	11.93	10.47	10.25
ELDZL4	49.21	31.92	16.38	11.93	10.47	10.25
ELDZL7	48.79	32.08	16.39	11.93	10.47	10.25
σ_1						
A [91]	1379.0	1183.0	1026.0	982.0	967.5	965.4
B [91]	1379.0	1183.0	1026.0	982.0	967.5	965.4
C [91]	487.6	796.8	948.0	961.8	964.3	964.5
ELDZL4	460.0	785.7	946.7	961.5	964.2	964.5
ELDZL7	494.0	795.5	947.6	961.7	964.3	964.5
τ_{12}						
A [91]	269.3	157.0	76.3	57.4	51.4	50.5
B [91]	269.3	157.0	76.3	57.4	51.4	50.5
C [91]	142.9	119.4	72.0	56.5	51.3	50.5
ELDZL4	144.8	118.8	71.9	56.5	51.3	50.5
ELDZL7	142.7	119.3	71.9	56.5	51.3	50.5

simply-supported square plate of thickness $h = 1$m is considered, consisting of three layers of equal thickness ($h_1 = h_2 = h_3 = h/3$). The lamination scheme is cross-ply, namely (0/90/0), and the material properties of each layer are the same of Eq. (114) except for the transverse Young modulus which is assumed equal to $E_2 = E_3 = 7 \times 10^9$ N/m^2. Furthermore, the thermal conduction coefficients are $k_{11} = 36.42$ J/mK and $k_{22} = k_{33} = 0.96$ J/mK, while the thermal expansion coefficients are assumed to be $a_{11} = 1$ K^{-1} and $a_{22} = a_{33} = 1125$ K^{-1}. The loading condition consists of a sinusoidal distribution of temperature variation at the top and bottom surfaces with magnitudes +1K and −1K, respectively. The results are reported in Table 5 and compared with those from Ref. [91]. Three different exact solutions are taken from the paper in hand. The first one, denoted by "A", is obtained from a 3D theory with linear through-the-thickness assumption of the temperature profile, while the solution "B" derives the temperature profile from the solution of the one-dimensional Fourier equations along the thickness of the shell, considering 300 mathematical layers. Finally, "C" refers to an exact solution of a 3D model which embeds, in addition to mechanical elasticity, the 3D version of the heat conduction equations. Even this solution is derived by using 300 mathematical layers. It should be noted that the vertical deflection of the plate, denoted by U_3, is presented in its normalized form, defined as $U_3^* = U_3^*/(L_1/h)^2$. This quantity is evaluated at the top surface ($\zeta = h/2$) for the points located at (s_1,s_2) = (0.5L_1,0.5L_2). The in-plane stress σ_1 is evaluated at the same point of the solid. On the other hand, in-plane shear stress τ_{12} is evaluated at the bottom surface ($\zeta = -h/2$) for (s_1,s_2) = (0,0). The results, reported in Table 5, are obtained using the ELW theory with various kinematic orders. It can be seen that the numerical predictions of the present model are perfectly aligned with those from 3D exact solutions, especially with the solution C, based on the complete three-dimensional modeling of thermo-elastic equations. This aspect is very important because it highlights the model accuracy and computational efficiency compared to 3D approaches.

A further example is now provided where the higher-order ELW model is validated against literature for M-D analyses. A squared rectangular plate is considered with $L_1 = L_2 = 1$m consisting of a single layer of cobalt ferrite. The 3D constitutive properties of the material in hand can be found in Table 1. The thickness of the plate is $h = 0.3$m. The structure is subjected to a sinusoidal mechanical load applied at the top surface, in line with Eq. (115) for $n = m = 1$, with wave amplitude $\overline{q}_\alpha^{(+)} = \overline{q}_3^{(+)} = 1$ N/m^2. As far as magnetic loads is concerned, an open-circuit sensor configuration is assumed, namely a null magnetic flux is applied at the top and bottom surfaces. The through-the-thickness distribution of the displacement field component U_1 is provided at (s_1,s_2) = (0, 0.5L_2). On the other hand, U_3 distribution, as well as that of the magnetic potential $\Delta\psi$, are provided at (s_1,s_2) = (0.5L_1,0.5L_2). Two reference solutions are considered for validation, derived from Refs. [89, 90], and the results are reported in Table 6. As can be seen, the displacement field components from 3D exact solutions are well predicted by the ED4 and the ELD4 model. On the other hand, a perfect alignment is observed between the magnetic potential distributions obtained from ED7, ELD7, and 3D modeling.

Next numerical investigation points out the accuracy of the recovery procedure in mechanical elasticity simulations. A simply-supported thick laminated circular cylinder is considered under mechanical surface pressure with sinusoidal distribution (115) at the top surface with $n = m = 1$ and magnitude $\overline{q}_\alpha^{(+)} = \overline{q}_3^{(+)} = 1 \times 10^3$ N/m^2. The reference surface of the structure is expressed in principal coordinates as follows:

$$\mathbf{r}(x,\vartheta) = R_2\cos\vartheta\mathbf{e}_1 - R_2\sin\vartheta\mathbf{e}_2 + x\mathbf{e}_3 \tag{117}$$

where $[0, L_1] \times [\vartheta_0,\vartheta_1]$ with $L_1 = 1$m, $\vartheta_0 = -\pi/3$ and $\vartheta_1 = \pi/3$ is the two-dimensional physical domain, while the radius is $R_2 = R = 0.2$m. The laminate consists of three layers with thickness $h_1 = 0.010$m, $h_2 = 0.015$m and $h_3 = 0.020$m, each of them made of graphite-epoxy. The material orientation in each layer is (0/90/0), while the engineering constants of the constituent materials are provided in the following:

Table 6
Validation of the theory for magneto-mechanical elasticity against literature results. Static analysis of laminated single-layered square plate made of cobalt ferrite in open-circuit sensor configuration. Through-the-thickness distribution of displacement field components and magnetic potential variation.

$\zeta/h + 1/2$	3D [89]	3D [90]	ED4	ED7	ELD4	ELD7
U_1 [$\times 10^{-11}$ m]						
0	0.31968	0.31968	0.31967	0.31968	0.31967	0.31968
0.33	0.10782	0.10782	0.10758	0.10794	0.10758	0.10794
0.66	−0.04676	−0.04676	−0.04655	−0.04691	−0.04655	−0.04691
1	−0.27657	−0.27657	−0.27656	−0.27657	−0.27656	−0.27657
U_3 [$\times 10^{-11}$ m]						
0	0.92335	0.92335	0.92332	0.92335	0.92332	0.92335
0.33	1.00760	1.00750	1.00740	1.00746	1.00740	1.00746
0.66	1.03780	1.03780	1.03766	1.03768	1.03766	1.03768
1	1.01120	1.01120	1.01119	1.01122	1.01119	1.01122
$\Delta\psi$[$\times 10^{-5}$A]						
0	−0.51965	−0.51967	−0.51959	−0.51966	−0.51959	−0.51966
0.33	−0.49108	−0.49108	−0.48979	−0.49070	−0.48979	−0.49070
0.66	−0.26590	−0.26589	−0.26659	−0.26586	−0.26659	−0.26586
1	0.00400	0.00398	0.00387	0.00396	0.00387	0.00396

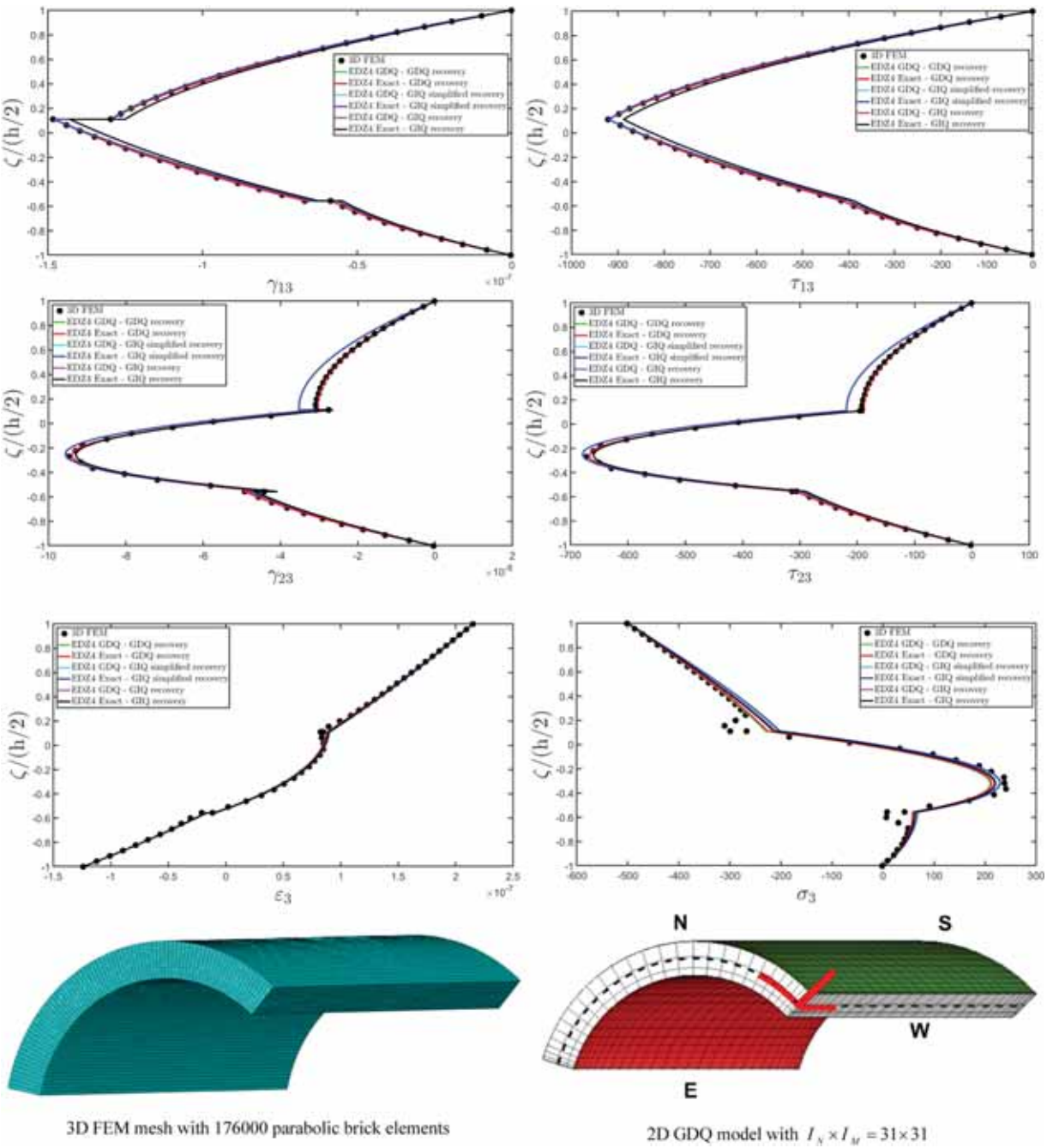

Fig. 2. Through-the-thickness distribution of out-of-plane stress and strain components at $(0.25L_1, 0.25L_2)$ in the physical domain for a simply-supported circular cylinder under sinusoidal loading. Comparison between 3D FEM results, numerical predictions from 2D GDQ model, and the exact solution. The results are obtained with different approaches for stress and strain recovery.

$$\begin{aligned} &E_1 = 137.90 \times 10^9\,\mathrm{N/m^2}, \quad E_2 = E_3 = 8.96 \times 10^9\,\mathrm{N/m^2} \\ &G_{12} = G_{13} = 7.10 \times 10^9\,\mathrm{N/m^2}, \quad G_{23} = 6.21 \times 10^9\,\mathrm{N/m^2} \\ &\nu_{12} = \nu_{13} = 0.3, \quad \nu_{23} = 0.49 \end{aligned} \tag{118}$$

A reference solution is provided, derived from a 3D FEM model from commercial software which accounts for 176000 C3D20 parabolic brick elements with 740285 nodes. Furthermore, the EDZ4 predictions are provided from the present analytical solution and from a GDQ-based numerical model developed previously. The results are provided for the point located at $(s_1,s_2) = (0.25L_1,0.25L_2)$ within the physical domain and reported in Fig. 2. In particular, these results in terms of out-of-plane 3D strain and stress components are obtained by using the classical GDQ-based recovery procedure, as well as the novel GIQ-based recovery. Furthermore, the simplified version of the GIQ recovery is used which does not consider the effect of curvature, as shown in the theory. A perfect alignment is observed between the various approaches, therefore it can be said that the novel methodology has the same accuracy of the classical GDQ-based recovery procedure for mechanical analysis.

At this point, a further preliminary example is conducted using a rectangular plate with geometric dimensions $L_1 = 0.010$m and $L_1 = 0.012$m. The geometry of the three-dimensional solid is described by Eq. (1). The following expression is assumed for the reference surface $\mathbf{r}(\alpha_1,\alpha_2)$, as indicated in Ref. [28]:

Table 7
Displacement field components and absolute temperature variation of a laminated rectangular plate subjected to thermal and mechanical sinusoidal loading at $(0.25L_1, 0.75L_2)$ within the physical domain along the thickness direction employing the ELDZL7 kinematic model. Furthermore, a numerical reference solution is provided from a 3D FEM model.

	$U_1[\times 10^{-12}\text{m}]$		$U_2[\times 10^{-12}\text{m}]$		$U_3[\times 10^{-11}\text{m}]$		$\Delta T[\times 10^{-4}\text{K}]$	
ζ+h/2 [10^{-3}m]	3D FEM	ELDZL7	3D FEM	ELDZL7	3D FEM	ELDZL7	3D FEM	ELDZL7
0.00	−0.11	−0.11	0.09	0.09	−1.86	−1.85	−0.25	−0.25
0.05	0.18	0.19	−0.15	−0.16	−1.86	−1.86	−0.32	−0.32
0.07	0.33	0.30	−0.27	−0.25	−1.86	−1.86	−0.35	−0.35
0.10	0.47	0.48	−0.39	−0.40	−1.86	−1.86	−0.39	−0.39
0.10	0.47	0.48	−0.39	−0.40	−1.86	−1.86	−0.39	−0.39
0.13	0.65	0.65	−0.54	−0.54	−1.86	−1.86	−0.43	−0.43
0.16	0.83	0.82	−0.70	−0.69	−1.87	−1.86	−0.48	−0.48
0.19	1.02	1.00	−0.85	−0.83	−1.87	−1.86	−0.53	−0.52
0.23	1.20	1.23	−1.00	−1.02	−1.87	−1.87	−0.57	−0.58
0.26	1.38	1.40	−1.15	−1.17	−1.87	−1.87	−0.62	−0.63
0.29	1.56	1.58	−1.30	−1.31	−1.87	−1.87	−0.67	−0.67
0.32	1.74	1.75	−1.45	−1.46	−1.88	−1.87	−0.71	−0.72
0.35	1.92	1.92	−1.60	−1.60	−1.88	−1.88	−0.76	−0.76
0.35	1.92	1.92	−1.60	−1.60	−1.88	−1.88	−0.76	−0.76
0.39	2.14	2.16	−1.78	−1.80	−1.88	−1.88	−0.81	−0.82
0.43	2.36	2.39	−1.97	−1.99	−1.88	−1.88	−0.87	−0.88
0.46	2.58	2.56	−2.15	−2.13	−1.89	−1.88	−0.92	−0.92
0.50	2.80	2.80	−2.33	−2.33	−1.89	−1.89	−0.98	−0.98
0.54	3.02	3.03	−2.51	−2.53	−1.89	−1.89	−1.03	−1.03
0.58	3.24	3.26	−2.70	−2.72	−1.90	−1.89	−1.09	−1.09
0.61	3.46	3.44	−2.88	−2.86	−1.90	−1.90	−1.14	−1.14
0.65	3.68	3.68	−3.07	−3.06	−1.90	−1.90	−1.20	−1.20
0.65	3.68	3.68	−3.07	−3.06	−1.90	−1.90	−1.20	−1.20
0.68	3.87	3.86	−3.22	−3.21	−1.91	−1.90	−1.25	−1.25
0.71	4.05	4.03	−3.38	−3.36	−1.91	−1.91	−1.30	−1.30
0.74	4.24	4.21	−3.53	−3.51	−1.92	−1.91	−1.36	−1.35
0.78	4.42	4.45	−3.69	−3.71	−1.92	−1.92	−1.41	−1.42
0.81	4.61	4.63	−3.84	−3.86	−1.93	−1.92	−1.47	−1.47
0.84	4.80	4.81	−4.00	−4.01	−1.93	−1.93	−1.52	−1.53
0.87	4.99	4.99	−4.16	−4.16	−1.94	−1.93	−1.58	−1.58
0.90	5.18	5.17	−4.31	−4.31	−1.94	−1.94	−1.63	−1.63
0.90	5.18	5.17	−4.31	−4.31	−1.94	−1.94	−1.63	−1.63
0.93	5.33	5.35	−4.44	−4.46	−1.94	−1.94	−1.67	−1.68
0.95	5.48	5.47	−4.57	−4.56	−1.95	−1.94	−1.71	−1.71
0.97	5.63	5.60	−4.69	−4.66	−1.95	−1.95	−1.75	−1.74
1.00	5.78	5.78	−4.82	−4.81	−1.95	−1.95	−1.79	−1.79

$$\mathbf{r}(\alpha_1, \alpha_2) = \mathbf{r}(x, y) = x\mathbf{e}_1 + y\mathbf{e}_2 \tag{119}$$

where $\mathbf{e}_1$,$\mathbf{e}_2$,$\mathbf{e}_3$ are the global Cartesian basis vectors. The lamination scheme consists of five layers, including external skins and a central core of cobalt ferrite with thickness $h_1 = h_5 = 0.10 \times 10^{-3}$m and $h_3 = 0.30 \times 10^{-3}$m. The second and fourth layers have thickness $h_2 = h_4 = 0.25 \times 10^{-3}$m, and are made of TME-I and TME-III composite materials, respectively, with fiber volume fractions equal to $V_f = 0.6$ and $V_f = 0.2$. The orientation angles for the layers are set to (90/0/0/0/90). The panel rests on an elastic foundation modelled according to the Winkler foundation theory, with spring constant of $k_{3f}^{(-)} = 5 \times 10^{10}\,\text{N/m}^3$. An external mechanical pressure $q_3^{(+)}$ with magnitude $\overline{q}_3^{(+)} = -5\,\text{N/m}^2$ is applied to the structure, following Eq. (49), along with thermal fluxes with magnitude $\overline{q}_{\text{T}}^{(+)} = 1\,\text{J/m}^2$ and $\overline{q}_{\text{T}}^{(-)} = 0.9\,\text{J/m}^2$ applied at the top and bottom surfaces, respectively. For each thermo-mechanical load, the surface distribution in Eq. (115) with $n = m = 1$ is considered with $\alpha = \text{T}$, 3. The thermo-mechanical response of the plate is evaluated using the ELW formulation with the ELDZL7 higher-order theory at $s_1 = 0.25L_1$ and $s_2 = 0.25L_2$ within the parametric domain. The reference solution is obtained from a 3D FEM model developed using commercial software, made up of 115200 parabolic brick elements with a coupled temperature-displacement shape function, named C3D20T, resulting in 4573068 variables. The results of numerical simulations are presented in Tables 7-10. More specifically, these tables provide the values of configuration, primary, and secondary variables at various heights along the thickness of the plate. As shown in Table 7, the assumption of a higher-order displacement field with seventh-order polynomials provides an excellent prediction of results from the three-dimensional simulations for both in-plane and out-of-plane displacement field components, as well as for temperature variation. Besides, the analysis indicates that the structure bends with non-uniform values of the out-of-plane displacement field component. Therefore, lower-order theories are unsuitable for the selected lamination scheme since they assume a uniform distribution in U_3 configuration variable along the thickness direction. Tables 8 and 9 present the dispersions of the three-dimensional strain and stress components, respectively. The results reveal that the laminate is compressed under external loads, with highest deformation magnitudes near the top surface. In this region, no out-of-plane distortions are observed due to the cross-ply behavior of the layers, which means that such deformations are induced by in-plane mechanical loads. Distortions occur in the central part of the lamination scheme due to interlaminar shear stresses, which get their maximum magnitude in this region, as indicated in Table 8. Note also that the σ_3 out-of-plane normal stress does not assume a null value at the bottom surface. This is due to the influence of the external elastic foundation, which induces surface actions depending on the bending deflection of the plate, as described by Eq. (51). In addition to the results regarding the mechanical response of the plate, Table 10 presents the thermal primary and secondary variables, which are the elements of the temperature gradient vector and of the thermal flux vector. That the out-of-plane thermal flux h_3 has been adjusted through the recovery procedure, ensuring that the thermal loading conditions are satisfied at both the top and bottom surfaces. Moreover, the profile derived from the ELDZL7 model aligns with the finite elements results even in the central laminae of the shell, indicating that the higher-order model produces

Table 8
Three-dimensional strain components of a laminated rectangular plate subjected to thermal and mechanical sinusoidal loading at $(0.25L_1, 0.75L_2)$ within the physical domain along the thickness direction employing the ELDZL7 kinematic model. A numerical reference solution is provided from a 3D FEM model.

	ε_1 [$\times 10^{-9}$m/m]		ε_2 [$\times 10^{-9}$m/m]		γ_{12} [$\times 10^{-9}$m/m]		γ_{13} [$\times 10^{-10}$m/m]		γ_{23} [$\times 10^{-11}$m/m]		ε_3 [$\times 10^{-9}$m/m]	
ζ+h/2 [10^{-3}m]	3D FEM	ELDZL7	3D FEM	ELDZL7	3D FEM	ELDZL7	3D FEM	ELDZL7	3D FEM	ELDZL7	3D FEM	ELDZL7
0.00	0.03	0.03	0.02	0.02	0.06	0.06	0.00	0.00	0.01	0.00	−0.48	−0.48
0.05	−0.06	−0.06	−0.04	−0.04	−0.09	−0.10	−0.23	−0.21	1.88	1.71	−0.50	−0.50
0.07	−0.10	−0.09	−0.07	−0.07	−0.17	−0.16	−0.32	−0.31	2.70	2.56	−0.52	−0.51
0.10	−0.15	−0.15	−0.10	−0.10	−0.25	−0.25	−0.41	−0.47	3.45	3.89	−0.53	−0.53
0.10	−0.15	−0.15	−0.10	−0.10	−0.25	−0.25	−0.40	−0.45	3.32	3.74	−0.57	−0.56
0.13	−0.21	−0.20	−0.14	−0.14	−0.34	−0.34	−0.51	−0.53	4.21	4.38	−0.59	−0.59
0.16	−0.26	−0.26	−0.18	−0.18	−0.44	−0.43	−0.60	−0.60	5.03	5.04	−0.62	−0.62
0.19	−0.32	−0.31	−0.22	−0.22	−0.53	−0.52	−0.69	−0.68	5.76	5.67	−0.65	−0.64
0.23	−0.38	−0.39	−0.26	−0.27	−0.63	−0.64	−0.77	−0.77	6.42	6.42	−0.68	−0.68
0.26	−0.43	−0.44	−0.30	−0.31	−0.72	−0.73	−0.84	−0.83	6.99	6.91	−0.70	−0.71
0.29	−0.49	−0.50	−0.34	−0.34	−0.82	−0.83	−0.90	−0.88	7.49	7.30	−0.73	−0.74
0.32	−0.55	−0.55	−0.38	−0.38	−0.91	−0.92	−0.95	−0.91	7.91	7.60	−0.76	−0.76
0.35	−0.60	−0.60	−0.42	−0.42	−1.01	−1.01	−0.99	−0.94	8.25	7.80	−0.79	−0.79
0.35	−0.60	−0.60	−0.42	−0.42	−1.01	−1.01	−1.03	−0.98	8.59	8.12	−0.70	−0.70
0.39	−0.67	−0.68	−0.47	−0.47	−1.12	−1.13	−1.03	−1.02	8.55	8.47	−0.72	−0.72
0.43	−0.74	−0.75	−0.51	−0.52	−1.24	−1.25	−1.00	−1.02	8.33	8.50	−0.74	−0.75
0.46	−0.81	−0.80	−0.56	−0.56	−1.35	−1.34	−0.96	−1.00	7.96	8.33	−0.77	−0.76
0.50	−0.88	−0.88	−0.61	−0.61	−1.46	−1.46	−0.89	−0.94	7.42	7.83	−0.79	−0.79
0.54	−0.95	−0.95	−0.66	−0.66	−1.58	−1.59	−0.81	−0.84	6.71	7.02	−0.81	−0.81
0.58	−1.02	−1.03	−0.71	−0.71	−1.70	−1.71	−0.70	−0.71	5.85	5.90	−0.84	−0.84
0.61	−1.09	−1.08	−0.75	−0.75	−1.81	−1.80	−0.58	−0.58	4.81	4.85	−0.86	−0.86
0.65	−1.16	−1.16	−0.80	−0.80	−1.93	−1.93	−0.43	−0.38	3.62	3.17	−0.88	−0.89
0.65	−1.16	−1.16	−0.80	−0.80	−1.93	−1.93	−0.39	−0.34	3.21	2.82	−1.33	−1.34
0.68	−1.21	−1.21	−0.84	−0.84	−2.02	−2.01	−0.42	−0.39	3.53	3.23	−1.39	−1.39
0.71	−1.27	−1.27	−0.88	−0.88	−2.12	−2.11	−0.46	−0.43	3.84	3.62	−1.44	−1.44
0.74	−1.33	−1.33	−0.92	−0.92	−2.22	−2.20	−0.50	−0.48	4.13	3.97	−1.49	−1.49
0.78	−1.39	−1.40	−0.97	−0.97	−2.32	−2.33	−0.53	−0.53	4.41	4.42	−1.55	−1.56
0.81	−1.45	−1.45	−1.01	−1.01	−2.42	−2.43	−0.56	−0.57	4.69	4.74	−1.60	−1.61
0.84	−1.51	−1.51	−1.05	−1.05	−2.51	−2.52	−0.59	−0.61	4.95	5.07	−1.66	−1.66
0.87	−1.57	−1.57	−1.09	−1.09	−2.61	−2.62	−0.62	−0.65	5.20	5.43	−1.71	−1.72
0.90	−1.63	−1.62	−1.13	−1.13	−2.71	−2.71	−0.65	−0.70	5.45	5.83	−1.77	−1.77
0.90	−1.63	−1.62	−1.13	−1.13	−2.71	−2.71	−0.73	−0.78	6.11	6.54	−1.14	−1.14
0.93	−1.67	−1.68	−1.16	−1.17	−2.79	−2.80	−0.56	−0.53	4.70	4.40	−1.16	−1.17
0.95	−1.72	−1.72	−1.20	−1.19	−2.87	−2.87	−0.38	−0.36	3.21	3.02	−1.18	−1.18
0.97	−1.77	−1.76	−1.23	−1.22	−2.95	−2.93	−0.20	−0.21	1.64	1.72	−1.20	−1.20
1.00	−1.82	−1.81	−1.26	−1.26	−3.03	−3.02	0.00	0.00	0.01	0.00	−1.21	−1.22

highly refined and accurate results. It is also important to note that in-plane components exhibit a higher variability in magnitude compared to the out-of-plane primary and secondary variable, θ_3 and h_3. At this point, the multifield static response of the same structure is evaluated under the same surface mechanical pressure, taking into account the magnetic effects. More specifically, the bending response of the panel is analyzed under closed-circuit magnetic conditions, where a null value of the variation in the scalar magnetic potential is enforced at both the top and bottom surfaces of the laminate. The results of the numerical simulation are presented in Tables 11-14 for the points along the thickness direction located at $(0.25L_1, 0.75L_2)$ within the rectangular parametric domain. The reference solution is provided using a 3D FEM model consisting of 115200 parabolic brick elements with piezomagnetic properties, named C3D20E. The model includes 1933700 variables. The displacement field components U_1, U_2, U_3 are reported in Table 11, along with the variation $\Delta\psi$ of the magnetostatic potential. Also in this case, the semi-analytical numerical predictions derived from the ELDZL7 theory match perfectly the 3D FEM results, despite the reduced computational cost. In particular, the magnetic potential profile fulfills the closed-circuit boundary conditions, because the model is based on the thickness functions of the ELW approach. In this way, a refined prediction of configuration variables can be reached directly addressing the multifield kinematic compatibility conditions. Table 12 presents the three-dimensional strain components, showing that the recovery procedure is essential for determining the actual distribution of the three-dimensional strain components in both in-plane and out-of-plane directions. Furthermore, the ELW model is accurate even in the interlaminar region, satisfying the kinematic coupling between subsequent laminae within the stacking sequence. Similar observations can be made for the three-dimensional stress components shown in Table 13, where the model exhibits a high agreement with the reference solution, particularly near the top surface. This accuracy stems from the recovery procedure, which is here based on a given value of external pressure. At the bottom surface, however, the loading conditions refer to actions induced by the elastic foundation, which depend on the U_3 displacement unknown of the model. As shown in Table 14, when an ELW model is used with prescribed values of the multifield configuration variables, only the in-plane primary and secondary variables align with those from three-dimensional simulations. Discrepancies are observed in the out-of-plane primary and secondary variables $\mathscr{H}_3, \mathscr{B}_3$, attributed to the magnetic loading conditions that consist of prescribed values of the scalar magnetic potential. Consequently, no magnetic fluxes, which are the secondary variables of the model, are directly enforced on the panel, and the loading conditions considered in the recovery procedure are derived from the prescribed potential value using the three-dimensional constitutive relationships. Therefore, in all subsequent examples, the magnetic loading conditions are modelled using an arbitrary value of the multifield flux components.

Following this preliminary validation, the model is employed to investigate curved panels with single curvature. More specifically, two distinct circular cylinders are considered. The first cylinder is characterized by a straight generatrix oriented along the α_2 principal direction. The reference surface of the panel is described using Eq. (117) employing the principal coordinates x, ϑ that vary within the rectangular domain $[0, L_1] \times [\vartheta_0, \vartheta_1]$ with $L_1 = 1.1 \times 10^{-2}$m, $\vartheta_0 = -\pi/2$ and $\vartheta_1 = \pi/6$. The radius of the cylinder is $R_2 = R = 6 \times 10^{-3}$m. In this example, the cylinder is made of five laminae with thicknesses $h_1 = h_5 = 0.10 \times 10^{-3}$m, $h_2 = h_4 = 0.25 \times 10^{-3}$m and $h_3 = 0.30 \times 10^{-3}$m. The

Table 9
Three-dimensional stress components of a laminated rectangular plate subjected to thermal and mechanical sinusoidal loading at $(0.25L_1, 0.75L_2)$ within the physical domain along the thickness direction employing the ELDZL7 kinematic model. A numerical reference solution is provided from a 3D FEM model.

	σ_1 [$\times 10^2$ N/m^2]		σ_2 [$\times 10^2$ N/m^2]		τ_{12} [$\times 10^2$ N/m^2]		τ_{13} [$\times 10^0$ N/m^2]		τ_{23} [$\times 10^0$ N/m^2]		σ_3 [$\times 10^0$ N/m^2]	
ζ+h/2 [10^{-3}m]	3D FEM	ELDZL7	3D FEM	ELDZL7	3D FEM	ELDZL7	3D FEM	ELDZL7	3D FEM	ELDZL7	3D FEM	ELDZL7
0.00	0.67	0.67	0.66	0.66	0.03	0.03	0.00	0.00	0.00	0.00	−0.93	−0.93
0.05	0.64	0.64	0.66	0.66	−0.05	−0.05	−1.02	−0.93	0.85	0.77	−0.94	−0.94
0.07	0.62	0.62	0.66	0.66	−0.10	−0.09	−1.47	−1.39	1.22	1.16	−0.96	−0.95
0.10	0.61	0.60	0.66	0.65	−0.14	−0.14	−1.88	−2.11	1.56	1.76	−0.98	−0.98
0.10	0.65	0.64	0.70	0.69	−0.13	−0.13	−1.88	−2.11	1.56	1.76	−0.98	−0.98
0.13	0.65	0.64	0.71	0.71	−0.18	−0.18	−2.38	−2.48	1.99	2.06	−1.02	−1.02
0.16	0.64	0.64	0.73	0.73	−0.24	−0.23	−2.84	−2.85	2.37	2.37	−1.06	−1.06
0.19	0.64	0.64	0.74	0.74	−0.29	−0.28	−3.26	−3.21	2.72	2.67	−1.11	−1.11
0.23	0.64	0.64	0.76	0.76	−0.34	−0.35	−3.63	−3.64	3.03	3.03	−1.17	−1.18
0.26	0.63	0.63	0.78	0.78	−0.39	−0.40	−3.96	−3.91	3.30	3.26	−1.23	−1.24
0.29	0.63	0.63	0.79	0.79	−0.44	−0.44	−4.24	−4.13	3.53	3.44	−1.30	−1.30
0.32	0.63	0.63	0.81	0.81	−0.49	−0.49	−4.47	−4.30	3.73	3.58	−1.37	−1.37
0.35	0.63	0.63	0.82	0.83	−0.54	−0.54	−4.67	−4.41	3.89	3.68	−1.45	−1.44
0.35	0.49	0.50	0.70	0.70	−0.57	−0.57	−4.67	−4.41	3.89	3.68	−1.45	−1.44
0.39	0.47	0.47	0.70	0.70	−0.63	−0.64	−4.65	−4.60	3.87	3.84	−1.54	−1.54
0.43	0.45	0.44	0.70	0.70	−0.70	−0.71	−4.53	−4.62	3.78	3.85	−1.63	−1.64
0.46	0.42	0.42	0.70	0.70	−0.76	−0.76	−4.33	−4.53	3.61	3.77	−1.72	−1.71
0.50	0.40	0.40	0.71	0.70	−0.83	−0.83	−4.03	−4.26	3.36	3.55	−1.81	−1.80
0.54	0.38	0.38	0.71	0.71	−0.89	−0.90	−3.65	−3.82	3.04	3.18	−1.88	−1.89
0.58	0.36	0.36	0.71	0.71	−0.96	−0.97	−3.18	−3.21	2.65	2.67	−1.95	−1.96
0.61	0.34	0.34	0.71	0.72	−1.02	−1.02	−2.62	−2.64	2.18	2.20	−2.01	−2.01
0.65	0.32	0.33	0.72	0.72	−1.09	−1.09	−1.97	−1.72	1.64	1.44	−2.05	−2.06
0.65	0.99	1.00	1.33	1.34	−0.94	−0.94	−1.96	−1.72	1.63	1.44	−2.05	−2.06
0.68	1.02	1.02	1.38	1.39	−0.99	−0.99	−2.15	−1.97	1.79	1.64	−2.09	−2.09
0.71	1.05	1.05	1.43	1.43	−1.04	−1.03	−2.34	−2.20	1.95	1.84	−2.12	−2.12
0.74	1.08	1.08	1.48	1.48	−1.09	−1.08	−2.52	−2.42	2.10	2.02	−2.17	−2.16
0.78	1.12	1.13	1.53	1.54	−1.13	−1.14	−2.69	−2.70	2.24	2.25	−2.21	−2.21
0.81	1.15	1.16	1.58	1.59	−1.18	−1.19	−2.86	−2.89	2.38	2.41	−2.25	−2.26
0.84	1.19	1.19	1.64	1.64	−1.23	−1.23	−3.02	−3.09	2.51	2.58	−2.30	−2.30
0.87	1.22	1.22	1.69	1.69	−1.28	−1.28	−3.17	−3.31	2.64	2.76	−2.36	−2.36
0.90	1.25	1.25	1.74	1.74	−1.33	−1.32	−3.32	−3.55	2.77	2.96	−2.41	−2.41
0.90	0.32	0.32	0.88	0.88	−1.53	−1.53	−3.32	−3.55	2.77	2.96	−2.41	−2.41
0.93	0.31	0.31	0.89	0.89	−1.58	−1.58	−2.55	−2.39	2.13	1.99	−2.45	−2.46
0.95	0.29	0.30	0.89	0.89	−1.62	−1.62	−1.74	−1.64	1.45	1.37	−2.48	−2.48
0.97	0.28	0.29	0.89	0.90	−1.67	−1.65	−0.89	−0.93	0.74	0.78	−2.50	−2.49
1.00	0.27	0.27	0.90	0.90	−1.71	−1.71	0.00	0.00	0.00	0.00	−2.50	-2.50

first, third, and fifth layers are made of cobalt ferrite, while the second and fourth laminae consist of TME-I and TME-III, respectively. The structure is subjected to a sinusoidal mechanical pressure from the top surface, as described by Eq. (119), with magnitude $\overline{q}_3^{(+)} = -7.5 \times 10^1$ N/m^2. In addition, sinusoidal thermal and magnetic loads are applied at the top and bottom surfaces, with magnitudes $\overline{q}_{\mathrm{T}}^{(+)} = 4.4$ J/m^2, $\overline{q}_{\mathrm{T}}^{(-)} = 4.08$ J/m^2 and $\overline{q}_{\mathrm{B}}^{(+)} = 1.94 \times 10^{-6}$ Wb/m^2, $\overline{q}_{\mathrm{B}}^{(-)} = 2.07 \times 10^{-6}$ Wb/m^2. Different multifield simulations are performed to study the static response of the laminate, involving coupled thermo-mechanical (T-D) and magneto-mechanical (M-D) simulations, where the structure is subjected to mechanical loads, along with thermal and magnetic fluxes, respectively. Then, a fully coupled multifield investigation (T-M-D) is conducted under simultaneous mechanical, thermal, and magnetic loads to highlight the coupling effects, when the panel is subjected to multifield loads. Semi-analytical solutions are provided using the ELDZL7 kinematic model, following the ESL approach outlined in Eq. (12). The results are presented in Figs. 3-7, which show the thickness plots of configuration, primary and secondary variables evaluated at the point $(0.75L_1, 0.75L_2)$. For the T-D and M-D cases, reference solutions are obtained using 3D FEM models from commercial software, consisting of 150336 parabolic brick elements with 629771 nodes. The through-the-thickness distribution of the displacement field components, the magnetic potential variation, and the temperature variation are reported for clarity and to facilitate comparisons in Table 15. As illustrated in Fig. 3, the displacement field, the magnetic potential, and temperature variation from 3D FEM model are predicted accurately by the higher-order ELW simulation for both in-plane and out-of-plane components, due to the use of higher-order polynomials in the description of configuration variables. The displacement field variables and temperature profile associated with the T-M-D case are very similar to those from the T-D simulation. However, a meaningful variation of the scalar magnetic potential occurs for coupled magnetic and thermal fields. Unlike T-D and M-D simulations, where the distribution of configuration variables is nearly linear, T-M-D multifield problems exhibit a typical zigzag behavior, especially for the quantities related to magnetism. Once the model is validated for homogeneous layers within the laminate, further simulations are performed where the material properties are varied within each lamina, following the approach of Eq. (112) and employing the EXP-I analytical expression detailed in Table 2. In particular, the mechanical properties of the first, third, and fifth layers are varied along the thickness, while homogeneous materials are assumed in the second and fourth laminae. In all simulations, the position parameter of the distribution is set to $\delta_0^{(k)} = 0$. The multifield response of the panel is assessed for different values of the parameter $\delta^{(k)}$. It is observed that the magnetic potential and temperature variation exhibit a profile variation as the scaling parameter increases. Moreover, the zigzag effect becomes more pronounced under non-uniform layers assumptions. The displacement field components and in-plane deformations are not significantly influenced by variations of the material properties, while the out-of-plane deformations and distortions vary with the layers properties. For T-D and M-D simulations conducted with homogeneous layers, we validate successfully the model against 3D FEM. Even in this case, the results from T-M-D models are similar to those from the T-D simulations, with a reduced variability observed in M-D results for different values of distribution parameter $\delta^{(k)}$. Furthermore, the variation of the material properties yields significant

Table 10
Temperature gradient components and thermal flux components of a laminated rectangular plate subjected to thermal and mechanical sinusoidal loading at $(0.25L_1, 0.75L_2)$ within the physical domain along the thickness direction employing the ELDZL7 kinematic model. A numerical reference solution is provided from a 3D FEM model.

	θ_1 $[\times 10^{-2}\mathrm{K/m}]$		θ_2 $[\times 10^{-2}\mathrm{K/m}]$		θ_3 $[\times 10^{1}\mathrm{K/m}]$		h_1 $[\times 10^{1}\mathrm{J/m^2}]$		h_2 $[\times 10^{1}\mathrm{J/m^2}]$		h_3 $[\times 10^{1}\mathrm{J/m^2}]$	
ζ+h/2 [10^{-3}m]	3D FEM	ELDZL7	3D FEM	ELDZL7	3D FEM	ELDZL7	3D FEM	ELDZL7	3D FEM	ELDZL7	3D FEM	ELDZL7
0.00	0.78	0.78	−0.65	−0.65	1.41	1.41	0.25	0.25	−0.21	−0.21	4.50	4.50
0.05	1.00	1.00	−0.83	−0.83	1.41	1.41	0.32	0.32	−0.27	−0.27	4.51	4.51
0.07	1.11	1.09	−0.92	−0.91	1.41	1.41	0.35	0.35	−0.30	−0.29	4.51	4.51
0.10	1.22	1.22	−1.02	−1.01	1.41	1.41	0.39	0.39	−0.33	−0.32	4.52	4.52
0.10	1.22	1.22	−1.02	−1.01	1.48	1.48	0.37	0.37	−0.31	−0.31	4.52	4.52
0.13	1.36	1.36	−1.14	−1.13	1.48	1.48	0.41	0.41	−0.34	−0.34	4.52	4.52
0.16	1.51	1.50	−1.26	−1.25	1.48	1.48	0.46	0.45	−0.38	−0.38	4.53	4.53
0.19	1.66	1.64	−1.38	−1.37	1.48	1.48	0.50	0.50	−0.42	−0.41	4.54	4.54
0.23	1.80	1.83	−1.50	−1.52	1.49	1.49	0.55	0.55	−0.45	−0.46	4.55	4.55
0.26	1.95	1.97	−1.62	−1.64	1.49	1.49	0.59	0.60	−0.49	−0.50	4.56	4.56
0.29	2.09	2.11	−1.74	−1.76	1.49	1.49	0.63	0.64	−0.53	−0.53	4.57	4.57
0.32	2.24	2.25	−1.87	−1.88	1.50	1.50	0.68	0.68	−0.57	−0.57	4.58	4.58
0.35	2.39	2.39	−1.99	−2.00	1.50	1.50	0.72	0.73	−0.60	−0.60	4.58	4.59
0.35	2.39	2.39	−1.99	−2.00	1.44	1.43	0.76	0.77	−0.64	−0.64	4.60	4.59
0.39	2.56	2.57	−2.13	−2.14	1.44	1.44	0.82	0.82	−0.68	−0.69	4.61	4.61
0.43	2.73	2.75	−2.27	−2.29	1.44	1.45	0.87	0.88	−0.73	−0.73	4.62	4.62
0.46	2.90	2.88	−2.41	−2.40	1.45	1.45	0.93	0.92	−0.77	−0.77	4.64	4.64
0.50	3.07	3.07	−2.56	−2.55	1.46	1.46	0.98	0.98	−0.82	−0.82	4.66	4.66
0.54	3.24	3.25	−2.70	−2.71	1.46	1.46	1.04	1.04	−0.86	−0.87	4.68	4.68
0.58	3.41	3.44	−2.84	−2.86	1.47	1.47	1.09	1.10	−0.91	−0.92	4.70	4.70
0.61	3.59	3.58	−2.99	−2.98	1.48	1.48	1.15	1.14	−0.96	−0.95	4.72	4.72
0.65	3.76	3.77	−3.13	−3.14	1.48	1.48	1.20	1.21	−1.00	−1.01	4.74	4.75
0.65	3.76	3.77	−3.13	−3.14	1.71	1.71	1.03	1.03	−0.86	−0.86	4.76	4.75
0.68	3.93	3.93	−3.27	−3.27	1.71	1.71	1.08	1.08	−0.90	−0.90	4.77	4.76
0.71	4.10	4.09	−3.41	−3.41	1.72	1.72	1.12	1.12	−0.94	−0.93	4.78	4.78
0.74	4.27	4.25	−3.55	−3.54	1.73	1.73	1.17	1.16	−0.97	−0.97	4.80	4.80
0.78	4.44	4.46	−3.70	−3.72	1.73	1.74	1.22	1.22	−1.01	−1.02	4.82	4.82
0.81	4.61	4.63	−3.84	−3.86	1.74	1.74	1.26	1.27	−1.05	−1.06	4.84	4.84
0.84	4.78	4.79	−3.98	−3.99	1.75	1.75	1.31	1.31	−1.09	−1.09	4.86	4.87
0.87	4.95	4.96	−4.12	−4.13	1.76	1.76	1.36	1.36	−1.13	−1.13	4.89	4.89
0.90	5.12	5.12	−4.27	−4.27	1.76	1.77	1.40	1.40	−1.17	−1.17	4.90	4.91
0.90	5.12	5.12	−4.27	−4.27	1.54	1.53	1.64	1.64	−1.37	−1.37	4.92	4.91
0.93	5.24	5.27	−4.37	−4.39	1.54	1.54	1.68	1.69	−1.40	−1.40	4.93	4.94
0.95	5.36	5.37	−4.47	−4.47	1.55	1.55	1.72	1.72	−1.43	−1.43	4.95	4.95
0.97	5.49	5.46	−4.57	−4.55	1.56	1.55	1.76	1.75	−1.46	−1.46	4.98	4.97
1.00	5.61	5.61	−4.67	−4.67	1.56	1.56	1.79	1.80	−1.50	−1.50	4.99	5.00

Table 11
Displacement field components and magnetic potential variation of a laminated rectangular plate subjected to magnetic and mechanical sinusoidal loading at $(0.25L_1, 0.75L_2)$ within the physical domain along the thickness direction employing the ELDZL7 kinematic model. A numerical reference solution is provided from a 3D FEM model.

	$U_1[\times 10^{-13}\text{m}]$		$U_2[\times 10^{-13}\text{m}]$		$U_3[\times 10^{-12}\text{m}]$		$\Delta\psi[\times 10^{-7}\text{A}]$	
ζ+h/2 [10^{-3}m]	3D FEM	ELDZL7	3D FEM	ELDZL7	3D FEM	ELDZL7	3D FEM	ELDZL7
0.00	−8.59	−8.59	7.16	7.16	−5.75	−5.75	0.00	0.00
0.05	−7.69	−7.69	6.41	6.41	−5.77	−5.76	1.28	1.30
0.07	−7.25	−7.34	6.04	6.11	−5.77	−5.77	1.86	1.75
0.10	−6.81	−6.81	5.67	5.67	−5.78	−5.78	2.41	2.36
0.10	−6.81	−6.81	5.67	5.67	−5.78	−5.78	2.41	2.36
0.13	−6.26	−6.28	5.22	5.23	−5.78	−5.78	2.98	2.94
0.16	−5.71	−5.75	4.76	4.80	−5.79	−5.79	3.49	3.46
0.19	−5.17	−5.24	4.31	4.36	−5.80	−5.79	3.96	3.92
0.23	−4.63	−4.54	3.86	3.79	−5.80	−5.80	4.37	4.47
0.26	−4.09	−4.02	3.41	3.35	−5.80	−5.80	4.74	4.82
0.29	−3.55	−3.51	2.96	2.92	−5.81	−5.81	5.05	5.13
0.32	−3.02	−2.99	2.51	2.49	−5.81	−5.81	5.32	5.41
0.35	−2.48	−2.48	2.07	2.07	−5.81	−5.81	5.53	5.63
0.35	−2.48	−2.48	2.07	2.07	−5.81	−5.81	5.53	5.63
0.39	−1.85	−1.80	1.54	1.50	−5.82	−5.82	5.77	5.84
0.43	−1.21	−1.13	1.01	0.94	−5.82	−5.82	5.92	5.97
0.46	−0.58	−0.62	0.48	0.52	−5.82	−5.82	6.01	6.02
0.50	0.06	0.06	−0.05	−0.05	−5.82	−5.82	6.03	6.04
0.54	0.69	0.73	−0.58	−0.61	−5.82	−5.82	5.97	5.98
0.58	1.33	1.41	−1.11	−1.17	−5.82	−5.82	5.84	5.85
0.61	1.96	1.92	−1.64	−1.60	−5.82	−5.82	5.64	5.72
0.65	2.60	2.60	−2.17	−2.17	−5.82	−5.81	5.36	5.47
0.65	2.60	2.60	−2.17	−2.17	−5.82	−5.81	5.36	5.47
0.68	3.14	3.11	−2.61	−2.60	−5.81	−5.81	5.16	5.28
0.71	3.68	3.64	−3.06	−3.03	−5.81	−5.81	4.92	5.03
0.74	4.22	4.15	−3.51	−3.46	−5.81	−5.81	4.63	4.76
0.78	4.76	4.84	−3.97	−4.03	−5.80	−5.80	4.31	4.32
0.81	5.30	5.37	−4.42	−4.48	−5.80	−5.80	3.94	3.95
0.84	5.85	5.89	−4.87	−4.91	−5.79	−5.79	3.53	3.52
0.87	6.40	6.42	−5.33	−5.35	−5.79	−5.79	3.08	3.04
0.90	6.95	6.95	−5.79	−5.79	−5.78	−5.78	2.58	2.51
0.90	6.95	6.95	−5.79	−5.79	−5.78	−5.78	2.58	2.51
0.93	7.39	7.48	−6.16	−6.23	−5.78	−5.78	1.99	1.86
0.95	7.84	7.83	−6.53	−6.53	−5.77	−5.77	1.37	1.38
0.97	8.28	8.19	−6.90	−6.83	−5.77	−5.77	0.70	0.86
1.00	8.73	8.73	−7.28	−7.28	−5.76	−5.76	0.00	0.00

Table 12
Three−dimensional strain components of a laminated rectangular plate subjected to magnetic and mechanical sinusoidal loading at $(0.25L_1, 0.75L_2)$ within the physical domain along the thickness direction employing the ELDZL7 kinematic model. A numerical reference solution is provided from a 3D FEM model.

	ε_1 [$\times 10^{-10}$m/m]		ε_2 [$\times 10^{-10}$m/m]		γ_{12} [$\times 10^{-10}$m/m]		γ_{13} [$\times 10^{-10}$m/m]		γ_{23} [$\times 10^{-10}$m/m]		ε_3 [$\times 10^{-10}$m/m]	
ζ+h/2 [10^{-3}m]	3D FEM	ELDZL7	3D FEM	ELDZL7	3D FEM	ELDZL7	3D FEM	ELDZL7	3D FEM	ELDZL7	3D FEM	ELDZL7
0.00	2.70	2.70	1.87	1.87	4.50	4.50	0.00	0.00	0.00	0.00	−2.83	−2.83
0.05	2.42	2.42	1.68	1.68	4.03	4.03	−0.29	−0.28	0.24	0.23	−2.54	−2.54
0.07	2.28	2.30	1.58	1.60	3.80	3.84	−0.41	−0.39	0.35	0.32	−2.40	−2.42
0.10	2.14	2.14	1.49	1.49	3.57	3.56	−0.54	−0.54	0.45	0.45	−2.25	−2.25
0.10	2.14	2.14	1.49	1.49	3.57	3.56	−0.51	−0.51	0.43	0.43	−2.13	−2.13
0.13	1.97	1.97	1.37	1.37	3.28	3.29	−0.64	−0.63	0.53	0.52	−1.96	−1.97
0.16	1.79	1.80	1.25	1.26	2.99	3.01	−0.75	−0.74	0.63	0.61	−1.80	−1.80
0.19	1.62	1.64	1.13	1.15	2.71	2.74	−0.85	−0.84	0.71	0.70	−1.63	−1.65
0.23	1.45	1.42	1.01	0.99	2.42	2.37	−0.95	−0.95	0.79	0.80	−1.46	−1.43
0.26	1.28	1.26	0.89	0.88	2.14	2.10	−1.03	−1.03	0.86	0.86	−1.30	−1.28
0.29	1.12	1.11	0.77	0.77	1.86	1.84	−1.10	−1.10	0.92	0.92	−1.14	−1.12
0.32	0.95	0.94	0.66	0.65	1.58	1.57	−1.16	−1.16	0.97	0.97	−0.97	−0.97
0.35	0.78	0.78	0.54	0.54	1.30	1.30	−1.21	−1.21	1.01	1.00	−0.81	−0.81
0.35	0.78	0.78	0.54	0.54	1.30	1.30	−1.27	−1.26	1.06	1.05	−0.85	−0.85
0.39	0.58	0.57	0.40	0.39	0.97	0.94	−1.32	−1.32	1.10	1.10	−0.65	−0.63
0.43	0.38	0.35	0.26	0.25	0.63	0.59	−1.36	−1.36	1.14	1.13	−0.44	−0.41
0.46	0.18	0.19	0.13	0.14	0.30	0.32	−1.38	−1.38	1.15	1.15	−0.24	−0.25
0.50	−0.02	−0.02	−0.01	−0.01	−0.03	−0.03	−1.39	−1.39	1.16	1.15	−0.03	−0.03
0.54	−0.22	−0.23	−0.15	−0.16	−0.36	−0.38	−1.38	−1.37	1.15	1.14	0.17	0.18
0.58	−0.42	−0.44	−0.29	−0.31	−0.69	−0.74	−1.35	−1.34	1.12	1.12	0.37	0.40
0.61	−0.62	−0.60	−0.43	−0.42	−1.03	−1.01	−1.30	−1.30	1.08	1.08	0.58	0.56
0.65	−0.82	−0.82	−0.57	−0.57	−1.36	−1.36	−1.24	−1.23	1.03	1.03	0.78	0.78
0.65	−0.82	−0.82	−0.57	−0.57	−1.36	−1.36	−1.09	−1.08	0.91	0.90	0.64	0.63
0.68	−0.99	−0.98	−0.68	−0.68	−1.64	−1.63	−1.05	−1.04	0.87	0.87	0.78	0.77
0.71	−1.16	−1.14	0.80	−0.79	−1.93	−1.90	−0.99	−0.99	0.83	0.82	0.93	0.91
0.74	−1.33	−1.30	−0.92	−0.91	−2.21	−2.17	−0.93	−0.93	0.77	0.78	1.08	1.06
0.78	−1.50	−1.52	−1.04	−1.06	−2.49	−2.54	−0.86	−0.84	0.72	0.70	1.22	1.24
0.81	−1.67	−1.69	−1.16	−1.17	−2.78	−2.81	−0.78	−0.76	0.65	0.64	1.37	1.38
0.84	−1.84	−1.85	−1.28	−1.29	−3.06	−3.08	−0.69	−0.68	0.58	0.57	1.52	1.53
0.87	−2.01	−2.01	−1.40	−1.40	−3.35	−3.36	−0.60	−0.59	0.50	0.49	1.67	1.68
0.90	−2.18	−2.18	−1.52	−1.52	−3.64	−3.64	−0.49	−0.49	0.41	0.41	1.83	1.82
0.90	−2.18	−2.18	−1.52	−1.52	−3.64	−3.64	−0.56	−0.56	0.47	0.47	2.19	2.19
0.93	−2.32	−2.35	−1.61	−1.63	−3.87	−3.91	−0.43	−0.40	0.36	0.33	2.33	2.36
0.95	−2.46	−2.46	−1.71	−1.71	−4.10	−4.10	0.30	−0.29	0.25	0.24	2.49	2.48
0.97	−2.60	−2.58	−1.81	−1.79	−4.34	−4.29	−0.15	−0.18	0.13	0.15	2.63	2.59
1.00	−2.74	−2.74	−1.91	−1.90	−4.57	−4.57	0.00	0.00	0.00	0.00	2.77	2.77

Table 13
Three-dimensional stress components of a laminated rectangular plate subjected to magnetic and mechanical sinusoidal loading at $(0.25L_1, 0.75L_2)$ within the physical domain along the thickness direction employing the ELDZL7 kinematic model. A numerical reference solution is provided from a 3D FEM model.

	σ_1 $[\times 10^1$ N/m$^2]$		σ_2 $[\times 10^1$ N/m$^2]$		τ_{12} $[\times 10^1$ N/m$^2]$		τ_{13} $[\times 10^0$ N/m$^2]$		τ_{23} $[\times 10^0$ N/m$^2]$		σ_3 $[\times 10^0$ N/m$^2]$	
ζ+h/2 [10^{-3}m]	3D FEM	ELDZL7	3D FEM	ELDZL7	3D FEM	ELDZL7	3D FEM	ELDZL7	3D FEM	ELDZL7	3D FEM	ELDZL7
0.00	6.29	6.12	5.36	5.19	2.54	2.54	−0.02	0.00	0.01	0.00	−0.28	−0.29
0.05	5.63	5.70	4.79	4.86	2.28	2.28	−1.27	−1.25	1.06	1.04	−0.29	−0.30
0.07	5.30	5.50	4.51	4.70	2.15	2.17	−1.85	−1.71	1.54	1.43	−0.31	−0.32
0.10	4.97	5.18	4.23	4.44	2.01	2.01	−2.39	−2.38	1.99	1.98	−0.34	−0.35
0.10	4.56	4.44	3.86	3.74	1.92	1.92	−2.39	−2.38	1.99	1.98	−0.34	−0.35
0.13	4.19	4.13	3.54	3.48	1.76	1.77	−2.97	−2.93	2.47	2.44	−0.38	−0.40
0.16	3.81	3.80	3.22	3.21	1.61	1.62	−3.50	−3.44	2.91	2.86	−0.44	−0.45
0.19	3.44	3.46	2.91	2.92	1.46	1.47	−3.98	−3.90	3.32	3.25	−0.50	−0.50
0.23	3.07	3.00	2.60	2.53	1.30	1.28	−4.41	−4.45	3.68	3.71	−0.57	−0.59
0.26	2.71	2.64	2.28	2.22	1.15	1.13	−4.80	−4.81	4.00	4.01	−0.65	−0.67
0.29	2.34	2.28	1.97	1.92	1.00	0.99	−5.13	−5.13	4.28	4.27	−0.73	−0.75
0.32	1.97	1.92	1.66	1.61	0.85	0.84	−5.42	−5.40	4.52	4.50	−0.82	−0.83
0.35	1.61	1.55	1.35	1.30	0.70	0.70	−5.66	−5.62	4.72	4.68	−0.91	−0.92
0.35	1.76	1.88	1.49	1.61	0.73	0.73	−5.66	−5.62	4.72	4.68	−0.91	−0.92
0.39	1.28	1.34	1.08	1.15	0.55	0.53	−5.90	−5.89	4.92	4.91	−1.03	−1.04
0.43	0.81	0.80	0.68	0.68	0.36	0.33	−6.07	-6.07	5.06	5.06	−1.15	−1.17
0.46	0.34	0.40	0.28	0.34	0.17	0.18	−6.16	−6.14	5.14	5.12	-1.27	−1.27
0.50	−0.13	−0.13	−0.13	−0.12	−0.02	−0.02	−6.18	−6.17	5.15	5.14	−1.40	−1.40
0.54	−0.61	−0.66	−0.53	−0.58	−0.20	−0.22	−6.13	−6.11	5.11	5.09	−1.52	−1.53
0.58	−1.08	−1.19	−0.94	−1.04	−0.39	−0.42	−6.00	−5.96	5.00	4.97	−1.65	−1.66
0.61	−1.55	−1.60	−1.34	−1.39	−0.58	−0.57	−5.80	−5.79	4.83	4.83	−1.76	−1.75
0.65	−2.03	−2.14	−1.75	−1.86	−0.77	−0.77	−5.52	−5.49	4.60	4.57	−1.88	−1.87
0.65	−1.58	−1.58	−1.34	−1.34	−0.67	−0.67	−5.52	−5.49	4.60	4.57	−1.88	−1.87
0.68	−1.90	−1.88	−1.60	−1.58	−0.80	−0.80	−5.29	−5.26	4.41	4.39	−1.97	−1.96
0.71	−2.21	−2.17	−1.86	−1.83	−0.94	−0.93	−5.01	−5.01	4.18	4.17	−2.05	−2.04
0.74	−2.52	−2.46	−2.13	−2.08	−1.08	−1.06	−4.70	−4.71	3.92	3.92	−2.13	−2.12
0.78	−2.84	−2.86	−2.39	−2.40	−1.22	−1.24	−4.34	−4.25	3.62	3.55	−2.21	−2.21
0.81	−3.15	−3.15	−2.65	−2.65	−1.36	−1.37	−3.94	−3.87	3.29	3.22	−2.28	−2.28
0.84	−3.47	−3.44	−2.92	−2.88	−1.50	−1.51	−3.50	−3.44	2.92	2.87	−2.34	−2.34
0.87	−3.78	−3.71	−3.18	−3.11	−1.64	−1.64	−3.02	−2.98	2.51	2.49	−2.40	−2.39
0.90	−4.10	−3.97	−3.45	−3.32	−1.78	−1.78	−2.49	−2.49	2.08	2.07	−2.44	−2.43
0.90	−5.27	−5.50	−4.51	−4.74	−2.06	−2.06	−2.49	−2.49	2.07	2.07	−2.44	−2.43
0.93	−5.59	−5.82	−4.79	−5.01	−2.19	−2.21	−1.92	−1.79	1.60	1.49	−2.47	−2.47
0.95	−5.92	−6.01	−5.07	−5.16	−2.32	−2.32	−1.32	−1.30	1.10	1.08	−2.49	−2.48
0.97	−6.25	−6.18	−5.35	−5.29	−2.45	−2.42	−0.69	−0.79	0.57	0.66	−2.50	−2.49
1.00	−6.58	−6.37	−5.64	−5.42	−2.58	−2.58	−0.02	0.00	0.01	0.00	−2.50	−2.50

Table 14
Magnetic field components and magnetic flux components of a laminated rectangular plate subjected to thermal and mechanical sinusoidal loading at $(0.25L_1, 0.75L_2)$ within the physical domain along the thickness direction employing the ELDZL7 kinematic model. A numerical reference solution is provided from a 3D FEM model.

	$\mathscr{H}_1$ [$\times 10^{-4}$A/m]		$\mathscr{H}_2$ [$\times 10^{-4}$A/m]		$\mathscr{H}_3$ [$\times 10^{-3}$A/m]		$\mathscr{B}_1$ [$\times 10^{-7}$Wb/m^2]		$\mathscr{B}_2$ [$\times 10^{-7}$Wb/m^2]		$\mathscr{B}_3$ [$\times 10^{-8}$Wb/m^2]	
ζ+h/2 [10^{-3}m]	3D FEM	ELDZL7	3D FEM	ELDZL7	3D FEM	ELDZL7	3D FEM	ELDZL7	3D FEM	ELDZL7	3D FEM	ELDZL7
0.00	0.00	0.00	0.00	0.00	−2.71	−2.84	0.00	0.03	0.00	−0.02	3.79	1.81
0.05	−0.40	−0.41	0.34	0.34	−2.41	−2.52	−0.39	−0.41	0.33	0.34	3.74	1.96
0.07	−0.59	−0.55	0.49	0.46	−2.26	−2.40	−0.57	−0.55	0.48	0.46	3.67	1.99
0.10	−0.76	−0.74	0.63	0.62	−2.11	−2.21	−0.74	−0.75	0.62	0.62	3.58	2.01
0.10	−0.76	−0.74	0.63	0.62	−1.90	−2.02	−0.49	−0.47	0.41	0.39	3.58	2.01
0.13	−0.94	−0.92	0.78	0.77	−1.73	−1.85	−0.60	−0.59	0.50	0.49	3.49	2.05
0.16	−1.10	−1.09	0.91	0.91	−1.57	−1.68	−0.71	−0.70	0.59	0.58	3.38	2.07
0.19	−1.24	−1.23	1.04	1.03	−1.40	−1.52	−0.81	−0.79	0.67	0.66	3.25	2.07
0.23	−1.37	−1.40	1.14	1.17	−1.24	−1.30	−0.89	−0.90	0.74	0.75	3.11	2.06
0.26	−1.49	−1.51	1.24	1.26	−1.09	-1.14	−0.97	−0.98	0.81	0.81	2.95	2.03
0.29	−1.59	−1.61	1.32	1.34	−0.93	−0.98	−1.03	−1.04	0.86	0.87	2.79	1.99
0.32	−1.67	−1.70	1.39	1.41	−0.77	−0.82	−1.09	−1.10	0.91	0.92	2.61	1.94
0.35	−1.74	−1.77	1.45	1.48	−0.62	−0.66	−1.14	−1.15	0.95	0.96	2.43	1.88
0.35	−1.74	−1.77	1.45	1.48	−0.71	−0.75	−1.72	−1.75	1.44	1.46	2.43	1.88
0.39	−1.81	−1.83	1.51	1.53	−0.52	−0.53	−1.80	−1.81	1.50	1.51	2.08	1.67
0.43	−1.86	−1.88	1.55	1.56	−0.33	−0.31	−1.85	−1.86	1.54	1.55	1.71	1.44
0.46	−1.89	−1.89	1.57	1.58	−0.13	−0.15	−1.88	−1.88	1.56	1.56	1.34	1.26
0.50	−1.89	−1.90	1.58	1.58	0.06	0.06	−1.88	−1.88	1.57	1.57	0.96	1.03
0.54	−1.88	−1.88	1.56	1.57	0.25	0.28	−1.86	−1.85	1.55	1.54	0.59	0.79
0.58	−1.83	−1.84	1.53	1.53	0.44	0.49	−1.82	−1.81	1.52	1.51	0.22	0.57
0.61	−1.77	−1.80	1.48	1.50	0.64	0.66	−1.76	−1.75	1.47	1.46	−0.14	0.41
0.65	−1.68	−1.72	1.40	1.43	0.83	0.87	−1.68	−1.67	1.40	1.39	−0.48	0.20
0.65	−1.68	−1.72	1.40	1.43	0.58	0.68	−0.41	−0.42	0.34	0.35	−0.48	0.20
0.68	−1.62	−1.66	1.35	1.38	0.71	0.82	−0.39	−0.40	0.33	0.33	−0.55	0.26
0.71	−1.55	−1.58	1.29	1.32	0.84	0.96	−0.37	−0.38	0.31	0.32	−0.61	0.32
0.74	−1.46	−1.49	1.21	1.25	0.97	1.11	−0.35	−0.36	0.29	0.30	−0.67	0.39
0.78	−1.35	−1.36	1.13	1.13	1.11	1.30	−0.32	−0.32	0.27	0.27	−0.73	0.48
0.81	−1.24	−1.24	1.03	1.03	1.24	1.45	−0.30	−0.29	0.25	0.24	−0.78	0.55
0.84	−1.11	−1.11	0.92	0.92	1.38	1.60	−0.26	−0.26	0.22	0.22	−0.82	0.63
0.87	−0.97	−0.96	0.81	0.80	1.52	1.75	−0.23	−0.23	0.19	0.19	−0.87	0.71
0.90	−0.81	−0.79	0.68	0.66	1.66	1.90	−0.19	−0.19	0.16	0.15	−0.90	0.81
0.90	−0.81	−0.79	0.68	0.66	2.29	2.39	−0.79	−0.76	0.66	0.64	−0.91	0.81
0.93	−0.63	−0.58	0.52	0.49	2.43	2.58	−0.61	−0.57	0.51	0.48	−1.00	0.82
0.95	−0.43	−0.43	0.36	0.36	2.58	2.70	−0.42	−0.43	0.35	0.36	−1.07	0.85
0.97	−0.22	−0.27	0.18	0.23	2.73	2.82	−0.22	−0.26	0.18	0.22	−1.11	0.89
1.00	0.00	0.00	0.00	0.00	2.88	3.02	0.00	0.02	0.00	−0.01	−1.13	1.00

variations in the slope of the out-of-plane strain distributions, as can be seen from Fig. 4. Fig. 5 presents the through-the-thickness dispersions of three-dimensional stress components for T-D, M-D and T-M-D simulations. The in-plane and out-of-plane displacement field components derived from 3D FEM model are accurately predicted using the ELDZL7 theory. Uniform or linear in-plane stress profiles are found within each layer, while the out-of-plane stress components exhibit parabolic distributions with singularities at each interface, which are predicted by the zigzag function. In all simulations, it is worth observing that the loading conditions at the top and bottom surfaces are perfectly satisfied, despite the model is two-dimensional, due to the adoption of the post-processing recovery procedure. The profiles along the thickness direction of the magnetic primary and secondary variables are collected in Fig. 6. For the M-D results, which are validated against the finite element simulations, a limited variability is observed as the material properties vary within the selected layers. On the other hand, the magnetic field and, consequently, the magnetic flux distributions from T-M-D simulations differ significantly from those in M-D simulations, indicating that the magnetic response of the laminate changes a thermal environment. Furthermore, in fully-coupled simulations, the results depend on the thickness distribution of the material properties, with the zigzag effects becoming more pronounced as the scaling parameter increases. Finally, Fig. 7 presents the results from T-D and M-T-D simulations in terms of temperature gradient components and thermal flux components. It is important to note that the cylindrical panel is in thermodynamic equilibrium conditions, such that the effect of the magnetic field on thermal conduction is not evident. Consequently, the T-M-D curves align with those associated with T-D simulations. The results demonstrate that the introduction of variation in the material properties leads to deviations from the linear or piecewise linear profiles of thermal primary variables, introducing a zigzag distribution for in-plane components and a linear variation in some layers, for the θ_3 dispersion.

At this point, a numerical investigation is conducted on another cylinder composed of four layers under various conditions. This example evaluates the performance of the GIQ-based recovery procedure and the sensitivity of the model to the position parameter $\delta_0^{(k)}$ when the material properties vary within an arbitrary layer of the shell. The reference surface of the laminate is described by Eq. (117) with $R_2 = R = 4 \times 10^{-2}$m, while the thicknesses of the layers are set to $h_1 = 2.50 \times 10^{-3}$m, $h_2 = 1.00 \times 10^{-3}$m, $h_3 = 3.00 \times 10^{-3}$m and $h_4 = 2.00 \times 10^{-3}$m. The physical domain $[0,L_1] \times [\vartheta_0,\vartheta_1]$ is defined, such that $L_1 = 5.0 \times 10^{-2}$m, $\vartheta_0 = -\pi/2$ and $\vartheta_1 = \pi/6$. The lamination scheme consists of two external transversely isotropic laminae made from TME-I material, while the second and third layer consist of TME-II and TME-III, respectively. The multifield properties of TME-II are detailed in Table 1. This material is characterized as a transversely isotropic composite with a fiber volume fraction equal to $V_f = 0.4$, while α_1,α_2 behaves as an isotropic plane. The homogenized multifield properties of TME-II, derived from the procedure outlined in Ref. [85], are scaled by 1/3 to obtain a softer layer with multifield properties. The panel rests on a Winkler elastic foundation with stiffness $k_{3f}^{(-)} = 5 \times 10^{10}$ N/m^3. A uniform external mechanical load of magnitude $\overline{q}_3^{(+)} = -1.0 \times 10^2$ N/m^2 is applied to the top surface. Following Eq. (49), uniform loads are modelled using the following expression for $\widetilde{q}_\alpha^{(\pm)} = \widetilde{q}_3^{(\pm)}$:

$$\widetilde{q}_\alpha^{(\pm)}(s_1, s_2) = 1 \tag{120}$$

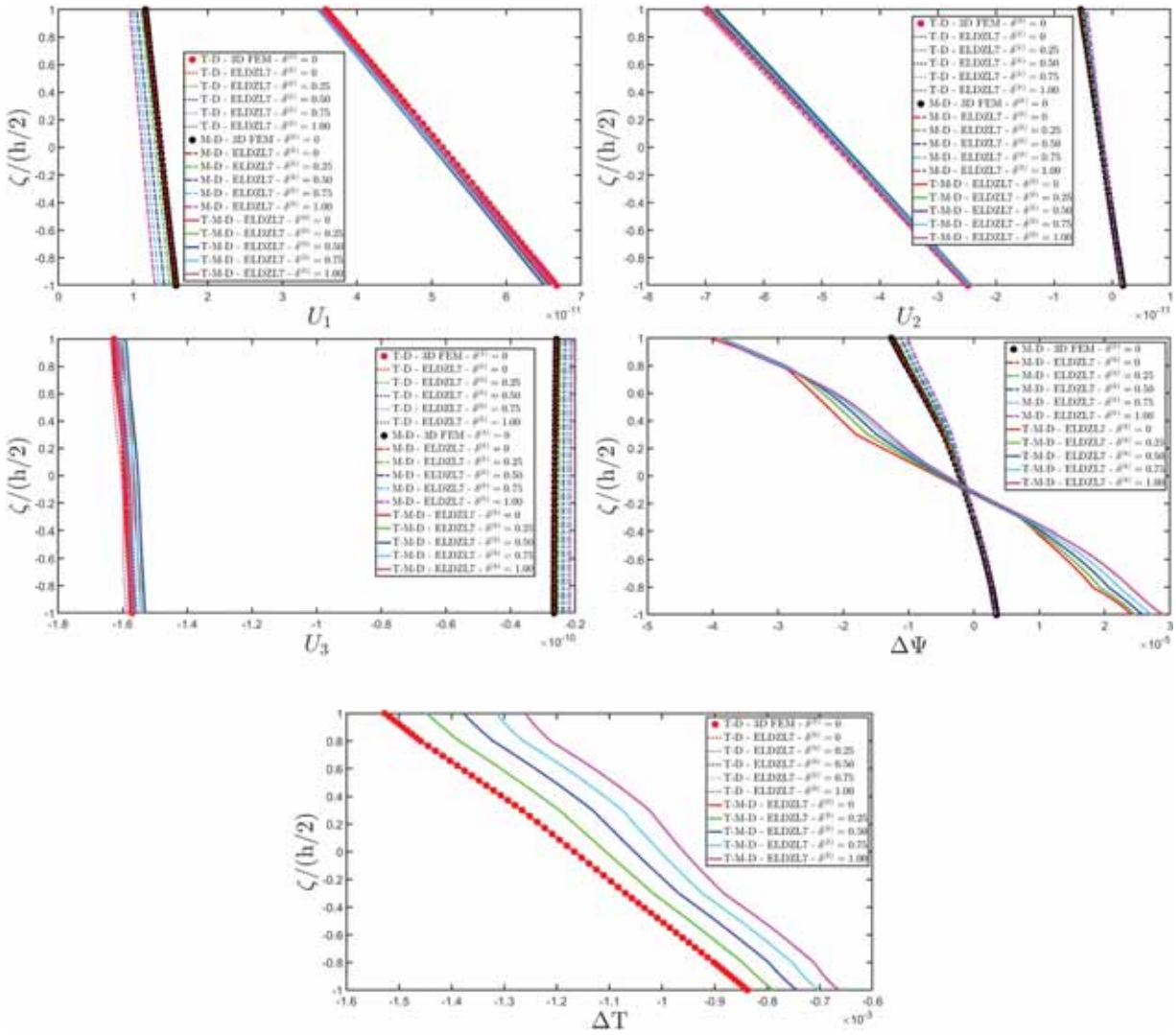

Fig. 3. Representation of the thickness profile of multifield configuration variables at $(0.75L_1, 0.75L_2)$ of a laminated circular cylinder under thermal, magnetic, and mechanical loads with sinusoidal distribution with $\widetilde{N} = \widetilde{M} = 1$. The displacement field components U_1,U_2,U_3 are expressed in [m], while the magnetic potential $\Delta\Psi$ with respect to the reference configuration is expressed in [A].The absolute temperature variation ΔT is expressed in [K]. Effect of the shape parameter $\delta^{(k)}$ of the material distribution.

Table 15
Thermo-magneto-mechanical response of a laminated circular cylinder with arbitrary variation of the material properties. The results are provided for the points located at $(0.75L_1, 0.75L_2)$ for various $\widetilde{z} = 2\zeta/h$.

$\delta^{(k)}$	$\widetilde{z} = -1$	$\widetilde{z} = -0.75$	$\widetilde{z} = -0.50$	$\widetilde{z} = -0.25$	$\widetilde{z} = 0$	$\widetilde{z} = 0.25$	$\widetilde{z} = 0.50$	$\widetilde{z} = 0.75$	$\widetilde{z} = 1$
Thermo-mechanical									
$U_1[\times 10^{-11}\text{m}]$									
0 (3D FEM)	6.67	6.29	5.91	5.53	5.15	4.76	4.37	3.98	3.58
0 (ELDZL7)	6.67	6.29	5.90	5.52	5.14	4.76	4.36	3.97	3.58
0.50 (ELDZL7)	6.59	6.21	5.84	5.46	5.07	4.69	4.30	3.91	3.52
1.00 (ELDZL7)	6.70	6.31	5.92	5.53	5.14	4.75	4.35	3.96	3.55
$U_2[\times 10^{-11}\text{m}]$									
0 (3D FEM)	−2.49	−3.04	−3.60	−4.15	−4.71	−5.27	−5.83	−6.40	−6.98
0 (ELDZL7)	−2.49	−3.04	−3.60	−4.15	−4.71	−5.27	−5.83	−6.40	−6.97
0.50 (ELDZL7)	−2.48	−3.04	−3.59	−4.14	−4.69	−5.25	−5.81	−6.37	−6.94
1.00 (ELDZL7)	−2.54	−3.11	−3.67	−4.23	−4.80	−5.37	−5.93	−6.51	−7.09
$U_3[\times 10^{-10}\text{m}]$									
0 (3D FEM)	−1.57	−1.58	−1.58	−1.59	−1.59	−1.60	−1.61	−1.62	−1.63
0 (ELDZL7)	−1.57	−1.57	−1.58	−1.59	−1.59	−1.60	−1.61	−1.62	−1.63
0.50 (ELDZL7)	−1.56	−1.56	−1.57	−1.57	−1.58	−1.59	−1.60	−1.60	−1.61
1.00 (ELDZL7)	−1.59	−1.60	−1.60	−1.60	−1.60	−1.62	−1.63	−1.63	−1.64
$\Delta T[\times 10^{-4}\text{K}]$									
0 (3D FEM)	−8.38	−9.18	−10.02	−10.86	−11.67	−12.49	−13.42	−14.39	−15.27
0 (ELDZL7)	−8.38	−9.18	−10.02	−10.86	−11.67	−12.50	−13.43	−14.39	−15.27
0.50 (ELDZL7)	−7.44	−8.14	−8.97	−9.83	−10.53	−11.19	−12.03	−13.01	−13.77
1.00 (ELDZL7)	−6.64	−7.27	−8.10	−8.96	−9.59	−10.13	−10.92	−11.91	−12.60
Magneto−mechanical									
$U_1[\times 10^{-11}\text{m}]$									
0 (3D FEM)	1.58	1.52	1.47	1.42	1.37	1.32	1.27	1.22	1.16
0 (ELDZL7)	1.58	1.52	1.47	1.42	1.37	1.32	1.27	1.22	1.16
0.50 (ELDZL7)	1.42	1.37	1.32	1.28	1.23	1.19	1.14	1.10	1.05
1.00 (ELDZL7)	1.29	1.25	1.20	1.16	1.12	1.08	1.04	1.00	0.95
$U_2[\times 10^{-12}\text{m}]$									
0 (3D FEM)	1.82	0.89	−0.02	−0.91	−1.80	−2.69	−3.58	−4.48	−5.39
0 (ELDZL7)	1.82	0.89	−0.02	−0.91	−1.80	−2.68	−3.58	−4.48	−5.39
0.50 (ELDZL7)	1.68	0.84	0.03	−0.77	−1.57	−2.37	−3.18	−3.98	−4.80
1.00 (ELDZL7)	1.55	0.79	0.06	−0.67	−1.39	−2.12	−2.85	−3.58	−4.33
$U_3[\times 10^{-11}\text{m}]$									
0 (3D FEM)	−2.65	−2.65	−2.65	−2.64	−2.63	−2.62	−2.61	−2.59	−2.58
0 (ELDZL7)	−2.65	−2.65	−2.65	−2.64	−2.63	−2.62	−2.61	−2.59	−2.58
0.50 (ELDZL7)	−2.38	−2.38	−2.38	−2.37	−2.37	−2.36	−2.35	−2.33	−2.32
1.00 (ELDZL7)	−2.17	−2.17	−2.16	−2.16	−2.15	−2.14	−2.13	−2.12	−2.11
$\Delta\psi[\times 10^{-6}\text{A}]$									
0 (3D FEM)	3.46	2.48	1.12	−0.45	−2.18	−4.16	−6.82	−9.78	−12.65
0 (ELDZL7)	3.45	2.46	1.12	−0.47	−2.19	−4.19	−6.79	−9.77	−12.63
0.50 (ELDZL7)	3.37	2.52	1.21	−0.31	−1.79	−3.52	−5.87	−8.63	−11.21
1.00 (ELDZL7)	3.30	2.54	1.28	−0.18	−1.50	−3.02	−5.19	−7.81	−10.16
Thermo-magneto-mechanical									
$U_1[\times 10^{-11}\text{m}]$									
0 (ELDZL7)	6.57	6.20	5.82	5.45	5.07	4.69	4.31	3.92	3.53
0.50 (ELDZL7)	6.50	6.13	5.76	5.39	5.01	4.63	4.25	3.86	3.47
1.00 (ELDZL7)	6.61	6.23	5.85	5.47	5.08	4.69	4.30	3.91	3.51
$U_2[\times 10^{-11}\text{m}]$									
0 (ELDZL7)	−2.44	−2.98	−3.53	−4.07	−4.62	−5.17	−5.73	−6.29	−6.86
0.50 (ELDZL7)	−2.44	−2.98	−3.52	−4.06	−4.60	−5.15	−5.71	−6.26	−6.83
1.00 (ELDZL7)	−2.50	−3.05	−3.60	−4.15	−4.71	−5.27	−5.84	−6.40	−6.98
$U_3[\times 10^{-10}\text{m}]$									
0 (ELDZL7)	−1.54	−1.55	−1.56	−1.56	−1.57	−1.57	−1.58	−1.60	−1.60
0.50 (ELDZL7)	−1.53	−1.54	−1.54	−1.55	−1.55	−1.56	−1.57	−1.58	−1.59
1.00 (ELDZL7)	−1.56	−1.57	−1.57	−1.57	−1.58	−1.59	−1.60	−1.61	−1.62
$\Delta\psi[\times 10^{-5}\text{A}]$									
0 (ELDZL7)	2.41	1.73	1.19	0.49	−0.57	−1.60	−2.24	−2.80	−4.05
0.50 (ELDZL7)	2.58	1.96	1.34	0.51	−0.48	−1.34	−1.95	−2.71	−3.85
1.00 (ELDZL7)	2.90	2.28	1.56	0.57	−0.42	−1.18	−1.80	−2.74	−3.86
$\Delta T[\times 10^{-4}\text{K}]$									
0 (ELDZL7)	−8.38	−9.18	−10.02	−10.86	−11.67	−12.50	−13.43	−14.39	−15.27
0.50 (ELDZL7)	−7.44	−8.14	−8.97	−9.83	−10.53	−11.19	−12.03	−13.01	−13.77
1.00 (ELDZL7)	−6.64	−7.27	−8.10	−8.96	−9.59	−10.13	−10.92	−11.91	−12.60

Thermal loads account for hydrostatic distributions of thermal fluxes, characterized by the magnitudes $\overline{q}_{\text{T}}^{(+)} = 1.0\,\text{J/m}^2$ and $\overline{q}_{\text{T}}^{(-)} = 0.7\,\text{J/m}^2$. The following distribution is, thus, adopted for the quantities $\widetilde{q}_{\alpha}^{(\pm)} = \widetilde{q}_{\text{T}}^{(\pm)}$:

$$\widetilde{q}_{\alpha}^{(\pm)}(s_1, s_2) = \frac{s_1}{L_1} \tag{121}$$

Finally, magnetic fluxes with magnitudes $\overline{q}_{\text{B}}^{(+)} = -6.0 \times 10^{-4}\,\text{Wb/m}^2$ and $\overline{q}_{\text{B}}^{(-)} = -9.0 \times 10^{-4}\,\text{Wb/m}^2$ are applied at the top and bottom surfaces of the shell, respectively. These fluxes follow an inverse hydrostatic distribution along α_1 principal direction, defined as follows with $\widetilde{q}_{\alpha}^{(\pm)} = \widetilde{q}_{\text{B}}^{(\pm)}$:

$$\widetilde{q}_{\alpha}^{(\pm)}(s_1, s_2) = 1 - \frac{s_1}{L_1} \tag{122}$$

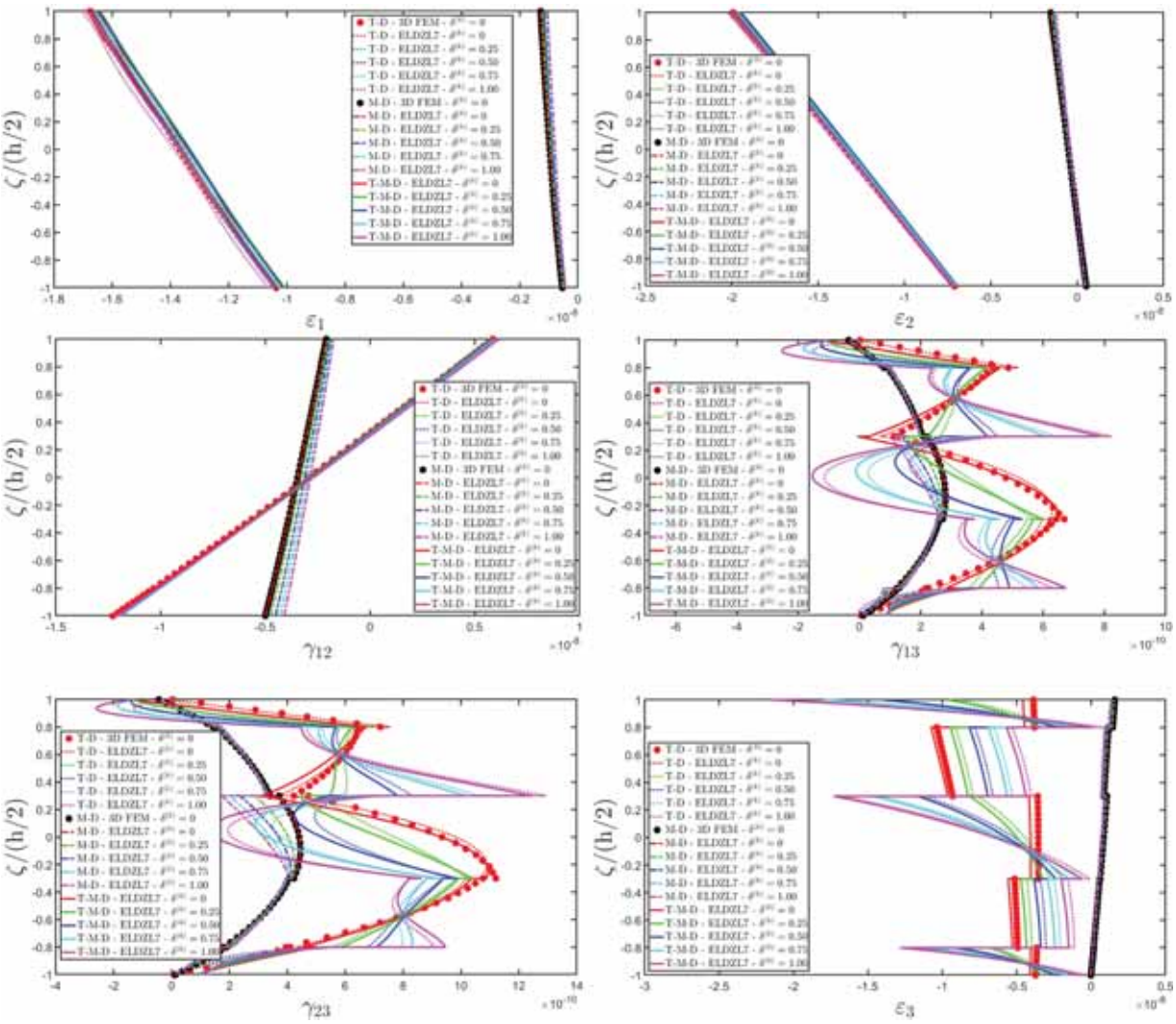

Fig. 4. Representation of the thickness profile at $(0.75L_1, 0.75L_2)$ of mechanical primary variables of a laminated circular cylinder under thermal, magnetic, and mechanical loads with sinusoidal distribution with $\widetilde{N} = \widetilde{M} = 1$. The three-dimensional strain components are expressed in [m /m]. Effect of the shape parameter $\delta^{(k)}$ of the material distribution.

It should be noted that the inverse hydrostatic distribution in Eq. (122) can be interpreted as the difference between a uniform distribution, as described in Eq. (120), and the hydrostatic distribution presented in Eq. (121).

To derive the multifield response of this structure, the ELDZL7 theory is adopted, taking into account $\widetilde{N} = \widetilde{M} = 150$ terms for the expansion of the unknown field. In this context, the following definitions [33] are introduced for the semi-analytical coefficients $Q^{(+)}_{\alpha snm}$ and $Q^{(-)}_{\alpha snm}$ in Eq. (73):

$$
\begin{aligned}
Q^{(\pm)}_{\alpha nm} &= \frac{4\overline{q}^{(\pm)}_{\alpha}}{\pi^2 nm}(1-\cos(n\pi))(1-\cos(m\pi)) \\
Q^{(\pm)}_{\alpha nm} &= -\frac{4\overline{q}^{(\pm)}_{\alpha}}{\pi^2 nm}\cos(n\pi)(1-\cos(m\pi))
\end{aligned}
\tag{123}
$$

More specifically, the first coefficient refers to Eq. (120), while the second one is associated with Eq. (121). Employing the superimposition principle, the subtraction of these coefficients yields the semi-analytical expansion terms for Eq. (122). A three-dimensional finite-element-based solution is provided, accounting for 61440 parabolic brick elements and 261961 nodes, resulting in a total number of 1047844 variables.

The through-the-thickness distributions of thermo-magneto-elastic configuration, primary, and secondary variables are evaluated at $(0.75L_1, 0.25L_2)$ and presented in Figs. 8-12. In particular, Fig. 8 illustrates that the in-plane displacement field varies almost linearly, while the U_3 component is characterized by a zigzag distribution even for uncoupled T-D and M-D simulations. This aspect is particularly evident in the distribution of magnetic potential and the absolute temperature variation. Once the uncoupled M-D and T-D models are successfully validated against the results from the 3D FEM model, the material properties of each layer in the stacking sequence are varied by setting $\delta^{(k)} = 1$. In this way, a parametric investigation is performed for a gradual decrease of position value $\delta_0^{(k)}$ of the material variation within the first and third lamina. In this case, it is crucial to select values of $\delta_0^{(k)}$ ensuring that each material property remains non-null, otherwise the results would be physically inconsistent. The first lamina is characterized by a L-I variation, while an SC-I material variation is considered for the second layer. In addition, the third and fourth laminae are characterized by UC-I and HT-I material properties variations, respectively. The results presented in Fig. 8 demonstrate that the variation for the in-plane deflection of the structure is more pronounced along the curved direction than the straight one. A significative deviation from the original temperature profile is also observed, with a reduction in the zigzag effect. Regarding the three-dimensional strain components shown in Fig. 9, it should be noted that the variation in the volume fraction

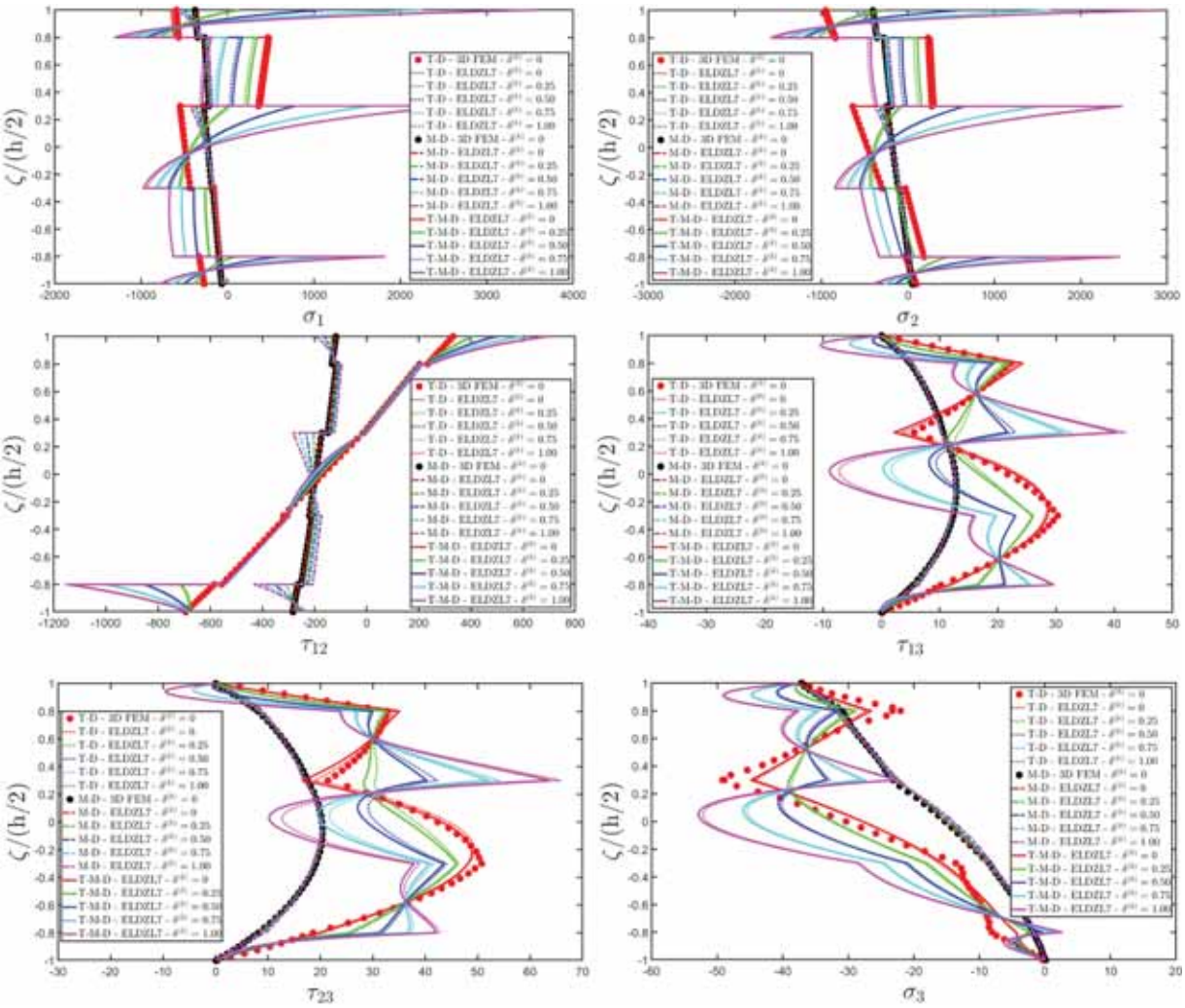

Fig. 5. Representation of the thickness profile at $(0.75L_1, 0.75L_2)$ of mechanical secondary variables of a laminated circular cylinder under thermal, magnetic, and mechanical loads with sinusoidal distribution with $\widetilde{N} = \widetilde{M} = 1$. The three-dimensional stress components are expressed in $\left[\mathrm{N/m^2}\right]$. Effect of the shape parameter $\delta^{(k)}$ of the material distribution.

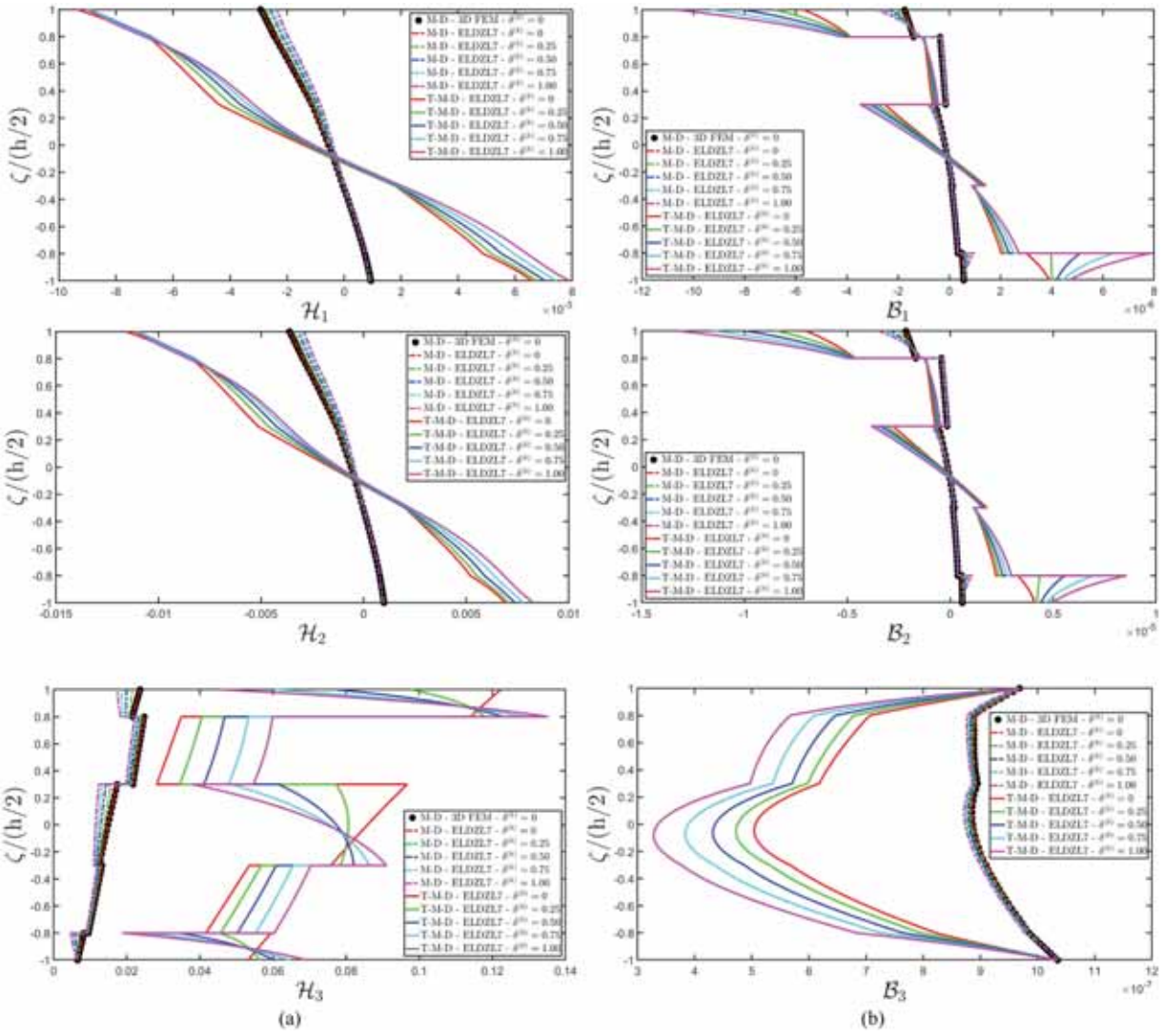

Fig. 6. Representation of the thickness profile at $(0.75L_1, 0.75L_2)$ of magnetic primary (a) and secondary (b) variables of a laminated circular cylinder under thermal, magnetic, and mechanical loads with sinusoidal distribution with $\widetilde{N} = \widetilde{M} = 1$. The magnetic field components are expressed in $[\mathrm{A/m}]$, while the magnetic flux components are expressed in $\left[\mathrm{Wb/m^2}\right]$. Effect of the shape parameter $\delta^{(k)}$ of the material distribution.

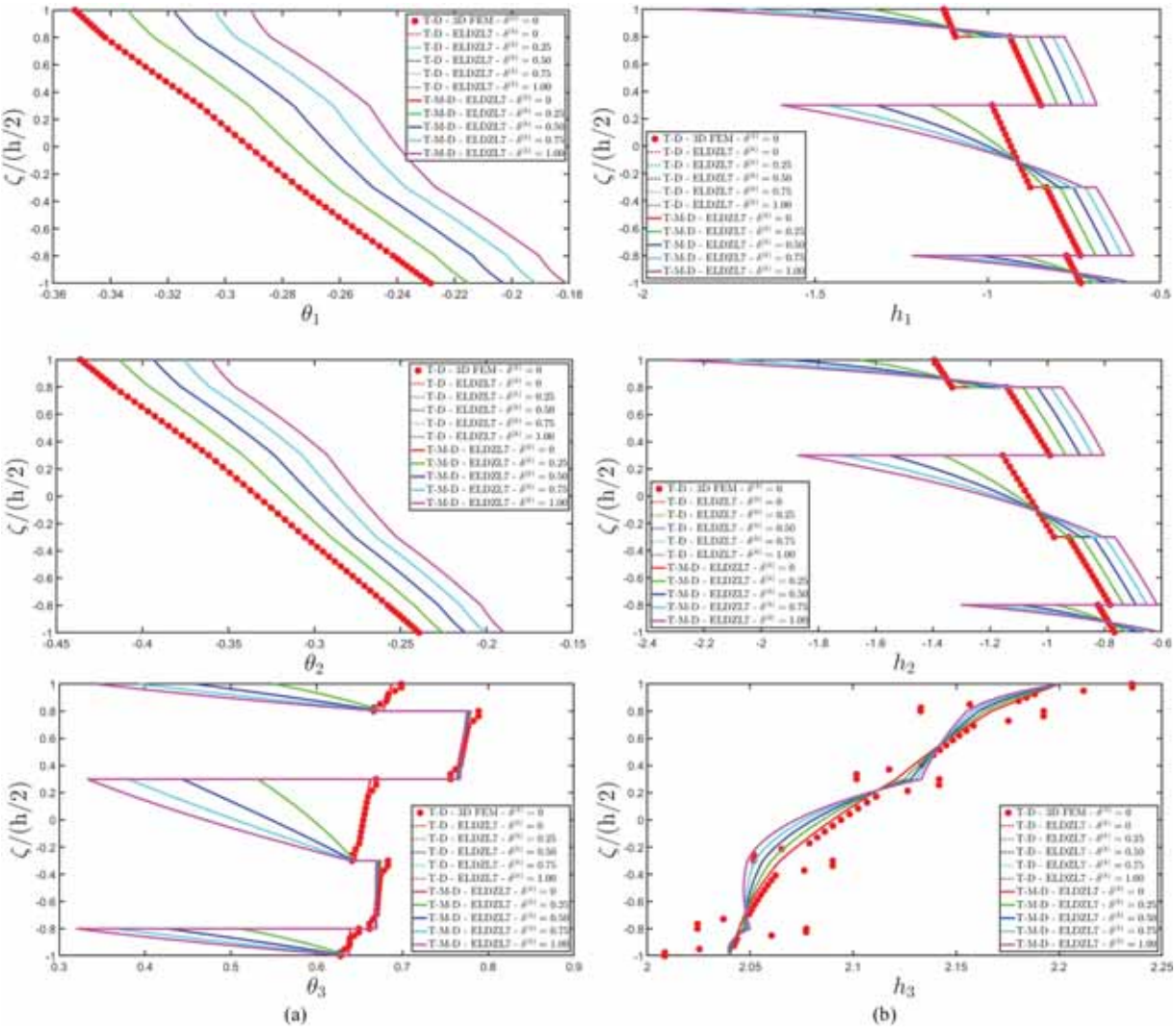

Fig. 7. Representation of the thickness profile at $(0.75L_1, 0.75L_2)$ of thermal primary (a) and secondary (b) variables of a laminated circular cylinder under thermal, magnetic, and mechanical loads with sinusoidal distribution with $\widetilde{N} = \widetilde{M} = 1$. The temperature gradient components are expressed in $[\mathrm{K}/\mathrm{m}]$, while the thermal flux components are expressed in $\left[\mathrm{J}/\mathrm{m}^2\right]$. Effect of the shape parameter $\delta^{(k)}$ of the material distribution.

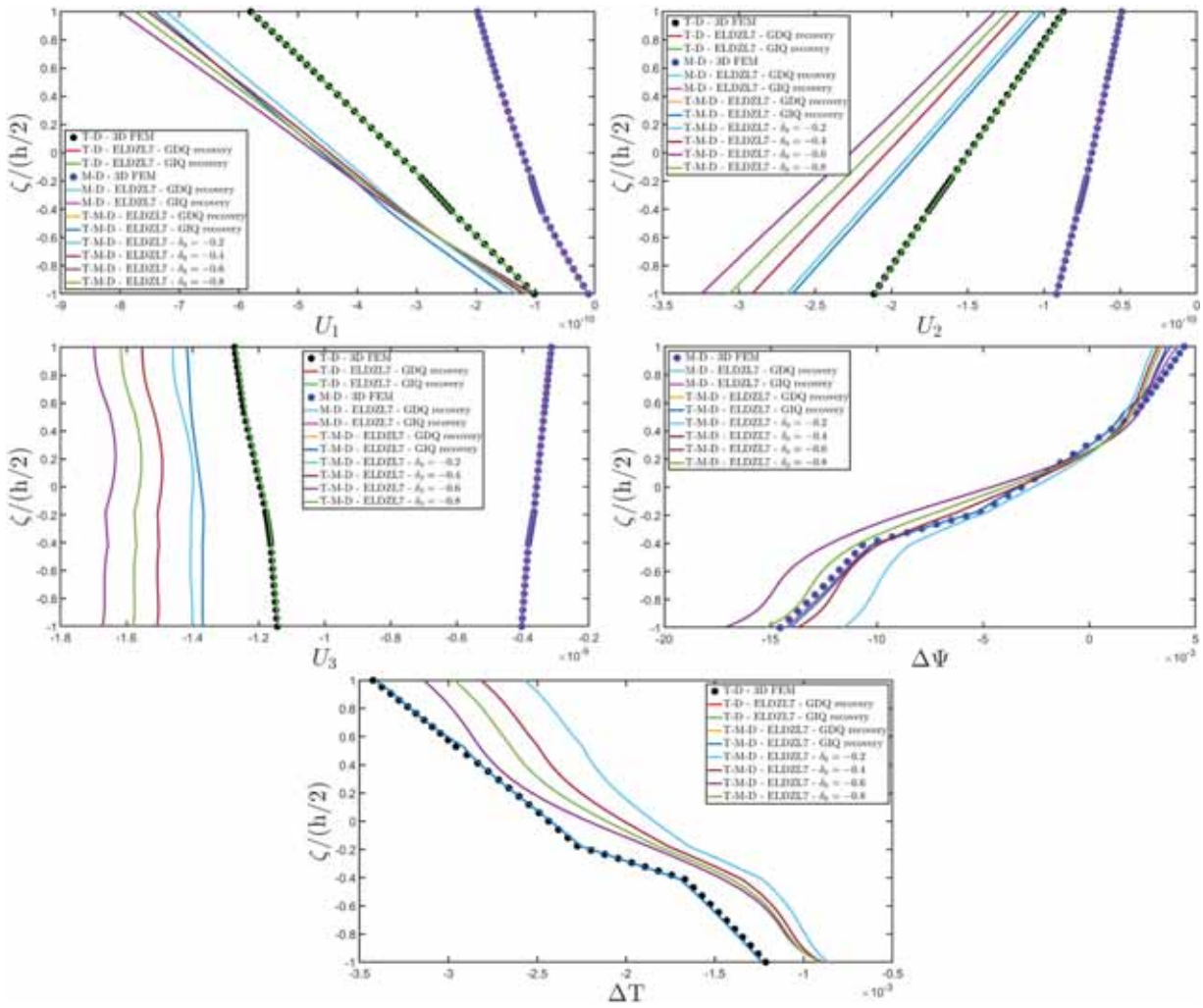

Fig. 8. Representation of the thickness profile at $(0.75L_1, 0.25L_2)$ of multifield configuration variables of a laminated circular cylinder under thermal, magnetic, and mechanical loads with uniform, hydrostatic, and inverse hydrostatic loads with $\bar{N} = \bar{M} = 150$. The displacement field components U_1,U_2,U_3 are expressed in [m], while the magnetic potential $\Delta\Psi$ with respect to the reference configuration is expressed in [A]. The absolute temperature variation ΔT is expressed in [K]. Effect of the position parameter δ_0 of the material distribution.

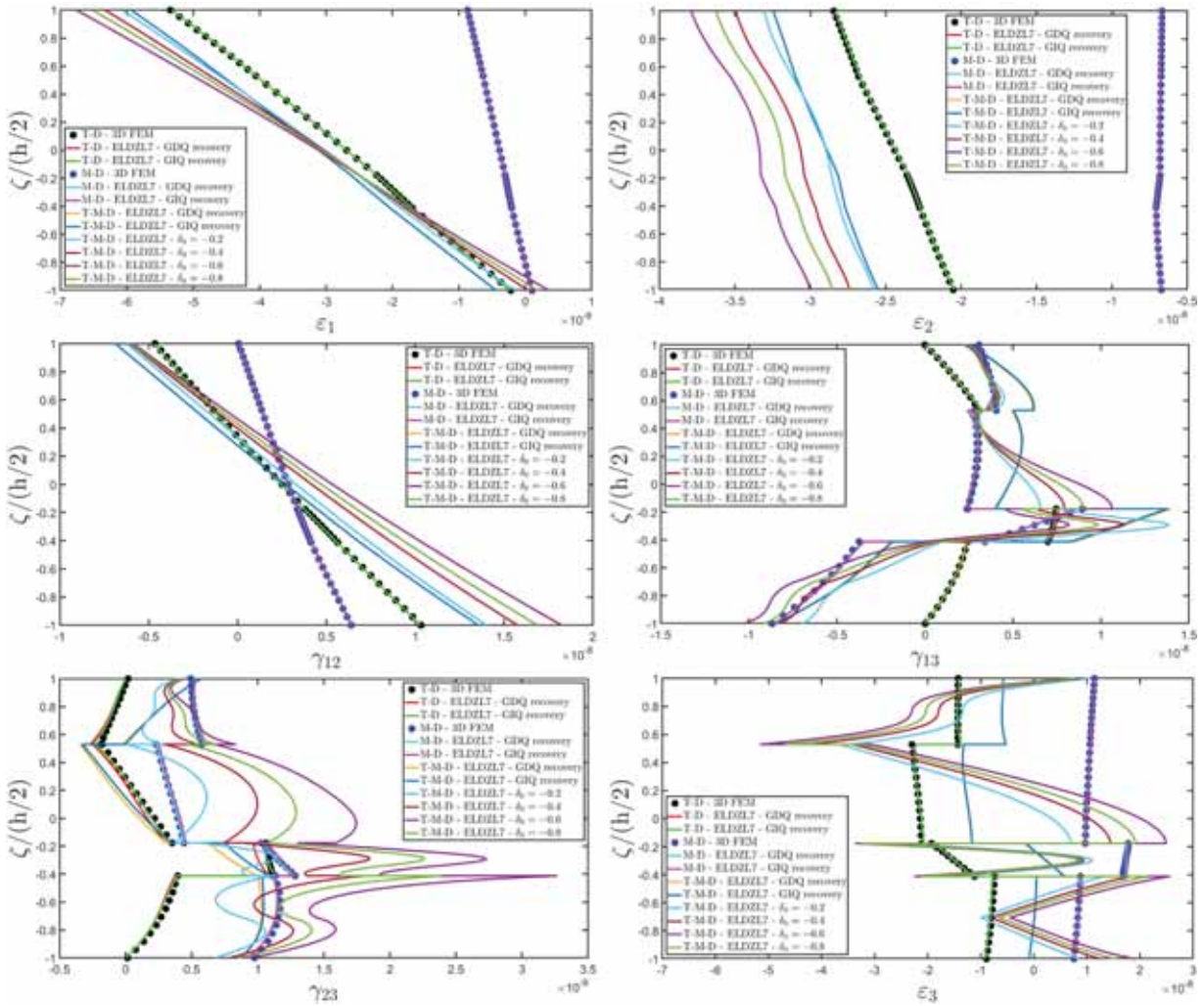

Fig. 9. Representation of the thickness profile at $(0.75L_1, 0.25L_2)$ of mechanical primary variables of a laminated circular cylinder under thermal, magnetic, and mechanical loads with uniform, hydrostatic, and inverse hydrostatic loads with $\widetilde{N} = \widetilde{M} = 150$. The three-dimensional strain components are expressed in [m /m]. Effect of the position parameter δ_0 of the material distribution.

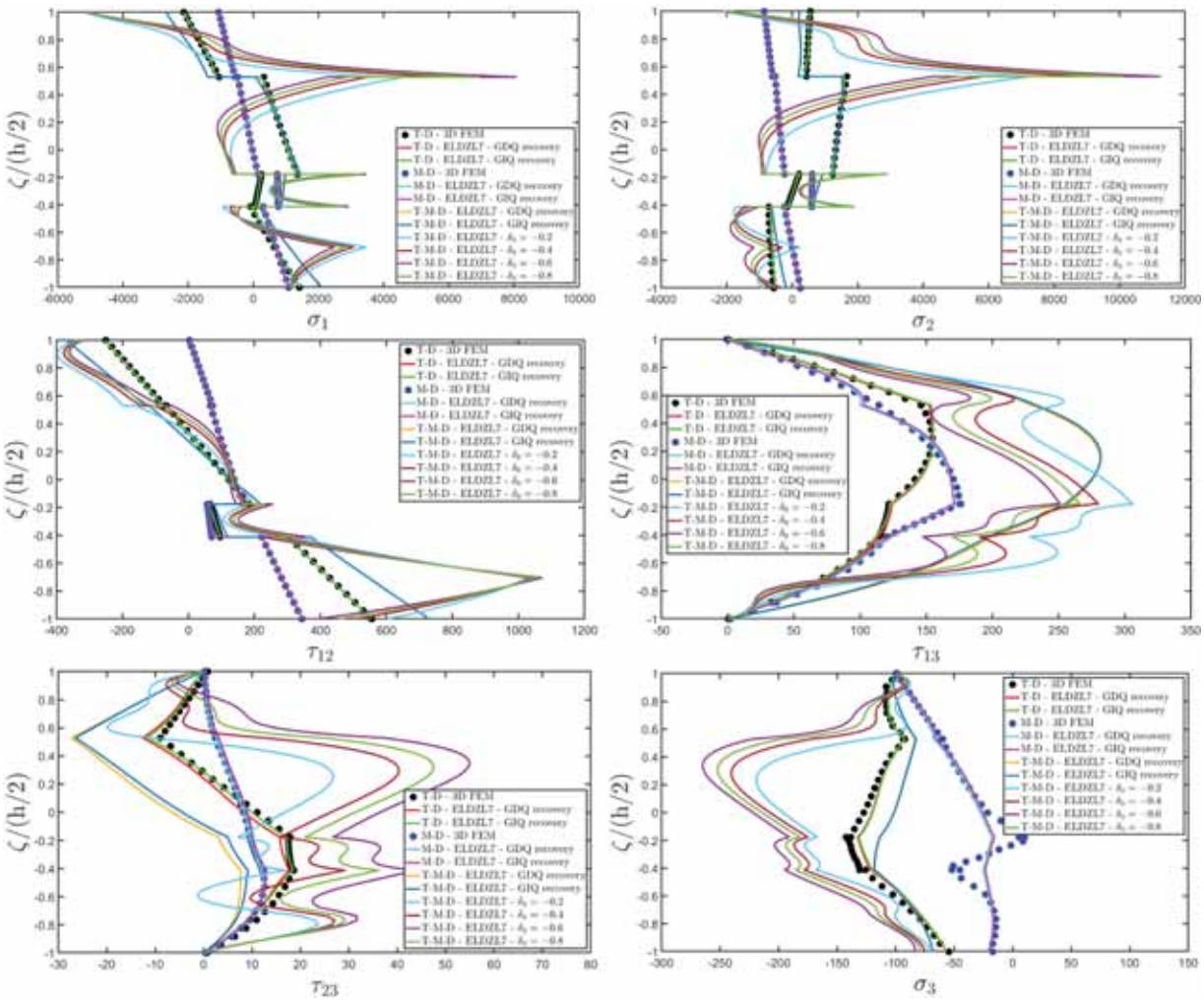

Fig. 10. Representation of the thickness profile at$(0.75L_1, 0.25L_2)$ of mechanical secondary variables of a laminated circular cylinder under thermal, magnetic, and mechanical loads with uniform, hydrostatic, and inverse hydrostatic loads with $\tilde{N} = \tilde{M} = 150$. The three-dimensional stress components are expressed in $\left[\mathrm{N/m^2}\right]$. Effect of the position parameter δ_0 of the material distribution.

between adjacent layers results in a piecewise uniform distribution of ε_3, while in plane strains ε_1,ε_2 remain linear. Based on T-D and M-D simulations, an excellent agreement is observed between the ELW results and 3D FEM predictions. Similar curves are obtained using the GDQ-based and GIQ-based recovery procedures. For this reason, parametric investigation in the T-M-D multifield simulation is performed using the novel GIQ-based procedure. It is worth noting that when the material properties are varied within each layer at the interlaminar stage, some jumps of primary and secondary variables occur between adjacent layers due to the abrupt variations in the volume fraction of the constituents. Furthermore, as the position parameter decreases, the structure exhibits additional strains due to the reduced stiffness of the laminate. Conversely, higher $\delta_0^{(k)}$ values lead to a decrease in the three-dimensional stress components, as illustrated in Fig. 10. Here, it is shown that the in-plane normal stresses exhibit peaks at each interface within the laminate, when variations in the material properties are introduced. Furthermore, a stress increment is noted in the middle of the first lamina, because the L-I variation accounts for a symmetric linear distribution. Conversely, the zigzag profile of the out-of-plane stress components is smoothed when fully coupling between thermal and magnetic field is considered in the model. Abrupt slope variations in the profile are observed at each interface upon introducing material variations within each lamina. Above all, it can be seen that the increase in $\delta_0^{(k)}$ leads to a shift in the stress profile. These stresses are then adjusted at the top and bottom surface through the recovery procedure to match the loading conditions of the shell. However, it should be noted that the loading conditions at the bottom surface depend on the displacement field component due to the presence of the elastic foundation. Consequently, stress variation is more evident at the middle thickness of the laminated curved panel.

In Fig. 11, the magnetic field components, along with the magnetic flux components derived from M-D and T-M-D simulations, are presented. The in-plane magnetic fields, evaluated as the gradient of the scalar magnetic potential, exhibit a typical zigzag profile. In contrast, the out-of-plane magnetic field shows a stepwise linear distribution. For the in-plane flux components, the piecewise linear curves are obtained, while a linear distribution is observed for the out-of-plane flux under external magnetic loads. Also, for the magnetic secondary variables, the recovery procedure based on GIQ provides an excellent match against the reference solution obtained from the 3D FEM model. The introduction of material properties variations within the model affects significantly the distribution of magnetic primary and secondary variables. On the other hand, the sensitivity of the magnetic field is more sensitive than the magnetic flux to a varying parameter $\delta_0^{(k)}$, especially in the out-of-plane direction. Conversely, the thermal primary and secondary variables are affected significantly by the position parameter $\delta_0^{(k)}$, as illustrated in Fig. 12. Here, a successful comparison with 3D FEM predictions is observed for coupled T-D simulations, employing either GDQ-

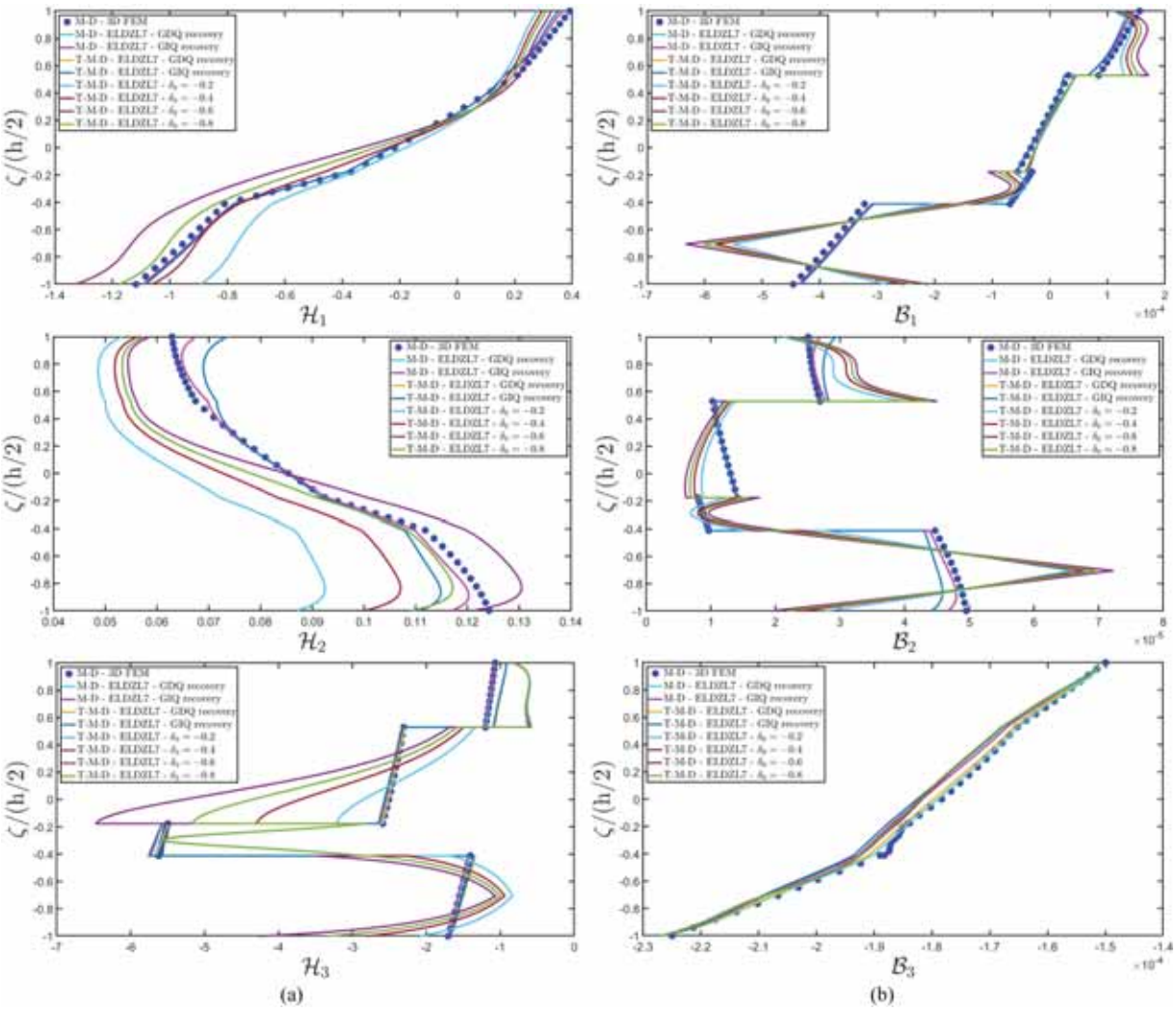

Fig. 11. Representation of the thickness profile at $(0.75L_1, 0.25L_2)$ of magnetic primary (a) and secondary (b) variables of a laminated circular cylinder under thermal, magnetic, and mechanical loads with sinusoidal distribution with $\widetilde{N} = \widetilde{M} = 150$. The magnetic field components are expressed in $[\mathrm{A/m}]$, while the magnetic flux components are expressed in $\left[\mathrm{Wb/m^2}\right]$. Effect of the position parameter δ_0 of the material distribution.

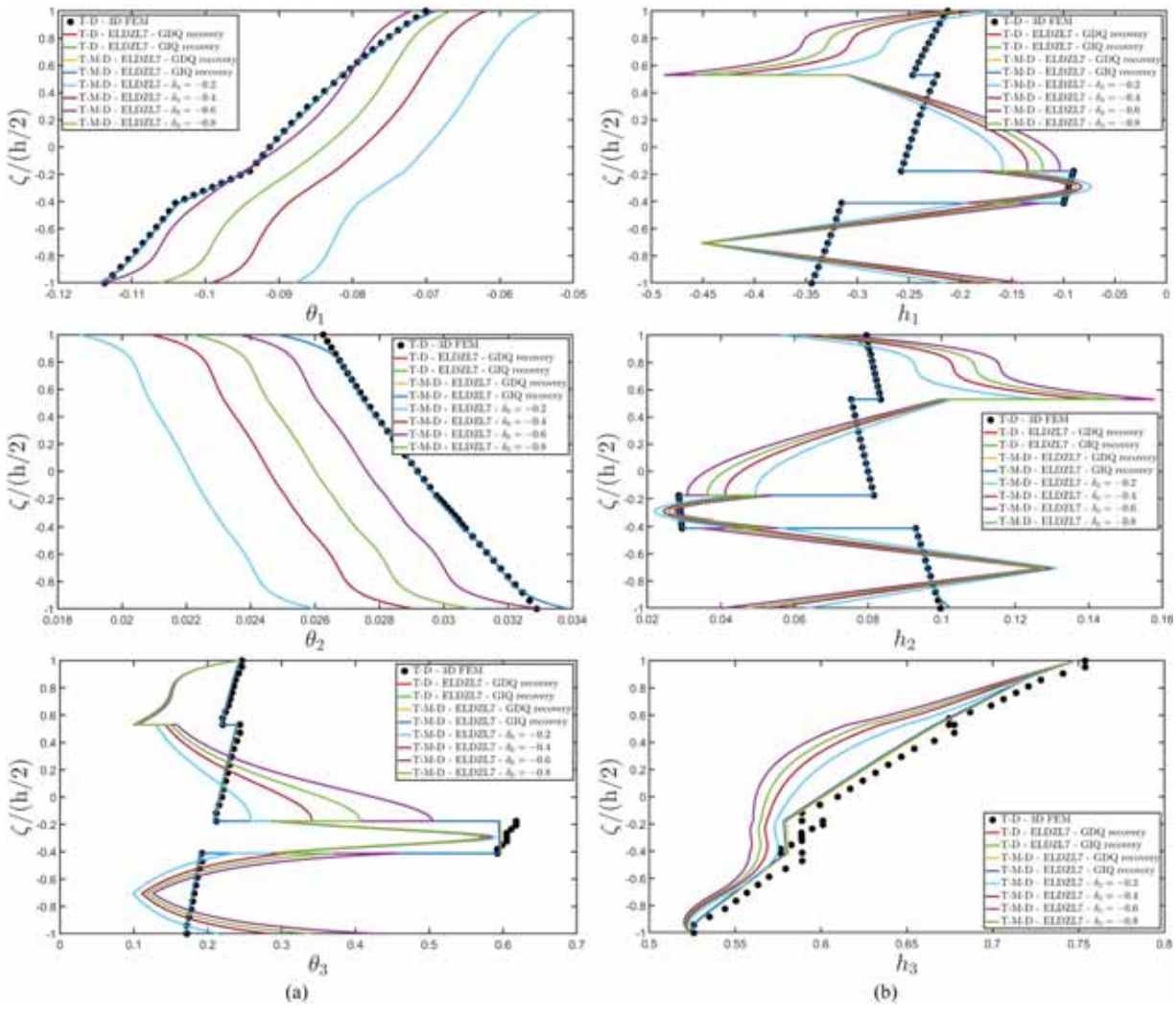

Fig. 12. Representation of the thickness profile at $(0.75L_1, 0.25L_2)$ of thermal primary (a) and secondary (b) variables of a laminated circular cylinder under thermal, magnetic, and mechanical loads with sinusoidal distribution with $\widetilde{N} = \widetilde{M} = 150$. The temperature gradient components are expressed in $[\mathrm{K/m}]$, while the magnetic flux components are expressed in $\left[\mathrm{J/m^2}\right]$. Effect of the position parameter δ_0 of the material distribution.

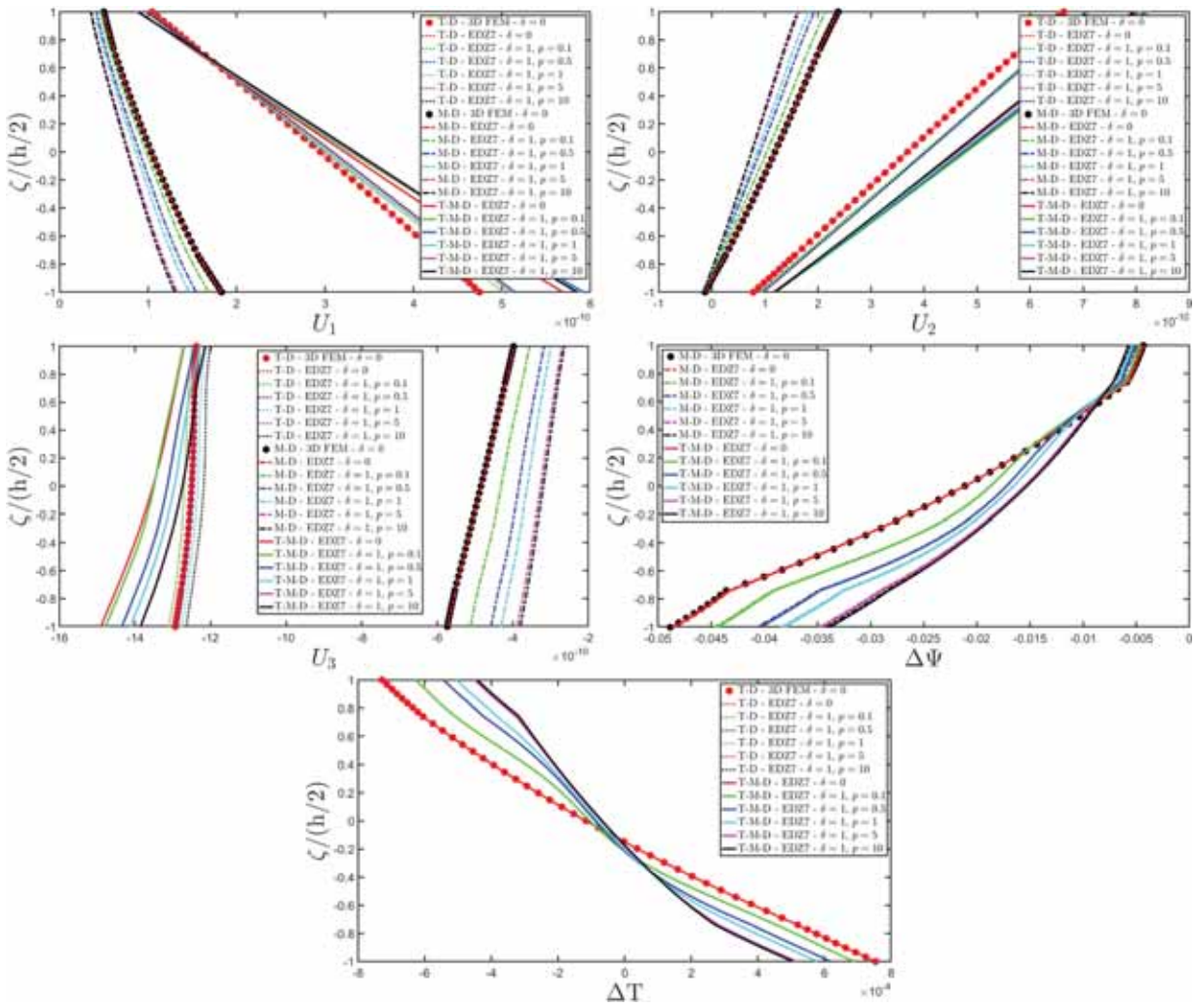

Fig. 13. Representation of the thickness profile at $(0.75L_1, 0.25L_2)$ of multifield configuration variables of a laminated circular cylinder under thermal, magnetic, and mechanical loads with butterfly, hydrostatic, and inverse hydrostatic loads with $\widetilde{N} = \widetilde{M} = 150$. The displacement field components U_1,U_2,U_3 are expressed in [m], while the magnetic potential $\Delta\Psi$ with respect to the reference configuration is expressed in [A]. The absolute temperature variation ΔT is expressed in [K]. Effect of the power coefficient p of the material distribution.

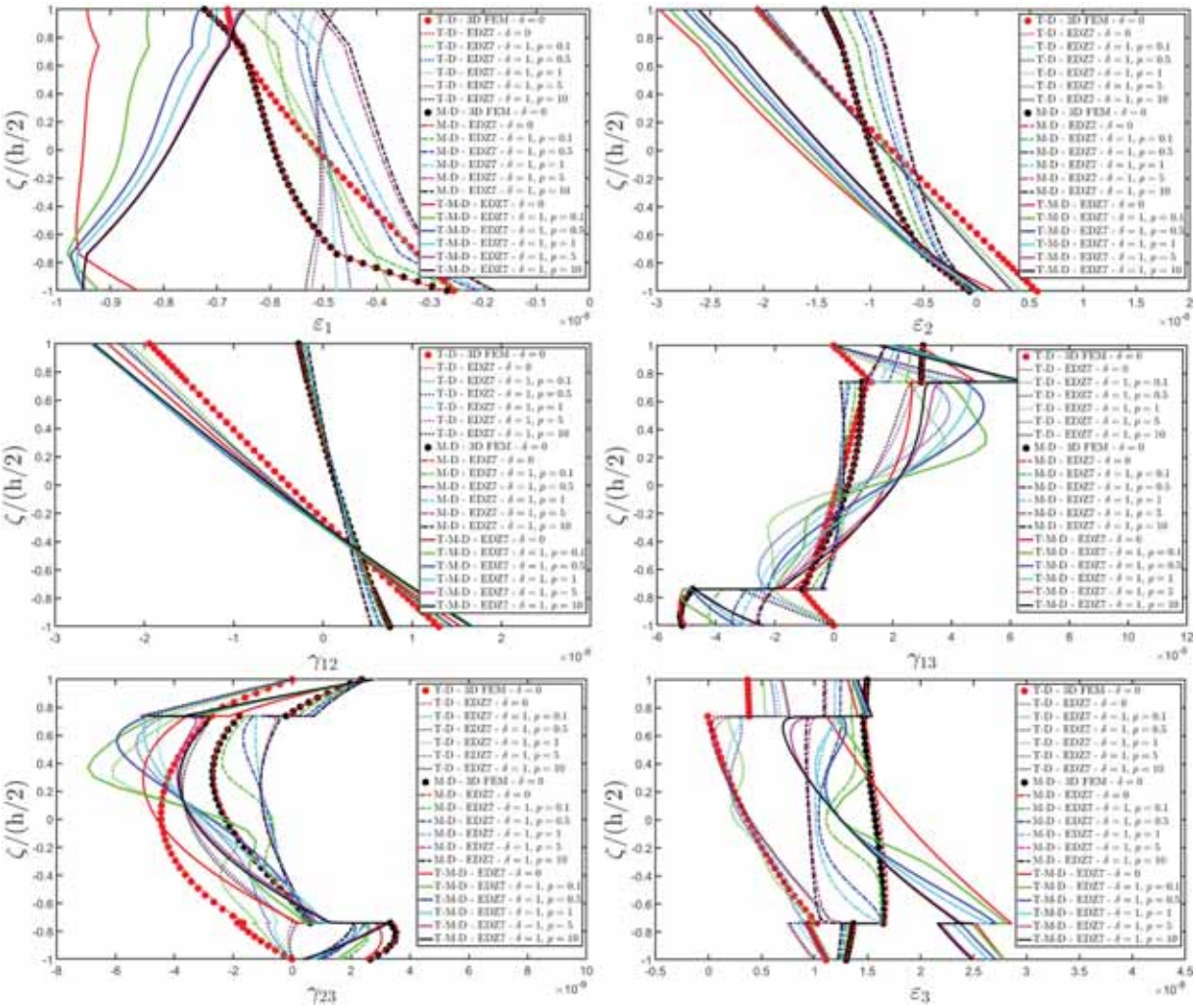

Fig. 14. Representation of the thickness profile at $(0.75L_1, 0.25L_2)$ of mechanical primary variables of a laminated circular cylinder under thermal, magnetic, and mechanical loads with butterfly, hydrostatic, and inverse hydrostatic loads with $\widetilde{N} = \widetilde{M} = 150$. The three-dimensional strain components are expressed in [m /m]. Effect of the power coefficient p of the material distribution.

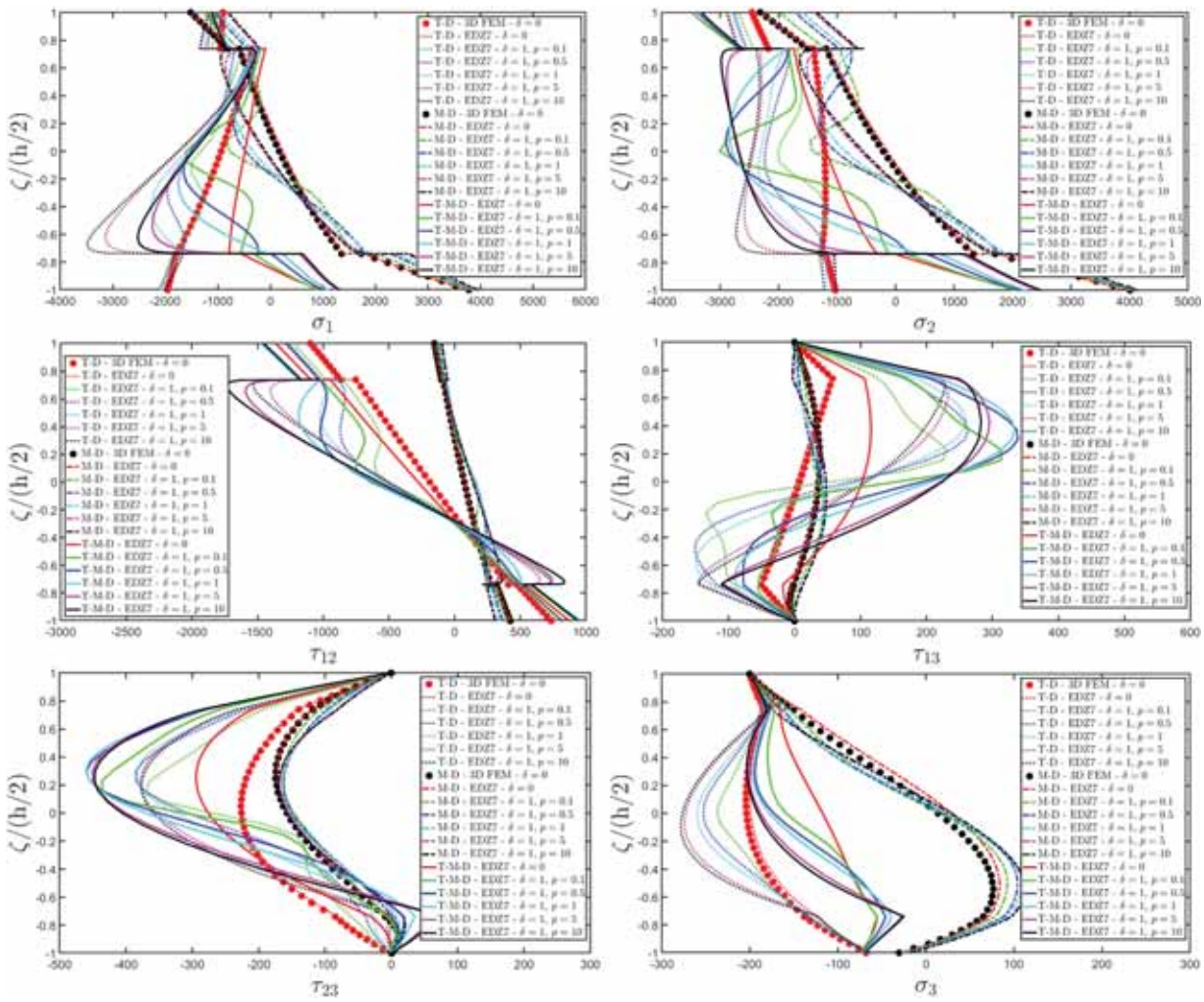

Fig. 15. Representation of the thickness profile at $(0.75L_1, 0.25L_2)$ of mechanical secondary variables of a laminated circular cylinder under thermal, magnetic, and mechanical loads with butterfly, hydrostatic, and inverse hydrostatic loads with $\widetilde{N} = \widetilde{M} = 150$. The three-dimensional stress components are expressed in $[\mathrm{N/m^2}]$. Effect of the power coefficient p of the material distribution.

based and GIQ-based recovery procedures. Furthermore, a material variation plays a crucial role in reducing the zigzag effect between adjacent layers, even though peak values are still evident for in-plane thermal flux components. The variability in the out-of-plane temperature gradient θ_3 distribution against $\delta_0^{(k)}$ is observed in the first and the third laminae, while a consistent profile is maintained within the second and fourth layers. On the other hand, a significant variation of h_3 thermal flux is observed in the third lamina.

The final numerical example focusing on a circular cylinder highlights the variation in the thermo-magneto-mechanical behavior of a three-layer laminated panel. This example considers an arbitrary variation in the material properties within a central thick layer, using an analytical function with a variable power index. The reference surface of the structure is described by the following relation [28]:

$$\mathbf{r}(\varphi, y) = R_1 \frac{\tan\varphi}{\sqrt{1+\tan^2\varphi}}\mathbf{e}_1 - y\mathbf{e}_2 + R_1\left(1 - \frac{1}{\sqrt{1+\tan^2\varphi}}\right)\mathbf{e}_3 \tag{124}$$

The rectangular parametric domain for Eq. (124) is defined as $[\varphi_0,\varphi_1] \times [0, L_2]$, with $\varphi_0 = -\pi/2$, $\varphi_1 = \pi/6$ and $L_2 = 7.0 \times 10^{-2}$m. The radius of the cylinder is $R_1 = R = 4.5 \times 10^{-2}$m, while the thickness of the two external layer is $h_1 = h_3 = 1.5 \times 10^{-3}$m. The lamination scheme consists of two external laminae of cobalt ferrite, with a central core composed of TME-III, as detailed in Table 1. Furthermore, an SC-II variation in the material properties in considered for this central layer, with the values $\delta_0^{(k)} = 0$ and $\delta^{(k)} = 1$ assigned to the position and scaling parameters of the distribution, respectively. The multifield response of the panel is analyzed for different values of the power index p. The material orientation within each layer follows the geometric reference system, therefore the value $\vartheta_k = 0$ with $k = 1, 2, 3$ is assigned to the material orientation angle. A Winkler-type elastic foundation is modelled at the bottom surface, characterized by a uniform distribution of linear elastic springs with stiffness $k_{3f}^{(-)} = 5 \times 10^{10}\,\mathrm{N/m^3}$. The multifield response of the cylinder is evaluated under mechanical, thermal, and magnetic loads. More specifically, a mechanical pressure with magnitude $\overline{q}_3^{(+)} = 1.0 \times 10^2\,\mathrm{N/m^2}$ is applied to the top surface. The surface distribution of this load follows a generalized linear relationship, dependent on the curvilinear coordinate s_2 along α_2 parametric lines, as expressed below:

$$\widetilde{q}_\alpha^{(-)}(s_1, s_2) = 1 - \widetilde{\omega}\frac{s_2}{L_2} \tag{125}$$

for $\widetilde{\omega} = 4$. In this configuration, the structure experiences a surface traction on a part of the top surface, while the remaining portion is subjected to a compressive load. Thermal and magnetic flux loads applied at the bottom of the laminate are characterized by an inverse hydrostatic distribution along α_2 principal direction, with magnitudes $\overline{q}_\mathrm{B}^{(-)} = -9.0 \times 10^{-4}\,\mathrm{Wb/m^2}$ and $\overline{q}_\mathrm{T}^{(-)} = 7.0 \times 10^{-1}\,\mathrm{J/m^2}$. In this context,

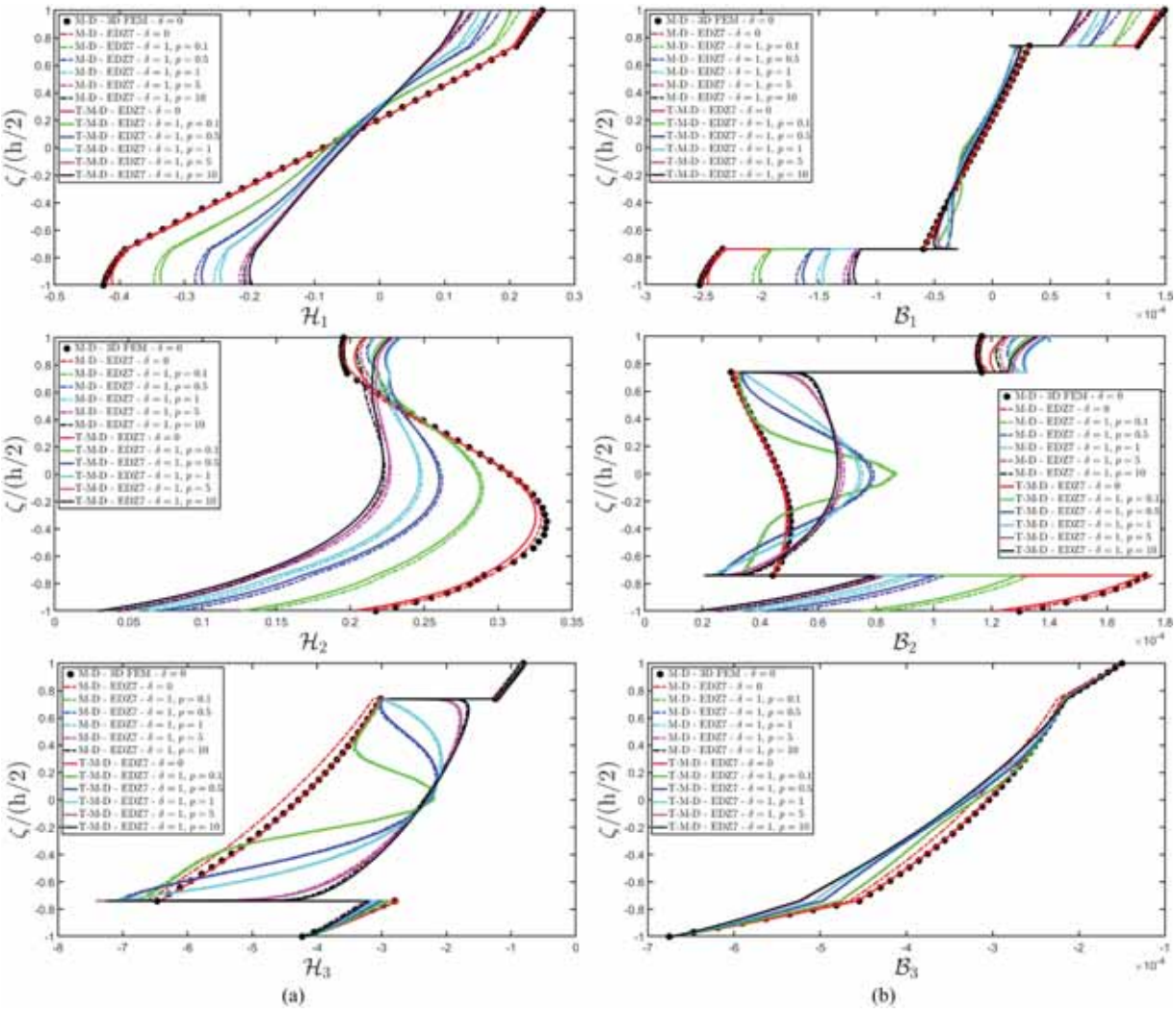

Fig. 16. Representation of the thickness profile at $(0.75L_1, 0.25L_2)$ of magnetic primary (a) and secondary (b) variables of a laminated circular cylinder under thermal, magnetic, and mechanical loads butterfly, hydrostatic, and inverse hydrostatic distributions with $\widetilde{N} = \widetilde{M} = 150$. The magnetic field components are expressed in $[\mathrm{A/m}]$, while the magnetic flux components are expressed in $\left[\mathrm{Wb/m^2}\right]$. Effect of the power coefficient p of the material distribution.

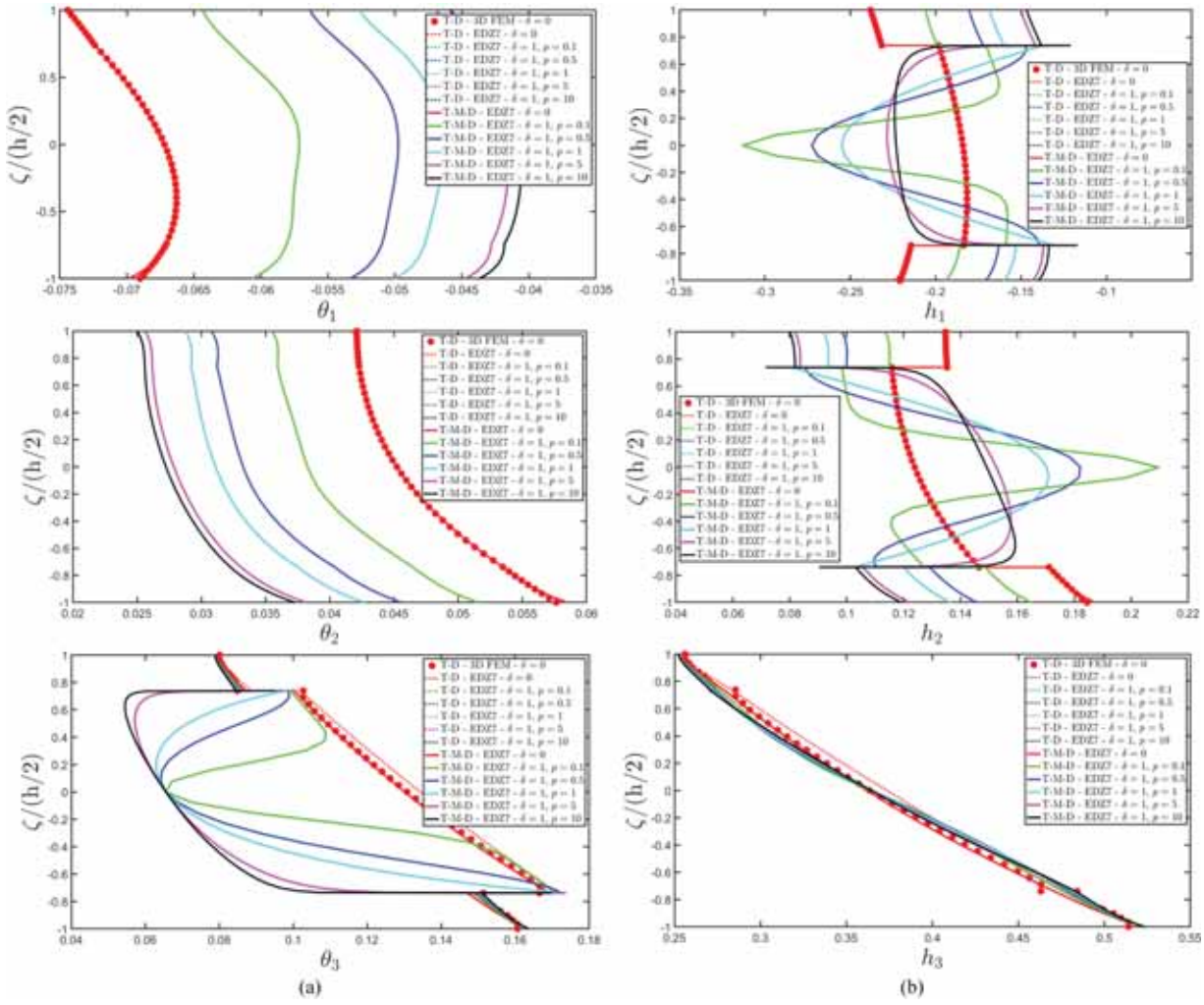

Fig. 17. Representation of the thickness profile at $(0.75L_1, 0.25L_2)$ of thermal primary (a) and secondary (b) variables of a laminated circular cylinder under thermal, magnetic, and mechanical loads butterfly, hydrostatic, and inverse hydrostatic distributions with $\widetilde{N} = \widetilde{M} = 150$. The temperature gradient components are expressed in $[\mathrm{K/m}]$, while the thermal flux components are expressed in $\left[\mathrm{J/m^2}\right]$. Effect of the power coefficient p of the material distribution.

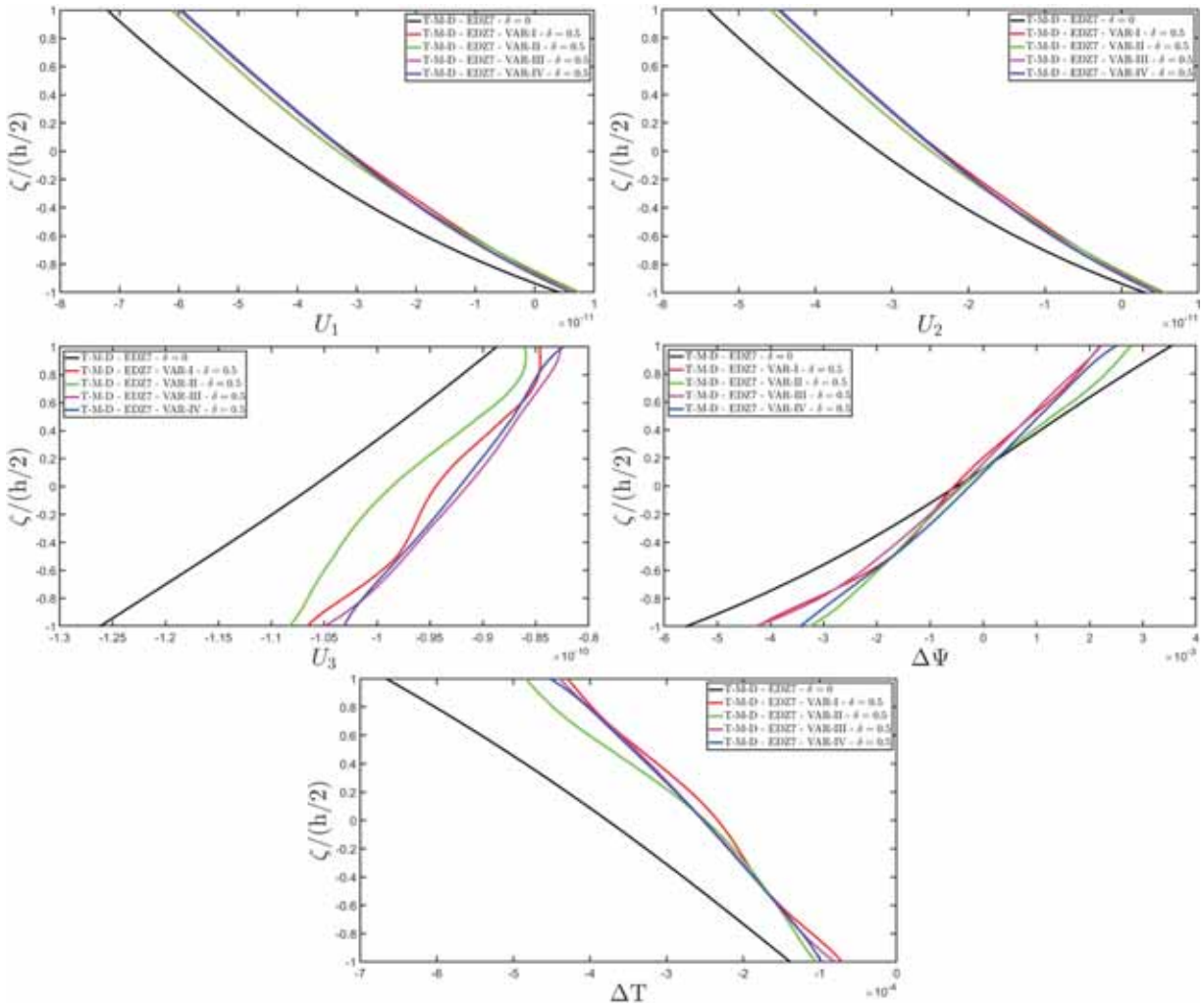

Fig. 18. Representation of the thickness profile at $(0.75L_1, 0.75L_2)$ of multifield configuration variables of a laminated spherical shell under thermal, magnetic, and mechanical loads with sinusoidal distribution. The displacement field components U_1,U_2,U_3 are expressed in [m], while the magnetic potential $\Delta\Psi$ with respect to the reference configuration is expressed in [A]. The absolute temperature variation ΔT is expressed in [K]. The material variations within each layer are modelled by assuming $\delta^{(k)} = 0.5$.

the quantity $\widetilde{q}_{\alpha}^{(-)} = \widetilde{q}_{\mathrm{B}}^{(-)}, \widetilde{q}_{\mathrm{T}}^{(-)}$ is expressed as in Eq. (125) with $\widetilde{\omega} = 1$. The semi-analytical coefficients $Q_{\alpha unm}^{(\pm)}$ and $Q_{\alpha h2nm}^{(\pm)}$ for the harmonic expansion of Eq. (125) are evaluated for an arbitrary $n = 1, ..., \widetilde{N}$ and $m = 1, ..., \widetilde{N}$, as $Q_{\alpha nm}^{(\pm)} = Q_{\alpha unm}^{(\pm)} - \widetilde{\omega} Q_{\alpha h2nm}^{(\pm)}$, as follows [33]:

$$
\begin{aligned}
Q_{\alpha unm}^{(\pm)} &= \frac{4\overline{q}_{\alpha}^{(\pm)}}{\pi^2 nm}(1-\cos(n\pi))(1-\cos(m\pi)) \\
Q_{\alpha h2nm}^{(\pm)} &= -\frac{4\overline{q}_{\alpha}^{(\pm)}}{\pi^2 nm}(1-\cos(n\pi))\cos(m\pi)
\end{aligned}
\tag{126}
$$

Referring to the top surface of the laminate, thermal and magnetic loads with magnitudes $\overline{q}_{\mathrm{T}}^{(-)} = 1.0\,\mathrm{J/m^2}$ and $\overline{q}_{\mathrm{B}}^{(+)} = -6.0 \times 10^{-4}\,\mathrm{Wb/m^2}$ follow the two-dimensional distribution outlined in Eq. (122). The numerical investigations are conducted by setting $\widetilde{N} = \widetilde{M} = 150$, and the through-the-thickness distributions of configuration, primary, and secondary variables are reported for the point located at $(0.75L_1, 0.25L_2)$ within the rectangular parametric domain in Figs. 13-17. The model is successfully validated by comparing the results with those from a 3D FEM model with 106352 parabolic brick elements and 448983 nodes employing C3D20T and C3D20E shape functions for T-D and M-D simulations, respectively.

As shown in Fig. 13, both-in-plane and out-of-plane displacement field components are characterized by linear distributions with a reduced zigzag effect. Similar observations can be made for the temperature variation. When the material distribution is varied by increasing the power index p in both M-D and T-M-D simulations, the profiles of these quantities exhibit a slope change at each interface. In contrast, the magnetic potential shows zigzag distributions in both M-D and T-M-D simulations for homogeneous layers. However, a smoother profile is obtained in the case of a non-homogeneous central core as the value of the quantity p increases. The three-dimensional strain components, illustrated in Fig. 14, exhibit different distributions based on the coupling between physical problems. More specifically, the profile of the ε_1 strain component is uniform in coupled T-M-D simulations when a uniform core is used, while a more general distribution is observed when a variation is assigned to the constituent material. In the case of ε_2, a linear profile is obtained for T-D simulation, whereas a zigzag distribution occurs for the M-D case. In the coupled T-M-D problem, the structure exhibits a linear distribution of ε_2. It is worth noting that the central core shows higher variability in the three-dimensional strains compared to the two outer layers. The difference in layer thickness results in significant deviations from uncoupled simulations, aligning well with the 3D FEM reference solution. Similar considerations apply to Fig. 15, which presents the three-dimensional stress components. The GIQ-based recovery procedure provides an efficient reconstruction of the out-of-plane quantities for T-D and M-D simulations. More

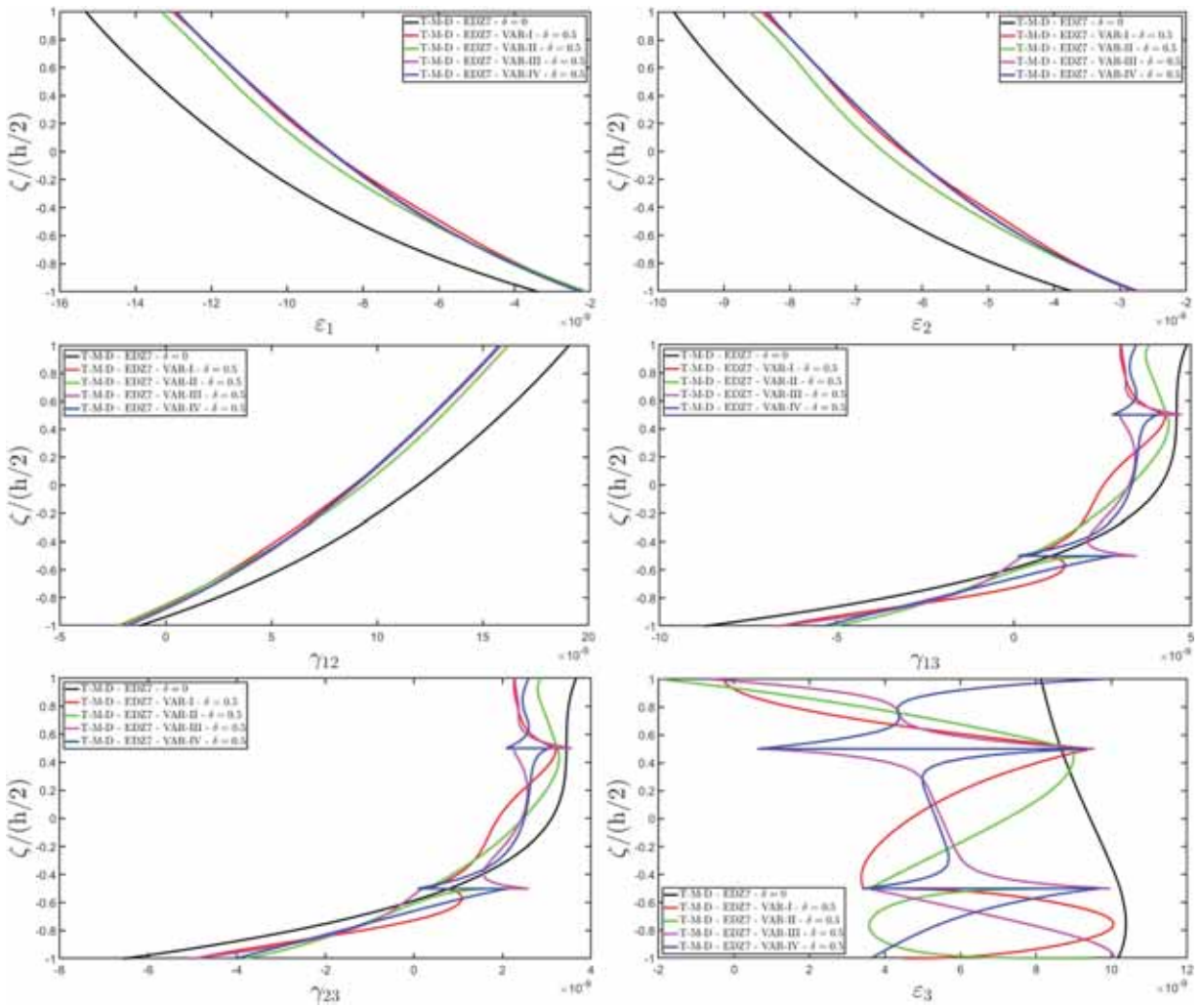

Fig. 19. Representation of the thickness profile at $(0.75L_1, 0.75L_2)$ of mechanical primary variables of a laminated spherical shell under thermal, magnetic, and mechanical loads with sinusoidal distribution. The three-dimensional strain components are expressed in [m/m]. The material variations within each layer are modelled by assuming $\delta^{(k)} = 0.5$.

specifically, since the U_3 displacement field component from T-M-D simulation is similar to that from the T-D case, the value assumed at the bottom surface for σ_3 is similar in these cases. A high variability in the in-plane stress components is observed, even for the external laminae. Out-of-plane shear stresses exhibit different through-the-thickness distributions depending on the value of parameter p. The primary and secondary variables for the magnetic and thermal problems can be found in Figs. 16 and 17, respectively. In particular, the magnetic field component along α_1 exhibits a zigzag profile, while $\mathscr{H}_2$ is characterized by a smoother distribution. A stepwise linear profile is obtained for $\mathscr{H}_3$ magnetic field component in case of uncoupled M-D simulations. Even though the results from T-M-D simulations deviate from those of the M-D case, the overall behavior of each curve remains unaltered. On the other hand, $\mathscr{H}_3$ exhibits a curved symmetric distribution during parametric investigation, while a linear distribution is observed within the cobalt ferrite laminae. Conversely, the out-of-plane magnetic flux component $\mathscr{B}_3$ is not significantly influenced by the material properties variation of the central lamina, even though a variation in the $\mathscr{B}_1$ profile is found at the external layers. A high sensitivity is found for $\mathscr{B}_2$ within the parametric investigation across the entire lamination scheme in both M-D and T-M-D simulations. It is important to highlight that the magnetic primary and secondary variables are affected by the pyromagnetic effect. The presence of a thermal field induces a variation for all components of the magnetic field. Thermal primary and secondary variables do not show any sensitivity to the magnetic field, because the formulation is based on the thermodynamic equilibrium conditions. As a consequence, identical distributions of temperature gradient and thermal flux components are found for both T-D and T-M-D cases. As indicated in Fig. 17, the results for uniform layers in the T-D case align with those from the finite element analysis. Furthermore, variations in the power index p within the central core result in a shift of θ_1 and θ_2 curves. On the other hand, the θ_3 profile is varied only within the central lamina, showing the highest variation at mid-thickness. When higher values of p are selected, a smooth profile emerges, which eventually becomes uniform within the second lamina. The out-of-plane stress components do not vary within the current parametric investigation, while a high variability for the in-plane thermal flux components is noted in both T-D and T-M-D analyses.

Last numerical investigation focuses on a structure with double curvature with $R_1 = R_2 = R = 3.2 \times 10^{-2}$m defined over the rectangular parametric domain $[\varphi_0,\varphi_1] \times [\vartheta_0,\vartheta_1]$ with $\varphi_0 = 5\pi/6$, $\varphi_1 = 7\pi/12$ and $\vartheta_0 = -\pi/9$, $\vartheta_1 = \pi/9$. The structure consists of two external layers, each with thickness $h_1 = h_3 = 1.0 \times 10^{-3}$m, made of TME-I material, while the central TME-I layer has a thickness equal to $h_2 = 2.0 \times 10^{-3}$m. For this case, the value $\theta_k = 0$ with $k = 1, 2, 3$ is assumed for the material orientation angle. Multifield external loads with a sinusoidal distribution, following Eq. (119), are applied to the top and bottom surfaces of the panel. More specifically, a mechanical load with magnitude $\overline{q}_3^{(+)} = -1.0 \times 10^2$ N/m^2 is applied at $\zeta = h/2$, along with thermal and

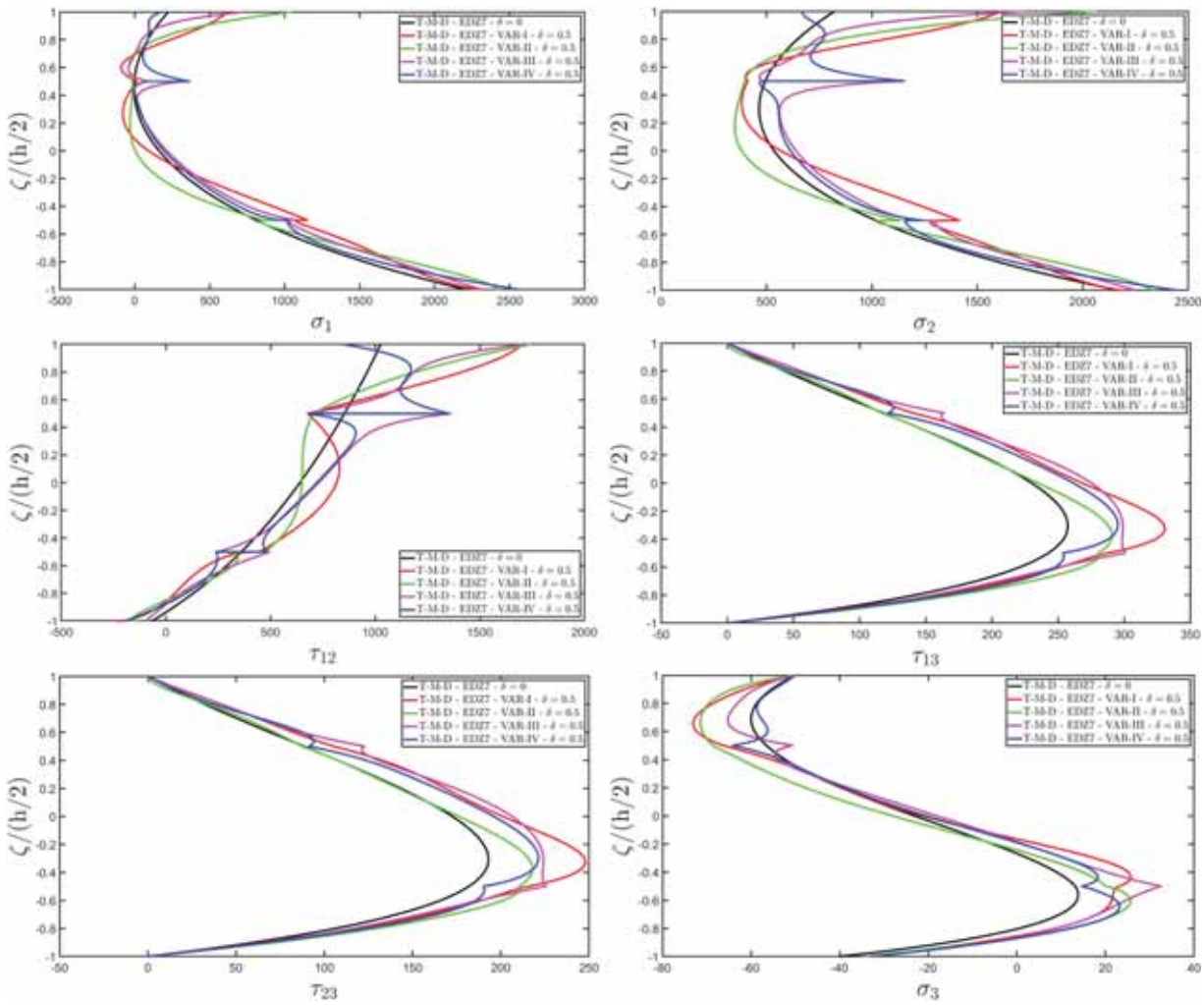

Fig. 20. Representation of the profile along the thickness direction at $(0.75L_1, 0.75L_2)$ of mechanical secondary variables of a laminated spherical shell under thermal, magnetic, and mechanical loads with sinusoidal distribution. The three-dimensional stress components are expressed in $[\mathrm{N/m^2}]$. The material variations within each layer are modelled by assuming $\delta^{(k)} = 0.5$.

magnetic fluxes with magnitudes $\overline{q}_{\mathrm{T}}^{(+)} = 1.0\,\mathrm{J/m^2}$ and $\overline{q}_{\mathrm{B}}^{(+)} = -6.0 \times 10^{-4}\,\mathrm{Wb/m^2}$, respectively. At the bottom surface, an elastic foundation is modelled according to the Winkler-Pasternak theory of Eq. (51), by setting the stiffnesses equal to $k_{3f}^{(-)} = 5 \times 10^9\,\mathrm{N/m^3}$ and $G_f^{(-)} = 5 \times 10^6\,\mathrm{N/m^2}$. In addition, a sinusoidal thermal flux with $\overline{q}_{\mathrm{T}}^{(-)} = 7.0 \times 10^{-4}\,\mathrm{J/m^2}$ and magnetic flux with a reference value $\overline{q}_{\mathrm{B}}^{(-)} = -9.0 \times 10^{-4}\,\mathrm{Wb/m^2}$ are applied at $\zeta = -h/2$. The multifield response of the shell is presented in Figs. 18-22, showing the through-the-thickness distribution, of thermal, magnetic, and mechanical variables evaluated at the point $(0.75L_1, 0.75L_2)$ within the physical domain. The analysis employs the EDZ7 higher-order theory, following the ESL approach outlined in Eq. (10). The quantities L_1, L_2 are calculated from Eq. (68). A preliminary T-M-D simulation demonstrates that the structure exhibits linear distributions of displacement field components, magnetic potential, and temperature variation along the thickness direction (Fig. 18). The multifield response of the panel is then evaluated by assuming arbitrary variations in the material properties within each layer, with $\delta_0^{(k)} = 0$ and $\delta^{(k)} = 1$. More specifically, in VAR-I simulation, the first layer uses an SC-I distribution, the second layer is characterized by UC-II variation, while UC-IV profile is adopted in the third lamina, following the nomenclature in Tab. 2. The VAR-II simulation assumes that the material varies with SC-II for $k = 1$, UC-III and EXP-I distributions are applied to the second and third layers, respectively. The VAR-III configuration considers the analytical expressions UC-I, HS-II with $p = 3$ and HT-II for the first, second, and third layer, respectively. Finally, VAR-IV accounts for EXP-II for $k = 1$, HS-II with $p = 3$ for $k = 2$, and HT-I variation for $k = 3$. Based on results, for panels with an arbitrary variation of the material properties, a shift occurs for all configuration variables, except for the magnetic potential, which exhibits a change in inclination. In addition, the out-of-plane displacement field component distribution deviates from a linear profile, which is also observed in temperature variation. In any case, any zigzag effect is observed among the configuration variables. In contrast, the out-of-plane strain components, shown in Fig. 19, exhibit a smooth distribution within each layer, with an abrupt variation in their slope at each interface between adjacent layers, depending on the specific material variation set in the simulation. Even though the in-plane strain components do not show a zigzag distribution when the material is varied along the thickness direction, the in-plane stress components deviate from their original smooth profile observed in homogeneous layers, particularly in the third lamina of the stacking sequence, as can be seen from Fig. 20. The variation in the out-of-plane shear stresses is more evident in the central lamina compared to the external layers, with the highest sensitivity of σ_3 distribution in the external layers. The highest deviations from results from a single homogeneous lamina are observed with VAR-I and VAR-II configurations. From Fig. 21, it is evident that simulations with a single lamina yield linear or parabolic smooth distributions of magnetic field

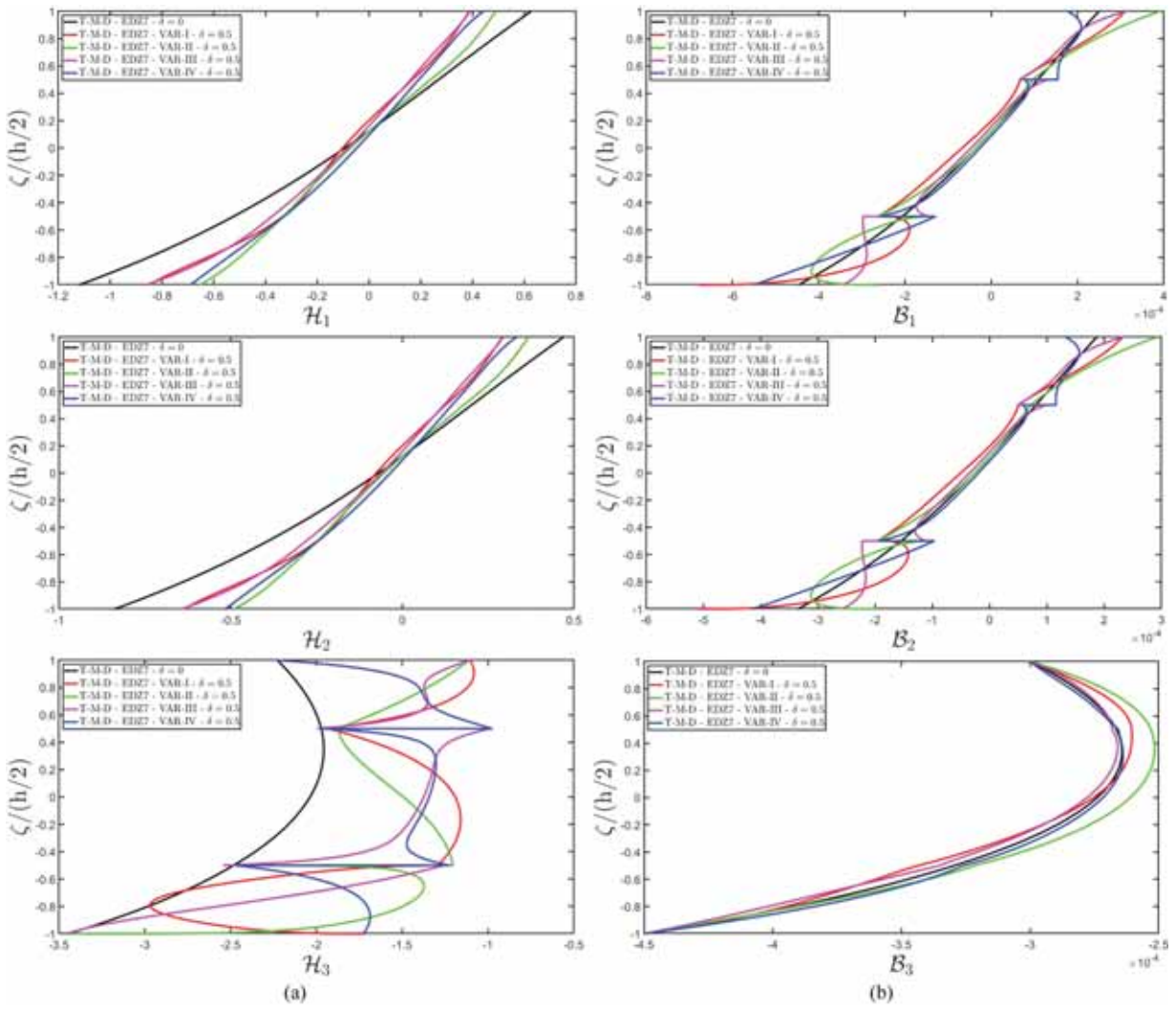

Fig. 21. Representation of the profile at $(0.75L_1, 0.75L_2)$along the thickness direction of magnetic primary (a) and secondary (b) variables of a laminated spherical shell under thermal, magnetic, and mechanical loads with sinusoidal distribution. The magnetic field components are expressed in $[\mathrm{A/m}]$, while the magnetic flux components are expressed in $\left[\mathrm{Wb/m^2}\right]$. The material variations within each layer are modelled by assuming $\delta^{(k)} = 0.5$.

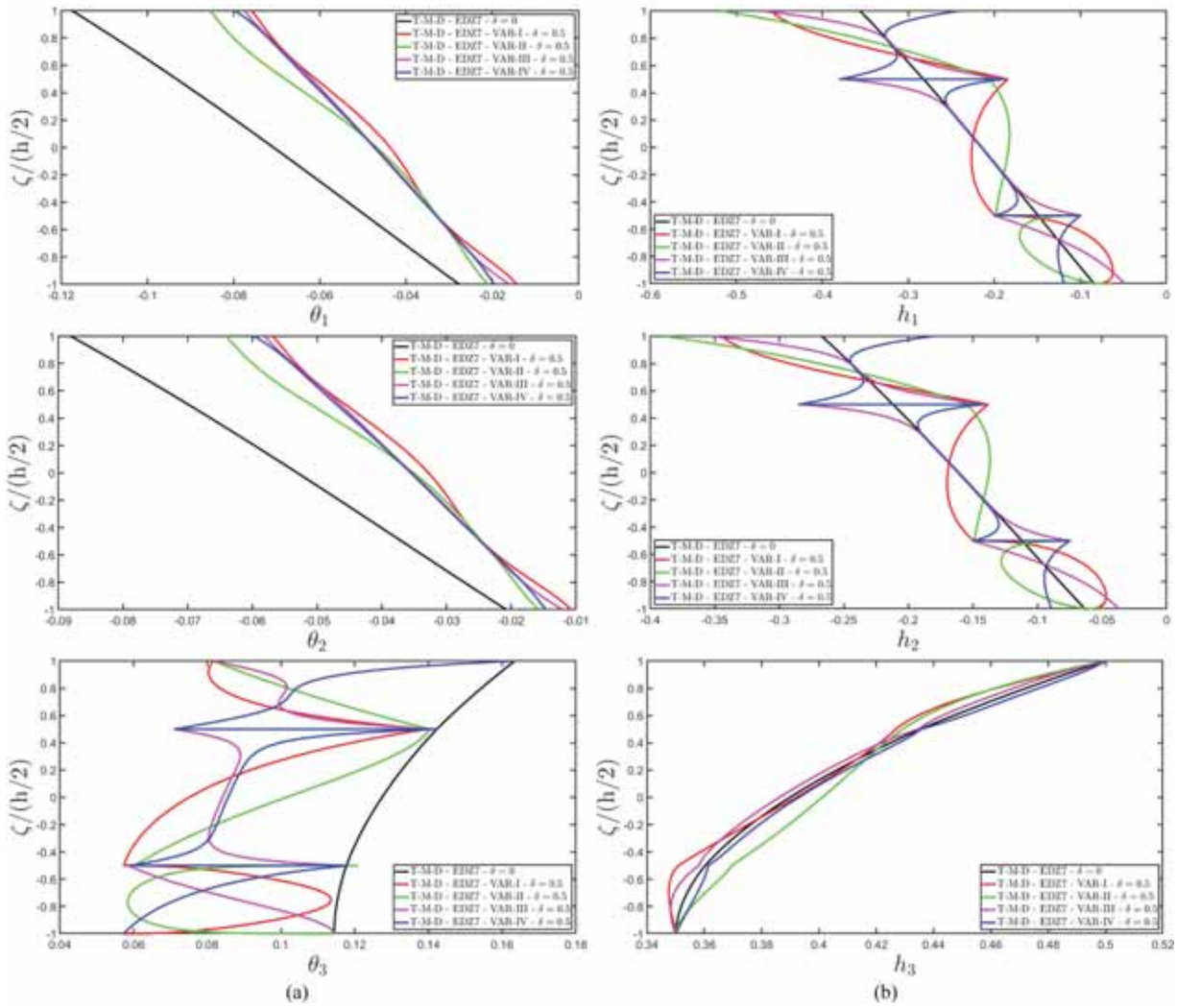

Fig. 22. Representation of the profile at $(0.75L_1, 0.75L_2)$ along the thickness direction of thermal primary (a) and secondary (b) variables of a laminated spherical shell under thermal, magnetic, and mechanical loads with sinusoidal distribution. The temperature gradient components are expressed in $[\mathrm{K}/\mathrm{m}]$, while the thermal flux components are expressed in $[\mathrm{J}/\mathrm{m}^2]$. The material variations within each layer are modelled by assuming $\delta^{(k)} = 0.5$.

and magnetic flux components along the entire thickness of the laminate. However, introducing arbitrary variations in the material properties results in smooth distributions of secondary variables within each lamina of the shell, while some zigzag effects are present at the interfacial level. In-plane magnetic field components display smooth through-the-thickness profiles. The quantity $\mathscr{K}_3$, related to the thickness direction, shows various distributions when the material properties are altered, while results for $\mathscr{B}_3$ remain similar to those observed in homogeneous layers. Similar considerations apply to temperature gradient and thermal flux components shown in Fig. 22. In the case of homogenous layers, smooth linear distributions are obtained for in-plane components, while θ_3,h_3 exhibit parabolic through-the-thickness distributions. The introduction of material variation within each k-th lamina leads to polynomial distributions for in-plane temperature gradients, with smooth distributions for θ_3 that exhibit singularities at the interfacial level. This behavior is also observed for in-plane thermal flux components, while h_3 is not significantly affected by the variation in the material properties, except for the zigzag effect occurring among consecutive layers.

6. Conclusions

A two-dimensional formulation has been developed for analyzing smart doubly-curved laminated panels subjected to thermal, magnetostatic, and mechanical multifield loads, accounting for the interactions between these physical phenomena. Following the generalized formulation approach, the model adopts higher-order thickness functions to describe the variation of unknown variables along the thickness direction. The fundamental equations, expressed in curvilinear principal coordinates and derived from the Master Balance principle, following both the ESL and ELW approaches. This allows the application of multifield surface loads, including mechanical, thermal, and magnetic loads. Furthermore, arbitrary values of displacement field, scalar magnetic potential and temperature variations are prescribed within the structure. An arbitrary variation of the material properties has been modelled along the thickness direction, taking into account both polynomial and non-polynomial distributions with symmetric, antimetric, and unsymmetric profiles. A classical Navier solution is obtained by expanding the unknown variables using harmonic functions, and a post-processing recovery procedure has been applied to determine the actual three-dimensional response of the structure. In this paper, the recovery procedure has been performed for the first time following a GIQ-based approach, which provides a high computational efficiency and accuracy. Numerical investigations demonstrate the model ability to analyze multifield problems of straight and curved laminated panels under various loading conditions, with external actions represented through

suitable expansions. In addition, the material properties are varied within each layer using different distribution profiles. The accuracy of the formulation has been checked by comparing our results with those from computationally expensive finite element models. The novel formulation presented in the paper enables new possibilities in various engineering fields for applying structures made of smart materials. In fact, thanks to this theory it is possible to investigate in a simple manner, above all, the multifield interactions in pyromagnetic materials, considering even the effects of thermal fields.

CRediT authorship contribution statement

Francesco Tornabene: Writing – review & editing, Validation, Supervision, Software, Methodology, Investigation, Formal analysis, Data curation, Conceptualization. **Matteo Viscoti:** Writing – original draft, Investigation, Data curation. **Rossana Dimitri:** Writing – review & editing, Supervision, Investigation, Formal analysis, Data curation. **Timon Rabczuk:** Writing – review & editing, Supervision, Methodology, Data curation.

Declaration of competing interest

The authors declare that they have no known competing financial interests or personal relationships that could have appeared to influence the work reported in this paper.

Appendix I

In the present section the complete expressions are reported of each element $L_{ijnm}^{(\tau\eta)\alpha_i\alpha_j}$ of the semi-analytical fundamental matrix $\mathbf{L}_{nm}^{(\tau\eta)}$ introduced in Eq. (75), for any $n = 1, ..., \widetilde{N}$ and $m = 1, ..., \widetilde{M}$. In what follows, the expressions refers to a doubly-curved laminated panel characterized by the geometric and constitutive material assumptions already outlined in Eqs. (67) and (74) according to the Navier's approach. As a consequence, the fundamental coefficients depend on the principal radii of curvature R_1,R_2. However, these expressions can be specialized for circular cylinders and rectangular plates by assuming $1/R_1 = 0$ or $1/R_2 = 0$ when straight directrix curves are present. Similar considerations are made for the semi-analytical coefficients $L_{11fnm}^{(\tau\eta)\alpha_i\alpha_j}$, $L_{22fnm}^{(\tau\eta)\alpha_i\alpha_j}$, $L_{33fnm}^{(\tau\eta)\alpha_i\alpha_j}$ associated with the additional stiffness induced by the external elastic foundation.

$$L_{11nm}^{(\tau\eta)\alpha_1\alpha_1} = -A_{11(20)}^{(\tau\eta)[00]\alpha_1\alpha_1}\left(\frac{n\pi}{L_1}\right)^2 - A_{66(02)}^{(\tau\eta)[00]\alpha_1\alpha_1}\left(\frac{m\pi}{L_2}\right)^2 - \frac{A_{44(20)}^{(\tau\eta)[00]\alpha_1\alpha_1}}{R_1^2} + \frac{A_{44(10)}^{(\tau\eta)[01]\alpha_1\alpha_1} + A_{44(10)}^{(\tau\eta)[10]\alpha_1\alpha_1}}{R_1} - A_{44(00)}^{(\tau\eta)[11]\alpha_1\alpha_1}$$

$$L_{12nm}^{(\tau\eta)\alpha_1\alpha_2} = -\left(A_{12(11)}^{(\tau\eta)[00]\alpha_1\alpha_2} + A_{66(11)}^{(\tau\eta)[00]\alpha_1\alpha_2}\right)\left(\frac{n\pi}{L_1}\right)\left(\frac{m\pi}{L_2}\right)$$

$$L_{13nm}^{(\tau\eta)\alpha_1\alpha_3} = \left(A_{13(10)}^{(\tau\eta)[01]\alpha_1\alpha_3} - A_{44(10)}^{(\tau\eta)[10]\alpha_1\alpha_3} + \frac{A_{11(20)}^{(\tau\eta)[00]\alpha_1\alpha_3} + A_{44(20)}^{(\tau\eta)[00]\alpha_1\alpha_3}}{R_1} + \frac{A_{12(11)}^{(\tau\eta)[00]\alpha_1\alpha_3}}{R_2}\right)\left(\frac{n\pi}{L_1}\right)$$

$$L_{14nm}^{(\tau\eta)\alpha_1\alpha_4} = \left(Q_{31(10)}^{(\tau\eta)[01]\alpha_1\alpha_4} - Q_{14(10)}^{(\tau\eta)[10]\alpha_1\alpha_4} + \frac{Q_{14(20)}^{(\tau\eta)[00]\alpha_1\alpha_4}}{R_1}\right)\left(\frac{n\pi}{L_1}\right)$$

$$L_{15nm}^{(\tau\eta)\alpha_1\alpha_5} = -Z_{11(10)}^{(\tau\eta)[00]\alpha_1\alpha_5}\left(\frac{n\pi}{L_1}\right)$$

$$L_{21nm}^{(\tau\eta)\alpha_2\alpha_1} = -\left(A_{12(11)}^{(\tau\eta)[00]\alpha_2\alpha_1} + A_{66(11)}^{(\tau\eta)[00]\alpha_2\alpha_1}\right)\left(\frac{n\pi}{L_1}\right)\left(\frac{m\pi}{L_2}\right)$$

$$L_{22nm}^{(\tau\eta)\alpha_2\alpha_2} = -A_{66(20)}^{(\tau\eta)[00]\alpha_2\alpha_2}\left(\frac{n\pi}{L_1}\right)^2 - A_{22(02)}^{(\tau\eta)[00]\alpha_2\alpha_2}\left(\frac{m\pi}{L_2}\right)^2 - \frac{A_{55(02)}^{(\tau\eta)[00]\alpha_2\alpha_2}}{R_2^2} + \frac{A_{55(01)}^{(\tau\eta)[01]\alpha_2\alpha_2} + A_{55(01)}^{(\tau\eta)[10]\alpha_2\alpha_2}}{R_2} - A_{55(00)}^{(\tau\eta)[11]\alpha_2\alpha_2}$$

$$L_{23nm}^{(\tau\eta)\alpha_2\alpha_3} = \left(A_{23(01)}^{(\tau\eta)[01]\alpha_2\alpha_3} - A_{55(01)}^{(\tau\eta)[10]\alpha_2\alpha_3} + \frac{A_{22(02)}^{(\tau\eta)[00]\alpha_2\alpha_3} + A_{55(02)}^{(\tau\eta)[00]\alpha_2\alpha_3}}{R_2} + \frac{A_{12(11)}^{(\tau\eta)[00]\alpha_2\alpha_3}}{R_1}\right)\left(\frac{m\pi}{L_2}\right)$$

$$L_{24nm}^{(\tau\eta)\alpha_2\alpha_4} = \left(Q_{32(01)}^{(\tau\eta)[01]\alpha_2\alpha_4} - Q_{25(01)}^{(\tau\eta)[10]\alpha_2\alpha_4} + \frac{Q_{25(02)}^{(\tau\eta)[00]\alpha_2\alpha_4}}{R_2}\right)\left(\frac{m\pi}{L_2}\right)$$

$$L_{25nm}^{(\tau\eta)\alpha_2\alpha_5} = -Z_{22(01)}^{(\tau\eta)[00]\alpha_2\alpha_5}\left(\frac{m\pi}{L_2}\right)$$

$$L_{31nm}^{(\tau\eta)\alpha_3\alpha_1} = \left(A_{13(10)}^{(\tau\eta)[10]\alpha_3\alpha_1} - A_{44(10)}^{(\tau\eta)[01]\alpha_3\alpha_1} + \frac{A_{11(20)}^{(\tau\eta)[00]\alpha_3\alpha_1} + A_{44(20)}^{(\tau\eta)[00]\alpha_3\alpha_1}}{R_1} + \frac{A_{12(11)}^{(\tau\eta)[00]\alpha_3\alpha_1}}{R_2}\right)\left(\frac{n\pi}{L_1}\right)$$

$$L_{32nm}^{(\tau\eta)\alpha_3\alpha_2} = \left(A_{23(01)}^{(\tau\eta)[10]\alpha_3\alpha_2} - A_{55(01)}^{(\tau\eta)[01]\alpha_3\alpha_2} + \frac{A_{12(11)}^{(\tau\eta)[00]\alpha_3\alpha_2}}{R_1} + \frac{A_{22(02)}^{(\tau\eta)[00]\alpha_3\alpha_2} + A_{55(02)}^{(\tau\eta)[00]\alpha_3\alpha_2}}{R_2}\right)\left(\frac{m\pi}{L_2}\right)$$

$$L_{33nm}^{(\tau\eta)\alpha_3\alpha_3} = -A_{44(20)}^{(\tau\eta)[00]\alpha_3\alpha_3}\left(\frac{n\pi}{L_1}\right)^2 - A_{55(02)}^{(\tau\eta)[00]\alpha_3\alpha_3}\left(\frac{m\pi}{L_2}\right)^2 - \frac{A_{11(20)}^{(\tau\eta)[00]\alpha_3\alpha_3}}{R_1^2} - \frac{A_{22(02)}^{(\tau\eta)[00]\alpha_3\alpha_3}}{R_2^2} - \frac{2A_{12(11)}^{(\tau\eta)[00]\alpha_3\alpha_3}}{R_1R_2} +$$

$$-\frac{A_{13(10)}^{(\tau\eta)[01]\alpha_3\alpha_3}+A_{13(10)}^{(\tau\eta)[10]\alpha_3\alpha_3}}{R_1}-\frac{A_{23(01)}^{(\tau\eta)[01]\alpha_3\alpha_3}+A_{23(01)}^{(\tau\eta)[10]\alpha_3\alpha_3}}{R_2}-A_{33(00)}^{(\tau\eta)[11]\alpha_3\alpha_3}$$

$$L_{34nm}^{(\tau s)\alpha_3\alpha_4}=-Q_{14(20)}^{(\tau\eta)[00]\alpha_3\alpha_4}\left(\frac{n\pi}{L_1}\right)^2-Q_{25(02)}^{(\tau\eta)[00]\alpha_3\alpha_4}\left(\frac{m\pi}{L_2}\right)^2-\frac{Q_{31(10)}^{(\tau\eta)[01]\alpha_3\alpha_4}}{R_1}-\frac{Q_{32(01)}^{(\tau\eta)[01]\alpha_3\alpha_4}}{R_2}-Q_{33(00)}^{(\tau\eta)[11]\alpha_3\alpha_4}$$

$$L_{35nm}^{(\tau\eta)\alpha_3\alpha_5}=\frac{Z_{11(10)}^{(\tau\eta)[00]\alpha_3\alpha_5}}{R_1}+\frac{Z_{22(01)}^{(\tau\eta)[00]\alpha_3\alpha_5}}{R_2}+Z_{33(00)}^{(\tau\eta)[10]\alpha_3\alpha_5}$$

$$L_{41nm}^{(\tau\eta)\alpha_4\alpha_1}=-\left(Q_{14(10)}^{(\tau\eta)[01]\alpha_4\alpha_1}-Q_{31(10)}^{(\tau\eta)[10]\alpha_4\alpha_1}-\frac{Q_{14(20)}^{(\tau\eta)[00]\alpha_4\alpha_1}}{R_1}\right)\left(\frac{n\pi}{L_1}\right)$$

$$L_{42nm}^{(\tau\eta)\alpha_4\alpha_2}=-\left(Q_{25(01)}^{(\tau\eta)[01]\alpha_4\alpha_2}-Q_{32(01)}^{(\tau\eta)[10]\alpha_4\alpha_2}-\frac{Q_{25(02)}^{(\tau\eta)[00]\alpha_4\alpha_2}}{R_2}\right)\left(\frac{m\pi}{L_2}\right)$$

$$L_{43nm}^{(\tau\eta)\alpha_4\alpha_3}=-Q_{14(20)}^{(\tau\eta)[00]\alpha_4\alpha_3}\left(\frac{n\pi}{L_1}\right)^2-Q_{25(02)}^{(\tau\eta)[00]\alpha_4\alpha_3}\left(\frac{m\pi}{L_2}\right)^2-\frac{Q_{31(10)}^{(\tau\eta)[10]\alpha_4\alpha_3}}{R_1}-\frac{Q_{32(01)}^{(\tau\eta)[10]\alpha_4\alpha_3}}{R_2}-Q_{33(00)}^{(\tau\eta)[11]\alpha_4\alpha_3}$$

$$L_{44nm}^{(\tau\eta)\alpha_4\alpha_4}=L_{11(20)}^{(\tau\eta)[00]\alpha_4\alpha_4}\left(\frac{n\pi}{L_1}\right)^2+L_{22(02)}^{(\tau\eta)[00]\alpha_4\alpha_4}\left(\frac{m\pi}{L_2}\right)^2+L_{33(00)}^{(\tau\eta)[11]\alpha_4\alpha_4}$$

$$L_{45nm}^{(\tau\eta)\alpha_4\alpha_5}=-W_{33(00)}^{(\tau\eta)[01]\alpha_4\alpha_5}$$

$$L_{51nm}^{(\tau\eta)\alpha_5\alpha_1}=0,\quad \widetilde{L}_{52nm}^{(\tau\eta)\alpha_5\alpha_2}=0,\quad \widetilde{L}_{53nm}^{(\tau\eta)\alpha_5\alpha_3}=0,\quad \widetilde{L}_{54nm}^{(\tau\eta)\alpha_5\alpha_4}=0$$

$$L_{55nm}^{(\tau\eta)\alpha_5\alpha_5}=K_{11(20)}^{(\tau\eta)[00]\alpha_5\alpha_5}\left(\frac{n\pi}{L_1}\right)^2+K_{22(02)}^{(\tau\eta)[00]\alpha_5\alpha_5}\left(\frac{m\pi}{L_2}\right)^2+K_{33(00)}^{(\tau\eta)[11]\alpha_5\alpha_5} \tag{A.1}$$

$$L_{11fnm}^{(\tau\eta)\alpha_1}=k_{1f}^{(-)}F_{\eta}^{(1)\alpha_1(-)}F_{\tau}^{(1)\alpha_1(-)}H_1^{(-)}H_2^{(-)}+k_{1f}^{(+)}F_{\eta}^{(l)\alpha_1(+)}F_{\tau}^{(l)\alpha_1(+)}H_1^{(+)}H_2^{(+)}$$

$$L_{22fnm}^{(\tau\eta)\alpha_2}=k_{2f}^{(-)}F_{\eta}^{(1)\alpha_2(-)}F_{\tau}^{(1)\alpha_2(-)}H_1^{(-)}H_2^{(-)}+k_{2f}^{(+)}F_{\eta}^{(l)\alpha_2(+)}F_{\tau}^{(l)\alpha_2(+)}H_1^{(+)}H_2^{(+)}$$

$$\begin{aligned}L_{33fnm}^{(\tau\eta)\alpha_3}=&\left(k_{3f}^{(-)}+G_f^{(-)}\left(\frac{1}{\left(H_1^{(-)}\right)^2}\left(\frac{n\pi}{L_1}\right)^2+\frac{1}{\left(H_2^{(-)}\right)^2}\left(\frac{m\pi}{L_2}\right)^2\right)\right)F_{\eta}^{(1)\alpha_3(-)}F_{\tau}^{(1)\alpha_3(-)}H_1^{(-)}H_2^{(-)}+\\&+\left(k_{3f}^{(+)}+G_f^{(+)}\left(\frac{1}{\left(H_1^{(+)}\right)^2}\left(\frac{n\pi}{L_1}\right)^2+\frac{1}{\left(H_2^{(+)}\right)^2}\left(\frac{m\pi}{L_2}\right)^2\right)\right)F_{\eta}^{(l)\alpha_3(+)}F_{\tau}^{(l)\alpha_3(+)}H_1^{(+)}H_2^{(+)}\end{aligned} \tag{A.2}$$

Appendix II

In this section, a smart material is homogenized with proper analytical expressions, as derived in Ref. [85]. The homogenization procedure is based on the Mori-Tanaka approach, and it is based on the computation of the Eshelby tensor for a cylindrical fiber (f) oriented along the thickness direction and immersed in an isotropic matrix (m). The corresponding volume fractions are denoted by V_f and V_m, respectively. These volume fractions are defined so that $V_m + V_f = 1$, namely it is assumed that no voids are present. The following constitutive relationship is considered for each phase of the unit cell:

$$
\begin{bmatrix}
\hat{\sigma}_1\\ \hat{\sigma}_2\\ \hat{\tau}_{12}\\ \hat{\tau}_{13}\\ \hat{\tau}_{23}\\ \hat{\sigma}_3\\ \hat{\mathrm{D}}_1\\ \hat{\mathrm{D}}_2\\ \hat{\mathrm{D}}_3\\ \hat{\mathrm{B}}_1\\ \hat{\mathrm{B}}_2\\ \hat{\mathrm{B}}_3\\ \eta\\ \mu\\ \hat{h}_1\\ \hat{h}_2\\ \hat{h}_3\\ \hat{c}_1\\ \hat{c}_2\\ \hat{c}_3
\end{bmatrix}
=
\left[\begin{array}{cccccc|ccc|ccc|ccc|ccc}
C_{11} & C_{12} & 0 & 0 & 0 & C_{13} & 0 & 0 & -p_{31} & 0 & 0 & -q_{31} & -z_{11} & -e_{11} & 0 & 0 & 0 & 0 & 0 & 0\\
C_{12} & C_{22} & 0 & 0 & 0 & C_{23} & 0 & 0 & -p_{32} & 0 & 0 & -q_{32} & -z_{22} & -e_{22} & 0 & 0 & 0 & 0 & 0 & 0\\
0 & 0 & \overline{C}_{66} & 0 & 0 & 0 & 0 & 0 & 0 & 0 & 0 & 0 & 0 & 0 & 0 & 0 & 0 & 0 & 0 & 0\\
0 & 0 & 0 & C_{44} & 0 & 0 & -p_{14} & 0 & 0 & -q_{14} & 0 & 0 & 0 & 0 & 0 & 0 & 0 & 0 & 0 & 0\\
0 & 0 & 0 & 0 & C_{55} & 0 & 0 & -p_{25} & 0 & 0 & -q_{25} & 0 & 0 & 0 & 0 & 0 & 0 & 0 & 0 & 0\\
C_{13} & C_{23} & 0 & 0 & 0 & C_{33} & 0 & 0 & -p_{33} & 0 & 0 & -q_{33} & -z_{33} & -e_{33} & 0 & 0 & 0 & 0 & 0 & 0\\
\hline
0 & 0 & 0 & p_{14} & 0 & 0 & l_{11} & 0 & 0 & d_{11} & 0 & 0 & 0 & 0 & 0 & 0 & 0 & 0 & 0 & 0\\
0 & 0 & 0 & 0 & p_{25} & 0 & 0 & l_{22} & 0 & 0 & d_{22} & 0 & 0 & 0 & 0 & 0 & 0 & 0 & 0 & 0\\
p_{31} & p_{32} & 0 & 0 & 0 & p_{33} & 0 & 0 & l_{33} & 0 & 0 & d_{33} & o_{33} & g_{33} & 0 & 0 & 0 & 0 & 0 & 0\\
\hline
0 & 0 & 0 & q_{14} & 0 & 0 & d_{11} & 0 & 0 & m_{11} & 0 & 0 & 0 & 0 & 0 & 0 & 0 & 0 & 0 & 0\\
0 & 0 & 0 & 0 & q_{25} & 0 & 0 & d_{22} & 0 & 0 & m_{22} & 0 & 0 & 0 & 0 & 0 & 0 & 0 & 0 & 0\\
q_{31} & q_{32} & 0 & 0 & 0 & q_{33} & 0 & 0 & d_{33} & 0 & 0 & m_{33} & w_{33} & f_{33} & 0 & 0 & 0 & 0 & 0 & 0\\
\hline
z_{11} & z_{22} & 0 & 0 & 0 & z_{33} & 0 & 0 & o_{33} & 0 & 0 & w_{33} & \xi_{11} & \xi_{12} & 0 & 0 & 0 & 0 & 0 & 0\\
\hline
e_{11} & e_{22} & 0 & 0 & 0 & e_{33} & 0 & 0 & g_{33} & 0 & 0 & f_{33} & \xi_{12} & \xi_{22} & 0 & 0 & 0 & 0 & 0 & 0\\
\hline
0 & 0 & 0 & 0 & 0 & 0 & 0 & 0 & 0 & 0 & 0 & 0 & 0 & 0 & k_{11} & 0 & 0 & y_{11} & 0 & 0\\
0 & 0 & 0 & 0 & 0 & 0 & 0 & 0 & 0 & 0 & 0 & 0 & 0 & 0 & 0 & k_{22} & 0 & 0 & y_{22} & 0\\
0 & 0 & 0 & 0 & 0 & 0 & 0 & 0 & 0 & 0 & 0 & 0 & 0 & 0 & 0 & 0 & k_{33} & 0 & 0 & y_{33}\\
\hline
0 & 0 & 0 & 0 & 0 & 0 & 0 & 0 & 0 & 0 & 0 & 0 & 0 & 0 & x_{11} & 0 & 0 & s_{11} & 0 & 0\\
0 & 0 & 0 & 0 & 0 & 0 & 0 & 0 & 0 & 0 & 0 & 0 & 0 & 0 & 0 & x_{22} & 0 & 0 & s_{22} & 0\\
0 & 0 & 0 & 0 & 0 & 0 & 0 & 0 & 0 & 0 & 0 & 0 & 0 & 0 & 0 & 0 & x_{33} & 0 & 0 & s_{33}
\end{array}\right]
\begin{bmatrix}
\hat{\varepsilon}_1\\ \hat{\varepsilon}_2\\ \hat{\gamma}_{12}\\ \hat{\gamma}_{13}\\ \hat{\gamma}_{23}\\ \hat{\varepsilon}_3\\ \hat{\mathrm{E}}_1\\ \hat{\mathrm{E}}_2\\ \hat{\mathrm{E}}_3\\ \hat{\mathrm{H}}_1\\ \hat{\mathrm{H}}_2\\ \hat{\mathrm{H}}_3\\ \Delta T\\ \Delta C\\ \hat{\theta}_1\\ \hat{\theta}_2\\ \hat{\theta}_3\\ \hat{\lambda}_1\\ \hat{\lambda}_2\\ \hat{\lambda}_3
\end{bmatrix}
\tag{A.3}
$$

In the previous relation, $\widehat{\varepsilon}_1, \widehat{\varepsilon}_2, \widehat{\varepsilon}_3, \widehat{\gamma}_{12}, \widehat{\gamma}_{13}, \widehat{\gamma}_{23}$ and $\widehat{\sigma}_1, \widehat{\sigma}_2, \widehat{\sigma}_3, \widehat{\tau}_{12}, \widehat{\tau}_{13}, \widehat{\tau}_{23}$ are the stress and strain components, respectively, while $\widehat{\mathscr{E}}_1$, $\widehat{\mathscr{E}}_2$, $\widehat{\mathscr{E}}_3$, $\widehat{\mathscr{D}}_1, \widehat{\mathscr{D}}_2, \widehat{\mathscr{D}}_3$ and $\widehat{\mathscr{H}}_1, \widehat{\mathscr{H}}_2, \widehat{\mathscr{H}}_3, \widehat{\mathscr{B}}_1, \widehat{\mathscr{B}}_2, \widehat{\mathscr{B}}_3$ are the primary and secondary variables of electricity and magnetism, respectively. Furthermore, the quantities $\widehat{\theta}_1, \widehat{\theta}_2, \widehat{\theta}_3$ and $\widehat{h}_1, \widehat{h}_2, \widehat{h}_3$ are associated with thermal conduction, and $\widehat{\lambda}_1, \widehat{\lambda}_2, \widehat{\lambda}_3$ and $\widehat{c}_1, \widehat{c}_2, \widehat{c}_3$ are the variables of moisture diffusion.

Preliminary computations

$$
j = 2V_f\frac{C_{44m}l_{11m}m_{11m} + p_{14m}^2m_{11m} + l_{11m}q_{14m}^2 - 2d_{11m}p_{14m} - d_{11m}^2C_{44m}}{(ic-gb)h + (fb-ia)e + (ga-fc)d}
$$

$$
a = V_m\Big(\big(q_{14f}-q_{14m}\big)\big(l_{11m}m_{11m}-d_{11m}^2\big) - \big(d_{11f}-d_{11m}\big)\big(p_{14m}m_{11m}-d_{11m}q_{14m}\big) - \big(m_{11f}-m_{11m}\big)\big(q_{14m}l_{11m}-d_{11m}p_{14m}\big)\Big)
$$

$$
b = V_m\Big(\big(p_{14f}-p_{14m}\big)\big(l_{11m}m_{11m}-d_{11m}^2\big) - \big(d_{11f}-d_{11m}\big)\big(q_{14m}l_{11m}-d_{11m}p_{14m}\big) - \big(l_{11f}-l_{11m}\big)\big(p_{14m}m_{11m}-d_{11m}q_{14m}\big)\Big)
$$

$$
\begin{aligned}
c = {} & V_m\Big(\big(C_{44f}-C_{44m}\big)\big(l_{11m}m_{11m}-d_{11m}^2\big) + \big(p_{14f}-p_{14m}\big)\big(p_{14m}m_{11m}-d_{11m}q_{14m}\big) + \big(q_{14f}-q_{14m}\big)\big(q_{14m}l_{11m}-d_{11m}p_{14m}\big)\Big) + \\
& + \frac{j}{V_f}\big((ic-gb)h + (fb-ia)e + (ga-fc)d\big)
\end{aligned}
$$

$$
\begin{aligned}
d = {} & V_m\Big(-\big(d_{11f}-d_{11m}\big)\big(d_{11m}C_{44m}+p_{14m}q_{14m}\big) + \big(p_{14f}-p_{14m}\big)\big(p_{14m}m_{11m}-d_{11m}q_{14m}\big) + \big(l_{11f}-l_{11m}\big)\big(q_{14m}^2+C_{44m}m_{11m}\big)\Big) + \\
& + \frac{j}{V_f}\big((ic-gb)h + (fb-ia)e + (ga-fc)d\big)
\end{aligned}
$$

$$
e = V_m\Big(\big(q_{14f}-q_{14m}\big)\big(d_{11m}C_{44m}+p_{14m}q_{14m}\big) + \big(C_{44f}-C_{44m}\big)\big(p_{14m}m_{11m}-d_{11m}q_{14m}\big) - \big(p_{14f}-p_{14m}\big)\big(q_{14m}^2+C_{44m}m_{11m}\big)\Big)
$$

$$
\begin{aligned}
f = {} & V_m\Big(-\big(d_{11f}-d_{11m}\big)\big(d_{11m}C_{44m}+p_{14m}q_{14m}\big) + \big(q_{14f}-q_{14m}\big)\big(q_{14m}l_{11m}-d_{11m}p_{14m}\big) + \big(m_{11f}-m_{11m}\big)\big(p_{14m}^2+C_{44m}l_{11m}\big)\Big) + \\
& + \frac{j}{V_f}\big((ic-gb)h + (fb-ia)e + (ga-fc)d\big)
\end{aligned}
$$

$$
g = V_m\Big(\big(p_{14f}-p_{14m}\big)\big(d_{11m}C_{44m}+p_{14m}q_{14m}\big) + \big(C_{44f}-C_{44m}\big)\big(q_{14m}l_{11m}-d_{11m}p_{14m}\big) - \big(q_{14f}-q_{14m}\big)\big(p_{14m}^2+C_{44m}l_{11m}\big)\Big)
$$

$$
h = V_m\Big(-\big(m_{11f}-m_{11m}\big)\big(d_{11m}C_{44m}-p_{14m}q_{14m}\big) + \big(q_{14f}-q_{14m}\big)\big(p_{14m}m_{11m}-d_{11m}q_{14m}\big) + \big(d_{11f}-d_{11m}\big)\big(q_{14m}^2+C_{44m}m_{11m}\big)\Big)
$$

$$
i = V_m\Big(-\big(l_{11f}-l_{11m}\big)\big(d_{11m}C_{44m}+p_{14m}q_{14m}\big) + \big(p_{14f}-p_{14m}\big)\big(q_{14m}l_{11m}-d_{11m}p_{14m}\big) + \big(d_{11f}-d_{11m}\big)\big(p_{14m}^2+C_{44m}l_{11m}\big)\Big) \tag{A.4}
$$

Density

$$
\rho = V_m\rho_m + V_f\rho_f \tag{A.5}
$$

Elastic stiffness coefficients

$$k = \frac{k_m k_f + V_f m_m k_f + V_m m_m k_m}{V_m k_f + V_f k_m + m_m}$$

$$m = \frac{m_m\left(k_m m_f + V_f k_m m_f + V_m k_m m_m + 2 m_m m_f\right)}{V_m k_m m_f + k_m m_m + V_f k_m m_m + 2 V_m m_m m_f + 2 V_f m_m^2}$$

$$C_{11} = C_{22} = k + m$$

$$C_{12} = k - m$$

$$C_{13} = C_{23} = C_{13m} + \frac{V_f\left(C_{13f} - C_{13m}\right)\left(k_m + m_m\right)}{V_m k_f + V_f k_m + m_m}$$

$$C_{33} = C_{33m} + V_f\left(C_{33f} - C_{33m} - \frac{V_m\left(C_{13m} - C_{13f}\right)^2}{V_m k_f + V_f k_m + m_m}\right)$$

$$C_{44} = C_{55} = C_{44m} + j\Big(\Big(p_{14f} - p_{14m}\Big)(fe - gh) + \left(C_{44f} - C_{44m}\right)(ih - fd) + \Big(q_{14f} - q_{14m}\Big)(gd - ie)\Big) \tag{A.6}$$

Piezomagnetic coefficients

$$q_{31} = q_{32} = q_{31m} + \frac{V_f\Big(q_{31f} - q_{31m}\Big)\left(k_m + m_m\right)}{V_m k_f + V_f k_m + m_m}$$

$$q_{33} = q_{33m} + V_f\left(q_{33f} - q_{33m} + \frac{V_m\left(C_{13m} - C_{13f}\right)\Big(q_{31f} - q_{31m}\Big)}{V_m k_f + V_f k_m + m_m}\right)$$

$$q_{14} = q_{25} = q_{14m} + j\Big(\Big(p_{14f} - p_{14m}\Big)(ch - ae) + \left(C_{44f} - C_{44m}\right)(ad - bh) + \Big(q_{14f} - q_{14m}\Big)(be - cd)\Big) \tag{A.7}$$

Magnetic permeability coefficients

$$m_{11} = m_{22} = m_{11m} + j\Big(\left(d_{11f} - d_{11m}\right)(ch - ae) + \Big(q_{14f} - q_{14m}\Big)(bh - ad) + \left(m_{11f} - m_{11m}\right)(be - cd)\Big)$$

$$m_{33} = m_{33m} + V_f\left(m_{33f} - m_{33m} + \frac{V_m\left(m_{31f} - m_{31m}\right)^2}{V_m k_f + V_f k_m + m_m}\right) \tag{A.8}$$

Thermal expansion coefficients

$$a_{11} = \frac{V_f E_f a_f + V_m E_m a_m}{E_1}$$

$$a_{22} = a_{33} = \left(1 + \nu_f\right) a_f V_f + \left(1 + \nu_m\right) a_m V_m - \nu_{12} a_{11} \tag{A.9}$$

Pyromagnetic coefficient

$$w_{33} = V_m w_{33m} + V_f w_{33f} - V_m V_f \frac{\Big(q_{31f} - q_{31m}\Big)\left(z_{11f} - z_{11m}\right)}{C_{11m} + V_m k_f - V_m k_m} \tag{A.10}$$

Specific heat capacity

$$c_p = \frac{V_f \rho_f c_{pf} + V_m \rho_m c_{pm}}{\rho} \tag{A.11}$$

Thermal conductivity

$$k_{11} = k_{22} = \frac{k_m k_f}{V_f k_m + V_m k_f}$$

$$k_{33} = V_m k_m + V_f k_f = \left(1 - V_f\right) k_m + V_f k_f = \left(k_f - k_m\right) V_f + k_m \tag{A.12}$$

Data availability

No data was used for the research described in the article.

References

[1] Fattah-alhosseini A, et al. A review of smart polymeric materials: Recent developments and prospects for medicine applications. Hybrid Adv 2024:100178.
[2] Narita F, Fox M. A review on piezoelectric, magnetostrictive, and magnetoelectric materials and device technologies for energy harvesting applications. Adv Eng Mater 2018;20:1700743.
[3] Han M, et al. Three-dimensional piezoelectric polymer microsystems for vibrational energy harvesting, robotic interfaces and biomedical implants. Nat Electron 2019;2:26–35.
[4] Vinyas M, Kattimani SC, Joladarashi S. Hygrothermal coupling analysis of magneto-electroelastic beams using finite element methods. J Therm Stress 2018; 41:1063–79.
[5] Kapuria S, Kumari P, Nath JK. Efficient modeling of smart piezoelectric composite laminates: a review. Acta Mech 2010;214:31–48.
[6] Osaretin IA, Rojas RG. Theoretical model for the magnetoelectric effect in magnetostrictive/piezoelectric composites. Phys Rev B 2010;82:174415.
[7] Xu K, Noor AK. Three-dimensional analytical solutions for coupled thermoelectroelastic response of multilayered cylindrical shells. AIAA J 1996;34: 802–12.
[8] Biao W. Three-dimensional analysis of an ellipsoidal inclusion in a piezoelectric material. Int J Solids Struct 1992;29:293–308.
[9] Brischetto S, Torre R, Cesare D. Three dimensional coupling between elastic and thermal fields in the static analysis of multilayered composite shells. Comput Model Eng Sci 2023;136.
[10] Lerch R. Simulation of piezoelectric devices by two-and three-dimensional finite elements. IEEE Trans Ultrason Ferroelectr Freq Control 1990;37:233–47.
[11] Beldjelili Y, Tounsi A, Mahmoud SR. Hygro-thermo-mechanical bending of S-FGM plates resting on variable elastic foundations using a four-variable trigonometric plate theory. Smart Struct Syst 2016;18:755–86.
[12] Zhang JP, et al. Thermo-mechanical coupling analysis of the orthotropic structures by using element-free Galerkin method. Eng Anal Bound Elem 2019;101:198–213.
[13] Brischetto S, Torre R. 3D shell model for the thermo-mechanical analysis of FGM structures via imposed and calculated temperature profiles. Aerosp Sci Technol 2019;85:125–49.
[14] Savoia M, Reddy JN. Three-dimensional thermal analysis of laminated composite plates. Int J Solids Struct 1995;32:593–608.
[15] Sih GC, Michopoulos JG, Chou SC. Hygrothermoelasticity. Martinus Nijhoff Publishers; 1986.
[16] Tornabene F, Viscoti M, Dimitri R. Thermo-mechanical analysis of laminated doubly-curved shells: higher order equivalent layer-wise formulation. Compos Struct 2024;335:117995.
[17] Wang J, Yong YK, Imai T. Finite element analysis of the piezoelectric vibrations of quartz plate resonators with higher-order plate theory. Int J Solids Struct 1999;36: 2303–19.
[18] Wang J, Yang Y. Higher-order theories of piezoelectric plates and applications. Appl Mech Rev 2000;53:87–99.
[19] Washizu K. Variational methods in elasticity & plasticity. Oxford: Pergamon Press; 1975.
[20] Reddy JN. A generalization of two-dimensional theories of laminated composite plates. Commun Appl NumerMethods 1987;3:173–80.
[21] Altay GA, Dökmeci MC. Some comments on the higher order theories of piezoelectric, piezothermoelastic and thermopiezoelectric rods and shells. Int J Solids Struct 2003;40:4699–706.
[22] Tornabene F, Viscoti M, Dimitri R, Reddy JN. Higher order theories for the vibration study of doubly-curved anisotropic shells with a variable thickness and isogeometric mapped geometry. Compos Struct 2021;267:113829.
[23] Reddy JN, Wang CM, Lee KH. Relationships between bending solutions of classical and shear deformation beam theories. Int J Solids Struct 1997;34:3373–84.
[24] Reddy JN. Mechanics of laminated composite plates and shells: theory and analysis. Boca Raton: CRC Press; 2003.
[25] Icardi U, Sola F. Assessment of recent zig-zag theories for laminated and sandwich structures. Composites Part B 2016;97:26–52.
[26] Murakami H. Laminated composite plate theory with improved in-plane responses. ASME JAppl Mech 1986;53:661–6.
[27] Abrate S, Di Sciuva M. Equivalent single layer theories for composite and sandwich structures: a review. Compos Struct 2017;179:482–94.
[28] Tornabene F. Hygro-thermo-magneto-electro-elastic theory of anisotropic doubly-curved shells. Bologna: Esculapio; 2023.
[29] Milazzo A. Layer-wise and equivalent single layer models for smart multilayered plates. Composites Part B 2014;67:62–75.
[30] Liew KM, Pan ZZ, Zhang LW. An overview of layerwise theories for composite laminates and structures: development, numerical implementation and application. Compos Struct 2019;216:240–59.
[31] Li D. Layerwise theories of laminated composite structures and their applications: a review. Arch Comput Methods Eng 2021;28:577–600.
[32] Robbins DH, Reddy JN. Analysis of piezoelectrically actuated beams using a layer-wise displacement theory. Comput Struct 1991;41:265–79.
[33] Tornabene F, Viscoti M, Dimitri R. Equivalent Layer-Wise theory for the hygro-thermo-magneto-electro-elastic analysis of laminated curved shells. Thin-Walled Struct 2024;198:111751.
[34] F. Tornabene, M. Viscoti, R. Dimitri, Hygro-thermo-mechanical equivalent layer-wise theory of laminated shell structures. Under Review, (2024).
[35] Tornabene F, Fantuzzi N, Bacciocchi M, Reddy JN. An equivalent layer-wise approach for the free vibration analysis of thick and thin laminated and sandwich shells. Appl Sci 2016;7:17.
[36] Zienkiewicz OC, Taylor RL. The finite element method: solid mechanics (Vol. 2). New York: McGraw-Hill; 1967.
[37] Reddy JN. Introduction to the finite element method. New York: McGraw-Hill Education; 2019.
[38] Ha KH. Finite element analysis of sandwich plates: an overview. Comput Struct 1990;37:397–403.
[39] Tornabene F, Viscoti M, Dimitri R. Equivalent single layer higher order theory based on a weak formulation for the dynamic analysis of anisotropic doubly-curved shells with arbitrary geometry and variable thickness. Thin-Walled Struct 2022; 174:109119.
[40] Khater AH, Temsah RS, Hassan M. A Chebyshev spectral collocation method for solving Burgers'-type equations. J Comput Appl Math 2008;222:333–50.
[41] Hussaini MY, Kopriva DA, Patera AT. Spectral collocation methods. Appl Numer Math 1989;5:177–208.
[42] Tornabene F. Generalized differential and integral quadrature. 2023. Esculapio, Bologna.
[43] Bert CW, Malik M. Differential quadrature method in computational mechanics: a review. 1996.
[44] Shu C, Chen W, Xue H, Du H. Numerical study of grid distribution effect on accuracy of DQ analysis of beams and plates by error estimation of derivative approximation. Int J Numer Methods Eng 2001;51:159–79.
[45] Shu C, Du H. A generalized approach for implementing general boundary conditions in the GDQ free vibration analysis of plates. Int J Solids Struct 1997;34: 837–46.
[46] Shu C. Differential quadrature and its application in engineering. Berlin: Springer Science & Business Media; 2000.
[47] Zong Z, Zhang Y. Advanced differential quadrature methods. New York: Chapman and Hall/CRC; 2009.
[48] Striz AG, Wang X, Bert CW. Harmonic differential quadrature method and applications to analysis of structural components. Acta Mech 1995;111:85–94.
[49] Shu C, Ding H, Yeo KS. Local radial basis function-based differential quadrature method and its application to solve two-dimensional incompressible Navier–Stokes equations. Comput Methods Appl Mech Eng 2003;192:941–54.
[50] Jang SK, Bert CW, Striz AG. Application of differential quadrature to static analysis of structural components. Int J Numer Methods Eng 1989;28:561–77.
[51] Du H, Lim MK, Lin RM. Application of generalized differential quadrature to vibration analysis. J Sound Vib 1995;181:279–93.
[52] Du H, Lim MK, Lin R. Application of generalized differential quadrature method to structural problems. Int J Numer Methods Eng 1994;37:1881–96.
[53] Hsu MH. Vibration analysis of edge-cracked beam on elastic foundation with axial loading using the differential quadrature method. Comput Methods Appl Mech Eng 2005;194:1–17.
[54] Shu C, Chew YT, Richards BE. Generalized differential and integral quadrature and their application to solve boundary layer equations. Int J Numer Methods Fluids 1995;21:723–33.
[55] Sarangan S, Singh BN. Higher-order closed-form solution for the analysis of laminated composite and sandwich plates based on new shear deformation theories. Compos Struct 2016;138:391–403.
[56] Thai HT, Kim SE. Analytical solution of a two variable refined plate theory for bending analysis of orthotropic Levy-type plates. Int J Mech Sci 2012;54:269–76.
[57] Chaudhuri RA, Kabir HR. Fourier analysis of clamped moderately thick arbitrarily laminated plates. AIAA J 1992;30:2796–8.
[58] Kabir HR, Chaudhuri RA. A generalized Navier's approach for solution of clamped moderately-thick cross-ply plates. Compos Struct 1991;17:351–66.
[59] Kabir HRH. A novel approach to the solution of shear flexible rectangular plates with arbitrary laminations. Composites Part B 1996;27:95–104.
[60] Tornabene F, Viscoti M, Dimitri R. On the importance of the recovery procedure in the semi-analytical solution for the static analysis of curved laminated panels: comparison with 3D finite elements. Materials 2024;17:588.
[61] Brischetto S, Tornabene F. Advanced GDQ models and 3D stress recovery in multilayered plates, spherical and double-curved panels subjected to transverse shear loads. Composites Part B 2018;146:244–69.
[62] Tornabene F, Viscoti M, Dimitri R. Static analysis of anisotropic doubly-curved shell subjected to concentrated loads employing higher order layer-wise theories. Comput Methods Eng Sci 2022:22237.
[63] Hodges D, Rajagopal A, Ho J, Yu W. Stress and strain recovery for the in-plane deformation of an isotropic tapered strip-beam. J Mech Mater Struct 2011;5: 963–75.
[64] Ducarne J, Thomas O, Deü JF. Placement and dimension optimization of shunted piezoelectric patches for vibration reduction. J Sound Vib 2012;331:3286–303.
[65] Tzou HS, Zhong JP. Electromechanics and vibrations of piezoelectric shell distributed systems. J Dyn Syst Meas Control 1993;115:506–17.
[66] Nie GJ, Zhong Z, Batra RC. Material tailoring for reducing stress concentration factor at a circular hole in a functionally graded material (FGM) panel. Compos Struct 2018;205:49–57.
[67] Parihar RS, Setti SG, Sahu RK. Recent advances in the manufacturing processes of functionally graded materials: a review. Sci Eng Compos Mater 2018;25:309–36.

[68] Reddy JN, Ruocco E, Loya JA, Neves AM. Theories and analyses of functionally graded circular plates. Composites Part C 2021;5:100166.
[69] Miyamoto Y, et al. Functionally graded materials: design, processing and applications. New York: Springer Science & Business Media; 1999.
[70] Naebe M, Shirvanimoghaddam K. Functionally graded materials: a review of fabrication and properties. Appl Mater Today 2016;5:223–45.
[71] Anthoine A. Second-order homogenisation of functionally graded materials. Int J Solids Struct 2010;47:1477–89.
[72] Zhao S, et al. Functionally graded graphene reinforced composite structures: a review. Eng Struct 2020;210:110339.
[73] Maskery I, et al. An investigation into reinforced and functionally graded lattice structures. J Cell Plast 2017;53:151–65.
[74] Choy SY, Sun CN, Leong KF, Wei J. Compressive properties of functionally graded lattice structures manufactured by selective laser melting. Mater Des 2017;131:112–20.
[75] Tornabene F, Viscoti M, Dimitri R, Aiello MA. Higher order formulations for doubly-curved shell structures with a honeycomb core. Thin-Walled Struct 2021;164:107789.
[76] Tornabene F, Viscoti M, Dimitri R, Aiello MA. Higher-order modeling of anisogrid composite lattice structures with complex geometries. Eng Struct 2021;244:112686.
[77] Benferhat R, et al. Static analysis of the FGM plate with porosities. Steel Compos Struct 2016;21:123–36.
[78] Tornabene F, Viscoti M, Dimitri R. Effect of porosity on the modal response of doubly-curved laminated shell structures made of functionally graded materials employing higher order theories. Structures 2024;60:105848.
[79] Barati MR, Sadr MH, Zenkour AM. Buckling analysis of higher order graded smart piezoelectric plates with porosities resting on elastic foundation. Int J Mech Sci 2016;117:309–20.
[80] Brischetto S, Cesare D. Three-dimensional vibration analysis of multilayered composite and functionally graded piezoelectric plates and shells. Compos Struct 2024;346:118413.
[81] Tsai S, Hann T. Introduction to composite materials. Lancaster: Technomic Publishing Company; 1980.
[82] Nemat-Nasser S, Hori M. Micromechanics: overall properties of heterogeneous materials. Amsterdam: Elsevier; 2013.
[83] Mori T, Tanaka K. Average stress in matrix and average elastic energy of materials with misfitting inclusions. Acta Metallurgica 1973;21:571–4.
[84] Huang JH, Chiu YH, Liu HK. Magneto-electro-elastic Eshelby tensors for a piezoelectric-piezomagnetic composite reinforced by ellipsoidal inclusions. J Appl Phys 1998;83:5364–70.
[85] Li JY, Dunn ML. Anisotropic coupled-field inclusion and inhomogeneity problems. Philos Mag A 1998;77:1341–50.
[86] Ren JG. Analysis of simply-supported laminated circular cylindrical shell roofs. Compos Struct 1989;11:277–92.
[87] Ray MC. Exact solutions of elasticity theories for static analysis of doubly curved antisymmetric angle-ply composite shells. Mech Adv Mater Struct 2024;31:7579–93.
[88] Dwibedi S, Ray MC. Analysis of doubly curved laminated composite shells using hybrid-Trefftz finite element model based on a high order shear deformation theory. Compos Struct 2024;337:118070.
[89] Heyliger PR, Pan E. Static fields in magnetoelectroelastic laminates. AIAA J 2004;42:1435–43.
[90] S. Brischetto, D. Cesare, A 3D shell model for static and free vibration analysis of multilayered magneto-elastic structures, Thin-Walled Struct, 206 (205), 112620.
[91] Brischetto S, Torre R. Thermo-elastic analysis of multilayered plates and shells based on 1D and 3D heat conduction problems. Compos Struct 2018;206:326–53.
[92] Kishore RA, Priya S. A review on design and performance of thermomagnetic devices. Renew Sustain Energy Rev 2018;81:33–44.